UNIVERSIDAD COMPLUTENSE DE MADRID
FACULTAD DE CIENCIAS QUÍMICAS

TESIS DOCTORAL

Convergent functionalisation of micellar probes for oncology and cardiovascular *in vivo* imaging and therapy

Funcionalización convergente de nanopartículas para oncología y cardiovascular *in vivo* imágenes y terapia

MEMORIA PARA OPTAR AL GRADO DE DOCTOR PRESENTADA POR

Hugo Groult

Directores

Jesús Ruiz-Cabello
Fernando Herranz Rabanal

Madrid, 2015

Convergent functionalisation of micellar probes for oncology and cardiovascular *in vivo* imaging and therapy

Funcionalización convergente de nanopartículas para oncología y cardiovascular *in vivo* imágenes y terapia

Hugo Groult

Convergent functionalisation of micellar probes for oncology and cardiovascular *in vivo* imaging and therapy

Funcionalización convergente de nanopartículas para oncología y cardiovascular in vivo imágenes y terapia

Hugo Groult

Directors : Jesús Ruiz-Cabello

Fernando Herranz Rabanal

To my family for being in each line of a book much vaster

To Jess Raw for particular pages of this same book

A. Einstein

Because science can play a double-edged knife in the future challenge we´ll have to face:

- Ne fais rien contre ta conscience, même si c'est l'Etat qui te le demande.

- La possession de merveilleux moyens de production n'a pas apporté la liberté, mais le souci et la famine.

Because the best involvement is our behavior in our day to day life:

- Nous savons de la vie quotidienne que nous existons d'abord pour d'autres personnes, car de leur sourire, de leur bien-être dépend notre propre bonheur.

- Trois idéaux ont éclairé ma route et m'ont souvent redonné le courage d'affronter la vie avec optimisme: la bonté, la beauté et la vérité.

Because science is not everything:

- La seule chose absolue dans un monde comme le nôtre, c'est l'humour.

- Un homme qui n'est plus capable de s'émerveiller a pratiquement cessé de vivre.

- L'imagination est plus importante que le savoir.

Table of Contents

Acknowledgments

Professional

Above all, I warmly thank my directors Jesús Ruiz-Cabello and Fernando Herranz for their supervision in the achievement of this phD during these 4 years of intense training which give me the opportunity of a great professional jump. Their teaching played a crucial role in the quality of this work and their wise advices have greatly contributed in the improvement of my knowledge in the pharmacochemistry field.

I would like then, to especially thank the closest collaborators for the different results achieved. Their contributions have been essential in such an interdisciplinary field as nanomedicine. In particular:

- Jesús Vázquez and Juan-Antonio López from the Vascular Biology & Inflammation department of CNIC, Izaskun Bilbao and Marina Benito from the Advanced Imaging Unit of CNIC for their participation to the development of "Phosphatidylcholine-Coated Iron Oxide Nanomicelles for *In Vivo* Prolonged Circulation Time with an Antibiofouling Protein Corona" (Chapter 1).

- Ana Victoria Lechuga and Jesús Mateo from the Advanced Imaging Unit of CNIC for their participation to the development of "Atherosclerosis plaque characterisation by enzymatic entrapment of phosphatidylcholine coated nanoparticles" (Chapter 2).

- Coral Velasco and Juan Pellico from the Advanced Imaging Unit of CNIC, Moreno Zamai from the Microscopy Unit of CNIC, Fernando Cusso, Eugenio Cantelar and Martina Dobrincic of Autonoma University of Madrid for their participation to the "Parallel multifunctionalisation of nanoparticles: A one-step modular approach for in vivo imaging" (Chapter 3).

- Alfonso Fernandez-Mayoralas, Isabel Garcia-Alvarez from Institute of General Organic Chemistry and Lorenzo Romero from Neural Plasticity group of Cajal Institute of CSIC for their participation to the "Antitumoural glycosides-coated iron oxide micelles" (Chapter 4).

Personal

My deep and warmly thanks are for a group people who have decided to dream from near and far within a hidden coloured district of Madrid. First Helena who introduced me to this group to thanks me that I let her alone at midnight in Fuencarral station for the support that is no less than the one of a little sister and for the septic tank "affair"; Elsa who shared the same passion for the philosophical shushi, Agatha for her "bzz bzz cumbia waves", Dani because she is hipster but much more, Ruth for the-day to-day "pompidup". A particular thank for Pablo "el Caracol" and his brother David who give a meaning to the word "encounter" but also to the words "tertulias sin fin bajo estrellas para soñar y reir y cantar y escuchar musica". Of course, el "grande" hip-hop man Fidel III, the veteran friend here that "molaaAAh". And all the other people of this group Nico, Ruben, Tania, Nata, Joa, or cousins of this group (Miguel, the American "Beauties"…). A special thought to Jess for the entire path travelled made of "bombaaas" memories, confistruction, Irn-Bru, and LL simplicity. From the "vueltas" given to the writing of this book, I probably miss of her own lines. Still holding the MJ mention, the 82 breaths matrress record, and the award of the original cakes.

Thanks to Cyrielle and Xose who always held a special place in my Madrid life for a special friendship, i wish them beautiful "Pulpo-coqsss".

Thanks to all my colleagues of CNIC and all the technical CNIC personal for the support during these hard years and the Friday noon "cervezas".

A special thanks to all the pre-doctoral members of the pulmonary imaging network of the "Marie Curie" European program especially Andrea, Alessia, Felix, Pablo, Shama and Asmund but also Dominique, Flavio and Pavla. I get to know them as colleague and they became very close friends based on the mutual support we shared in front of the same challenges we faced and a multicultural aspect that I particularly cherish. Guys, if you begin to forget the crazy moments just asked to the "magic bowl" otherwise "Duck pouet pouet" will charge to make you a speech.

My thanks go also for the colleagues with whom I shared my first laboratory in Marañon Hospital. I especially think to Juan Antonio whom humanism and open mind should be a model in all the scientific organisations but also his dance move.

Other special thanks go for the "group of the second floor" of the Institute of General Organic Chemistry of CSIC (Isa 1, Isa 2, Dani, Isra, Juanan, Elisa, Lourdes and many others). The friendship we built in a former research centre expands far from the laboratory. Their team skills, spirit of relationship in a work atmosphere is until now the most inspiring I met as well as their concept of "sobremesa".

Thanks to the "Chikasses" (Didine, Ju, Sandrine, Fouxi, Tuture, Geogeo, Jb, Présidente) and members of the "aramine team". They always remind me that friendship is above geographic distance (or at least the distance of a golf ball). Choice of living abroad is never easy and this confidence is one of the most important key.

Thanks to the people of theatre classes "Casa de los Jacintos" to believe that all misfortune is also a gift to play with. Hope we soon play to "pilla-pilla" in the market soon.

I would like also to thanks the "Erasmus" (converted now in: "close") friends and the" friends of these friends" (converted as well: in "close"): Fabian, Sandra, Fifi, Elena, Yuri Gargarine, Atuk el grande, Paloma, Aitor

Finally and evidently, my biggest thoughts are for my family whom Flo the biggest Arlequin ever

List of abbreviation

ApoE-KO : Apolipoprotein E (apo E) deficiency

AuNP : Gold nanoparticles

BSA : Bovine serum albumin

CT : Computed tomography

DLS : Dynamic light scattering

DFO : Deferoxamine

DMEM : Dulbecco's modified eagle medium

DOTA : 1,4,7,10-tetraazacyclododecane-1,4,7,10-tetraacetic acid

EPR : Enhanced and permeability retention effect

18F-FDG : Fluorodeoxyglucose

FDR : False discovery rate

FTIR : Fourier transformed infrared spectroscopy

ID 50 : Inhibitory dose 50%

IONP : Iron oxide nanoparticle

I.V.A : IntraVenous Administration

(LC)-MS : (Liquid chromatography)-Mass spectroscopy

M Φ : Macrophage

MAFs : Mouse adult fibroblasts

MEFs : Mouse embryonic fibroblasts

MRI : Magnetic resonance imaging

MS : Mass spectrometry

MW : Molecular weight

NMR : Nuclear magnetic resonance

NP : Nanoparticle

NIR : Near infrared

OA : Oleic acid

OI : Optical imaging

OM : Oleylamine

P80 : Polysorbate 80

PBS : Phosphate buffer saline

PC : Phosphatidylcholine

PC-PLC . Phosphatidylcholine specific phosphalipase C

PDI : Polydispersity index

PEG : Poly(ethylene glycol)

PET : Positron emission tomography

RES : Reticuloendothelial system

RGD: Peptide targeting Integrins $\alpha_v\beta_3$

ROI : Region of interest

RPMI : Roswell park memorial institute medium

SPC : Spectral peptide count

TEM / HRTEM : (High resolution) transmission electronic microscopy

TGA : Thermogravimetric analysis

UCNP: Upconverting nanophosphors

US : Ultrasound

UV/VIS : Ultraviolet/Visible

VSM : Vibrating sample magnetometer

XRD : X-Ray diffraction

Introduction

1. Nanotechnology in Medicine

1.1 Nanomedicine

Nanotechnology studies materials and systems whose structures and components exhibit novel or significantly improved physical, chemical and biological properties, phenomena and processes due to their nanoscale size (according to the definition given by the US Nanotechnology Initiative in 2000).[1] This definition based on size, is very broad and includes a large panel of different entities, from physical devices to molecular self-assemblies, for a wide range of applications in numerous areas.
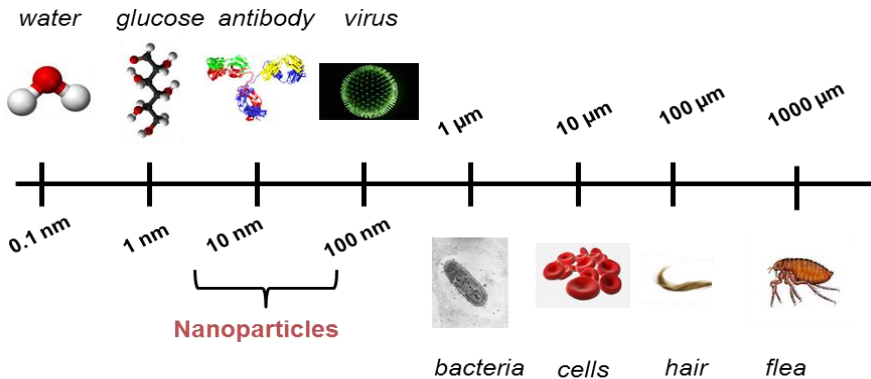
Figure I.1 Size of different biological entities in comparison with nanoparticles.

When nanotechnology is used specifically for medical applications, we refer then to "Nanomedicine". It is nowadays mostly related to the application of nanostructures for treatment, diagnosis, monitoring and control of biological systems according to the National Institutes of Health in USA.[2] The most remarkable property of the nanomaterials for medicine is their ability to work at the frontier of the molecular and cellular levels (Figure I.1). It allows

3

overcoming many biological barriers and acting in the process of the disease, as a bridge between the biomolecular pathways and the microscopic cells or pathogenic agents. Moreover, nanoparticles have a high ratio of surface area to volume allowing a high versatility for their engineering. The fruitful marriage of nanotechnology and medicine has been already demonstrated with many examples published or in the clinic but the most promising perspectives are still to come.[3] Besides, it seems that the importance of nanomedicine is taken with great attention as NIH classified it among the top priorities and more than $3.8 billion is allocated in research and development for nanotechnology each year.[4]

Key to understand: A piece of history of nanomedicine

Starting in 1959 with the famous talk of Richard Feynman at the annual meeting of the American Physical Society where he developed the vision of manipulating and controlling things on a small scale,[5] nanoscience progressively grow up to become one of the most important field in research and investment (2 billion euros estimated for 2015)[3] Although the application of nanoscience to medicine is relatively new, several basic approaches were published a few decades ago. The pioneer example of lipid vesicles, knows today as liposomes, date from 1965. An example of the controlled release of a drug was proposed in 1976. The 80´s witnessed the popularisation of metallic nanoparticles for medical imaging. First long circulating stealth polymeric nanoparticle was proposed in 1994 showing the beginning of a more complete vision (considering the physical and biological behavior) in the investigation of the nanoparticle.[6] More recently, we have witnessed the apparition of quantum dots in 1998 and up-converting nanophosphors and nanowire sensors in 2001.[7]

Table I-1 shows examples of the most common nanomaterials commercially available or in advanced phases of clinical trials. This table includes just a few of the most remarkable nanomaterials.[2] A complete table would take several pages since the number a type of nanoparticles is endless; a clear demonstration of how active this field is these days. Due to their versatility, these nanomaterials are being used *in vitro* for. e.g. tests of biological samples based on nanoparticles (urine pregnancy, human immunodeficiency virus or polymerase-chain reaction assays)[2] and *in vivo* where nanoparticles find multiple applications as contrast agents for different medical imaging techniques and as drug-delivery platforms.[6] For instance, nanoparticulate contrast agents can accumulate passively in tumours by the enhanced permeability and retention effect (leaky vasculature around the cancerous cells) for diagnostic imaging.[8] Labelling studies in preclinical applications also employ nanomaterials which includes radionuclides or fluorophores in their coating.[1] Nanomedicine is also widely used for drug delivery. Again a major application is related with controlled-release or delivery of anticancer compounds. Drug release polymers, liposomes or viral and protein structures are examples of common classes preferentially used as nanovectors in drug delivery research.[9]

Table I.1 Example of nanomaterials on the market and in clinical trial.

Nanomaterial	Trade Name	Application	Target	Current Status
Metallic				
Iron oxide	Rienso	MRI contrast	Liver	FDA approved
	Combidex		Lymph nodes	Phase 3 clinical trials
	Nanotherm	Cancer therapy	Various forms	Phase 3 clinical trials
Gold	Verigen	*In vitro* diagnostic	Genetic	FDA approved
	Aurimmune	Cancer therapy	Various forms	Phase 2 clinical trials
Nanoshells	Auroshell	Cancer therapy	Head and neck	Phase 3 clinical trials
SemiConductor				
	QDots, EviTags, nanocrystal		Molecular sensing structure	Research use only
Organic				
Protein	Abraxane	Cancer therapy	Breast	FDA approved
Liposome	Doxyl/Caelyx	Cancer therapy	Various forms	FDA approved
Polymer	Oncaspar	Cancer therapy	Leukemia	FDA approved
	CALAA-01		Various forms	Phase 2 clinical trials
Dendrimer	VivaGel	Microbicide	Cervicovaginal	Phase 2 clinical trials
micelle	Genexol-PM	Cancer therapy	Various forms	Phase 4 clinical trials

The term Nanoparticle (NP) is used in medicine in a generic way including a wide range of distinct nanostructures some of them hybrid or combination of different ones. When used in the literature it can means a plethora of very different chemicals; micelles, liposomes, dendrimers, polymeric nanoparticles, nanobubbles, metallic nanoparticles, silica particles, carbon nanotubes, quantum dots, viral based nanoparticles, etc. In this work we have focused in metallic nanoparticles since they show very interesting properties for imaging. Hereafter, the term NP we will be used to call mainly metallic nanoparticles.

1.2 Characteristic of nanoparticles for nanomedicine

NP have special structures which places them at the cross of many different disciplines. They are basically composed of a metallic core surrounded by an organic coating bound to the surface (Figure I.2).[10] To fully understand their physicochemical and biological properties both components must be fully characterised. The metallic core provides the size-dependent properties for which the material is most well-known. This is the case for the three types of nanomaterials and associated properties that we will describe in this work; superparamagnetism, surface plasmon resonance and up-conversion fluorescence. Table I.2 shows the type of NP currently used for the most important imaging techniques; ultrasound (US), magnetic resonance imaging (MRI), computed tomography (CT), positron emission tomography (PET) and optical imaging (OI).[11] Thus, the research in nanomedicine is usually centred in one of three aspects: new properties of the nanomaterial core, new bioconjugation techniques on the surface or new applications.[10]

The surface of the NP is of paramount importance, it determines the targeting capabilities, colloidal stability and much of the *in vivo* fate of the NP.[12] Most recent advances deal with the term functionalisation; the attachment of molecules on the surface of the particles to provide colloidal stability and/or biological targeting.[13] Surface coating is responsible for a range of specific requirements for the *in vivo* biological use of the NP, which concern multidisciplinary fields such as biochemistry, molecular and cell biology, pharmacokinetics or toxicity.[14]

Table I.2 Type of NP used in the different imaging techniques.

Technique	Advantages	Disadvantages	Nanoparticles used
US	Easy to perform / cheap Non invasive Nonionizing radiation	Low resolution high reflection and attenuation	Emulsion s and gadolinium oxide NP
CT	Wide field of view Cross sectional images Differentiation of body tissues	Lack of contrast agent Radiations Costs	Gold and silver nanoparticles, iodine based products.
PET	Can image biochemical anf physiological phenomena	Radiations Motion artifact Resolution Expensive	NP tagged or conjugated with radioisotopes (19F, 68Ga, 89Zr)
MRI	Higher resolution Anatomical details Not ionizing	Expensive	Iron oxide NP or NP tagged with gadolinium chelates
OI	High sensitivity High resolution Easy to perform /cheap	Low penetration, almost only limited to pre-clinical applications	NP tagged with organic fluorophores Up-converting nanophosphors

We detail below the structure (Figure I.2) and main features of the coating of metallic NP in relation with the purposes they require to fulfil. The possibility of introducing several imaging agents and/or biological targeting moieties and drugs, summarize under the expression "multifunctionality" is one of the unique features of this new type of chemistry. However, this multiplex incorporation still presents some challenges, particularly the need to reduce numerous sequential steps of the synthesis for reproducibility and scaling-up production issues.[15–17]
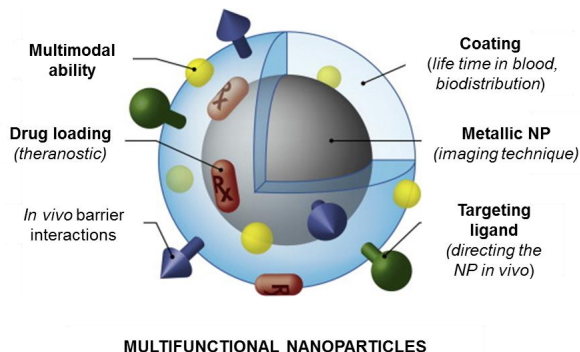
Figure I.2 Schematic representation of the structure of metallic nanoparticles.

*Biodistribution and pharmacokinetic*s: The coating has to provide a good colloidal stability to the NP in physiological media and minimise their natural tendency to aggregation. Another important role is to protect the probe from a rapid opsonisation and clearance by the immune system before its bio-action.[18] Polymers surfactants (also called "stealth" layer) like dextran, polyethylene glycol (PEG) or poly(lactic-co-glycolic acid) (PLGA) are examples of coatings designed to extend blood circulation times *in vivo* and reduces NP uptake by the reticuloendothelial system or mononuclear phagocyte system, and are now widely used for the synthesis of blood pool agent.[19] It has also been demonstrated that toxicity of the NP can be modulated by the help of suitable coatings.[20] Liposomes and micelles are other very popular organic coating nanostructures. They are amphiphilic non covalent organic assemblies and can integrate the NP either in the hydrophilic or lipophilic portion of the assemblies according to the hydrophilicity of the NP. These structures present important advantages especially when used at the same time for drug delivery and excellent properties for encapsulation of imaging probes.[21,22] Finally protein carriers have been also proposed for NP transport and colloidal stabilisation.[23]

Targeting: Another important feature is the possibility of adding to the coating a targeting ligand towards a biomolecule associated with a disease, enabling the ability of a selective recognition. A plethora of biomolecules has been assessed for directing NP *in vivo*. Small organic molecules, peptides, proteins, antibodies or aptamers conjugated to the coating have successfully implemented targeting abilities via ligand/cell receptors interactions (Table I.3).[24] Development of new specific or selective ligands is nowadays a hot topic in the whole nanomedicine research, as well as all the chemistry for the surface modification with these ligands.[25]

Table I.3 Examples of targeting ligand receptors combined with NP.

Type	Name	Target	Application
Small molecules	Folic acid	Folate receptor	Breast cancer imaging
	Methotrexate	Folate receptor	Brain tumour imaging and therapy
	Non peptide RGD mimetic	Avβ3 Integrin	Integrin positive cell imaging
	Mimetic of the sialyl Lewis	E-selectin	inflammatory disease imaging
Peptides	RGD	Avβ3 Integrin	Breast cancer imaging
	Chlorotoxin	MMP-2	Brain tumour imaging and therapy
	Synaptotagmin	Phospholipids	Apoptosis imaging
	VHSPNKK	VCAM-1	Cardiovascular disease imaging
Aptamers	A 10 RNA aptamer	Prostate-specific membrane antigen	Prostate cancer imaging
	Thrm-A and Thrm B DNA aptamer	Alpha-thrombin protein	Serum protein dection
Proteins	Annexin V	Phosphatidylserine	Apoptosis imaging
	Luteinizing hormone relasing (LHRH)	LHRH receptor	Breast cancer imaging
	Transferrin	Transferrin receptor	Breast cancer imaging
Antibodies	Monoclonal antibody A7	Colorectal carcinoma	Colon cancer imaging
	Herceptin	Her2/neu	Breast cancer imaging and therapy
	Rituxan	CD20 antigen	Lymphoma imaging therapy

Multimodality: Medical imaging is now reaching an inflexion point by combining different techniques. The aim is to get simultaneous or sequential images of improved quality and complementary information. For instance PET/MRI and PET/CT hybrid systems were developed with the idea of gaining sensitivity and improved spatial resolution. The metallic core of NP usually provides one or several (for instance the UpConverting Nanophoshors or the core/shell structure) imaging ability.[16] Surface modification of the coating is also a preferential way to integrate other organic imaging modules especially chelates for radioisotopes (for PET/SPECT imaging) or Gd^{3+} (MRI contrast agent) and fluorophores for OI (Table I.2).[26]

Drug loading: Nanoassemblies, often called nanovectors or nanocarriers when used in the drug delivery field, today are probably one of the most promising options in the drug delivery research.[27] It offers many benefits among others: targeting, pass through various biological barriers, local action (allowing reduced dosage and fewer side effects), better drug stability, possibility of sustain and controlled release, overcome drug solubility issue, etcetera. The core of metallic NP provides an imaging possibility itself, and thus tracking of the delivery is also possible. [9]

_____

Key to understand: Theranostic

The new field of theranostics refers to the simultaneous integration of diagnosis and therapy aiming at a rapid, selective and more efficient therapeutic intervention. The term derived from thera(py) and (diag)nostics to merge both fields for advanced applications. The main features of the NP, multifunctionality and targeting, appear ideal for this new trend.[28] Nanotheranostic, represents then, a NP which gathers diagnostic and therapeutic functions. In fact, considering the main applications and uses of nanomedicine described above, this opportunity emerged as the natural

evolution of the field. Again, if targeting properties are added, it is possible to obtain highly elaborated probes for the future.[29] Advanced theranostic nanomedicine is multifunctional in nature, capable of diagnosis and delivery of therapy to the diseased cells with the help of target. Consequently, many structures are proposed, they gather one or several imaging modalities (principally for MRI, PET, CT, US, OI) with a therapeutic function, many times encapsulating a molecular or biological drug or just designates an additional physicochemical property of the NP itself that can be used for therapy (hyperthermia or photothermal).[30] Almost all the NP cited reported in Table I.2, have been applied as well as nanotheranostic agents.

2. Iron oxide Nanoparticles

Because of the importance of iron oxide nanoparticles (IONP) in nanomedicine and as this work mainly focus on the synthesis and biological application of new IONP, we will briefly describe the main features of this kind of NP. Two additional sections will also briefly described the up-converting nanophosphors (UCNP) and gold nanoparticles (AuNP) which also appear in this research work.

2.1 Properties of Iron oxide Nanoparticles

IONP are particles of iron oxide of with a core size usually between 2 to 50 nm, exist under two main chemical forms: magnetite (Fe_3O_4) and its oxidised relative, maghemite (γ-Fe_2O_3) which are biocompatible and with very low toxicity.[31] Because of their nanometric size, both hold the particularity to be superparamagnetic, a type of magnetism. The magnetism in a solid basically depends on the type of electrons and the type of occupied orbitals in the atoms of the material. For some materials, by applying an external magnetic field, the electrons generate magnetic dipoles that, on average, align with the field creating a net magnetic moment. The phenomenon of superparamagnetism appears when the size of the NP is smaller than the

magnetic domain. Then the magnetic moments are randomly oriented, due to Brownian motion, until an external field is applied. In this case, typically for MRI applications, all the NP align with the external field generating a permanent dipole much stronger than the one generated in paramagnetic compounds (i.e. gadolinium chelates). Once the field disappear, the magnetic moments (NP) come back to be randomly oriented and the dipole (net magnetisation) disappear.[32] This property is the origin of the applications for which are used the IONP such as MRI, magnetic delivery, isolation/purification of biomolecules.[33,34] The last application introduced in the field is magnetic particle imaging, a new preclinical imaging technique that still need further technical development.[35]

2.2 Applications of Iron oxide Nanoparticles

Because of the superparamagnetic aspect combined also with the general features of the NP (section 1.2), IONP serve at numerous exciting applications in biomedicine.[36–38]

Contrast agent for MRI :

Key to understand: Magnetic resonance imaging[39]

MRI is a routine non-invasive medical imaging technique for diagnostic applications in the clinic. MRI is based on the principles of nuclear magnetic resonance (NMR) spectroscopy. To perform NMR studies, we need a set of nuclei, a very powerful external magnetic field and radiofrecuency pulses to perturb the resultant magnetisation aligned with the magnetic field. The resulting response to the external perturbing electromagnetic field is the phenomenon that is exploited in NMR spectroscopy and MRI (although for imaging we need extra gradients to code the information spatially). All nuclei

13

with a nonzero nuclear spin experience this phenomenon, but the most frequently used in biomedicine are the ones of spin ½, in particular the protons of the water. When the nuclear spin is of ½, the presence of a powerful external magnetic field leads to an energy splitting in two different energy levels. At the thermal equilibrium, the two energy states corresponding to this energy splitting are not equally populated, and a net magnetic moment is established. Upon application of an additional electromagnetic fields this energy states are perturbed and the effect of relaxation is to take magnetisation back to original net magnetic moment at thermal equilibrium. The time dependence on relaxation is different for longitudinal and transverse magnetisation; Longitudinal relaxation tends to a constant value M_0, decaying to M_0 exponentially with a time constant T_1. Transverse relaxation tends to zero, decaying exponentially with a time constant T_2. They both depend on the main magnetic field, temperature, intrinsic properties of the sample (proton density in the tissue, diffusion) and the type of sequences of the additional radiofrequency pulses. Consequently, relaxation times are different according to the tissue and when they are monitored by an MRI scanner, produce different intensity to create an image. Contrast agents affect this relaxation process to change the signal intensity in the neighbouring tissues (Figure I.4).
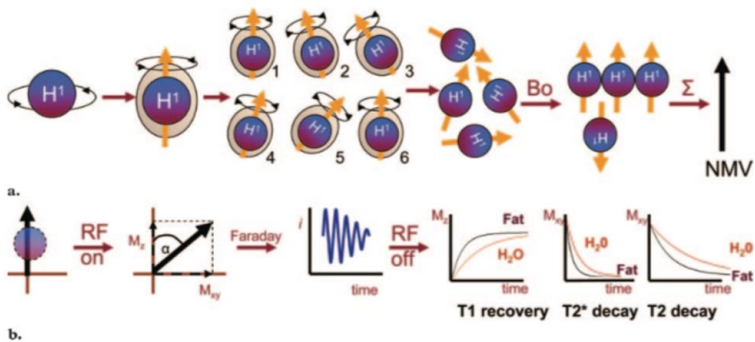

Figure I.4 Basic principles of MRI.

Because of their magnetism, IONP will alter the magnetic field interacting with the local magnetic field produced by the spins of protons. It causes a shortening of the longitudinal and transversal relaxation times (T_1 and T_2) of these protons after their submission to external magnetic field

14

stimuli. This effect is traduced in contrast enhanced MRI either by a positive or, more frequently, a negative or signal void in the area where the superparamagnetic IONP have accumulated. In the case of IONP, they normally shorten considerably T_2 which explains they acts as negative contrast agent in the traditional MRI sequences. Alteration of the T_1 process require a closer interaction with the contrast agent and only ultrasmall IONP can acts for positive signal enhancement, although some special MRI sequences have been also showed to get positive enhancement.[40] This last decade, the investigation of functionalised IONP has executed in parallel with the technical advances achieved in MRI, with the possibility of visualising biological events at the cellular level.[41] Several ferrofluids are already on the market or in clinical trials (Table I.1) but also above all plethora of functionalised IONP have been proposed for advance applications in preclinical research. For instance, integral targeted IONP for multimodal cancer imaging which integrate a therapeutic function are regularly proposed, we refer here to the excellent review of McCarthy and Weissleder on this topic.[42] IONP have been also proposed as MRI contrast agents for several other clinical applications in cardiovascular medicine *via* their uptake by macrophages in inflamed areas, stem cell tracking or diabetes.[43,44]

Drug delivery vehicles and therapy: As described before, because of the possible "multifunctionality" character of the NP, IONP can be designed to release conventional drug/therapeutic loaded/integrated in its assemblies, with the normal advantages associated to the NP structure (Figure I.2).[45] From the applications specific to the IONP, the main ones are magnetic drug targeting and hyperthermia. The first one uses a local magnet field (either external or implanted internally) to drive the IONP until the region of interest by magnetic attraction. For applications with tumours, several successful studies in small animal models and clinical trials have already reported demonstrating partial

remission.[46] On the contrary, the treatment with targeted hyperthermia is based on the fact that abnormal cells or bacteria suffer apoptosis if exposed to slightly higher temperatures. The main limitation is the low discrimination between healthy and malignant cells with concomitant harmful effects. Iron oxide cores can produce a local heating if submit to an alternating magnetic field and reach only the affected zone if pretargeted beforehand. Magnetic hyperthermia treatment is now in some clinical phase II studies and highly used in preclinical research.[47]

Finally, nanoparticle driven gene therapy with optimised transfection or biosensing (detectors sensible to the presence of a biomolecule) are others non-negligible applications of IONP.[48,49]. Moreover, the chemical engineering of the organic coating is under constant development to improve/enhance the complex route of synthesis or *in vivo* behavior of the probe to reach the final biomedical objective of the probe.[31,36,50]

2.3 Synthesis of Iron oxide Nanoparticles

Due to the relevance and wide spectrum of applications with IONP, there has been a tremendous increase in the synthetic methodologies in the past years. The most relevant approaches include methods such as coprecipitation[51], thermal decomposition[52], sonolysis[53], sol-gel processes[54], spray and laser pyrolysis[55], hydrothermal and high temperature synthesis[56,57], nanoreactors such as protein cages[58], vesicles[59], microemulsions[60] and microwave-assisted synthesis[61–63]. For the sake of simplicity, we will focus here only on the most interesting ones from the biomedical point of view: coprecipitation, thermal decomposition and microwave-assisted synthesis. Particularly, thermal decomposition has a higher prevalence and projection in the field and it is the method we have applied throughout this work.

Co-Precipitation Method. This is one of the most employed methodologies for the synthesis of IONP for biomedical applications. This process involves a reaction of the aqueous mixture of Fe^{2+}/Fe^{3+} salt solutions with a base. Under these conditions, magnetite NP are formed by aggregation of primary particles within a $Fe(OH)_2$ gel. This methodology, developed by Massart *et al.*, was carried out initially without the incorporation of any stabilizing molecule on the surface of the nanoparticles.[64] In this pioneered work, authors reported the controlled preparation of IONP through alkaline precipitation of $FeCl_3$ and $FeCl_2$. Magnetite (Fe_3O_4) particles formed were roughly spherical with diameter of 8 nm. In this approach magnetite is prepared by adding a base to an aqueous mixture of Fe^{2+} and Fe^{3+} salts in a 1:2 molar ratio. The overall reaction may be written as follows, leading to the precipitation of black magnetite:[64]

$$Fe^{2+} + 2Fe^{3+} + 8OH^- \rightarrow Fe_3O_4 + 4H_2O$$
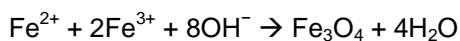
A wide variety of parameters must be considered in this method in order to control size, magnetic characteristics and colloidal stability in the solution. Magnetisation can vary drastically with synthesis variations even within particles of similar size, due to incorporation of impurities into the crystal structure and involvement of surface effects.[65] Generally, saturation magnetisation values of magnetite NP obtained by this method are in the range of 30–50 emu/g; lower than the 90 emu/g reported for their bulk form.[66] In addition, an exhaustive control of different parameters in both the synthesis and purification steps, such as the pH, is essential to obtain NP with specific size.. As a result, the production of narrowly dispersed particles remains a significant challenge in this method.[67] Other factors like the fine adjustment of $Fe^{3+}:Fe^{2+}$ ratios, heating regimes, and the coating–iron ratios must also be strictly controlled.[68] After the initial development by Massart *et al.*, the number

of coatings that have been used, vary from polymers[69,70], to dendrimers[71] and organic acids[72]. The main advantage of the co-precipitation process is that large amount of water-stable NPs are obtained. However, the control of particle size distribution is limited, because only kinetic factors are affecting the growth of the crystal. This leads to the synthesis of somehow heterogeneous samples in terms of size and shape. Another problem that can be found with this approach is the weak attachment of the surfactant to the surface and the reduced number of functional groups that can be found on the surface. All these drawbacks complicate the final functionalisation of the NP for biomedical applications.

       Thermal Decomposition of Organic Precursors. High temperature decomposition of iron organic precursors mixed with surfactants in organic solvents is progressively becoming the standard way for the preparation of IONP. This method yields NP of narrow size distribution, good crystallinity and high magnetisation saturation values (Figure I.5).[31] The first synthesis introduced by Aliviastos et al. reported the injection of $FeCup_3$ (Cup:N-nitrosophenylhydroxylamine) solutions in hot trioctylamine resulting into NP of 4 to 10 nm average diameters as a function of the temperature (250 °C to 300 °C) and the quantity of iron precursors added.[73] A second method consisted in the preparation of iron NP by injection of the organic $Fe(CO)_5$ precursor in the surfactant mixture followed by an in situ oxidation phase to produce highly crystalline and monodispersed maghemite NP with sizes from 4 to 16 nm.[74–76] Although the hot injection technique guarantees instant nucleation and homogenous growth for an optimal quality of the NP, it also shows drawbacks mainly related to safety and toxicological issues.[77] Heating up processes were then proposed with iron oleate, an intermediate prepared from $FeCl_3$ and the mechanisms of crystallisations studied.[78,79] In 2002, Sun et al. described a single step synthesis using iron acetilacetonate thermal degradation by

18

progressive heating in diphenyl ether in presence of alcohol, oleylamine and oleic acid surfactants.[52,80] The magnetite NP prepared with this method have dimensions in the 3 to 20 nm range adjusted by a control of the reaction time or the amount of the low complexing reactants. A summary of the most relevant approaches using the thermal decomposition of organic precursors can be found in Table I.4.
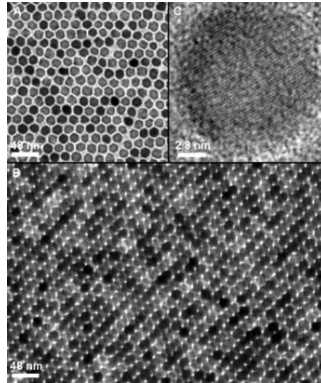
Figure I.5 TEM images of 16 nm size IONP synthesised by the decomposition of organic precursors: (A) a monolayer assembly, (B) a multilayer assembly, (C) HRTEM image of a single Fe_3O_4 NP.

The size and morphology of the NP are the resultant of the growth mechanism during the thermal decomposition method. We will focus here only on the influence of the different reaction conditions, further details of the growth mechanism models have been reviewed in several occasions like in Gao *et al.*[33] For instance, the time of reaction for the growth phase clearly regulates the size.[81] Also, IONP prepared with higher temperatures lead to larger sizes; successfully employed by heating with various solvents of high boiling points.[78] Another critical variable on the structural features of the NP is the surfactant or mixture used for emulsifying the systems and to control nucleation. It was observed that the size of the NP is inversely proportional to

the tendency of the surfactant to coordinate with the iron atom.[82] Thus, common methods often control the size of the NP by addition of a low complexing surfactant.[83] Sizes can also be modified depending on the molar proportion Fe:surfactant.[84] It has also been shown that the affinity properties of the solvent for iron can play a major role in this process.[73] Finally, although few studies have also assessed the influence of the organic iron precursors, preliminary observations showed that a narrower and controlled particle size distribution is favoured with a specific iron intermediate complex before the generation of the cores.[85]

Shape-controlled synthesis of iron oxide IONP with this method can be performed under thermodynamic or kinetic control. Thermodynamic control is the key aspect when working with low concentration of precursors, yielding spherical NP to minimize the surface energy. When working at high concentration conditions, kinetic control will lead to the formation of particles with other morphologies such as cubic or elongated particles.[73,79,86]

The above described thermal decomposition synthesis is a powerful method to produce IONP of higher quality than the ones prepared by the aqueous routes.[83] One drawback of this approach is that the hydrophobic character of the NP makes compulsory a second step to transfer IONP to water. The requirement of rendering hydrophilic nanomaterials for *in vivo* applications has boosted the appearance of new efficient chemical routes for the functionalisation of NP. Before the use of these new alternatives, the efforts focused in the modification of the thermal decomposition method with hydrophilic surfactants and/or polar solvents to provide hydrophilic IONP in a one-pot synthesis route. Gao's group first reported the use of 2-pyrrolidone, a strong polar organic solvent.[87] In a first attempt, 2-pyrrolidone had also the role of surfactant with $Fe(acac)_3$ as the iron precursor. This method was assessed also with $FeCl_3 \cdot 6H_2O$ as precursor to obtain IONP with average size between 4 to 60 nm.[88] In order to synthesize IONP stable in physiological

solutions, mono or di carboxylic-terminated poly(ethylene glycol) polymers were introduced as surfactant.[89,90]

Table I.4 Main aspects of the synthesis of IONP by Thermal Decompostion methods.

Iron precursors	Surfactant	Solvent	T/°C	Shape and Size
FeCup$_3$	Octylamine	Trioctylamine	250–300 °C	4–10 nm
Fe(CO)$_5$	Oleic acid	Dioctyl ether	300 °C	4–16 nm
Fe(CO)$_5$	TOPO or DDA	Ortho-dichlorobenzene	180 °C	12 nm variation possible (diamond, triangle, spherical) <20 nm
Fe(acac)$_3$	Oleic acid Oleyl amine	Phenyl ether or benzyl ether	259–298 °C	Seed mediated growth: 20 nm
Fe(oleate)$_3$ from FeCl$_3$ and sodium oleate	Oleic acid	1hexadecane or trioctylamine	274–365 °C	5–22 nm
FeO(OH)	Oleic acid	1-octadecene	320 °C	6–30 nm
Fe(acac)$_3$ FeCl$_3$	2-pyrrolidone 2-pyrrolidone	2-pyrrolidone 2-pyrrolidone	245 °C	5 nm Seed mediated growth: 11 nm
Fe(acac)$_3$	m PEG-COOH d PEG-COOH	2-pyrrolidone 2-pyrrolidone	240 °C 240 °C	12–30 nm
Fe(acac)$_3$	PVP	N-vinyl-2-pyrrolidone	200 °C	4–40 nm
FeCl$_3$	PAA	Diethylenglycol	220 °C	3–12 nm

The amphiphilic character of the PEG coating confers on IONP important properties such as high stability and solubility in different media.[87] Moreover di-substituted carboxylic polymers have the advantage of showing a reactive group on the surface for further functionalisation. These results opened a range of new studies assessing others polar organic solvents and surfactants such as Polyacrylic acid, *N*-vinyl-2-pyrrolidone, glycols or diphenyl oxide.[91,92]

Microwave-Assisted Synthesis. In general, most of the synthetic reactions to obtain IONP include heating through traditional heat transfer systems, such as oil baths, sand baths and heating jackets. These heating techniques are, however, rather slow and a temperature gradient can develop within the sample leading to local overheating spots. All these parameters may have an important effect both in the nucleation and growing steps of the synthesis. A fundamental aspect of the microwave approach is the dielectric heating; under these conditions the energy is introduced into the reactor remotely. The microwave radiation passes through the walls of the vessel and heats only the reactants and solvent and not the reaction vessel itself. In modern pressurised equipment, the temperature increase is uniform throughout the sample, and facilitates heating far above the conventional boiling point of the solvent. All these features allow for the synthesis of IONP with greater control/reproducibility of size and dispersity, as well as enhanced crystallinity. The characteristics we just highlighted are attracting the attention of many scientists working in the synthesis of NP. Currently there are examples in the literature on the use of microwaves for the synthesis of maghemite NP[61,62,93], mixed maghemite and magnetite NP[94] and pure magnetite[63]. Due to the novelty of the approach most of the recent publications focused more in the synthesis of the nanoparticle core and rather poorly in the colloidal stability of the synthesised NP in water. This is gradually changing and there are examples already using PEG and dextran as surfactants for biomedical applications.[57,95,96]

2.4 Biofunctionalisation of Iron Oxide Nanoparticles

When developing nanoparticles for biomedical applications, one of the key point is the functionalisation of the nanoparticles' surface. Ideally, this functionalisation should confer NP with very good colloidal stability in the usual conditions for *in vivo* administration (*i.e.*, 0.9% NaCl, PBS, *etc.*) and as many as possible functional groups to facilitate the binding of target or specific biomolecules. The strategy is different depending on the hydrophilic character of the initial IONP. For those obtained by the coprecipitation method, the next step after the synthesis is eventually the attachment of the biomolecule of interest. This sometimes can be a problem since the number of functional groups on the surface is usually low. For those obtained by thermal decomposition, a previous step of aqueous stabilisation is first required. Since the IONP obtained by the thermal decomposition are usually of superior quality, we will detail in this section the three main different approaches for the phase transfer of the hydrophobic IONP to aqueous based solution: the ligand exchange, the use of amphiphilic nanostructures and the direct chemical modification of the organic surfactant (Figure I.6). These approaches can at the same time include the conjugation of biomolecules of interest but it is also possible, as for the initial hydrophilic NP, to perform additional steps for biofunctionalisation, following classic interface chemistry techniques like direct NP conjugations, linker chemistry conjugations or physical adsorption.[24]
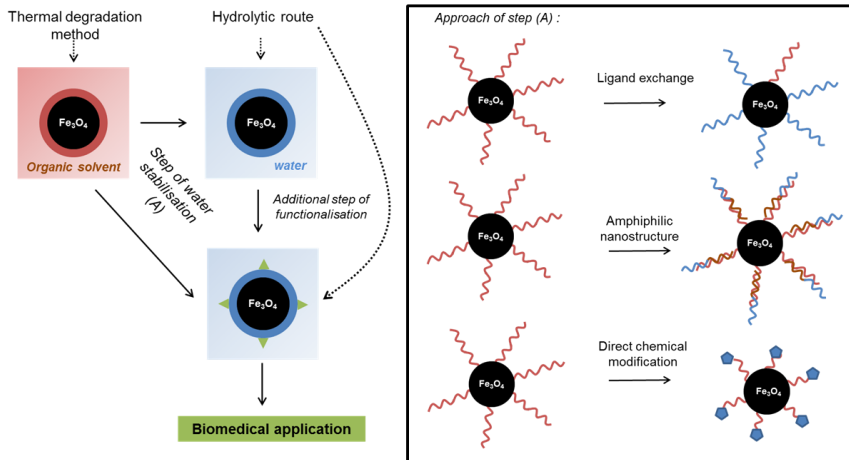
Figure I.6 Steps in the synthesis of IONP for preclinical imaging. and scheme of the different approaches and steps for the phase transfer to a water-based solution.

Ligand exchange. The ligand exchange approach is based on a mixture of hydrophobic IONP with a very high concentration of the hydrophilic molecule. In such conditions, the hydrophilic ligands eventually displace the hydrophobic surfactant due to its affinity towards IONP surface and thus yielding aqueous stable NP.[97] The most remarkable aspects of this approach is the simplicity and versatility due to the enormous number of hydrophilic ligands that can be used for this purpose, like carboxylates, phosphates, polymers and inorganic materials. [18,98,99] However, this approach also presents some disadvantages. One of them is the degree of exchange. If this is not high, the surface of the nanoparticle will contain hydrophobic moieties leading to stabilisation problems and most importantly, to a significant reduction in the number of reactive functional groups for further functionalisation.[50] In general, the ligands utilised in this approach can be classified as small organic molecules and large polymeric compounds. In small organic molecules group, dimercaptosuccinic acid due to the carboxylic

groups, shows for instance a high affinity towards the IONP surface, thus providing high stability in aqueous media and enough free functional groups for further biomolecule conjugation with many applications.[100]. These NP are widely employed for MRI[104] and also drug delivery[105]. Citric acid is another carboxylic-based ligand for the ligand exchange approach of common use. This acid may be adsorbed on the surface of the magnetite nanoparticles via one of the two carboxylate groups, depending on steric hindrance and the curvature of the surface. This leaves at least one these functional groups exposed to the solvent, which should be responsible for making the surface negatively charged and hydrophilic.[31] Another kind of ligands with good properties for the exchange approach are silanes. These compounds present the general chemical formula $X-(CH_2)_n-SiR_3$, where SiR_3 is the anchor group having good affinity for the surface of the nanoparticle, $(CH_2)_n$ is the hydrophobic chain and X is the head group providing the hydrophilicity. Further surface modifications are possible depending on the X group.[101] Other small molecules that have been used in this approach are phosphonates of several compositions.[102] The utilisation of large polymeric compounds for the exchange approach includes dendrimers, polyacrylic acid and PEG. In the case of dendrimers the most common is poly(amido)amine. This dendrimer has been conjugated with targeting ligands, imaging moities and drug molecules for its application in cancer therapy.[103] Moreover, poly(amido)amine coated IONP are a suitable platform for further functional modifications to increase the circulation time of the NP in blood.[71] Polyelectrolytes such as poly(acrylic acid) and poly(allylamine) are also polymers employed to replace the original hydrophobic ligands on the surface of IONP. As we have mentioned before, nanoparticle PEGgylation is well-established to optimize the stabilisation of NP and to prolong their circulation time in blood after administration.[104,105] Regarding the utilisation of this polymer by the ligand exchange approach, one of the best examples is the use of Dopamine-PEG-

COOH, a synthetic compound produced from the polyethylene glycol diacid formulation, in which, one of the acid groups reacts with the terminal free amine of dopamine through a conventional N-hydroxysuccinimide reaction. After the ligand exchange reaction, water stable NP are achieved even with different length chains of PEG. These probes have proven much less uptake by macrophages, indicating that these can evade recognition from the cells of the immune system.[106]

Amphiphilic nanostructure. The utilisation of amphiphilic structures for the stabilisation and functionalisation of IONP is a second approach usually selected when synthesizing these compounds by thermal degradation method.[22,107,108] This method takes advantage of the structure of these amphiphilic molecules. The formation of weak van der Waals interactions between the hydrophobic part of these molecules and the organic tail of the nanoparticle coating, to minimize the interaction with water, produces very stable NP with excellent reproducibility (Figure I.7). Furthermore the possibility of a previous modification on the amphiphilic molecule allows for the stabilisation and functionalisation of the IONP to be carried out in a single step, although this opportunity has not been fully addressed. To obtain such micelle-like structures, usually the first option is to use a polymeric amphiphilic compound. The hydrophobic structure is inserted between the hydrophobic chains of the surfactant/ligand adsorbed on the IONP, while the hydrophilic part stands around the outer surface to assure the dispersion of the IONP in biological media. Many kinds of polymers have been assessed, like pluronic[109,110], poly(maleic anhydride alt-1-tetradecene)[111], cyclodextrins[112], PEG-phospholipids conjugates[113,114], or other triblock polymers[115–117]. Other advantages of the method are the possibility of further crosslinking for better stabilisation or encapsulation of small hydrophobic drugs in the hydrophobic bilayer that is created (as well as small organic fluorescent molecules). Final

stability of the structure depends mainly on the nature of the polymers, *i.e.*, amphiphilic balance, molecular weight, length of the chains or conformation.[115] To achieve the insertion of the polymers several methods are possible, such as reverse evaporation [118,119], progressive increase of the solvent polarity[115] or nanoemulsion[120]. The encapsulation of hydrophobic NP in polymeric micelles is very similar to the insertion option.[121] Many examples are in the bibliography using diblock polymers, such as polylactide-b-poly(ethylene-maleimide) [22,122], poly(styrene-block-acrylic acid)[115], poly(e-caprolactone)-b-poly(ethylene glycol)[123] or dendrimers[124]. Control of self-assembly structures can be achieved from micelles to vesicles, based on the nature of the solvent used and other different conditions.[117] Liposomes, vesicles composed of a lipid bilayer, are for instance another important structure based on amphiphilic compounds and an excellent platform for drug delivery and imaging applications. We refer to the review of Torchilin *et al.* in 2005 and Alen *et al.* in 2013 for explanations in detail of their utilisation, advantages and applications in the design of IONP probes.[21,125–127] High density lipoprotein-liked nanoparticles were also developed by Fayad and Mulder *et al.*[128] with multimodal imaging properties, by including additional labels in the corona of the particles, such as iron oxides, gold and quantum dots. Protein or viral based carrier of hydrophobic IONP can also in a sense be included to the amphiphilic nanostructure approach.
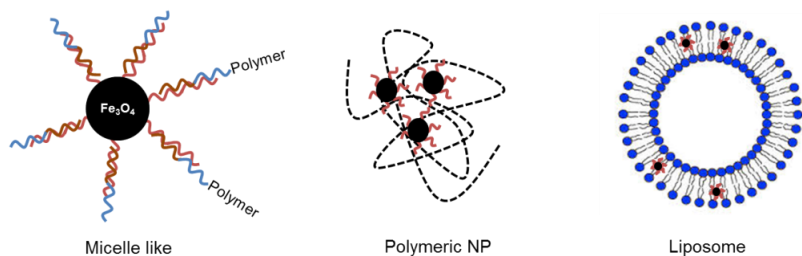
Figure I.7. Examples of amphiphilic nanostructures for the aqueous stabilisation of IONP prepared by thermal degradation method.

Chemical Modification of the Surfactant. This is a new approach based on the direct chemical modification of the surfactant, usually oleic acid. Although different alternatives can be foreseen, the most logical one is to perform chemistry on the carbon-carbon double bond. The final intention of this method is to bring all organic chemistry tools for the synthesis and functionalisation of hydrophilic molecules. This approach was demonstrated for the first time in IONP, by using the very well-known double-bond oxidation with $KMnO_4$ to generate a carboxylic group. The reaction is performed in a two-phase system, a mixture of organic solvent, where the oleic acid NP are dispersed, and an aqueous phase where the $KMnO_4$ is soluble and where the IONP are eventually dispersed. In this procedure, a phase-transfer catalyst is used to get enough concentration of the MnO_4^- ion in the organic phase. This modification renders water-stable particles, and at the same time, also, a functional group ready for further binding of biomolecules, from small organic molecules to dyes and proteins.[129,130] Two of the most remarkable features of these modifications are that the nanoparticle is always protected by a layer of surfactant, thus minimizing the aggregation and that, by using an excess of the oxidant, a complete transformation of the oleic acid is achieved. A second recent initiative is the direct modification of oleic acid using another well-

28

known reaction in organic chemistry, the olefin cross-metathesis. The idea behind this is to take advantage of the functional group in the oleic acid. However, with the olefin metathesis option, one step further can be passed. Since it is possible to incorporate a terminal olefin in many peptides, proteins and biomolecules, it can be utilised for, in a single step, transfering the NP to water and providing specificity for biomedical applications.[131]

3. Up-Converting Nanophosphors (UCNP)

Recently, a new class of nanomaterial, the rare-earth upconversion nanophosphors (UCNP) has been described as an interesting alternative for *in vivo* fluorescence imaging.[132] It shows the unique feature of converting low energy near infrared (NIR) light into higher visible light and/or NIR emission through 2 or 3 sequential photon absorption, together with energy transfers (Figure I.8).[7] This overcomes the drawbacks of classical luminescent probes and confers very attractive advantages to a UCNP-based fluorescence imaging: less harmful excitation, no autofluorescence, high fluorescence lifetime, narrow emission spectra, no toxicity, low cost techniques and, last but not least, very low excitation power densities for a high penetration depth.[133] For all these reasons, the knowledge used for the engineering of common metallic NP was rapidly applied to UCNP to get multifunctionalised targeted probes for pioneering fluorescent or multimodal pre-clinical imaging studies.[134] Phototherapy and drug released triggered by fluorescence also take advantage of this new class of metallic NP. Great attention was initially paid on the β-phase host lattice NaYF4 NP doped with a combination of $Yb3^+$ and Er^{3+}/Tm^{3+} ions because it was proved to be the most efficient UC host materials under a 980 nm laser excitation.[135] Multiple methods for the synthesis of NaYF4 UCNP and applications have been published in the last years.[136,137,138]This has led to an improvement in the thermal degradation

synthesis that has boosted the interest for other classes of UCNP.[139] Among others, addition of passive shells on the nanoparticles[140] and the use of different lanthanides have improved the UC fluorescence[141] of the probes and opened the way to multimodal UCNP-based contrast agents.[142]
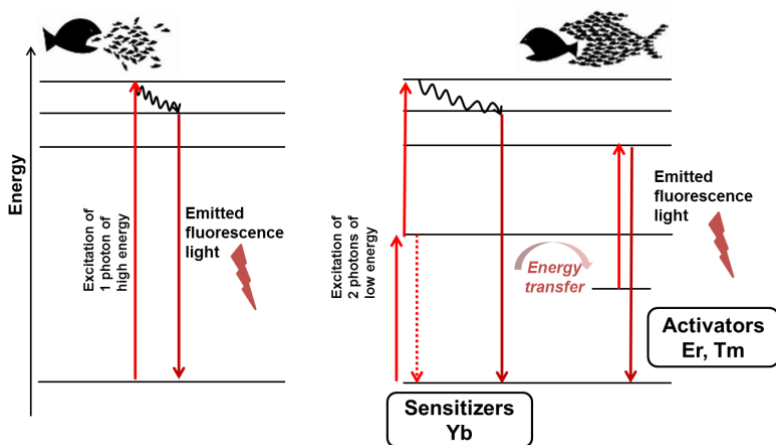
Figure I.8 Comparison of the principles of the traditional and up converting fluorescence.

We have focused on the promising β-NaGdF$_4$:Yb,Tm@β-NaGdF$_4$ nanomaterial because of its very good NIR to NIR UC luminescence and the possibility of use as MRI probe due to the presence of gadolinium.[143,144] On this regard non-doped NaGdF$_4$ has been described as an efficient T1 MRI contrast agent with several advantages compared to the traditional gadolinium chelates contrast media (e.g. Gd^{3+} leaking problem, easier functionalisation).[145]

4 Gold Nanoparticles (AuNP)

Colloidal gold is a suspension of nanometer-sized particles of gold (AuNP). The colour of this solution can vary from strong red to blue in function of the shape, size of the NP and environment. AuNP exhibit interesting optical properties because in the presence of an electromagnetic field, the free electrons of the metallic NP undergo oscillation with respect to the metallic lattice that is resonant at a particular frequency of the light. This phenomenon is known as surface plasmon resonance causing the absorption or reflection of certain bands of the visible spectra. After absorption the surface plasmon can suffer radiative (light scattering) or nonradiative decay processes (conversion of the light adsorbed into heat).[10] Because of this, the range of applications using AuNP includes: coloured based sensor, drug delivery, targeted thermal therapy and many other.[146] The strategies of synthesis of AuNP follow a similar pattern than those seen for other metallic NP. Thus, it exists common hydrolytic routes which use the reduction of chloroauric acid followed by possible functionalisations with various organic ligands and thermal degradation approaches which led to AuNP of much better quality but with a second step needed for aqueous stabilisation similar to the ones exposed in section 2.3 for IONP.

5 Bibliography

(1) Riehemann, K., Schneider, S. W., Luger, T. A., Godin, B., Ferrari, M., and Fuchs, H. (2009) Nanomedicine-Challenge and Perspectives. *Angew. Chemie Int. Ed. 48*, 872–897.
(2) Kim, B. Y. S., Rutka, J. T., and Chan, W. C. W. (2010) Nanomedicine. *N. Engl. J. Med. 363*, 2434–2443.
(3) Sanhai, W. R., Sakamoto, J. H., Canady, R., and Ferrari, M. (2008) Seven challenges for nanomedicine. *Nat. Nanotechnol. 3*, 242–244.
(4) Ratner, M. A. (2003) Nanotechnology: a gentle introduction to the next big idea. Prentice Hall, Upper Saddle River, NJ.
(5) Richard P. Feynman. (1959) There's Plenty of Room at the Bottom.

(6) Farokhzad, O., and Langer, R. (2006) Nanomedicine: Developing smarter therapeutic and diagnostic modalities☆. *Adv. Drug Deliv. Rev. 58*, 1456–1459.

(7) Haase, M., and Schäfer, H. (2011) Upconverting Nanoparticles. *Angew. Chemie Int. Ed. 50*, 5808–5829.

(8) Liu, Y., Miyoshi, H., and Nakamura, M. (2007) Nanomedicine for drug delivery and imaging: A promising avenue for cancer therapy and diagnosis using targeted functional nanoparticles. *Int. J. Cancer 120*, 2527–2537.

(9) Shaffer, C. (2005) Nanomedicine transforms drug delivery. *Drug Discov. Today 10*, 1581–1582.

(10) Mody, V., Siwale, R., Singh, A., and Mody, H. (2010) Introduction to metallic nanoparticles. *J. Pharm. Bioallied Sci. 2*.

(11) (2008) Nanoparticles in biomedical imaging: emerging technologies and applications. *Fundam. Biomed. Technol.*, p 524. Springer, New York.

(12) Schladt, T. D., Schneider, K., Schild, H., and Tremel, W. (2011) Synthesis and bio-functionalization of magnetic nanoparticles for medical diagnosis and treatment. *Dalt. Trans. 40*.

(13) Lu, A.-H., Salabas, E. L., and Schüth, F. (2007) Magnetic Nanoparticles: Synthesis, Protection, Functionalization, and Application. *Angew. Chemie Int. Ed. 46*, 1222–1244.

(14) Hall, J. B., Dobrovolskaia, M. A., Patri, A. K., and McNeil, S. E. (2007) Characterization of nanoparticles for therapeutics. *Nanomedicine 2*, 789–803.

(15) Sanvicens, N., and Marco, M. P. (2008) Multifunctional nanoparticles – properties and prospects for their use in human medicine. *Trends Biotechnol. 26*, 425–433.

(16) Cheng, Z., Al Zaki, A., Hui, J. Z., Muzykantov, V. R., and Tsourkas, A. (2012) Multifunctional Nanoparticles: Cost Versus Benefit of Adding Targeting and Imaging Capabilities. *Science (80-.). 338*, 903–910.

(17) Hao, R., Xing, R., Xu, Z., Hou, Y., Gao, S., and Sun, S. (2010) Synthesis, Functionalization, and Biomedical Applications of Multifunctional Magnetic Nanoparticles. *Adv. Mater. 22*, 2729–2742.

(18) Moghimi, S. M., Hunter, A. C., and Murray, J. C. (2001) Long-circulating and target-specific nanoparticles: theory to practice. *Pharmacol. Rev. 53*, 283–318.

(19) Romberg, B., Hennink, W. E., and Storm, G. (2007) Sheddable Coatings for Long-Circulating Nanoparticles. *Pharm. Res. 25*, 55–71.

(20) Tong, S., Hou, S., Zheng, Z., Zhou, J., and Bao, G. (2010) Coating Optimization of Superparamagnetic Iron Oxide Nanoparticles for High T_2 Relaxivity. *Nano Lett. 10*, 4607–4613.

(21) Torchilin, V. P. (2005) Recent advances with liposomes as pharmaceutical carriers. *Nat. Rev. Drug Discov. 4*, 145–160.

(22) Nasongkla, N., Bey, E., Ren, J., Ai, H., Khemtong, C., Guthi, J. S., Chin, S.-F., Sherry, A. D., Boothman, D. A., and Gao, J. (2006) Multifunctional Polymeric Micelles as Cancer-Targeted, MRI-Ultrasensitive Drug Delivery Systems. *Nano Lett. 6*, 2427–2430.

(23) Hawkins, M. J., Soon-Shiong, P., and Desai, N. (2008) Protein nanoparticles as drug carriers in clinical medicine. *Adv. Drug Deliv. Rev. 60*, 876–885.

(24) Veiseh, O., Gunn, J. W., and Zhang, M. (2010) Design and fabrication of magnetic nanoparticles for targeted drug delivery and imaging. *Adv. Drug Deliv. Rev. 62*, 284–304.

(25) Wang, M., and Thanou, M. (2010) Targeting nanoparticles to cancer. *Pharmacol. Res. 62*, 90–99.

(26) Xie, J., Chen, K., Huang, J., Lee, S., Wang, J., Gao, J., Li, X., and Chen, X. (2010) PET/NIRF/MRI triple functional iron oxide nanoparticles. *Biomaterials 31*, 3016–3022.

(27) Emerich, D. F., and Thanos, C. G. (2006) The pinpoint promise of nanoparticle-based drug delivery and molecular diagnosis. *Biomol. Eng. 23*, 171–184.

(28) Muthu, M. S., Mei, L., and Feng, S.-S. (2014) Nanotheranostics: advanced nanomedicine for the integration of diagnosis and therapy. *Nanomedicine 9*, 1277–1280.

(29) Janib, S. M., Moses, A. S., and MacKay, J. A. (2010) Imaging and drug delivery using theranostic nanoparticles. *Adv. Drug Deliv. Rev. 62*, 1052–1063.

(30) Xie, J., Lee, S., and Chen, X. (2010) Nanoparticle-based theranostic agents. *Adv. Drug Deliv. Rev. 62*, 1064–1079.

(31) Laurent, S., Forge, D., Port, M., Roch, A., Robic, C., Vander Elst, L., and Muller, R. N. (2008) Magnetic Iron Oxide Nanoparticles: Synthesis, Stabilization, Vectorization, Physicochemical Characterizations, and Biological Applications. *Chem. Rev. 108*, 2064–2110.

(32) Neuberger, T., Schöpf, B., Hofmann, H., Hofmann, M., and von Rechenberg, B. (2005) Superparamagnetic nanoparticles for biomedical applications: Possibilities and limitations of a new drug delivery system. *J. Magn. Magn. Mater. 293*, 483–496.

(33) Qiao, R., Yang, C., and Gao, M. (2009) Superparamagnetic iron oxide nanoparticles: from preparations to in vivo MRI applications. *J. Mater. Chem. 19*.

(34) Mahmoudi, M., Sant, S., Wang, B., Laurent, S., and Sen, T. (2011) Superparamagnetic iron oxide nanoparticles (SPIONs): Development, surface modification and applications in chemotherapy. *Adv. Drug Deliv. Rev. 63*, 24–46.

(35) Gleich, B., and Weizenecker, J. (2005) Tomographic imaging using the nonlinear response of magnetic particles. *Nature 435*, 1214–1217.

(36) Gupta, A. K., and Gupta, M. (2005) Synthesis and surface engineering of iron oxide nanoparticles for biomedical applications. *Biomaterials 26*, 3995–4021.

(37) Fang, C., and Zhang, M. (2009) Multifunctional magnetic nanoparticles for medical imaging applications. *J. Mater. Chem. 19*.

(38) Pankhurst, Q. A., Connolly, J., Jones, S. K., and Dobson, J. (2003) Applications of magnetic nanoparticles in biomedicine. *J. Phys. D. Appl. Phys. 36*, R167–R181.

(39) Huettel, S. A. (2008) Functional magnetic resonance imaging 2nd ed. Sinauer Associates, Sunderland, Mass.

(40) Na, H. Bin, Song, I. C., and Hyeon, T. (2009) Inorganic Nanoparticles for MRI Contrast Agents. *Adv. Mater. 21*, 2133–2148.

(41) Lewin, M., Carlesso, N., Tung, C. H., Tang, X. W., Cory, D., Scadden, D. T., and Weissleder, R. (2000) Tat peptide-derivatized magnetic nanoparticles allow in vivo tracking and recovery of progenitor cells. *Nat. Biotechnol. 18*, 410–414.

(42) Mccarthy, J., and Weissleder, R. (2008) Multifunctional magnetic nanoparticles for targeted imaging and therapy✵. *Adv. Drug Deliv. Rev. 60*, 1241–1251.

(43) Sosnovik, D. E., Nahrendorf, M., and Weissleder, R. (2008) Magnetic nanoparticles for MR imaging: agents, techniques and cardiovascular applications. *Basic Res. Cardiol. 103*, 122–130.

(44) Herranz, F., Salinas, B., Groult, H., Pellico, J., Lechuga-Vieco, A., Bhavesh, R., and Ruiz-Cabello, J. (2014) Superparamagnetic Nanoparticles for Atherosclerosis Imaging. *Nanomaterials 4*, 408–438.

(45) Arruebo, M., Fernández-Pacheco, R., Ibarra, M. R., and Santamaría, J. (2007) Magnetic nanoparticles for drug delivery. *Nano Today 2*, 22–32.

(46) Lübbe, A. S., Alexiou, C., and Bergemann, C. (2001) Clinical Applications of Magnetic Drug Targeting. *J. Surg. Res. 95*, 200–206.

(47) Mornet, S., Vasseur, S., Grasset, F., and Duguet, E. (2004) Magnetic nanoparticle design for medical diagnosis and therapy. *J. Mater. Chem. 14*.

(48) Dobson, J. (2006) Gene therapy progress and prospects: magnetic nanoparticle-based gene delivery. *Gene Ther. 13*, 283–287.

(49) Haun, J. B., Yoon, T.-J., Lee, H., and Weissleder, R. (2010) Magnetic nanoparticle biosensors. *Wiley Interdiscip. Rev. Nanomedicine Nanobiotechnology 2*, 291–304.

(50) Wu, W., He, Q., and Jiang, C. (2008) Magnetic Iron Oxide Nanoparticles: Synthesis and Surface Functionalization Strategies. *Nanoscale Res. Lett. 3*, 397–415.

(51) Lee, S.-J., Jeong, J.-R., Shin, S.-C., Kim, J.-C., and Kim, J.-D. (2004) Synthesis and characterization of superparamagnetic maghemite nanoparticles prepared by coprecipitation technique. *J. Magn. Magn. Mater. 282*, 147–150.

(52) Sun, S., and Zeng, H. (2002) Size-Controlled Synthesis of Magnetite Nanoparticles. *J. Am. Chem. Soc. 124*, 8204–8205.

(53) Hee Kim, E., Sook Lee, H., Kook Kwak, B., and Kim, B.-K. (2005) Synthesis of ferrofluid with magnetic nanoparticles by sonochemical method for MRI contrast agent. *J. Magn. Magn. Mater. 289*, 328–330.

(54) Yu, S., and Chow, G. M. (2006) Synthesis of Monodisperse Iron Oxide and Iron/Iron Oxide Core/Shell Nanoparticles via Iron-Oleylamine Complex. *J. Nanosci. Nanotechnol. 6*, 2135–2140.

(55) Morales, M. P., Bomati-Miguel, O., Pérez de Alejo, R., Ruiz-Cabello, J., Veintemillas-Verdaguer, S., and O'Grady, K. (2003) Contrast agents for MRI based on iron oxide nanoparticles prepared by laser pyrolysis. *J. Magn. Magn. Mater. 266*, 102–109.

(56) Hyeon, T. (2003) Chemical synthesis of magnetic nanoparticles. *Chem. Commun.* 927–934.

(57) Wang, J., Sun, J., Sun, Q., and Chen, Q. (2003) One-step hydrothermal process to prepare highly crystalline Fe3O4 nanoparticles with improved magnetic properties. *Mater. Res. Bull. 38*, 1113–1118.

(58) Wong, K. K. W., Douglas, T., Gider, S., Awschalom, D. D., and Mann, S. (1998) Biomimetic Synthesis and Characterization of Magnetic Proteins (Magnetoferritin). *Chem. Mater. 10*, 279–285.

(59) De Cuyper, M., and Joniau, M. (1991) Mechanistic aspects of the adsorption of phospholipids onto lauric acid stabilized magnetite nanocolloids. *Langmuir 7*, 647–652.

(60) Chin, A. B., and Yaacob, I. I. (2007) Synthesis and characterization of magnetic iron oxide nanoparticles via w/o microemulsion and Massart's procedure. *J. Mater. Process. Technol. 191*, 235–237.

(61) Parsons, J. G., Luna, C., Botez, C. E., Elizalde, J., and Gardea-Torresdey, J. L. (2009) Microwave-assisted synthesis of iron(III) oxyhydroxides/oxides characterized using transmission electron microscopy, X-ray diffraction, and X-ray absorption spectroscopy. *J. Phys. Chem. Solids 70*, 555–560.

(62) Wang, W.-W., Zhu, Y.-J., and Ruan, M.-L. (2006) Microwave-assisted synthesis and magnetic property of magnetite and hematite nanoparticles. *J. Nanoparticle Res. 9*, 419–426.

(63) Khollam, Y. B., Dhage, S. R., Potdar, H. S., Deshpande, S. B., Bakare, P. P., Kulkarni, S. D., and Date, S. K. (2002) Microwave hydrothermal preparation of submicron-sized spherical magnetite (Fe3O4) powders. *Mater. Lett. 56*, 571–577.

(64) Massart, R. Preparation of aqueous magnetic liquids in alkaline and acidic media. *IEEE Trans. Magn. 17*, 1247–1248.

(65) Gazeau, F., Bacri, J. C., Gendron, F., Perzynski, R., Raikher, Y. ., Stepanov, V. I., and Dubois, E. (1998) Magnetic resonance of ferrite nanoparticles: *J. Magn. Magn. Mater. 186*, 175–187.

(66) Binh, V. T., Purcell, S. T., Semet, V., and Feschet, F. (1998) Nanotips and nanomagnetism. *Appl. Surf. Sci. 130–132*, 803–814.

(67) Jolivet, J.-P. (2000) Metal oxide chemistry and synthesis: from solution to solid state. John Wiley, Chichester ; New York.

(68) Hadjipanayis, C. G., Bonder, M. J., Balakrishnan, S., Wang, X., Mao, H., and Hadjipanayis, G. C. (2008) Metallic nanoparticles 2–6.

(69) Berret, J.-F., Schonbeck, N., Gazeau, F., El Kharrat, D., Sandre, O., Vacher, A., and Airiau, M. (2006) Controlled clustering of superparamagnetic nanoparticles using block copolymers: design of new contrast agents for magnetic resonance imaging. *J. Am. Chem. Soc. 128*, 1755–1761.

(70) Thünemann, A. F., Schütt, D., Kaufner, L., Pison, U., and Möhwald, H. (2006) Maghemite nanoparticles protectively coated with poly(ethylene imine) and poly(ethylene oxide)-block-poly(glutamic acid). *Langmuir ACS J. surfaces colloids 22*, 2351–2357.

(71) Shi, X., Thomas, T. P., Myc, L. A., Kotlyar, A., and Baker Jr, J. R. (2007) Synthesis, characterization, and intracellular uptake of carboxyl-terminated poly(amidoamine) dendrimer-stabilized iron oxide nanoparticles. *Phys. Chem. Chem. Phys. PCCP 9*, 5712–5720.

(72) Shieh, D.-B., Cheng, F.-Y., Su, C.-H., Yeh, C.-S., Wu, M.-T., Wu, Y.-N., Tsai, C.-Y., Wu, C.-L., Chen, D.-H., and Chou, C.-H. (2005) Aqueous dispersions of magnetite nanoparticles with NH3+ surfaces for magnetic manipulations of biomolecules and MRI contrast agents. *Biomaterials 26*, 7183–7191.

(73) Yin, Y., and Alivisatos, A. P. (2005) Colloidal nanocrystal synthesis and the organic–inorganic interface. *Nature 437*, 664–670.

(74) Hyeon, T., Lee, S. S., Park, J., Chung, Y., and Na, H. Bin. (2001) Synthesis of Highly Crystalline and Monodisperse Maghemite Nanocrystallites without a Size-Selection Process. *J. Am. Chem. Soc. 123*, 12798–12801.

(75) Woo, K., Hong, J., Choi, S., Lee, H.-W., Ahn, J.-P., Kim, C. S., and Lee, S. W. (2004) Easy Synthesis and Magnetic Properties of Iron Oxide Nanoparticles. *Chem. Mater. 16*, 2814–2818.

(76) Park, J., Lee, E., Hwang, N.-M., Kang, M., Kim, S. C., Hwang, Y., Park, J.-G., Noh, H.-J., Kim, J.-Y., Park, J.-H., and Hyeon, T. (2005) One-Nanometer-Scale Size-Controlled Synthesis of Monodisperse Magnetic Iron Oxide Nanoparticles. *Angew. Chemie Int. Ed. 44*, 2872–2877.

(77) Murray, C. B., Sun, S., Gaschler, W., Doyle, H., Betley, T. A., and Kagan, C. R. (2001) Colloidal synthesis of nanocrystals and nanocrystal superlattices. *IBM J. Res. Dev. 45*, 47–56.

(78) Park, J., An, K., Hwang, Y., Park, J.-G., Noh, H.-J., Kim, J.-Y., Park, J.-H., Hwang, N.-M., and Hyeon, T. (2004) Ultra-large-scale syntheses of monodisperse nanocrystals. *Nat. Mater. 3*, 891–895.

(79) Jana, N. R., Chen, Y., and Peng, X. (2004) Size- and Shape-Controlled Magnetic (Cr, Mn, Fe, Co, Ni) Oxide Nanocrystals via a Simple and General Approach. *Chem. Mater. 16*, 3931–3935.

(80) Sun, S., Zeng, H., Robinson, D. B., Raoux, S., Rice, P. M., Wang, S. X., and Li, G. (2004) Monodisperse MFe_2O_4 (M = Fe, Co, Mn) Nanoparticles. *J. Am. Chem. Soc. 126*, 273–279.

(81) Kwon, S. G., Piao, Y., Park, J., Angappane, S., Jo, Y., Hwang, N.-M., Park, J.-G., and Hyeon, T. (2007) Kinetics of Monodisperse Iron Oxide Nanocrystal Formation by "Heating-Up" Process. *J. Am. Chem. Soc. 129*, 12571–12584.

(82) Cheon, J., Kang, N.-J., Lee, S.-M., Lee, J.-H., Yoon, J.-H., and Oh, S. J. (2004) Shape Evolution of Single-Crystalline Iron Oxide Nanocrystals. *J. Am. Chem. Soc. 126*, 1950–1951.

(83) Tartaj, P., Morales, M. a del P., Veintemillas-Verdaguer, S., Gonz lez-Carre o, T., and Serna, C. J. (2003) The preparation of magnetic nanoparticles for applications in biomedicine. *J. Phys. D. Appl. Phys. 36*, R182–R197.

(84) Yu, W. W., Falkner, J. C., Yavuz, C. T., and Colvin, V. L. (2004) Synthesis of monodisperse iron oxide nanocrystals by thermal decomposition of iron carboxylate salts. *Chem. Commun. (Camb).* 2306–2307.

(85) Bronstein, L. M., Huang, X., Retrum, J., Schmucker, A., Pink, M., Stein, B. D., and Dragnea, B. (2007) Influence of Iron Oleate Complex Structure on Iron Oxide Nanoparticle Formation. *Chem. Mater. 19*, 3624–3632.

(86) Cozzoli, P. D., Snoeck, E., Garcia, M. A., Giannini, C., Guagliardi, A., Cervellino, A., Gozzo, F., Hernando, A., Achterhold, K., Ciobanu, N., Parak, F. G., Cingolani, R., and Manna, L. (2006) Colloidal Synthesis and Characterization of Tetrapod-Shaped Magnetic Nanocrystals. *Nano Lett. 6*, 1966–1972.

(87) Li, Z., Chen, H., Bao, H., and Gao, M. (2004) One-Pot Reaction to Synthesize Water-Soluble Magnetite Nanocrystals. *Chem. Mater. 16*, 1391–1393.

(88) Li, Z., Sun, Q., and Gao, M. (2005) Preparation of Water-Soluble Magnetite Nanocrystals from Hydrated Ferric Salts in 2-Pyrrolidone: Mechanism Leading to Fe_3O_4. *Angew. Chemie Int. Ed. 44*, 123–126.

(89) Hu, F. Q., Wei, L., Zhou, Z., Ran, Y. L., Li, Z., and Gao, M. Y. (2006) Preparation of Biocompatible Magnetite Nanocrystals for In Vivo Magnetic Resonance Detection of Cancer. *Adv. Mater. 18*, 2553–2556.

(90) Hu, F., Li, Z., Tu, C., and Gao, M. (2007) Preparation of magnetite nanocrystals with surface reactive moieties by one-pot reaction. *J. Colloid Interface Sci. 311*, 469–474.

(91) Wan, J., Cai, W., Meng, X., and Liu, E. (2007) Monodisperse water-soluble magnetite nanoparticles prepared by polyol process for high-performance magnetic resonance imaging. *Chem. Commun.*

(92) Ge, J., Hu, Y., Biasini, M., Dong, C., Guo, J., Beyermann, W. P., and Yin, Y. (2007) One-Step Synthesis of Highly Water-Soluble Magnetite Colloidal Nanocrystals. *Chem. - A Eur. J. 13*, 7153–7161.

(93) Liao, X., Zhu, J., Zhong, W., and Chen, H.-Y. (2001) Synthesis of amorphous Fe_2O_3 nanoparticles by microwave irradiation. *Mater. Lett. 50*, 341–346.

(94) Jiang, F. Y., Wang, C. M., Fu, Y., and Liu, R. C. (2010) Synthesis of iron oxide nanocubes via microwave-assisted solvolthermal method. *J. Alloys Compd. 503*, L31–L33.

(95) Yang, D.-P., Gao, F., Cui, D.-X., and Yang, M. (2009) Microwave Rapid Synthesis of Nanoporous Fe3O4 Magnetic Microspheres. *Curr. Nanosci. 5*, 485–488.

(96) Osborne, E. A., Atkins, T. M., Gilbert, D. A., Kauzlarich, S. M., Liu, K., and Louie, A. Y. (2012) Rapid microwave-assisted synthesis of dextran-coated iron oxide nanoparticles for magnetic resonance imaging. *Nanotechnology 23*.

(97) Bloemen, M., Brullot, W., Luong, T. T., Geukens, N., Gils, A., and Verbiest, T. (2012) Improved functionalization of oleic acid-coated iron oxide nanoparticles for biomedical applications. *J. Nanoparticle Res. 14*.

(98) Sahoo, Y., Pizem, H., Fried, T., Golodnitsky, D., Burstein, L., Sukenik, C. N., and Markovich, G. (2001) Alkyl Phosphonate/Phosphate Coating on Magnetite Nanoparticles: A Comparison with Fatty Acids. *Langmuir 17*, 7907–7911.

(99) Lin, J., Zhou, W., Kumbhar, A., Wiemann, J., Fang, J., Carpenter, E. E., and O'Connor, C. J. (2001) Gold-Coated Iron (Fe@Au) Nanoparticles: Synthesis, Characterization, and Magnetic Field-Induced Self-Assembly. *J. Solid State Chem. 159*, 26–31.

(100) Na, H. Bin, Lee, J. H., An, K., Park, Y. Il, Park, M., Lee, I. S., Nam, D.-H., Kim, S. T., Kim, S.-H., Kim, S.-W., Lim, K.-H., Kim, K.-S., Kim, S.-O., and Hyeon, T. (2007) Development of a T1 contrast agent for magnetic resonance imaging using MnO nanoparticles. *Angew. Chem. Int. Ed. Engl. 46*, 5397–5401.

(101) De Palma, R., Peeters, S., Van Bael, M. J., Van den Rul, H., Bonroy, K., Laureyn, W., Mullens, J., Borghs, G., and Maes, G. (2007) Silane Ligand Exchange to Make Hydrophobic Superparamagnetic Nanoparticles Water-Dispersible. *Chem. Mater. 19*, 1821–1831.

(102) Das, M., Mishra, D., Dhak, P., Gupta, S., Maiti, T. K., Basak, A., and Pramanik, P. (2009) Biofunctionalized, Phosphonate-Grafted, Ultrasmall Iron Oxide Nanoparticles for Combined Targeted Cancer Therapy and Multimodal Imaging. *Small 5*, 2883–2893.

(103) Majoros, I. J., Myc, A., Thomas, T., Mehta, C. B., and Baker Jr, J. R. (2006) PAMAM dendrimer-based multifunctional conjugate for cancer therapy: synthesis, characterization, and functionality. *Biomacromolecules 7*, 572–579.

(104) Rocha, N., Mendes, J., Durães, L., Maleki, H., Portugal, A., Geraldes, C. F. G. C., Serra, A., and Coelho, J. (2014) Poly(ethylene glycol)-block-poly(4-vinyl pyridine) as a versatile block copolymer to prepare nanoaggregates of superparamagnetic iron oxide nanoparticles. *J. Mater. Chem. B 2*.

(105) Wadajkar, A. S., Menon, J. U., Tsai, Y.-S., Gore, C., Dobin, T., Gandee, L., Kangasniemi, K., Takahashi, M., Manandhar, B., Ahn, J.-M., Hsieh, J.-T., and Nguyen, K. T. (2013) Prostate cancer-specific thermo-responsive polymer-coated iron oxide nanoparticles. *Biomaterials 34*, 3618–3625.

(106) Xie, J., Xu, C., Kohler, N., Hou, Y., and Sun, S. (2007) Controlled PEGylation of Monodisperse Fe3O4 Nanoparticles for Reduced Non-Specific Uptake by Macrophage Cells. *Adv. Mater. 19*, 3163–3166.

(107) Jain, T. K., Morales, M. A., Sahoo, S. K., Leslie-Pelecky, D. L., and Labhasetwar, V. (2005) Iron Oxide Nanoparticles for Sustained Delivery of Anticancer Agents. *Mol. Pharm. 2*, 194–205.

(108) Yu, W. W., Chang, E., Sayes, C. M., Drezek, R., and Colvin, V. L. (2006) Aqueous dispersion of monodisperse magnetic iron oxide nanocrystals through phase transfer. *Nanotechnology 17*.

(109) Jain, T. K., Foy, S. P., Erokwu, B., Dimitrijevic, S., Flask, C. A., and Labhasetwar, V. (2009) Magnetic resonance imaging of multifunctional pluronic stabilized iron-oxide nanoparticles in tumor-bearing mice. *Biomaterials 30*, 6748–6756.

(110) Lin, J.-J., Chen, J.-S., Huang, S.-J., Ko, J.-H., Wang, Y.-M., Chen, T.-L., and Wang, L.-F. (2009) Folic acid-Pluronic F127 magnetic nanoparticle clusters for combined targeting, diagnosis, and therapy applications. *Biomaterials 30*, 5114–5124.

(111) Bronstein, L. M., Shtykova, E. V, Malyutin, A., Dyke, J. C., Gunn, E., Gao, X., Stein, B., Konarev, P. V, Dragnea, B., and Svergun, D. I. (2010) Hydrophilization of Magnetic Nanoparticles with Modified Alternating Copolymers. Part 1: The Influence of the Grafting. *J. Phys. Chem. C. Nanomater. Interfaces 114*, 21900–21907.

(112) Su, H., Liu, Y., Wang, D., Wu, C., Xia, C., Gong, Q., Song, B., and Ai, H. (2013) Amphiphilic starlike dextran wrapped superparamagnetic iron oxide nanoparticle clsuters as effective magnetic resonance imaging probes. *Biomaterials 34*, 1193–1203.

(113) Huang, H.-C., Chang, P.-Y., Chang, K., Chen, C.-Y., Lin, C.-W., Chen, J.-H., Mou, C.-Y., Chang, Z.-F., and Chang, F.-H. (2009) Formulation of novel lipid-coated magnetic nanoparticles as the probe for in vivo imaging. *J. Biomed. Sci. 16.*

(114) Erogbogbo, F., Yong, K.-T., Hu, R., Law, W.-C., Ding, H., Chang, C.-W., Prasad, P. N., and Swihart, M. T. (2010) Biocompatible magnetofluorescent probes: luminescent silicon quantum dots coupled with superparamagnetic iron(III) oxide. *ACS Nano 4*, 5131–5138.

(115) Kim, B.-S., Qiu, J.-M., Wang, J.-P., and Taton, T. A. (2005) Magnetomicelles: Composite Nanostructures from Magnetic Nanoparticles and Cross-Linked Amphiphilic Block Copolymers. *Nano Lett. 5*, 1987–1991.

(116) Zhu, J., and Hayward, R. C. (2008) Spontaneous Generation of Amphiphilic Block Copolymer Micelles with Multiple Morphologies through Interfacial Instabilities. *J. Am. Chem. Soc. 130*, 7496–7502.

(117) Hickey, R. J., Haynes, A. S., Kikkawa, J. M., and Park, S.-J. (2011) Controlling the Self-Assembly Structure of Magnetic Nanoparticles and Amphiphilic Block-Copolymers: From Micelles to Vesicles. *J. Am. Chem. Soc. 133*, 1517–1525.

(118) Pellegrino, T., Manna, L., Kudera, S., Liedl, T., Koktysh, D., Rogach, A. L., Keller, S., Rädler, J., Natile, G., and Parak, W. J. (2004) Hydrophobic Nanocrystals Coated with an Amphiphilic Polymer Shell: A General Route to Water Soluble Nanocrystals. *Nano Lett. 4*, 703–707.

(119) Xie, J., Peng, S., Brower, N., Pourmand, N., Wang, S. X., and Sun, S. (2006) One-pot synthesis of monodisperse iron oxide nanoparticles for potential biomedical applications. *Pure Appl. Chem. 78*, 1003–1014.

(120) Park, J., Yu, M. K., Jeong, Y. Y., Kim, J. W., Lee, K., Phan, V. N., and Jon, S. (2009) Antibiofouling amphiphilic polymer-coated superparamagnetic iron oxide nanoparticles: synthesis, characterization, and use in cancer imaging in vivo. *J. Mater. Chem. 19*.

(121) Quarta, A., Curcio, A., Kakwere, H., and Pellegrino, T. (2012) Polymer coated inorganic nanoparticles: tailoring the nanocrystal surface for designing nanoprobes with biological implications. *Nanoscale 4*.

(122) Wang, L., Neoh, K.-G., Kang, E.-T., Shuter, B., and Wang, S.-C. (2010) Biodegradable magnetic-fluorescent magnetite/poly(dl-lactic acid-co-α,β-malic acid) composite nanoparticles for stem cell labeling. *Biomaterials 31*, 3502–3511.

(123) Ai, H., Flask, C., Weinberg, B., Shuai, X.-T., Pagel, M. D., Farrell, D., Duerk, J., and Gao, J. (2005) Magnetite-Loaded Polymeric Micelles as Ultrasensitive Magnetic-Resonance Probes. *Adv. Mater. 17*, 1949–1952.

(124) Boni, A., Albertazzi, L., Innocenti, C., Gemmi, M., and Bifone, A. (2013) Water dispersal and functionalization of hydrophobic iron oxide nanoparticles with lipid-modified poly(amidoamine) dendrimers. *Langmuir ACS J. surfaces colloids 29*, 10973–10979.

(125) Allen, T. M., and Cullis, P. R. (2013) Liposomal drug delivery systems: From concept to clinical applications. *Adv. Drug Deliv. Rev. 65*, 36–48.

(126) Mulder, W. J. M., Strijkers, G. J., van Tilborg, G. A. F., Cormode, D. P., Fayad, Z. A., and Nicolay, K. (2009) Nanoparticulate Assemblies of Amphiphiles and Diagnostically Active Materials for Multimodality Imaging. *Acc. Chem. Res. 42*, 904–914.

(127) Martina, M.-S., Fortin, J.-P., Ménager, C., Clément, O., Barratt, G., Grabielle-Madelmont, C., Gazeau, F., Cabuil, V., and Lesieur, S. (2005) Generation of Superparamagnetic Liposomes Revealed as Highly Efficient MRI Contrast Agents for in Vivo Imaging. *J. Am. Chem. Soc. 127*, 10676–10685.

(128) Cormode, D. P., Skajaa, T., van Schooneveld, M. M., Koole, R., Jarzyna, P., Lobatto, M. E., Calcagno, C., Barazza, A., Gordon, R. E., Zanzonico, P., Fisher, E. A., Fayad, Z. A., and Mulder, W. J. M. (2008) Nanocrystal Core High-Density Lipoproteins: A Multimodality Contrast Agent Platform. *Nano Lett. 8*, 3715–3723.

(129) Herranz, F., Morales, M. P., Roca, A. G., Vilar, R., and Ruiz-Cabello, J. (2008) A new method for the aqueous functionalization of superparamagnetic Fe2O3 nanoparticles. *Contrast Media Mol. Imaging 3*, 215–222.

(130) Herranz, F., Schmidt-Weber, C. B., Shamji, M. H., Narkus, A., Ruiz-Cabello, J., and Vilar, R. (2012) Superparamagnetic iron oxide nanoparticles conjugated to a grass pollen allergen and an optical probe. *Contrast Media Mol. Imaging 7*, 435–9.

(131) Salinas, B., Ruiz Cabello, J., Morales, M. P., and Herranz, F. (2012) Olefin metathesis for the functionalization of superparamagnetic nanoparticles. *Bioinspired, Biomim. Nanobiomaterials 1*, 166–172.

(132) Zhou, J., Liu, Z., and Li, F. (2012) Upconversion nanophosphors for small-animal imaging. *Chem. Soc. Rev. 41*.

(133) Gainer, C. F., and Romanowski, M. (2013) Multiphoton imaging of upconverting lanthanide nanoparticles in three dimensional models of cancer (Parak, W. J., Osinski, M., and Yamamoto, K., Eds.), p 85950O–85950O–8.

(134) Lim, S. F., Riehn, R., Tung, C., Ryu, W. S., Zhuo, R., Dalland, J., and Austin, R. H. (2009) Upconverting nanophosphors for bioimaging. *Nanotechnology 20*.

(135) Zhang, J., Mi, C., Wu, H., Huang, H., Mao, C., and Xu, S. (2012) Synthesis of NaYF4:Yb/Er/Gd up-conversion luminescent nanoparticles and luminescence resonance energy transfer-based protein detection. *Anal. Biochem. 421*, 673–679.

(136) Yi, G. S., and Chow, G. M. (2006) Synthesis of Hexagonal-Phase NaYF4:Yb,Er and NaYF4:Yb,Tm Nanocrystals with Efficient Up-Conversion Fluorescence. *Adv. Funct. Mater. 16*, 2324–2329.

(137) Liang, S., Liu, Y., Tang, Y., Xie, Y., Sun, H., Zhang, H., and Yang, B. (2011) A User-Friendly Method for Synthesizing High-Quality NaYF4:Yb,Er(Tm) Nanocrystals in Liquid Paraffin. *J. Nanomater. 2011*, 1–7.

(138) Shan, J., Qin, X., Yao, N., and Ju, Y. (2007) Synthesis of monodisperse hexagonal NaYF 4 :Yb, Ln (Ln = Er, Ho and Tm) upconversion nanocrystals in TOPO. *Nanotechnology 18*.

(139) Wang, F., and Liu, X. (2009) Recent advances in the chemistry of lanthanide-doped upconversion nanocrystals. *Chem. Soc. Rev. 38*.

(140) Vetrone, F., Naccache, R., Mahalingam, V., Morgan, C. G., and Capobianco, J. A. (2009) The Active-Core/Active-Shell Approach: A Strategy to Enhance the Upconversion Luminescence in Lanthanide-Doped Nanoparticles. *Adv. Funct. Mater. 19*, 2924–2929.

(141) Wang, F., Wang, J., and Liu, X. (2010) Direct Evidence of a Surface Quenching Effect on Size-Dependent Luminescence of Upconversion Nanoparticles. *Angew. Chemie 122*, 7618–7622.

(142) Xing, H., Bu, W., Zhang, S., Zheng, X., Li, M., Chen, F., He, Q., Zhou, L., Peng, W., Hua, Y., and Shi, J. (2012) Multifunctional nanoprobes for upconversion fluorescence, MR and CT trimodal imaging. *Biomaterials 33*, 1079–1089.

(143) Chen, F., Bu, W., Zhang, S., Liu, X., Liu, J., Xing, H., Xiao, Q., Zhou, L., Peng, W., Wang, L., and Shi, J. (2011) Positive and Negative Lattice Shielding Effects Co-existing in Gd (III) Ion Doped Bifunctional Upconversion Nanoprobes. *Adv. Funct. Mater. 21*, 4285–4294.

(144) Kumar, R., Nyk, M., Ohulchanskyy, T. Y., Flask, C. A., and Prasad, P. N. (2009) Combined Optical and MR Bioimaging Using Rare Earth Ion Doped NaYF 4 Nanocrystals. *Adv. Funct. Mater. 19*, 853–859.

(145) Johnson, N. J. J., Oakden, W., Stanisz, G. J., Scott Prosser, R., and van Veggel, F. C. J. M. (2011) Size-Tunable, Ultrasmall NaGdF 4 Nanoparticles: Insights into Their T 1 MRI Contrast Enhancement. *Chem. Mater. 23*, 3714–3722.

(146) Giljohann, D. A., Seferos, D. S., Daniel, W. L., Massich, M. D., Patel, P. C., and Mirkin, C. A. (2010) Gold Nanoparticles for Biology and Medicine. *Angew. Chemie Int. Ed. 49*, 3280–3294.

Objectives

As we have explained in the introduction, the investigation on the coating of NP is facing exciting challenges (e.g, reproducibility, simplicity, flexibility, etc.) both in surface chemistry for easier synthesis or functionalisation of NP, and prediction and control of the *in vivo* behaviour and knowledge of the interaction with the biological interfaces for improved bioapplications. The main goals of this thesis are then:

1- Synthesis of NP with long *in vivo* circulating times provided by innovative coatings.

2- Understand how the interactions of the NP with the proteins of the blood affect its *in vivo* fate.

3- Design NP aimed at specific advanced bioapplications as contrast agent for detection and characterisation of tumour or atherosclerosis plaques.

4- Development of new easier generic and standardised synthetic approaches for different hydrophobic NP of different composition.

5- Design and synthesis of a theranostic NP gathering detection and therapy of tumours.

Chapter 1

Phosphatidylcholine-Coated Iron Oxide Nanomicelles for *In Vivo* Prolonged Circulation Time with an Antibiofouling Protein Corona

Abstract

We report the synthesis of micellar Phosphatidylcholine-coated Superparamagnetic Iron Oxide Nanoparticles as a new long circulation contrast agents for magnetic resonance imaging. Oleic acid-coated Fe_3O_4 nanoparticles were first prepared via thermal degradation and then encapsulated into small clusters with a Phosphatidylcholine coating to obtain hydrophilic nanomicelles. A thoroughly characterisation confirmed the chemical nature of the coating and the excellent colloidal stability of these nanomicelles in aqueous media. Magnetisation and relaxivity properties proved their suitability as MRI contrast agent and *in vitro* cell viability data showed low toxicity. Vascular lifetime and elimination kinetics in liver were assessed by blood relaxometry and *in vivo* MRI in rats and compared with "control" particles prepared with a polyethylene glycol derivative. These micellar particles had a lifetime in blood of more than 10 hours, much longer than the control nanoparticles (~ 2 hours) really remarkable considering that the coating molecule is a small biocompatible zwitterionic phospholipid. The protein corona was characterised after incubation with rat serum at different times by high-throughput proteomics, showing a higher proportion of bound apolipoproteins and other dysopsonins for the Phosphatidylcholine particles. The antibiofouling properties of this corona and its resistance to the adsorption of proteins corroborate the observed enhanced stability and prolonged systemic circulation.

1. Introduction

Iron oxide nanoparticles are widely used for preclinical and clinical applications, especially as contrast agents in magnetic resonance imaging.[1] One of the key challenges in the development of IONP for biomedical applications is their functionalisation to ensure good colloidal, circulating and targeting properties *in vivo.*[2,3]. High-temperature decomposition of organic iron precursors in organic solvents yield the best IONP in terms of size, size dispersion, crystallinity and reproducibility of the synthesis.[2] However, this method yields IONP that are only stable in organic solvents, thus requiring a second step to make them stable in aqueous media suitable for *in vivo* applications. The main approaches used for this are direct chemical modification of the oleic acid structure, ligand exchange, and stabilisation within a hydrophilic coating matrix.[4–6] These hydrophilic coatings should minimise the natural tendency of IONP to aggregate while conferring reduced toxicity and good biocompatibility to the probe.[7] Polyethylene glycol[8] and dextran[9] are established examples of such biocompatible surfaces that confer aqueous stability and hinder IONP from the reticuloendothelial system (RES). Small zwitterion molecules begin also to be proposed as an alternative coating with antibiofouling properties. However they are generally anchored or covalently conjugated to the surface of other type of inorganic NP[10–12] and few studies have reported IONP stabilisation within micelles made of only small molecules[13,14] mainly because encapsulation of inorganic NP inside such micelles is a chemosynthetic challenge. Indeed, the hydrophilic/hydrophobic balance of the coating is crucial for the formation of hydrophobic IONP encapsulated micelles, a requirement that often makes small amphiphilic molecules unsuitable, leading to unstable structures which form aggregates, or fail to incorporate the IONP cargo.[15] Consequently micelles formed from

amphiphilic polymers whose hydrophilic part often includes PEG chains, like di-block copolymers or lipid-derived polymers,[15–17] are often preferred for their ease of synthesis, good drug-delivery properties and long circulating lifetimes as antibiofouling coatings.[18] We report here oleic acid OA IONP encapsulated into nanomicelles of small phosphatidylcholine (PC) molecule by a nanoemulsion method and we investigate whether physicochemical properties, *in vivo* behaviour and vascular circulating times comparable to micelles of PEG coating can be obtained. We selected zwiterionic PC because it plays important biological roles as the major component of mammalian cell membrane. Also, its phospholipid structure allows easy formation of a micelle over the OA of the hydrophobic Fe_3O_4 NP as shown by its usual inclusion in solid lipid NP, microbubbles or liposome formulations.[19] For comparison, we selected the PEG derivative polysorbate 80 (P80), a polymeric coating known by its blood pool properties.[18] After a detailed characterisation of the probes especially as possible MRI contrast agent, the vascular lifetimes of the both nanomicelles were estimated by relaxometric techniques. We also studied the rate of PC IONP elimination in the liver by MRI in rats. The biological fate and uptake of NP by the RES is strongly influenced by the composition of the protein corona i.e the set of plasma proteins that adsorb onto their surface upon intravenous injection, this one being specific to each nanomaterial.[20,21] It is now an ongoing issue to understand better how the IONP synthetic identity influence the composition of the corona to improve the biological fate of the probes.[22] To investigate the correlations between the difference in the vascular lifetimes obtained with the PEG and PC IONP with their protein corona, we resolved by proteomic analysis, the composition of the corona of the both nanomicelles incubated *in vitro* with rat serum.

_____

Key to understand: Protein Corona

Definition. When nanoparticles enter in the vascular system, they first contact with the entire set of the plasma proteins (> 3000) and the other components of the blood. Therefore some of these proteins or other biomolecules compete to adsorb to the surface of the nanomaterial leading to what is called "protein corona". This protein corona provides a biological identity to the nanoparticles which will have an important role in the physiological response, in particular for the opsonisation and clearance.[20]

Structure. The adsorption of proteins on the surface of NP evidently depends of protein-nanoparticles binding affinities but also on protein-protein interactions. The current model stands that the corona can be subdivided in two parts. The "hard" corona names the component that adsorb with high affinity to the surface of the NP while the "soft" corona designates the loosely bound proteins, which interact principally with the proteins of the "hard" corona. Studies are focusing principally on the composition of the "hard corona" as it seems the most influent part that influences the physiological response. During biophysical events, soft corona rapidly dissociate during translocation while hard corona shows much larger exchange times.[23]

Dynamic evolution. An important notion is that the proteins adsorbed on the NP are in a continuous state of exchange. This means that the corona has a dynamic composition and constantly changes along time. This competitive adsorption of proteins on the surface is referred as the "Vroman effect" and is a complex result of different variables such as incubation time, concentration and lifetime of a protein in plasma as well as its binding affinity for the nanoparticle´s surface.[24] For instance, proteins of high abundance in plasma rapidly adsorbed to the surface but are finally replaced with other proteins that have lower abundance but higher affinity; on other hand proteins of high affinity can also be exchanged with others of slower association rates but longer residence time. This illustrates how difficult is to predict the composition of the protein corona. Thus, it is usual to distinguish the "early" and "late" stages of a protein corona for a better understanding of the biological behaviour of the nanoparticles.[25]

Composition. The composition of a protein corona is unique to each material. However, from the different studies, general trends have been clarified. A general structure draws a group of about ten proteins adsorbed in high abundance together with plenty others adsorbed in low abundance. Albumin, apolipoproteins, immunoglobulins, coagulation factors and fibrinogens are class of proteins frequently found in the corona.[20]

Biological effects of the protein corona. Protein corona is part of the biological identity of the nanomaterials, which determines its interaction with biomolecules and biological barriers of the body. It has strong consequences in signalling, kinetic and biodistribution of the probes. A strong correlation has been observed between the cells uptake of the NP and their protein corona. Especially, the protein corona is associated with the biological process of opsonisation and consecutive uptake by the cells of the reticuloendothelial system and mononuclear phagocyte system (macrophages). Importantly, it has been demonstrated that the presence of opsonins and/or dysopsonins in the corona either favour the clearance or increase the vascular lifetime of nanomaterials.[26]

Factors of the NP affecting the protein corona. Multiple parameters can have an effect on the composition of the protein corona. In fact, all the physicochemical characteristics of a NP, termed as synthetic identity, will affect the protein corona and biological identity. Controlling and understanding these factors are crucial in order to improve the final biological role the probes are designed for. Among all the parameters, we highlight surface charge, hydrophobicity, size, shape and nature of the coating.[23]

Characterisation. Elucidation of the protein corona associated to a NP is a very complex process. As the corona is dynamic, its description only corresponds to a given time. The experiments are realised most of the times *in vitro,* by incubation of the NP with serum. It has been observed that many parameters can dramatically affects the results, above all the concentration of the NP used during the experiment. Moreover isolation of the proteins is very difficult and it is almost impossible to make an exhaustive characterisation. The two techniques most use, differential centrifugation or size exclusion chromatography, will inevitably disturb the composition and cause a loss of the weakly bound proteins. Concerning the identification step, great progress has

been performed. The apparition of liquid chromatography coupled to high throughput mass spectrometry (MS) overcomes many limitations of the previous technique (electrophoresis followed by traditional MS) for greater sensitivity. Other secondary characterisations like protein corona thickness, surface charge, density and strength of protein interaction can be described by dynamic light scattering (DLS), transmission electronic microscopy, colorimetric or calorimetric titration.[27,28]

2. Results and discussion

2.1 Synthesis of oleic acid coated magnetite nanoparticles, OA IONP
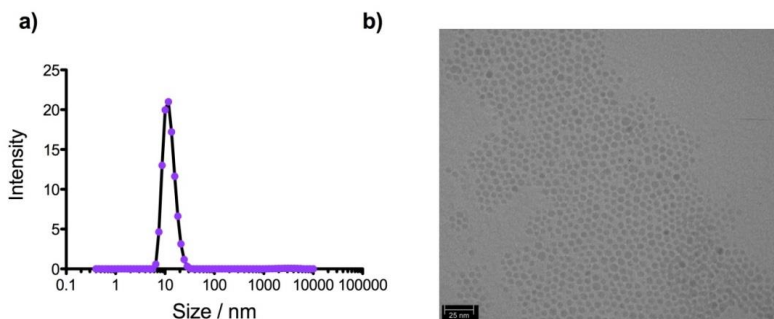

Figure 1.1 a) Hydrodynamic size and b) TEM of OA IONP.

Oleic acid-coated magnetite OA IONP were synthesised by thermal decomposition method addressed previously in detail in the section 2.3 of the Introduction. We used here the decomposition of iron(III) acetylacetonate at high temperature in an oleylamine (OM)-OA mixture following a well-known method described in the Materials and Methods section of this first chapter.[29] NP were uniform, with a polydispersity index (PDI) of 0.24, and had a hydrodynamic size of 10 ± 3 nm and a core diameter of 7 ± 2 nm (Figure

1.1a). Transmission electron microscopy (TEM) showed the particles to be spherical and well-dispersed (Figure 1.1b). In the diffractogram obtained by X-ray diffraction XRD tool (Figure 1.2), we observed clearly the peaks corresponding to the crystalline structure of the magnetite phase Fe_3O_4 (Powder Diffraction File Card No. 16-0629).
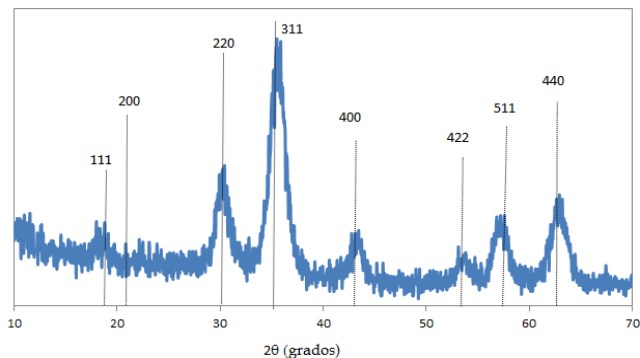

Figure 1.2 Typical XRD for OA IONP nanoparticles obtained in this work.

Surfactant coating has been characterised by Fourier Transformed Infrared Spectroscopy (FTIR) shown in Figure 1.3. Spectrum displayed the characteristic vibration peaks of the OA. The ones of the aliphatic moieties were found at 2920 cm^{-1} (v_a C-H) and 2850 cm^{-1} (v_s C-H) while the ones of the carboxylic group appeared at 1625 cm^{-1} (v C-O) and 1530 cm^{-1} (v C-O). In comparison to the free carboxylic group, these last peaks were found at 1) a frequency lower than the C=O vibration band but 2) higher than the frequency of the C-O vibration band, also 3) the differences between the two bands were less than 110 cm^{-1}. All these information suggest that the carboxylic group of the oleic acid is coordinated to the iron atoms of the surface of the magnetite core through a bidentate complex with the oxygens. Indeed, as already mentioned, OA has a high affinity for the iron ions. Finally the stretching band

at 590 cm^{-1} is characteristic of the Fe-O bound of the inorganic crystalline core structure.
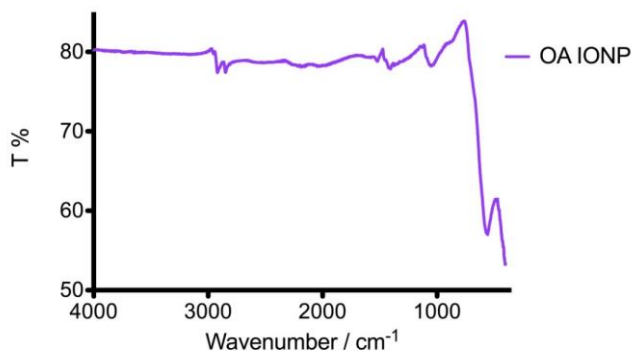

Figure 1.3 Typical FTIR of OA IONP obtained in this work.

Coating can be also characterised by mass spectroscopy (MS). The mass spectrum of the OA IONP is clearly representative of the OA adducts with peaks at m/z = 208 and 563 g.mol^{-1}, respectively the MW of OA subtracted of one proton and its double multiple. No peaks representative of OM, a side products used in the reaction and weak cheating ligand of magnetite core, were detected with MS highly sensitive technique. It confirmed the surfactant recovering the NP is made of only OA. (data not shown)

Finally thermogravimetric analysis (TGA) shows that the organic coating (corresponding to the removal of OA surfactant between 190ºC and 300ºC) represents 15 % of the total weight of OA IONP (Figure 1.4). This also indicates a high strength of union formed by the complex between carboxylic acid of OA and Fe, as no loss of surfactant is observed before 190ºC. First slight decrease of the weight between 0 and 190ºC is due to the combined evaporation of the remaining water and un-adsorbed OA.
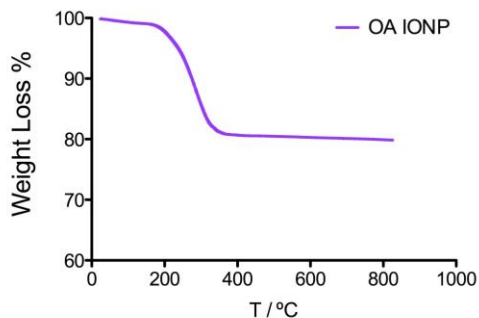
56

Figure 1.4 TGA of OA IONP.

One of the most important properties of the Fe3O4 NP further taken advantage of for bioapplications especially MRI, is their magnetism (Details in Introduction, Section 2.1. One of the characterisations is performed with a vibrating sample magnetometer (VSM). On the figure 1.5, it can be easily observed a superparamagnetism behaviour (no hysteresis loop and coercivity) with a high saturated magnetisation of 70 emu.g^{-1}.
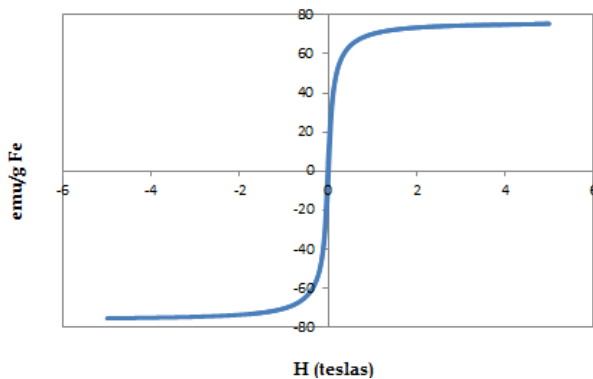

Figure 1.5 Magnetisation curve for OA IONP used in this work.

2.2 Synthesis and characterisation of Phosphatidylcholine coated iron oxide nanoparticles, PC IONP

OA IONP were then stabilised within a micelle composed of the amphiphilic molecule PC. We used a nanoemulsion method which involved mixing a small volume of the OA IONP in n-hexane within a larger volume of aqueous phosphate buffer containing PC. This entails the formation of a PC monolayer, which forms spontaneously at 1% hexane. Attempts with other solvents such as $CHCl_3$ were unsuccessful.[30] Under sonication and stirring, an oil-in-water emulsion is formed that converts progressively into a single aqueous solution after hexane evaporation.[31] In this process, the hydrophobic fatty acid PC tails surround the OA aliphatic chain of the OA IONP through hydrophobic interactions, while the hydrophilic choline heads line up around the outer surface of the micelle, providing water-dispersibility by masking the hydrophobic layer (Figure 1.6).
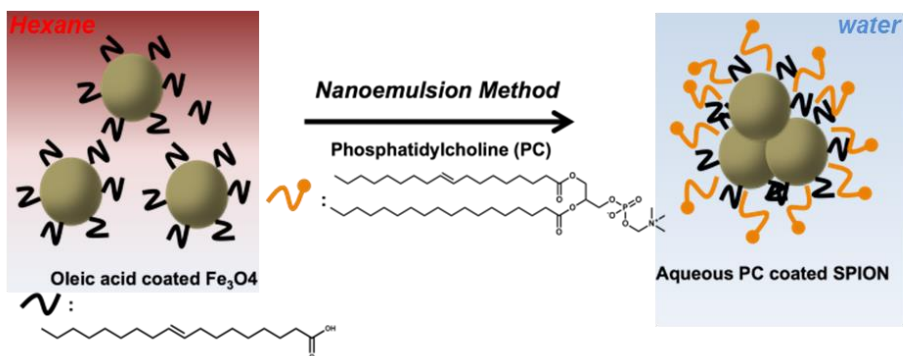

Figure 1.6 Method for the synthesis of PC IONP.

The nanoemulsion method presents several advantages over common reverse evaporation procedures for micelles preparation, including

reproducibility, simplicity, speed, and a narrow micelle size distribution. Successful formation of hydrophilic nanomicelles was first indicated by the observation that PC IONP did not re-disperse after mixing with hexane (Figure 1.7, inset). The nanomicelles had hydrodynamic size of 74.9 nm with a PDI of 0.14, showing that the method yields a very homogeneous dispersion (Figure 1.7). The difference in hydrodynamic size between OA IONP precursors and the PC IONP is attributable to the formation of micelles containing several OA IONP packed together, confirmed in TEM images showing OA IONP in small assemblies of overall diameter around 80 nm. High resolution transmission electronic microscopy (HRTEM) showed the lattice fringes on the Fe_3O_4 cores, demonstrating excellent crystallinity (Figure 1.7).[3]
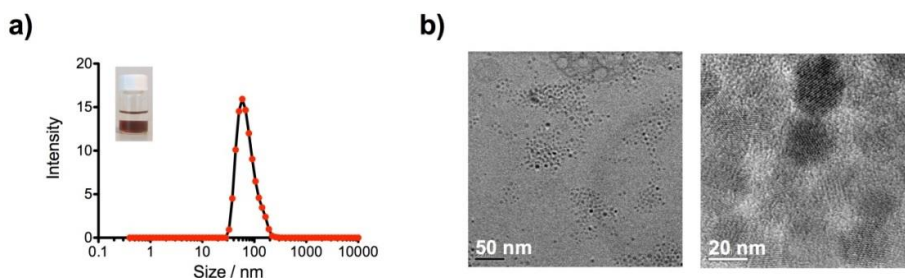

Figure 1.7 a) Hydrodynamic size of PC IONP. (inset photo of a 1:1 mixture of hexane/ PC IONP in water). b) TEM of PC IONP at two magnifications.

To evaluate the stability and colloidal properties of the nanomicelles, we measured zeta potential (ζ) variation as a function of pH and the effect of different high-salt-content buffers on hydrodynamic size. PC is a zwitterionic molecule, with a negative charge due to the glycerophosphate group and a positive charge due to the trimethylethanolammoniun group. Accordingly, the measured value of ζ (Figure 1.8a) predicts excellent stability of PC IONP over the whole range of pH below and above pH 5, at which the micelles surface

has no net electrical charge. Such good colloidal properties are confirmed in literature concerning the zwitterionic coatings.[12] At physiological pH we obtained a negative potential of -11.5 mV, which stabilises the micellar preparation through repulsive electrostatic interactions. The nanomicelles also showed excellent stability in the commonly used culture media Dulbecco's Modified Eagle's Medium (DMEM) and Roswell Park Memorial Institute (RPMI) and in Phosphate buffered saline (PBS), with no increase in hydrodynamic size over time, even in 10x PBS (Figure 1.8b).
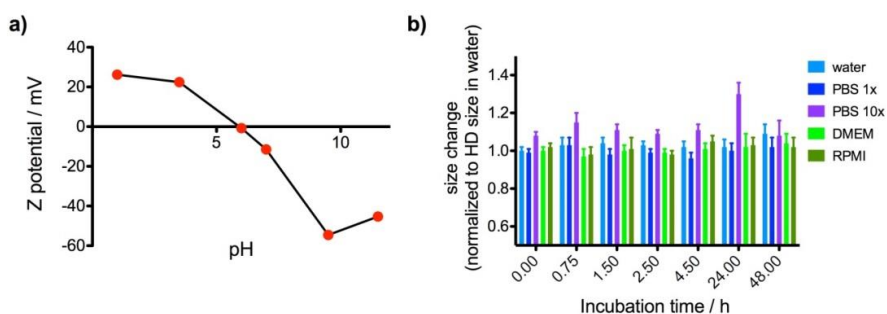

Figure 1.8 a) Zeta potential of PC IONP as a function of pH. (b) Change of hydrodynamic size of these nanomicelles with time in high ionic strength solutions.

The composition of PC IONP (*1.1*) was fully characterised by FTIR, TGA and MS (Figure 1.9). PC IONP showed the characteristic absorption spectrum of PC, with bands at 2920 cm^{-1} (v_a C-H), 2850 cm^{-1} (v_s C-H) and 1625 cm^{-1} (v_s C=O) for the fatty acid chains of the PC, which superimposed with the signals of the aliphatic chain of OA. Specific absorption bands of PC corresponding to the choline head were found at 1150 cm^{-1} (v P=O) and 1000 cm^{-1} (v N-C). TGA displayed that PC coating degraded from 200 to 400ºC and represented less than 10% of the total weight of the nanomicelles (after subtraction of the OA contribution to the total organic weight). This low weight

suggested that a single cap of PC intercalate with fatty chains of OA. The mass spectrum of the PC IONP organic coating (diluted in MeOH/H₂O and analysed in an acidic mixture to promote ionisation, with m/z=760) was representative of the expected PC and OA adducts, the two organic molecules in the composition of the micelles.
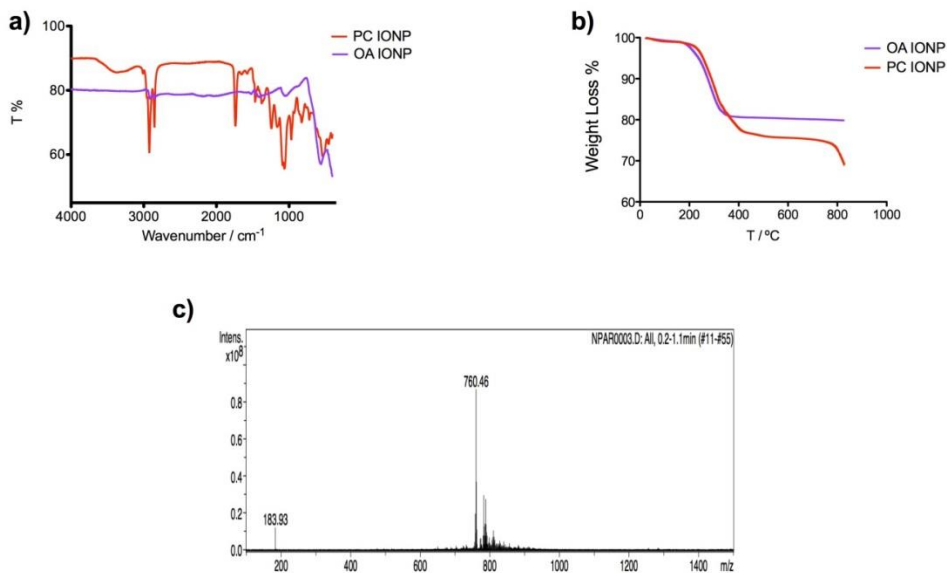
Figure 1.9 (a) FTIR spectra of OA IONP and PC IONP, (b) TGA of OA IONP and PC IONP and (c) MS of PC IONP.

Magnetic properties of the PC IONP as MRI contrast agent. IONP are mainly used as contrast agents for MRI, so the magnetic properties of the synthesised nanomicelles are essential for further applications. The PC IONP maintained a superparamagnetic behaviour with a saturation magnetisation value of 60 emu g^{-1}, which is of the same order as the hydrophobic OA IONP precursors (70 emu g^{-1}) (Figure 1.10a). This illustrates that there was low

surface oxidation of the iron core during the nanoemulsion procedure for micellar preparation. The good superparamagnetic behaviour of *1.1* is mostly a consequence of the thermal preparation step, which provides highly crystalline iron oxide cores. Saturation magnetisation is also enhanced by the encapsulation and formation of clusters.[32] To assess the efficacy of the nanomicelles as contrast agents for T_2-weigthed MRI, NMR relaxometric properties were investigated. The longitudinal (R_1) and transverse (R_2) relaxation rates were measured as a function of the iron concentration for a set of diluted PC IONP (Figure 1.10b). Good linearity was observed and the longitudinal (r_1) and transverse (r_2) relaxivities were calculated from the slope of the linear regression, yielding values of 1.3 $s^{-1}mM^{-1}$ and 147.4 $s^{-1}mM^{-1}$, respectively. The r_1 value is much smaller than the typical value for hydrophilic IONP with a dextran coating (from 3 to 10 $s^{-1}mM^{-1}$) due to the lower accessibility of water and limited influence of the IONP in the middle of the cluster.[33] The major factors contributing to the high r_2 value are the size and crystallinity of the iron oxide core. Cluster size has a strong influence on r_2, with an optimum value of 80 nm, precisely in the range of our nanomicelles.[34]
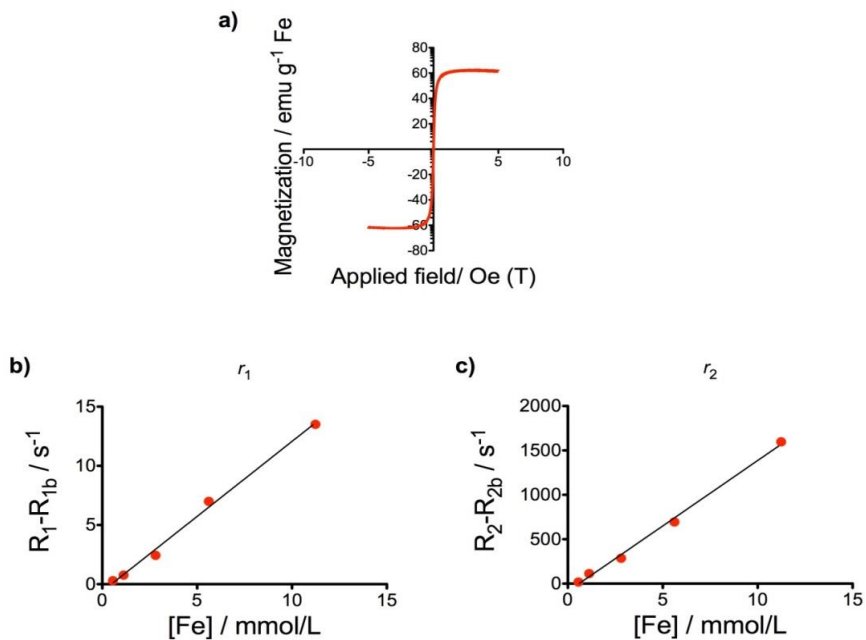
Figure 1.10 (a) Magnetisation curve at 298 K and plot of (b) longitudinal (T_1) and (c) transverse (T_2) relaxation rates against iron concentration of PC IONP.

Cytotoxicity effects. The potential toxicity of PC IONP was evaluated by incubation with C57BL/6 mouse embryonic fibroblasts (MEFs) over 72 hours. Iron uptake analysis confirmed that the MEFs effectively internalised the nanomicelles in a time and concentration-dependent manner (Figure 1.11a). Cell growth and viability analysis (propidium iodide staining of necrotic cells) showed low toxicity for the 40 μg/mL dose (Fig. 1.11b). Detailed cytometry analysis confirmed that a small proportion of MEFs exposed to *1.1* underwent apoptosis (Fig. 1.12) possibly caused by the high internalisation of PC IONP inside the cells. These results were confirmed by cell proliferation experiments (Fig. 1.11c), which showed a slight inhibition of cell population growth in the presence of 40 μg/mL PC IONP at 48h (at 72 hours, stabilisation

of population growth of control cells reflected cell confluence). These toxicity data suggest that low-doses of PC IONP can be safely used *in vivo* as a T_2-MRI contrast agent. Low cytotoxicity for *1.1* could be anticipated because PC (a component of lecithin) is nontoxic and extensively used in a wide range of applications.[35] This low toxicity is also indicative of the robustness of the micellar assembly, since liberation of hydrophobic OA IONP would have toxic effects.
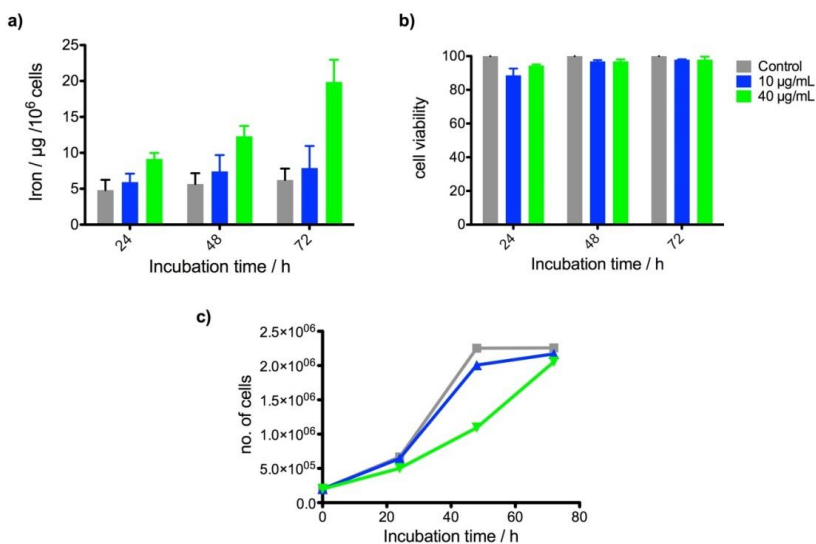
Figure 1.11 (a) Iron uptake by MEFs incubated with PC IONP (at 10 µg.ml⁻¹ and 40 µg.ml⁻¹ iron concentrations; 24, 48, 72 hours). (b) Cell viability of MEFs incubated with PC IONP (at 10 µg.ml⁻¹ and 40 µg.ml⁻¹ iron concentrations; 24, 48, 72 hours). (c) Number of MEFs cells after incubation with these nanomicelles (at 10 µg.ml⁻¹ and 40 µg.ml⁻¹ iron concentrations; 24, 48, 72 hours).
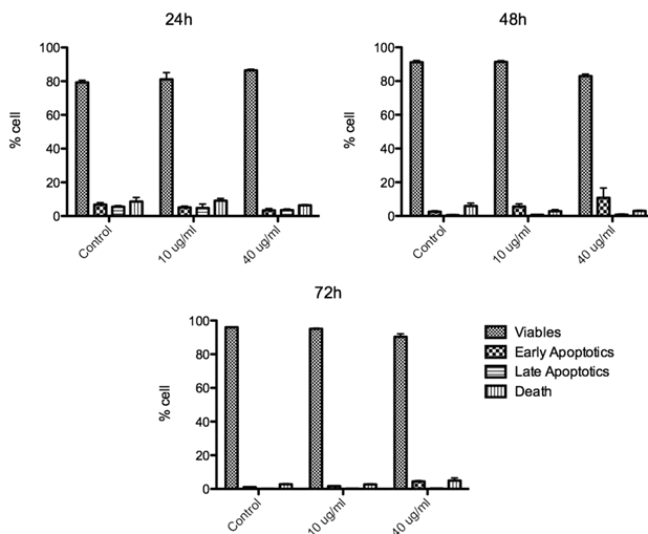
Figure 1.12 Relative proportions (%) of viable, early apoptotic, late apoptotic and dead cell populations of MEFs incubated with PC IONP (at 10 µg.ml^{-1} and 40 µg.ml^{-1} iron concentrations; 24, 48, 72 hours).

2.3 Circulation lifetime and *in vivo* MRI of PC IONP

An essential requirement for the intravenous use of NP in targeted nanomedicine, for example as drug-delivery agents, is the ability to remain in the bloodstream until the target organ is reached [36]. This is equally a requirement for the use of NP as blood pool contrast agents for tumour perfusion or detection of angiogenesis. Long circulation times favour passive tumour targeting *via* the enhanced permeability and retention effect (EPR).[37,38] To assess the performance of PC IONP (*1.1*) we compared them with nanomicelles P80 IONP (*1.2*), prepared by the same nanoemulsion method but coated with the PEG-derivative P80, a large nonionic molecule with a lipophilic OA moiety attached to PEG polyether groups [39] PEG is described as a golden standard for coating providing good blood pool properties to NP.

Table 1.1. Comparison of the physicochemical characterisation of micellar PC and P80 IONP.

	PC IONP	P80 IONP
Hydrodynamic size (nm)	74.9	25
Pdi	0.14	0.19
Zeta potential (pH=7.1) (mV)	-11.5	-4
Saturation magnetisation	70	65
Relaxivity ($s^{-1}.mM^{-1}$)	r_1: 1.3	r_1 : 2.3
	r_2 : 147.4	r_2 : 127.2
Estimated vascular life time (relaxometric method)	10 h	2h

Detailed characterisation of the P80 IONP micelles (*1.2*) are presented in Figure 1.13. These main physicochemical properties of P80 IONP are compared with PC IONP in Table 1.1. The control P80 IONP had a hydrodynamic size of 25 nm, an almost neutral charge at physiological pH, and magnetic properties of the same order as the PC IONP.

Vascular lifetime after intravenous administration (i.v.a) of PC IONP was first estimated by T_2 relaxometry of rat blood samples. After i.v.a of the probe, blood aliquots were collected at different times post-injection and their transverse T_2 relaxation times measured (Figure 1.14a). T_2 shortening below basal levels is an index of the presence of the iron-containing nanomicelles in the blood aliquots. The analysis showed extended circulation of injected PC IONP (*1.1*) for about 10 h. This circulation time, significantly longer than described for other IONP in literature, was confirmed by measuring the clearance rate in rat liver from the loss of the MRI signal in this organ. The decrease in signal intensity in the liver was measured at different times after i.v.a. by averaging signal intensities from a selected region of interest (ROI) and normalizing to the basal image (Figure 1.14b and 1.14c). We observed, by *in vivo* liver MRI, a signal reduction reaching a minimum 19 hours after injection. These data complement the *ex vivo* NMR relaxometric measurements.
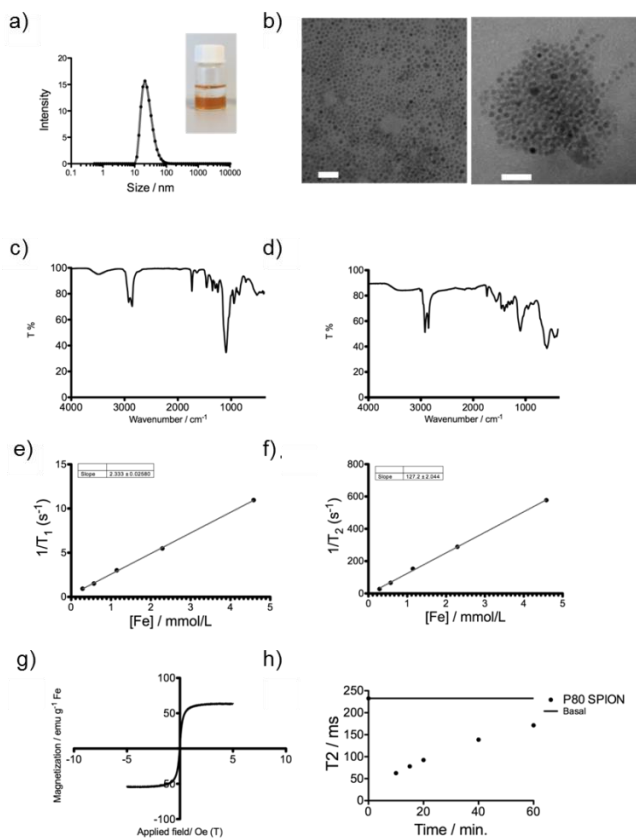
Figure 1.13 Characterisation of the control P80 IONP typically obtained in this study.
(a) Hydrodynamic size (inset: photo of a 1:1 mixture of hexane/P80 IONP in water). (b)
TEM images; scale bars, 30 nm and 25 nm (b2). (c) FTIR spectra of P80 IONP (d)
FTIR spectra of P80 IONP. (e) Plot of the longitudinal ($1/R_1$) and (f) transverse ($1/R_2$)
relaxation rates of P80 IONP against iron concentration. (g) Magnetisation curves of
these nanomicelles at 298 k. (h) T_2 relaxation times in rat blood samples after i.v.a. of
P80 IONP over time plotted against the T_2 baseline value.

Due to their size, IONP (> 50 nm or average around 80 nm) are rapidly taken up by the RES; also known as the mononuclear phagocyte system (MPS). Consequently *in vivo* applications are currently limited to the organs of this system (liver, spleen, bone marrow, and lymph node).[40] This limitation has prompted the development of nanoparticle systems with coatings and sizes that support longer circulation lifetimes (for example, a half-life >5 h in rats) and that are optimised for drug delivery or use as contrast agents for imaging. To achieve steric stabilisation, different carriers have been surface-engineered with large neutral polymeric molecules, such as PEG, which shields and minimises the particle surface opsonic modification with blood proteins and makes particles less susceptible to ingestion by phagocytic cells. Yet even the best PEG-ylated IONP candidates, including polymeric micelles, liposomes or lipoplexes, have a vascular lifetime in rats of only a few hours.[41] Longer circulating times are achieved with ultrasmall superparamagnetic iron oxide NP (< 50nm), which have reported lifetimes of dozens of hours, within the intensity limitation range detected here [42]. In comparison, even despite their smaller size, the vascular lifetime of P80 IONP (*1.2*) in rats after i.v.a., determined by the same relaxometric technique, was around 2 hours only (Figure 1.13g and Table 1.1). The PC coating thus provides micellar IONP with properties that ensure a significantly longer circulation time. This significantly improved resistance to blood clearance has been already shown for PC-coated gold NP.[43]
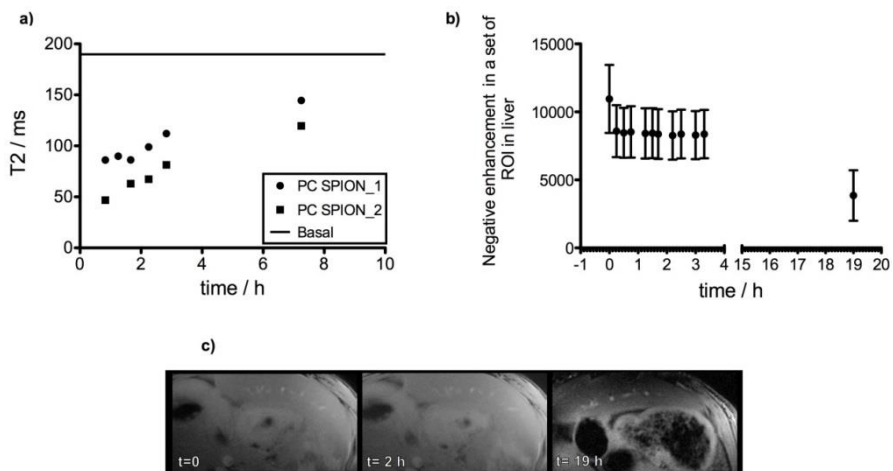
Figure 1.14 a) T_2 relaxation time of rat blood samples after i.v.a. of PC IONP plotted over time relative to the T_2 blood baseline value (black line). b) Signal decrease is observed for a set of ROI in rat liver and c) liver MR Images after i.v.a. of PC IONP.

2.4 Serum protein identification and quantification of the corona of PC and P80 IONP

When NP enter the vascular system, plasma proteins and other biomolecules rapidly adsorb to their surface, leading to the formation of a dynamic protein corona that significantly determines the *in vivo* biological behaviour. In particular, the uptake of the NP by the phagocytes of the RES is strongly associated with the presence of specific proteins in the corona.[21] The composition of this corona is highly dependent of the physicochemical features of the NP (size, superficial charge, nature of the coating). For instance, a PEG coating reduces the total amount of nonspecific protein adsorbed on the nanoparticle surface.[44] Zwitterionic ligands or polymers are also reported to resist the adsorption of nonspecific plasma proteins, and this

69

may contribute to the long circulation times of the PC IONP.[45,46] To characterise the composition of the hard protein coronas (i.e the strongly adsorbed proteins) of PC and P80 IONP, we incubated *in vitro* the nanomicelles in rat serum for 15, 90 and 180 min, isolated the NP-protein complexes, and analysed them by high-throughput liquid chromatography (LC)-MS. The incubation times were chosen in accordance with the estimated vascular lifetime of the probes and based on representative changes found in the literature.[28] The sensitive analysis used allowed us to identify ≥300 proteins in each corona, with a false discovery rate (FDR) below 1% (Results of the proteomics characterisation. The bioinformatic analysis of the results showed that the identified proteins are representative of pathways related to inflammation and the immune system, among others.
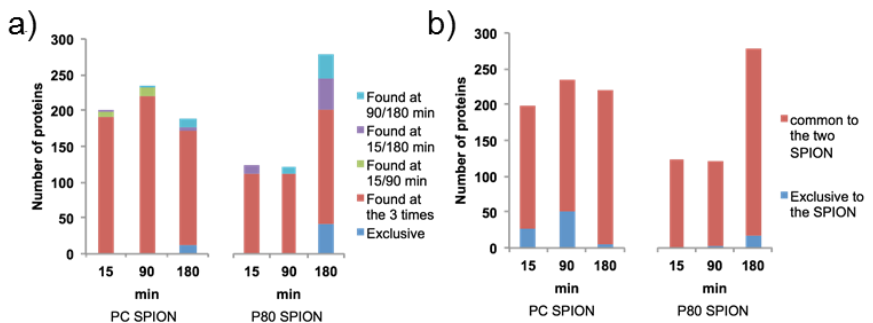
Figure 1.15 a) Qualitative comparison of protein coronas over time (15, 90 and 180 min) for the PC and P80 IONP. The charts show the numbers of same proteins (SPC >2, FDR>1%) present in the coronas at the three times of incubation, at two times of incubation, and exclusive to one time of incubation. b) Qualitative comparison of PC and P80 IONP coronas at each time. The charts show the numbers of same proteins common to both nanomicelles types or exclusive to one (SPC >2, FDR>1%).

The corona compositions of the two IONP were qualitatively similar at all three incubation times (Figure 1.15), which is expected since both IONP are micellar structures. Proteins exclusive to the corona of one micellar IONP type were generally detected in lower abundance, with a spectral peptide count (SPC) <4.[47] These lower-abundance proteins are unlikely to have a significant influence for the *in vivo* behaviour of the micelles. For semi-quantitative analysis, the percentage in weight of each corona protein was estimated on the assumption that the number of peptides identified per protein is roughly proportional to its concentration after normalisation.[48] Proteins with reported fouling (opsonins) and antifouling (dysopsonins) properties were grouped and classed according to their biological function in the circulatory system. Both types of micellar IONP showed a decrease over time in the relative amount of dysopsonins in the corona (Figure 1.15), as we could expect in a progressive opsonisation process. However, at each time point, *1.1* bound more dysopsonins than *1.2*. In contrast, opsonin levels were lower in the PC corona at the 15 and 90 min incubation times. Thus, the *in vivo* opsonisation shall be slower and less pronounced for longer circulating times in PC IONP. Similar studies also concluded that a strong representation of dysopsonins in the corona of NP favour their longer vascular circulation times.[21,23,49]
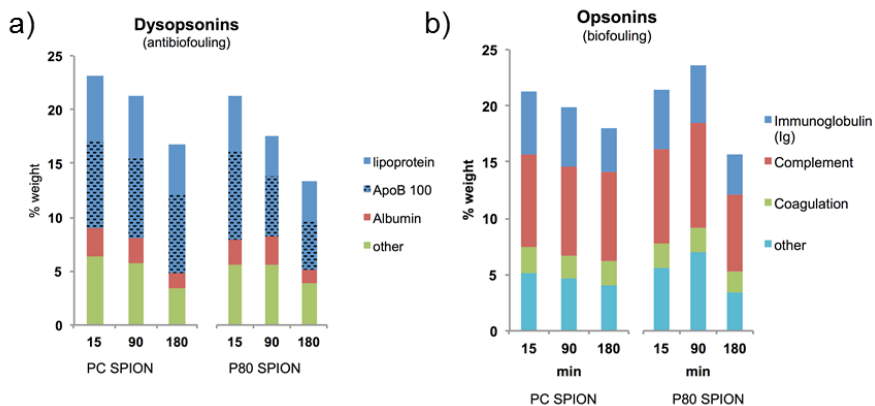
Figure 1.16 Relative % weight of the proteins with known (a) antibiofouling properties (dysopsonins) and (b) biofouling properties (opsonins) classified by their biological function in the coronas of micellar PC and P80 IONP at 15, 90 and 180 min *in vitro* incubation in rat serum. Data labels represent the % weight of the single ApoB 100.

For further details, we listed the key proteins which underlie these differences in the biological fates of PC and P80 IONP, looking among the abundant coronal proteins (relative proportion in weight > 0.6 %) those that were at 15 min incubation time significantly more abundant (threshold set>1.25 fold) in the PC IONP corona than in the P80 IONP corona. Most of these proteins have antifouling properties, many of them being apolipoproteins or regulators of the complement immune system (Table 1.2a) and are also reported to interact with phospholipids. Many of the specific proteins associated with the PC IONP corona showed significant decreases in 15 to 180 min incubation times (relative fold threshold set< 0.8, Table 1.3), confirming the important role of this set of proteins in delaying opsonisation. We also observed that the amounts of the dysopsonin apolipoprotein B100 (the most abundant protein in all the coronas) decreased sharply over time in the P80 IONP corona while remaining stable in the PC one, thus ensuring a

72

more sustained antibiofouling behaviour for *1.1* (Figure 1.16). Moreover, at 180 min incubation times, the listed key proteins, which bound in a significantly higher proportion to the P80 IONP (threshold >1.25, Table 1.2b) have been reported with biofouling roles, particularly in relation to vesicular transport and endocytosis . This can justify the faster and stronger opsonisation of P80 IONP. In this case, this set of proteins was not correlated with the profile of proteins, which abundance significantly increased in the corona over time. The proteomics analysis, with caution due to the *in vitro* aspect of the experiments, thus provides general evidences that (i) dysopsonins/lipoproteins have a strong representation in the PC IONP corona, because of a special affinity for the coating and (ii) protect these nanomicelles from opsonisation which (iii) follow a similar pattern than P80 IONP but, with an effect that is delayed and less pronounced. These preliminary proteomics characterisations are correlated with the longer vascular lifetime of the PC IONP.

Table 1.2 Coronal proteins with a relative % weight > 0.6% that were significantly more abundant (quotient of relative % weight > 1.25) in (a) PC IONP at 15 min incubation time, and (b) P80 IONP at 180 min incubation time.

a)

PC IONP at 15 min	relative % weight in PC corona	relative % weight in P80 corona	fold	classification
Apolipoprotein A-IV	1.96	1.50	**1.31**	Lipoprotein
Apolipoprotein A-I	1.72	1.31	**1.31**	Lipoprotein
Protein Cfh	1.57	0.47	**3.37**	Regulator Complement
T-kininogen 1	1.05	0.84	**1.25**	Acute phase
Protein Dsp	1.05	0.28	**3.74**	Cellular junction
Ig gamma-2B chain C	0.81	0.65	**1.24**	Immunoglobulin
Alpha-1B-glycoprotein	0.76	0.47	**1.63**	Lipoprotein
Plasminogen	0.72	0.47	**1.53**	Coagulation inhibitor
Oxidation resistance protein 1	0.62	0.19	**3.32**	Stress response

b)

P80 IONP at 180 min	relative % weight in P80 corona	relative % weight in PC corona	fold	classification
Transferrin receptor protein	1.75	1.28	**1.37**	Endocytosis
Thyroglobulin	1.46	0.90	**1.62**	Interaction with Heat shock
Clathrin heavy chain	1.10	1.17	**1.22**	Endocytosis / cytoplasmic vehicle

Table 1.2 (Cont.)

Cytoplasmic dynein 1 heavy chain	1.10	0.85	**1.29**	Degradation / Transport
Major vault protein	0.94	0.37	**2.95**	Transport
Heat shock cognate protein	0.77	0.69	**1.35**	Degradation/ Transport
Band 3 anion transport protein	0.61	0.48	**1.61**	Transport
Integrin	0.61	0.48	**1.27**	Coagulation

Table 1.3 Proteins with a relative % weight >0.7 % in the corona of the PC IONP at 15 min incubation which showed the strongest decreases in relative % weight over time (quotient of relative % weight between 180 and 15 min < 0.8). Proteins in bold are those already presented in Table 1.2.

PC IONP	relative % weight at 15 min	relative % weight at 180 min	Relative fold decrease
Serum albumin	2.67	1.33	**0.50**
Serotransferrin	2.19	1.17	**0.53**
Apolipoprotein A-IV	1.96	1.54	**0.79**
Apolipoprotein A-I	1.72	0.90	**0.53**
Protein Cfh	1.57	0.37	**0.24**
Hemopexin	1.24	0.64	**0.51**
Murinoglobulin-1	1.05	0.74	**0.71**
Haptoglobin	1.05	0.59	**0.56**
T-kininogen	1.05	0.32	**0.30**
Ig gamma-2B chain C region	0.81	0.64	**0.79**
Fibrinogen-like 2	0.81	0.53	**0.66**
Alpha-1B-glycoprotein	0.76	0.37	**0.49**
Plasminogen	0.72	0.27	**0.37**

3. Conclusions

A popular method for aqueous stabilisation of OA IONP prepared by thermal decomposition is the use of organic micelles formed through intercalation of amphiphilic polymers or loading in polymeric micelles. Nanoemulsion is an easy and convenient synthesis method allowing precise control of the micelles. Here we developed an alternative probe for T_2 MRI by encapsulating OA IONP into nanomicelles composed of the small zwitterionic molecule PC. The PC IONP are easily and reproducibly prepared, and their final hydrodynamic size of ~ 80 nm (pdi 0.14) is mostly made up of small clusters of the encapsulated OA IONP. The PC IONP have equivalent or superior physicochemical, colloidal and magnetic properties than most of the reported micellar-stabilised IONP micelles with organic polymers. Above all, the PC IONP have a prolonged circulation time in blood (> 10 hours in rats), which was reflected by the composition of the protein corona with high affinity of a set of dysopsonins for the PC coating and resistance against the adsorption of nonspecific proteins (opsonisation). Keeping NP in the circulation, together with the EPR effect, e.g. accumulation in tumours or target other diseases, in which the endothelium becomes leaky, are promoted. Hence these nanomicelles are promising contrast agents for preclinical and clinical *in vivo* MRI. Moreover, small hydrophobic drugs or molecular imaging probes can be easily encapsulated in the nanomicelles together with the OA IONP leading to potential candidates for multimodal drug delivery platform. Interactions of the PC coating with phospholipid pathway associated to pathologies may also be sought.

4. Materials and Methods

Materials

All chemicals for the preparation of the nanomicelles were purchased from Sigma-Aldrich Co. (St. Louis, USA). All reagents were of analytical grade except for the phosphatidylcholine (90%) and were used without any further purification. Distilled water (milliQ) or phosphate buffered saline PBS were used throughout the experiments.

Synthesis

Synthesis of OA IONP

Protocol described in Chapter "General Materials and Methods"

Synthesis of micellar phosphatidylcholine coated superparamagnetic iron oxide nanoparticles (PC IONP), (*1.1*)

Phosphatidylcholine (60 mg, 0.078 mmol) was first dispersed in 15 ml of PBS (pH=7.2, 5 mM). A 1 ml aliquot of OA IONP (10 mg Fe/ml) dispersed in hexane was then added to the solution and the resulting mixture was sonicated (Branson 250, 42 +/- 6 KHz) under robust stirring for 20 min at 37 °C. The oil in water (o/w) nanoemulsion was kept under sonication for a further 1h to evaporate all traces of hexane, resulting in the formation of a homogenous aqueous solution. Aggregates were removed by filtration (0.22 μm, MILIPORE, Sterivex-GP) and excess phosphatidylcholine was removed by gel filtration in a PD-10 column (GE Healthcare).

*Synthesis of micellar polysorbate 80-coated superparamagnetic iron oxide nanoparticles (P80 IONP), (*1.2*).*

Polysorbate 80 (150 mg, 0.11 mmol) was first dispersed in 12 ml of PBS (pH=7.2, 5 mM). A 1 ml aliquot of OA IONP (10 mg Fe/ml) dispersed in hexane was then added to the solution and the resulting mixture was sonicated (Branson 250, 42 +/- 6 KHz) under robust stirring for 20 min at 37 °C. The oil in water (o/w) nanoemulsion was kept under sonication for a further 1h to evaporate all traces of hexane, resulting in the formation

of a homogenous aqueous solution. Aggregates were removed by filtration (0.22 μm, MILIPORE, Sterivex-GP) and excess polysorbate 80 was removed by gel filtration in a PD-10 column (GE Healthcare) [39].

Cell toxicology

*Cell lines and media.*C57BL/6 mouse embryonic fibroblasts (MEFs) were grown in DMEM (Dulbecco's Modified Eagle Medium) supplemented with 10% fetal bovine serum (FBS), 1% penicillin-streptomycin and 1 mM sodium pyruvate. Cytotoxicity and iron uptake were assessed in MEFs exposed to PC IONP at different Fe concentrations (10 or 40 $\mu g.ml^{-1}$) and times of incubation (24h, 48h and 72h). Control cells were treated with vehicle (water).

Cytotoxicity assays. In the presence of Ca2+, annexin V binds to phosphatidylserine residues exposed on the outer surface of the plasma membrane of apoptotic cells. We collected 106 cells in 500 μl PBS and washed them. Cells were pelleted and resuspended in 195 μL binding buffer (10mM HEPES/NaOH, pH 7.4; 140 mM NaCl; 2.5 mM CaCl2). APC-Annexin V (BD PharmingenTM) was added (5 μl) and cells were incubated for 15 minutes at 25ºC in the dark. The viability marker propidium iodide was then added to a final concentration of 0.001% (w/v), and cells were analysed by flow-cytometry using the BD FACSCanto™ II system. All experiments were performed in triplicate. As a result, viable cells are negative for both APC Annexin V and PI; early apoptotic cells are APC Annexin V positive and PI negative; and late apoptotic and dead cells are both APC Annexin V and PI positive. Cytotoxicity was estimated by comparing the proportion of viable cells in populations exposed to the PC IONP with that in control cells.

Iron uptake quantification. Approximately 1x106 treated cells were lysed with 300 μl lysis buffer (50 mM NaCl, 50 mM TrisCl pH 8, 0.2% SDS) for 3 h at 55 ºC and mixed with the same volume of 10 mM HCl. Then, 150 μL 1.4 M HCl and 150 μL 4.5% KMnO4 were added. After 2 h at 60ºC, 90 μl of a detection solution containing 6.5 mM ferrozine, 6.5 mM neocuproine, 2.5 M ammonium acetate and 1 M ascorbic acid was added. The absorbance at 550 nm was measured after a further 30 minutes. The concentration of internalised Fe was calculated from a standard curve of FeCl3 (0 to 300 uM).

Vascular circulating times and clearance

All animal experiments conducted in this work were approved by the ethics and animal welfare committee at CNIC and were developed according to the Spanish and UE legislation.

Blood relaxometry. Rats (n = 2, Wistar male, 6 weeks old) were anesthetised with 2% isoflurane in a mixture of N2/O2 (80:20). The baseline blood sample (200 µl) was collected through the tail vein before administration of PC IONP (0.15 mg.kg^{-1}). Blood samples (200 µl) were collected at intervals from 5 min to 24 h. T2 relaxation times of the samples were measured in a Bruker Biospec spectrometer with a T2 Carr-Purcell-Meiboom-Gill sequence (Bruker Biospec 47/40, 1.5 T, Bruker Biospin, Germany) and plotted against the T2 of the baseline blood sample.

Evaluation of nanomicelles uptake in liver by MRI. Rats (n = 2, Wistar male, 6 weeks old) were anesthetised with 2% isoflurane in a mixture of N2/O2 (80:20). Baseline images were acquired before intravenous administration of PC IONP (0.15 mg.kg^{-1}). MR images of rat liver were acquired at intervals from 5 minutes up to a few hours after injection. The images were acquired with a 7 T Agilent/Varian 7T DD1 spectrometer (Agilent 2) with a 31 cm horizontal bore, using a 72 mm inner diameter quadrature birdcage volume coil (Rapid Biomedical GmBH, Germany). Rats were kept anaesthetised with the isoflurane-gas mix via a facial mask and placed prone in a customised plastic holder. Body temperature was kept constant by delivering warm air to the magnet bore, and the respiratory cycle was monitored constantly. For each animal, 8 axial 1 mm thick slices were acquired to image the liver. Images were acquired in free-breathing animals, using a gradient echo sequence with 4 ms/40 ms echo/repetition times, BW of 100 kHz, FOV of 6 cm x 6 cm, for a total acquisition time of about 80 seconds; the flip angle (FA) was fixed at 20 degrees.

Characterisation of the protein "hard corona" of PC IONP and P80 IONP

Experiments. PC IONP or P80 IONP (200 µl in PBS, 0.1 mg.ml^{-1} iron concentrations) were incubated in 80% rat serum (800 µl) at 37ºC with gently stirring at 100 rpm. After incubation for 15 min, 90 min or 180 min, the micelle-protein corona complexes were immediately separated from the serum by centrifugation (2h, 16000 g, 10ºC). Pellets were collected and redispersed in PBS before another centrifugation cycle. After three

similar washing steps the micelle-protein corona complexes were processed for proteomics.

Protein Digestion. Control of the sample quality was previously performed with state of art SDS polyacrylamide gel electrophoresis. The proteins of the corona bound to a fixed amount of NP were eluted by boiling in Tris-SDS gel loading buffer containing 50 mM DTT, and loaded onto 10% SDS-polyacrylamide gels to concentrate the proteins in a single band at the stacking/separating gel interface. Briefly, after band visualisation with colloidal Coomassie Brilliant blue staining, the acrylamide band was cut into 1mm^3 plugs for protein digestion. Gel pieces were incubated with 10 mM DTT (Sigma Aldrich) in 50 mM ammonium bicarbonate (99% purity; Sigma) for 30min at 56ºC. After reduction, samples were alkylated with 55 mM iodoacetamide (Sigma Aldrich) in 50 mM ammonium bicarbonate for 20min at RT. Gel plugs were washed with 50 mM ammonium bicarbonate in 50% acetonitrile (gradient, HPLC grade, Sigma), and dried in a Speedvac. Dry gel pieces were then embedded in sequencing grade modified porcine trypsin (Promega, Madison, WI, USA) at a final concentration of 20 ng/µL [at 40:1 protein:trypsin (w/w) ratio] in 50 mM ammonium bicarbonate and 5% acetonitrile. After digestion at 37 ºC overnight, peptides were re-extracted with 30% acetonitrile in 0.5% trifluoroacetic acid (99.5% purity; Sigma Aldrich), dried in a Speedvac, and finally desalted onto C18 Oasis-HLB cartridges (Waters) and dried-down [50]. The digested samples were resuspended in 10µL Buffer A (0.1% (v/v) formic acid) for LC-MS/MS separation and analysis.

Mass spectrometry data collection and analysis Samples were analysed by LC-MS/MS using a nano-HPLC system (EASY-nLC 1000, Thermo-Proxeon) coupled to an Orbitrap Elite mass spectrometer (Thermo Fisher Scientific). Peptides were separated using an Acclaim PepMap 100 C18 nano-column (75 µm I.D. x 25 cm, 2 µm particle size; Thermo Fisher Scientific) with Buffer A at a flow rate of 200 nl min^{-1}, and eluted with a linear gradient from 0-40% Buffer B (90% acetonitrile, 0.1% formic acid (vol/vol)) for 120 min. A survey scan was performed in the Orbitrap analyzer using a mass range of m/z 390–1,500, followed by data-dependent MS/MS scans of the twenty most-intense ions in profile mode. The survey scan was done at 35,000 resolution using a target value of 1,000,000 ions, 60 ms of injection time, and 1 microscan. Fragmentation was performed by CID with a 1.5 Da isolation mass width, 17,500 resolution, a target

80

value of 50,000 ions, and 80 ms of injection time. Proteins were identified using the SEQUEST algorithm (Proteome Discoverer 1.4, Thermo Fisher Scientific). The raw MS/MS files were searched against the rat Complete Proteome database (Uniprot at July 23th, 2013; 49,050 sequences) and a pseudo-inverted version of the same database. SEQUEST searches were performed allowing optional modifications (methionine oxidation) and fixed modifications (cysteine carboxamidomethylation), 2 missed cleavages, and 600 ppm and 1.2 Da ppm of mass tolerance for precursor and fragment ions, respectively. False discovery rate (FDR) was determined by the probability ratio method [51], followed by a post-search 12 ppm precursor mass filtering and the refined FDR calculation method [52]. Only peptides with FDR below 1% and identified with at least two peptides were selected for further analysis. Statistical analysis of data were performed using QuiXoT [53,54].

5. Bibliography

(1) Reddy, L. H., Arias, J. L., Nicolas, J., and Couvreur, P. (2012) Magnetic Nanoparticles: Design and Characterization, Toxicity and Biocompatibility, Pharmaceutical and Biomedical Applications. *Chem. Rev. 112*, 5818–5878.

(2) Laurent, S., Forge, D., Port, M., Roch, A., Robic, C., Vander Elst, L., and Muller, R. N. (2008) Magnetic Iron Oxide Nanoparticles: Synthesis, Stabilization, Vectorization, Physicochemical Characterizations, and Biological Applications. *Chem. Rev. 108*, 2064–2110.

(3) Mahmoudi, M., Sant, S., Wang, B., Laurent, S., and Sen, T. (2011) Superparamagnetic iron oxide nanoparticles (SPIONs): Development, surface modification and applications in chemotherapy. *Adv. Drug Deliv. Rev. 63*, 24–46.

(4) Herranz, F., Morales, M. P., Roca, A. G., Desco, M., and Ruiz-Cabello, J. (2008) A New Method for the Rapid Synthesis of Water Stable Superparamagnetic Nanoparticles. *Chem. - Eur. J. 14*, 9126–9130.

(5) Veiseh, O., Gunn, J. W., and Zhang, M. (2010) Design and fabrication of magnetic nanoparticles for targeted drug delivery and imaging. *Adv. Drug Deliv. Rev. 62*, 284–304.

(6) Sun, C., Lee, J., and Zhang, M. (2008) Magnetic nanoparticles in MR imaging and drug delivery. *Adv. Drug Deliv. Rev. 60*, 1252–1265.

(7) Longmire, M., Choyke, P. L., and Kobayashi, H. (2008) Clearance properties of nano-sized particles and molecules as imaging agents: considerations and caveats. *Nanomed. 3*, 703–717.

(8) Sun, C., Du, K., Fang, C., Bhattarai, N., Veiseh, O., Kievit, F., Stephen, Z., Lee, D., Ellenbogen, R. G., Ratner, B., and Zhang, M. (2010) PEG-Mediated Synthesis of

Highly Dispersive Multifunctional Superparamagnetic Nanoparticles: Their Physicochemical Properties and Function *In Vivo. ACS Nano 4*, 2402–2410.

(9) Tassa, C., Shaw, S. Y., and Weissleder, R. (2011) Dextran-Coated Iron Oxide Nanoparticles: A Versatile Platform for Targeted Molecular Imaging, Molecular Diagnostics, and Therapy. *Acc. Chem. Res. 44*, 842–852.

(10) Muro, E., Pons, T., Lequeux, N., Fragola, A., Sanson, N., Lenkei, Z., and Dubertret, B. (2010) Small and Stable Sulfobetaine Zwitterionic Quantum Dots for Functional Live-Cell Imaging. *J. Am. Chem. Soc. 132*, 4556–4557.

(11) Estephan, Z. G., Jaber, J. A., and Schlenoff, J. B. (2010) Zwitterion-Stabilized Silica Nanoparticles: Toward Nonstick Nano. *Langmuir 26*, 16884–16889.

(12) Breus, V. V., Heyes, C. D., Tron, K., and Nienhaus, G. U. (2009) Zwitterionic Biocompatible Quantum Dots for Wide pH Stability and Weak Nonspecific Binding to Cells. *ACS Nano 3*, 2573–2580.

(13) Liu, J., Yang, X., Wang, K., He, Y., Zhang, P., Ji, H., Jian, L., and Liu, W. (2012) Single Nanoparticle Imaging and Characterization of Different Phospholipid-Encapsulated Quantum Dot Micelles. *Langmuir 28*, 10602–10609.

(14) Kim, D., Chae, M. K., Joo, H. J., Jeong, I., Cho, J.-H., and Lee, C. (2012) Facile Preparation of Zwitterion-Stabilized Superparamagnetic Iron Oxide Nanoparticles (ZSPIONs) as an MR Contrast Agent for in Vivo Applications. *Langmuir 28*, 9634–9639.

(15) Dubertret, B. (2002) In Vivo Imaging of Quantum Dots Encapsulated in Phospholipid Micelles. *Science 298*, 1759–1762.

(16) Ma, Y., Tong, S., Bao, G., Gao, C., and Dai, Z. (2013) Indocyanine green loaded SPIO nanoparticles with phospholipid-PEG coating for dual-modal imaging and photothermal therapy. *Biomaterials 34*, 7706–7714.

(17) Nasongkla, N., Bey, E., Ren, J., Ai, H., Khemtong, C., Guthi, J. S., Chin, S.-F., Sherry, A. D., Boothman, D. A., and Gao, J. (2006) Multifunctional Polymeric Micelles as Cancer-Targeted, MRI-Ultrasensitive Drug Delivery Systems. *Nano Lett. 6*, 2427–2430.

(18) Gupta, A. K., and Gupta, M. (2005) Synthesis and surface engineering of iron oxide nanoparticles for biomedical applications. *Biomaterials 26*, 3995–4021.

(19) Al-Jamal, W. T., and Kostarelos, K. (2011) Liposomes: From a Clinically Established Drug Delivery System to a Nanoparticle Platform for Theranostic Nanomedicine. *Acc. Chem. Res. 44*, 1094–1104.

(20) Walkey, C. D., and Chan, W. C. W. (2012) Understanding and controlling the interaction of nanomaterials with proteins in a physiological environment. *Chem. Soc. Rev. 41*, 2780.

(21) Aggarwal, P., Hall, J. B., McLeland, C. B., Dobrovolskaia, M. A., and McNeil, S. E. (2009) Nanoparticle interaction with plasma proteins as it relates to particle biodistribution, biocompatibility and therapeutic efficacy. *Adv. Drug Deliv. Rev. 61*, 428–437.

(22) Mahon, E., Salvati, A., Baldelli Bombelli, F., Lynch, I., and Dawson, K. A. (2012) Designing the nanoparticle–biomolecule interface for "targeting and therapeutic delivery." *J. Controlled Release 161*, 164–174.

(23) Rahman, M., Laurent, S., Tawil, N., Yahia, L., and Mahmoudi, M. (2013) Protein-Nanoparticle Interactions. Springer Berlin Heidelberg, Berlin, Heidelberg.

(24) Vroman, L., Adams, A. L., Fischer, G. C., and Munoz, P. C. (1980) Interaction of high molecular weight kininogen, factor XII, and fibrinogen in plasma at interfaces. *Blood 55*, 156–159.

(25) Lynch, I., and Dawson, K. A. (2008) Protein-nanoparticle interactions. *Nano Today 3*, 40–47.

(26) Nagayama, S., Ogawara, K., Fukuoka, Y., Higaki, K., and Kimura, T. (2007) Time-dependent changes in opsonin amount associated on nanoparticles alter their hepatic uptake characteristics. *Int. J. Pharm. 342*, 215–221.

(27) Thode, K., Lück, M., Semmler, W., Müller, R. H., and Kresse, M. (1997) Determination of plasma protein adsorption on magnetic iron oxides: sample preparation. *Pharm. Res. 14*, 905–910.

(28) Tenzer, S., Docter, D., Kuharev, J., Musyanovych, A., Fetz, V., Hecht, R., Schlenk, F., Fischer, D., Kiouptsi, K., Reinhardt, C., Landfester, K., Schild, H., Maskos, M., Knauer, S. K., and Stauber, R. H. (2013) Rapid formation of plasma protein corona critically affects nanoparticle pathophysiology. *Nat. Nanotechnol. 8*, 772–781.

(29) Sun, S., and Zeng, H. (2002) Size-Controlled Synthesis of Magnetite Nanoparticles. *J. Am. Chem. Soc. 124*, 8204–8205.

(30) Cássia-Moura, R. (1993) Activation kinetics of the incorporation of colicin Ia into an artificial membrane: A Markov or a fractal model? *Bioelectrochem. Bioenerg. 32*, 175–180.

(31) Yang, J., Lee, T.-I., Lee, J., Lim, E.-K., Hyung, W., Lee, C.-H., Song, Y. J., Suh, J.-S., Yoon, H.-G., Huh, Y.-M., and Haam, S. (2007) Synthesis of Ultrasensitive Magnetic Resonance Contrast Agents for Cancer Imaging Using PEG-Fatty Acid. *Chem. Mater. 19*, 3870–3876.

(32) Chen, H., Yeh, J., Wang, L., Khurshid, H., Peng, N., Wang, A. Y., and Mao, H. (2010) Preparation and control of the formation of single core and clustered nanoparticles for biomedical applications using a versatile amphiphilic diblock copolymer. *Nano Res. 3*, 852–862.

(33) Ai, H., Flask, C., Weinberg, B., Shuai, X.-T., Pagel, M. D., Farrell, D., Duerk, J., and Gao, J. (2005) Magnetite-Loaded Polymeric Micelles as Ultrasensitive Magnetic-Resonance Probes. *Adv. Mater. 17*, 1949–1952.

(34) Pöselt, E., Kloust, H., Tromsdorf, U., Janschel, M., Hahn, C., Maßlo, C., and Weller, H. (2012) Relaxivity Optimization of a PEGylated Iron-Oxide-Based Negative Magnetic Resonance Contrast Agent for T_2-Weighted Spin–Echo Imaging. *ACS Nano 6*, 1619–1624.

(35) Royal Society of Chemistry (Great Britain). (2013) The Merck index: an encyclopedia of chemicals, drugs, and biologicals (O'Neil, M. J., Heckelman, P. E., Dobbelaar, P. H., Roman, K. J., Kenny, C. M., and Karaffa, L. S., Eds.) 15th ed. Royal Society of Chemistry, Cambridge, UK.

(36) Corot, C., Robert, P., Idée, J.-M., and Port, M. (2006) Recent advances in iron oxide nanocrystal technology for medical imaging. *Adv. Drug Deliv. Rev. 58*, 1471–1504.

(37) Cole, A. J., David, A. E., Wang, J., Galbán, C. J., Hill, H. L., and Yang, V. C. (2011) Polyethylene glycol modified, cross-linked starch-coated iron oxide nanoparticles for enhanced magnetic tumor targeting. *Biomaterials 32*, 2183–2193.

(38) Cho, K., Wang, X., Nie, S., Chen, Z., and Shin, D. M. (2008) Therapeutic Nanoparticles for Drug Delivery in Cancer. *Clin. Cancer Res. 14*, 1310–1316.

(39) Park, J., Yu, M. K., Jeong, Y. Y., Kim, J. W., Lee, K., Phan, V. N., and Jon, S. (2009) Antibiofouling amphiphilic polymer-coated superparamagnetic iron oxide nanoparticles: synthesis, characterization, and use in cancer imaging in vivo. *J. Mater. Chem. 19*, 6412.

(40) Wang, Y. X., Hussain, S. M., and Krestin, G. P. (2001) Superparamagnetic iron oxide contrast agents: physicochemical characteristics and applications in MR imaging. *Eur. Radiol. 11*, 2319–2331.

(41) Moghimi, S. M., Hunter, A. C., and Murray, J. C. (2001) Long-circulating and target-specific nanoparticles: theory to practice. *Pharmacol. Rev. 53*, 283–318.

(42) Weissleder, R., Bogdanov, A., Neuwelt, E. A., and Papisov, M. (1995) Long-circulating iron oxides for MR imaging. *Adv. Drug Deliv. Rev. 16*, 321–334.

(43) Liu, X., Li, H., Chen, Y., Jin, Q., Ren, K., and Ji, J. (2014) Mixed-Charge Nanoparticles for Long Circulation, Low Reticuloendothelial System Clearance, and High Tumor Accumulation. *Adv. Healthc. Mater.* n/a–n/a.

(44) Gref, Lück, Quellec, Marchand, Dellacherie, Harnisch, Blunk, and Müller. (2000) "Stealth" corona-core nanoparticles surface modified by polyethylene glycol (PEG): influences of the corona (PEG chain length and surface density) and of the core composition on phagocytic uptake and plasma protein adsorption. *Colloids Surf. B Biointerfaces 18*, 301–313.

(45) Ladd, J., Zhang, Z., Chen, S., Hower, J. C., and Jiang, S. (2008) Zwitterionic Polymers Exhibiting High Resistance to Nonspecific Protein Adsorption from Human Serum and Plasma. *Biomacromolecules 9*, 1357–1361.

(46) Estephan, Z. G., Schlenoff, P. S., and Schlenoff, J. B. (2011) Zwitteration As an Alternative to PEGylation. *Langmuir 27*, 6794–6800.

(47) Groult, H., Ruiz-Cabello, J., Lechuga-Vieco, A. V., Mateo, J., Benito, M., Bilbao, I., Martínez-Alcázar, M. P., Lopez, J. A., Vázquez, J., and Herranz, F. F. (2014) Phosphatidylcholine-Coated Iron Oxide Nanomicelles for In Vivo Prolonged Circulation Time with an Antibiofouling Protein Corona. *Chem. - Eur. J.* n/a–n/a.

(48) Ishihama, Y., Oda, Y., Tabata, T., Sato, T., Nagasu, T., Rappsilber, J., and Mann, M. (2005) Exponentially modified protein abundance index (emPAI) for estimation of absolute protein amount in proteomics by the number of sequenced peptides per protein. *Mol. Cell. Proteomics MCP 4*, 1265–1272.

(49) Moghimi, S. M., and Szebeni, J. (2003) Stealth liposomes and long circulating nanoparticles: critical issues in pharmacokinetics, opsonization and protein-binding properties. *Prog. Lipid Res. 42*, 463–478.

(50) Bonzon-Kulichenko, E., Perez-Hernandez, D., Nunez, E., Martinez-Acedo, P., Navarro, P., Trevisan-Herraz, M., del Carmen Ramos, M., Sierra, S., Martinez-Martinez, S., Ruiz-Meana, M., Miro-Casas, E., Garcia-Dorado, D., Redondo, J. M., Burgos, J. S., and Vazquez, J. (2011) A Robust Method for Quantitative High-throughput Analysis of Proteomes by 18O Labeling. *Mol. Cell. Proteomics 10*, M110.003335–M110.003335.

(51) Martinez-Bartolome, S., Navarro, P., Martin-Maroto, F., Lopez-Ferrer, D., Ramos-Fernandez, A., Villar, M., Garcia-Ruiz, J. P., and Vazquez, J. (2008) Properties of Average Score Distributions of SEQUEST: The Probability Ratio Method. *Mol. Cell. Proteomics 7*, 1135–1145.

(52) Navarro, P., and Vázquez, J. (2009) A Refined Method To Calculate False Discovery Rates for Peptide Identification Using Decoy Databases. *J. Proteome Res. 8*, 1792–1796.

(53) Navarro, P., Trevisan-Herraz, M., Bonzon-Kulichenko, E., Núñez, E., Martínez-Acedo, P., Pérez-Hernández, D., Jorge, I., Mesa, R., Calvo, E., Carrascal, M., Hernáez, M. L., García, F., Bárcena, J. A., Ashman, K., Abian, J., Gil, C., Redondo, J. M., and Vázquez, J. (2014) General Statistical Framework for Quantitative Proteomics by Stable Isotope Labeling. *J. Proteome Res. 13*, 1234–1247.

(54) Jorge, I., Navarro, P., Martinez-Acedo, P., Nunez, E., Serrano, H., Alfranca, A., Redondo, J. M., and Vazquez, J. (2009) Statistical Model to Analyze Quantitative Proteomics Data Obtained by 18O/16O Labeling and Linear Ion Trap Mass Spectrometry: Application to the Study of Vascular Endothelial Growth Factor-induced Angiogenesis in Endothelial Cells. *Mol. Cell. Proteomics 8*, 1130–1149.

Chapter 2

Atherosclerotic plaque characterisation by enzymatic entrapment of phosphatidylcholine coated nanoparticles

Abstract

In this study, we propose iron oxide coated phosphatidylcholine micelles (PC IONP) (*1.1*) as an imaging probe for the molecular characterisation of atherosclerotic plaque formation. Phosphatidylcholine-specific phospholipase C (PC-PLC) is involved in atherosclerosis as a regulator of apoptosis and autophagy in vascular endothelial cells (VECs). Because PC-PLC can specifically degrade the polar moiety of phosphatidylcholine, we examined if this enzymatic regulation could trigger the accumulation of PC IONP (*1.1*) by changing their colloidal stability. We first considered the *in vitro* interaction between PC-PLC and the iron oxide micelles in order to demonstrate the effectiveness of enzymatic cleavage of PC coating leading to the formation of hydrophobic aggregates. We then showed the consequences of this enzymatic degradation in the uptake of PC IONP and associated cytotoxicity effects in cellular cultures of macrophages. Finally, we studied the intravenous injection of PC IONP in ApoE-KO mice for multimodal *in vivo* visualisation and imaging characterisation of atherosclerotic plaques, underlining the importance of the interaction of the probe with the PC-PLC enzyme and the uptake by macrophages. The proposed probe represents a new platform for targeting of atherosclerosis thanks to an original enzymatically driven entrapment route, which opens promising bioapplications not only for specific diagnosis (quantification of plaque burden) but also to predict clinical relevant events for potential anti-inflammatory therapies in the context of atherosclerosis. Our approach allows studying the regulation of this pro-atherogenic enzyme in the plaque progression and thus contributing with new molecular imaging solutions to understand different biochemical processes in the context of atheriosclerosis.

1. Introduction

Atherosclerosis is the principal origin of many cardiovascular diseases, the leading cause of worldwide mortality.[1] It refers to a multifactorial, chronic inflammatory pathology characterised by the irreversible thickening of arterial walls to form atheroma plaques, a slow and silent process over decades.[2] This process leads to a decrease in the supply of oxygen-rich blood to main organs and potential rupture of the plaques leading to multiple complications such as myocardial infarction or stroke.[3] Thus, clinical symptoms are often lethal or the manifestation of an advanced stage of the disease, making treatment more complicated with high risk of recurrence.[4] Recent developments in drug delivery and molecular imaging techniques offer promising advances for combating this issue, offering early non-invasive and reliable diagnosis, characterisation before an uncontrolled step in the course of the disease and combined therapeutic solutions.[5–7] The prolonged evolution and the complex composition at different stages of atherosclerotic lesions, offer a wide window of possible biological targets for the design of imaging probes.[6,8,9] In particular, macrophages are one of the most commonly used targets due to their key role during inflammation, known to be present along the entire plaque development.[10] Many different NP-based probes for MRI, PET/CT, US or fluorescence have already been described either as passive targeting (taking advantage of the phagocytic activities) or active, with ligands specific to surface receptors or molecular products of macrophages.[11–16] Other important biochemical targets derived from the atherogenic process have been also suggested for active targeting, as circulating monocytes, adhesion molecules, metalloproteinases, cathepsins or angiogenesis receptors.[6,9]

However, apart from the macrophage phagocytosis, few other pathways for the passive extracellular accumulation of NP contrast agents in plaques have been used. As far as we know, no NP which use an enzymatic

modification for atherosclerosis detection has been proposed, as can do molecular imaging probes like ^{18}F-FDG for inflammatory characterisation of the plaque or fluorescent sensors.[17–19] This radiochemical can detect cells with altered metabolism, because specific enzymatic events let a radiolabel substrate to be entrapped inside the disregulated cells.[20] We hypothesised the use of NP to accumulate in the plaque driven by a different enzymatic mechanism. Phosphatidylcholine-specific phospholipase C (PC-PLC) is a member of the phospholipase C family which catalyses the cleavage of the ester linkage between the glycerol and phosphate moieties of phospholipids, generating two of the most important messengers in the cellular pathway.[21] PC-PLC is expressed in cytoplasm, nucleus and external plasma membrane of cells where its activity has been reported.[22] Increasing evidence shows that this enzyme is implicated in several cellular signalling pathways such as metabolism, cell growth, apoptosis and autophagy of mammalian cells.[23–25] In particular, its pro-inflammatory properties and its role in vascular endothelial cell apoptosis (two important parameters in atherosclerosis) have been recently pointed out.[26,27] Extracellular stimuli, including hormones, growth factors, and neurotransmitters, promote activation of phospholipase C.[22] Importantly, oxidised low-density lipoprotein (oxLDL), one of the key atherogenic factors, has a strong effect on PC-PLC expression and activity. It was demonstrated for apolipoprotein E knockout mice (ApoE-KO) that PC-PLC is up-regulated in the aortic endothelium of atherotrombotic plaques and involved in the progression of the pathology.[28] Oxidised phospholipids, particularly oxidised phosphatidylcholine, are ligands for macrophage scavenger receptors implicated in vascular plaque progression where oxidised phosphatidylcholine is often abundant.[29] Interestingly, the inhibition of PC-PLC enzymatic activity reduced the progression and promoted the stabilisation of atherosclerotic lesions.[30]

Therefore, we wanted to investigate whether and how the function and over-expression of PC-PLC in atherosclerotic plaques can be used as a new tool for imaging in the early detection of atherosclerosis. We addressed this issue by developing a long circulating PC-coated iron oxide contrast agent PC IONP and assessed if it can be rapidly degraded by PC-PLC into hydrophobic aggregates resistant to macrophage phagocytosis.[31] We showed, in an apoE-KO mice model, that the probe effectively accumulates within the atherosclerotic plaque due to the PC-PLC activity and it can be applied for *in vivo* MRI detection of atherosclerosis, also providing a future new target and theranostic nanoparticle in atherosclerotic plaque targeted therapy.

2. Results and discussion

2.1 Synthesis and characterisation of Phosphatidylcholine coated iron oxide nanoparticles, PC IONP.

Synthesis and characterisation of PC IONP (*1.1*) have been detailed in Chapter 1, section 2.2. As we described, we first synthesised OA Fe_3O_4 magnetite nanoparticle by thermal degradation method (as described in Chapter 1, section 2.1). The latter were then stabilised with a nanoemulsion method into a micelle made of the amphiphilic PC molecule. This resulted in aqueous PC IONP micelles of about 75 nm hydrodynamic size, containing several magnetite cores (Figure 2.1).
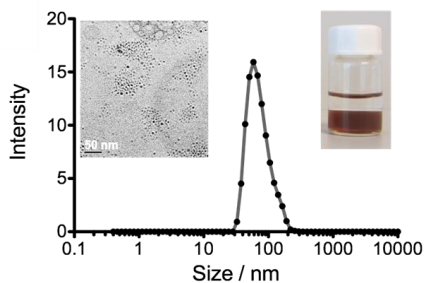
Figure 2.1. Hydrodynamic size of PC IONP (Inset TEM picture and PC IONP in a 1:1 hexane/PBS solution in v/v).

The main physicochemical characterisation performed is summarised in Table 2.1. In this work, to allow multimodal visualisation, we also prepared a variant in which a minor fraction of a phospholipid derivative, fluorescent dye DiI(18), is integrated into the coating formulation of the PC IONP.

Table 2.1. Summary of the main physicochemical properties of PC IONP.

	PC IONP
Hydrodynamic size (nm)	75
Pdi	0.14
Zeta potential (pH=7.1) (mV)	-11.5
Saturation magnetisation	70
Relaxivity (s^{-1}.mM^{-1})	r_1: 1.3 r_2: 147.4
Estimated vascular life time	10 h
Apolipoprotein present among the 10 most abundant protein	Apo B100, A-IV, A-I

2.2 *In vitro* degradation of PC IONP by PC-PLC.

First we assessed the *in vitro* activity of PC-PLC towards the PC IONP (*1.1*), to test whether phosphate moieties of PC can be effectively cleaved when PC of the probe is under a rigid micelle-like form. In the micelle

93

structure, the choline hydrophilic head around the coating guarantees aqueous stabilisation and good colloidal properties to the nanoparticles. Therefore, we hypothesised that if the enzymatic reaction occurs, PC IONP will progressively aggregate, with an increase in the hydrodynamic size and a consequent change of their relaxometric properties (Figure 2.2). To demonstrate this, we first followed the evolution of the hydrodynamic size of *1.1* dispersion by DLS in presence of PC-PLC at different time points (Figure 2.3a). Shortly after PC-PLC was added, we clearly observed the formation of aggregates and a wider size distribution (illustrate by increase of the pdi) while the size of the control dispersions without the enzyme remained stable along time (Figure 2.3a).
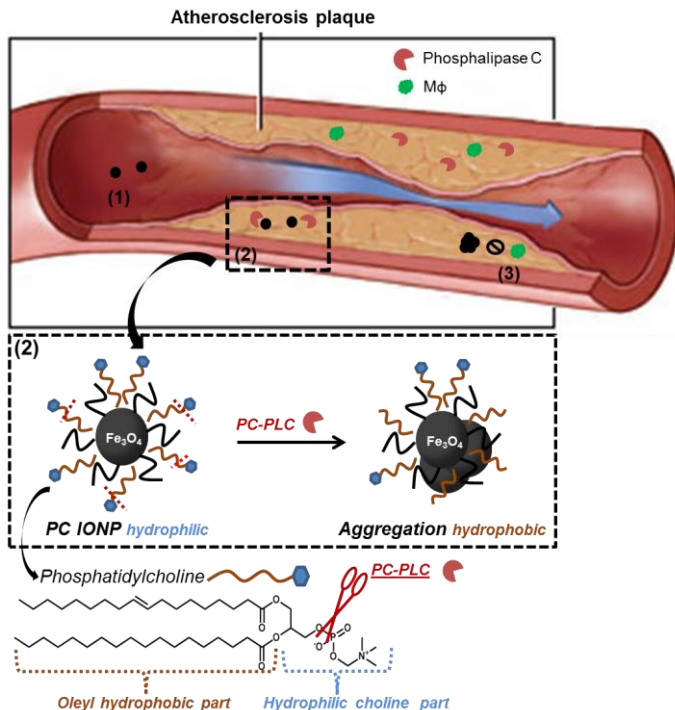

Figure 2.2. Illustration of the principles of the enzymatic entrapment of PC IONP in the atherosclerotic plaque.

Relaxometry was then used for a more detailed study of the kinetics of the enzymatic reaction. It has been previously shown that the modification in the aggregation state of the NPs can be detected by changes in the relaxation values.[31–33] PC IONP dispersion was mixed with different PC-PLC concentrations (0.1 U, 0.3 U and 0.6 U) and the T_2 measured along time (*1 U unit will liberate 1.0 µmole of water soluble organic phosphorus from egg yolk L-α-phosphatidylcholine per min at pH 7.3 at 37 °C.*). As shown in Figure 2.3b, due to the formation of aggregates, T_2 values linearly increase in a dose and time-dependent manner. In the double control samples, T_2 values remained stable for both the blank solution (same solution with no PC-PLC added) and the control NPs solution (solution of control NPs inert towards PC-PLC). Up to 0.6 U, the evolution of T_2 remains the same, so we assumed that we reach the maximum speed of the kinetic and the saturation of the enzymatic activity. Altogether, these results confirm the enzyme capacity to rapidly cleave the ester linkage of PC present in the micelle coating, resulting in the formation of large aggregates in the micrometer range. This is an essential requirement to enable PC IONP (*1.1*) for *in vivo* enzymatic entrapment in the plaque.

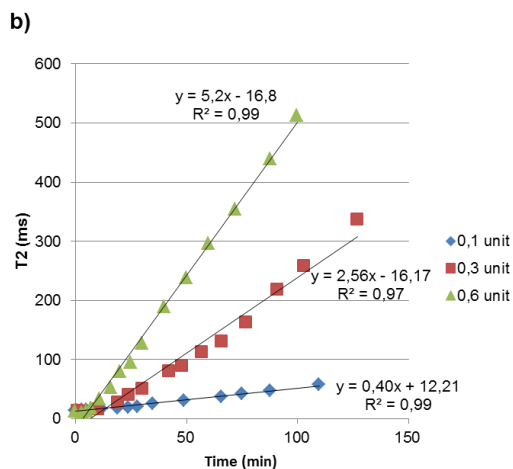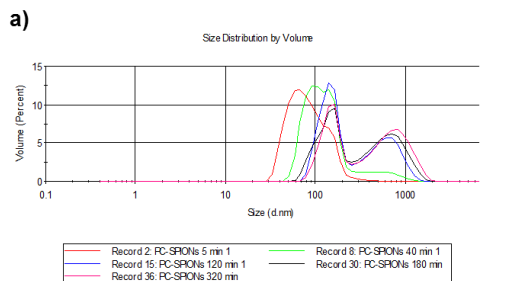**Figure 2.3.** a) Time course of the hydrodynamic sizes of PC IONP (0.035 mg Fe.ml^{-1}) along incubation times at 37ºC in presence of PC-PLC (0.6 U) b) Time course of T$_2$ relaxation times of a PC IONP solution (0.035 mg Fe.ml^{-1}) along incubation times at 37 ºC in presence of PC-PLC (0.1 U, 0.3 U and 0.6 U).

2.3 Macrophage uptake of PC IONP micelles and influence of PC-PLC activity.

There are two major macrophage (MΦ) subsets called M1 and M2 MΦs, which are phenotypically and functionally different. Activation to M1 ("classical" activation) often encourages inflammation, triggering the immune response, while M2 activation ("alternative") decreases inflammation and encourages tissue repair. Both classes are infiltrated and play important roles in atherosclerosis plaque which is characterised by unregulated inflammation.[34] We investigated the influence of PC-PLC enzymatic degradation of the PC IONP on their uptake *in vitro* by MΦ. For this purpose, murine macrophages were first differentiated into M1 and M2 subclasses, induced by treatment with interferon-gamma and tumour necrosis factor-alpha for M1, or with interleukin-4 for M2. The differentiated cells were subsequently incubated for 24h in three conditions plus control (vehicle, PBS) with: (A) only PC-PLC, (B) only PC IONP and (C) a mixture of both PC-PLC and PC IONP (PC-PLC $2mU.ml^{-1}$, [Fe]=0.05 $mg.ml^{-1}$). Interestingly, in conditions (B) and (C), we observed for both types of MΦ, although much more pronounced for M1 MΦ, a change in the cellular morphology while the treatment with the enzyme alone (condition (A)) did not produce any changes on MΦs. This modification of the phenotypic pattern may be an indication of NP uptake or apoptosis events.
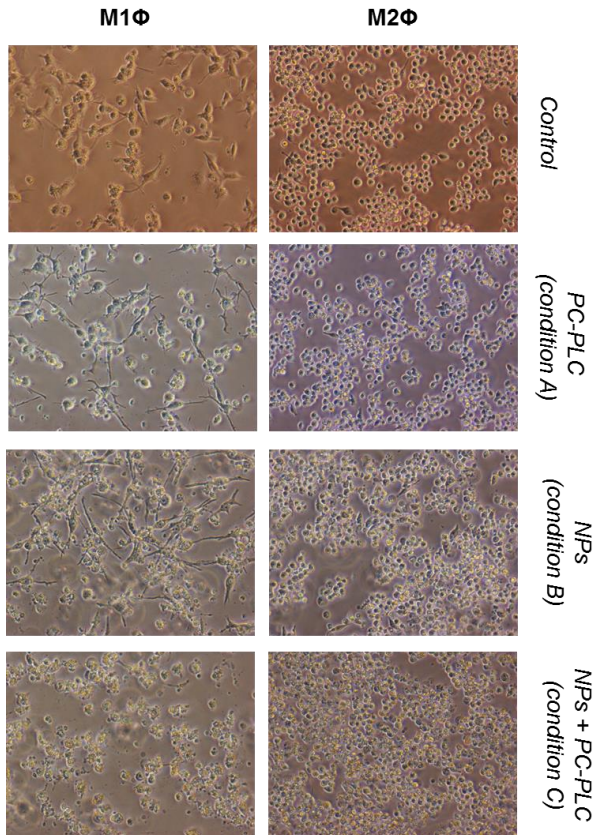
Figure 2.4. Pictures of the MΦ cell cultures in conditions (A), (B) and (C).

In detail, flow-cytometry analysis measuring side-scattered light indicated that in condition (B), it occurred a high increase of the cell complexity for both MΦ cell lines with an effect much more pronounced for M1 (SSC-H median of 28000) than for M2 (SSC-H median of 12000) MΦs. When exogenous PC-PLC was added (conditions (C)), it contributed to an additional increase of the complexity for M1 MΦ (SSC-H median of 41000) while for M2 MΦ, it remained equal to condition (B) (SSC-H median of 12000).
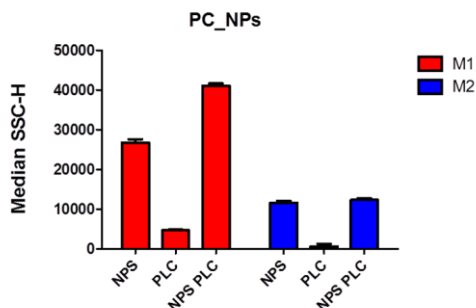
Figure 2.5. Changes in cell complexity after NPs incubation. Median of Side-Scattered Light (SSC-H) (intensity arbitrary units) of the MΦ cell cultures in conditions (A), (B) and (C).

Concerning the analysis of cytotoxicity by flow cytometry (DAPI staining for necrotic cells), results showed that a significant cytotoxic effect was observed for M1 MΦ in condition (C) (Figure 2.6). This can explain the additional increase of the complexity in this condition, which gathers uptake and cytotoxic effect. For a deeper analysis we labelled the PC IONP with the fluorophore "Dil(18)". Thus, we could visualise the cell cultures in condition (B) by confocal fluorescence microscopy with immunofluorescence staining of PC-PLC. These results showed that, a high proportion of Dil(18) labelled NPs co-localised with the M1 MΦ and looked aggregated. Subcellular co-localisation indicates an intercalation of the probe in the external cell membranes and to a lesser extent in the cytoplasm (Figure 2.7). The same cell-adherence behaviour was previously reported in other studies for phospholipid based NPs.[35] In condition (C), i.e. when PC-PLC is added to the medium, large free aggregates of Dil(18) labelled PC IONP were observed surrounded by PC-PLC (indicating of the enzymatic activity on the coating of the NPs).
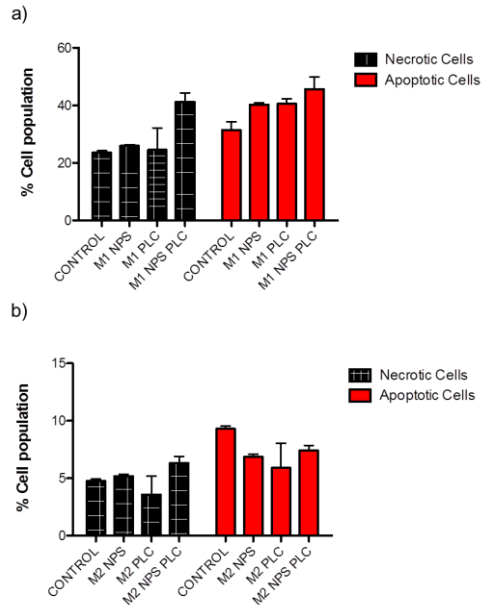
Figure 2.6. Cell viability study of the a) M1 MΦ and b) M2 MΦ cell cultures in conditions (A), (B) and (C).
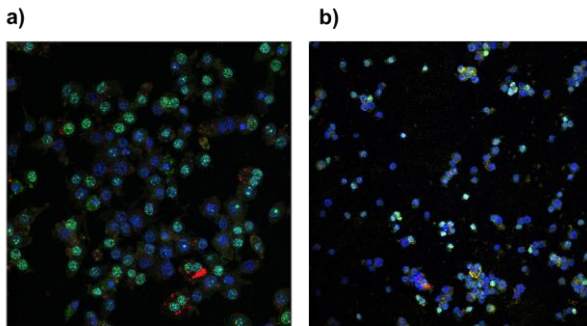

Figure 2.7 Confocal fluorescence microscopy of a) M1 and b) M2Φ in condition (B). We can observed nucleous (DAPI 1:1000-blue), protein PC-PLC (PC-PLC antibody 1:30 - green) and Dil(18) labelled PC IONP.

We finally check the endogenous expression of PC-PLC in the two types of macrophage by western blot (Figure 2.8). High amount of enzyme was detected inside M1 MΦ whereas M2 MΦ showed a much lower expression. This was also the case on the confocal microscopic images (PC-PLC staining detected inside the M1 macrophages) (Figure 2.7). This endogenous expression can explains that the effects caused by PC IONP incubation and its accumulation in macrophages are more pronounced for the M1 MΦ because of its proper PC-PLC enzymatic activity.
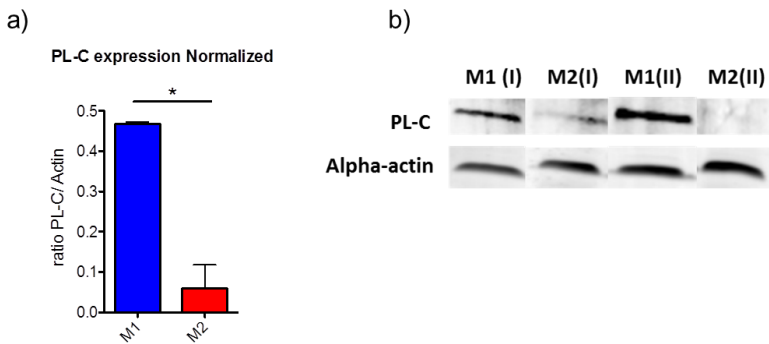

Figure 2.8. a) Western blot assay for endogenous PC-PLC. Normalised by alpha-actin. b) blot quantification of the endogenous PC-PLC protein expression in M1 and M2Φ.

Taken together, these results indicate that *in vitro* activated macrophages interact with PC IONP (*1.1*) at the surface membrane before phagocytosis; and that the exogenous enzymatic PC-PLC activity on *1.1* promotes the aggregation of the micelles hardening their interactions with the MΦs. The effect is much more pronounced for the class of pro-inflammatory macrophage M1, probably because of a higher proportion of endogenous PC-PLC. Because PC-PLC is upregulated in the cells of the aortic endothelium of atheroma plaque, we can hypothesise that PC IONP that finally penetrate

inside the plaque will aggregate and thus will see impaired its elimination by the hosting specific macrophages. This will reinforce the possibility to use PC IONP as a molecular agent for characterisation of pro-inflammatory responses that promotes atherogenesis through to their accumulation following their modification by PC-PLC. Moreover, the cytotoxic effects on M1 MΦ caused by the PC IONP enzymatic degradation (endogenous and/or exogenous) could be of interest for possible anti-inflammatory outcomes in the plaque, and serving as theranostic agent. This cytotoxicity probably comes from the sub-products released (diacylglycerol and phosphocholine) after the cleavage of PC by the PC-PLC reaction. Indeed, literature already report the role of these sub-products as molecular messengers in apoptosis events.[29,36,37]

2.4 Accumulation of PC IONP in atherosclerosis plaque for *in vivo* imaging.

Encouraged by these *in vitro* results, we have assessed whether our probe can accumulate in the atherosclerotic plaque *in vivo*, by conducting two experiments. In the first experiment, PC IONP (*1.1*) ([Fe]= 0.5 mg.ml^{-1}) were intravenously injected in 48 weeks old ApoE-KO mice with a high cholesterol diet for 18 weeks. *In vivo* MRI performed 24 h after injection in a 7 T scanner, revealed a clear hypointense region in a diseased zone of the aorta on the T_2-weigthed images (Figure 2.9a).
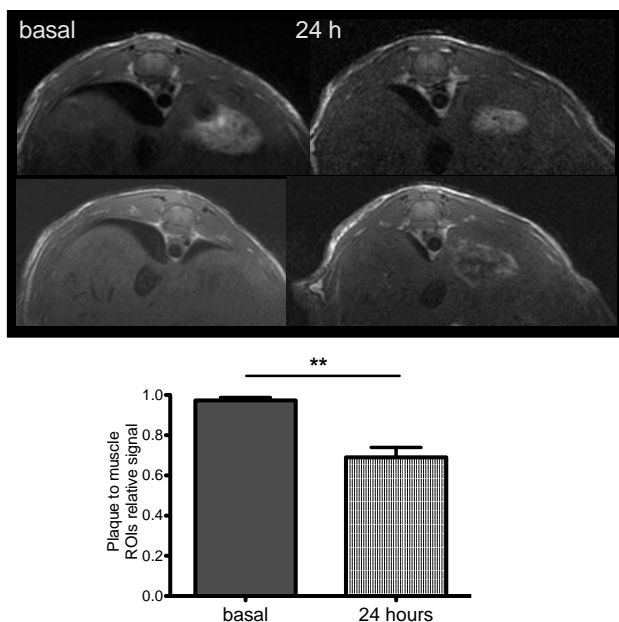
Figure 2.9. a) Transversal T_2 weighted MRI slices of apoE-KO mice aorta after i.v.a of PC IONP at 1h and 24 h b) muscle to plaque "relative signal intensity.

The images show the typical hypointese areas in the plaque lesion 24 h post-injection due to the iron oxide deposition. Since sometime the so-called negative contrast or signal loss can be difficult to identify, accompanying graph (Inset, Figure 2.9b) summarizes the plaque to muscle signal intensity ratios , showing a more than 20% signal decrease from the basal image. As shown in Chapter 1, the more conclusive results obtained for PC IONP are: 1) a vascular lifetime up to 10h, much longer than the standard for this type of nanomaterials, and 2) a high proportion of dysopsonin found in its protein corona, in particular from the apolipoprotein class (Table 2.1).[31] We believe that these two properties contribute to the penetration of PC IONP in the lesions. Indeed, long circulation time favours the passive diffusion and it has

103

been already demonstrated that presence of apolipoproteins in the coating of NP promote their accumulation in the plaques.
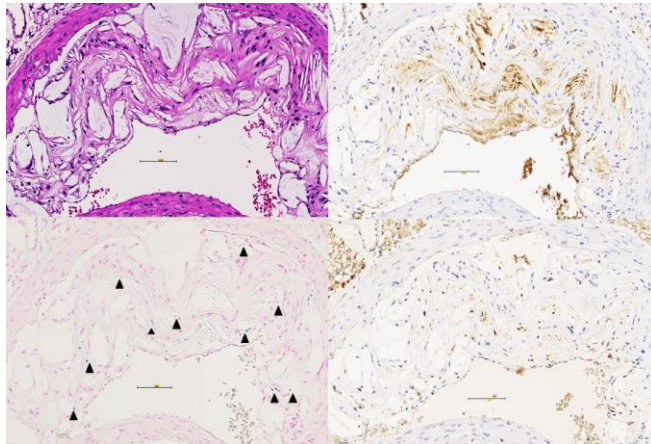

Figure 2.10. Histological analysis of colocalisation between NPs, endogenous PC-PLC and macrophages (consecutive slides) in ApoE-KO mice with atheroma plaque. Inmunohistochemical staining for PC-PLC and macrophages (F480 antibody).

To corroborate that the signal enhancement comes from the iron oxide deposition and to elucidate the interactions between PC IONP, PC-PLC and MΦ in the plaque, we conducted histological validation. Bright field microscopy of consecutive sections of the aorta with different immunohistochemistry stainings specific for iron, macrophages and PC-PLC was performed (Figure 2.10). These results revealed that: 1) an important number of NPs aggregated in the fibrous cap of the atherosclerotic plaque, 2) a high degree of co-localisation between the PC-PLC and the NPs (presume an enzymatic activity at the surface of the micelle´s coating) and 3) numerous

matches between the NPs and the macrophages. In the second experiment, DiI(18) labelled PC IONP were i.v. injected into apoE-KO mice which were sacrificed after 24h and perfused with PBS before their aortas were excised. The distribution of the DiI(18) labelled PC IONP in whole aortas was investigated by *ex vivo* fluorescence. Importantly, accumulation of the fluorescent probe was observed in plaque-rich regions (Figure 2.11). Furthermore, plaque sections were studied by fluorescence microscopy. Representative images displayed in Figure 2.11 revealed colocalisation of the NPs with PC-PLC immunostaining in the aortic root but little correlation of the probe with MΦ, confirming the results of the first experiment.
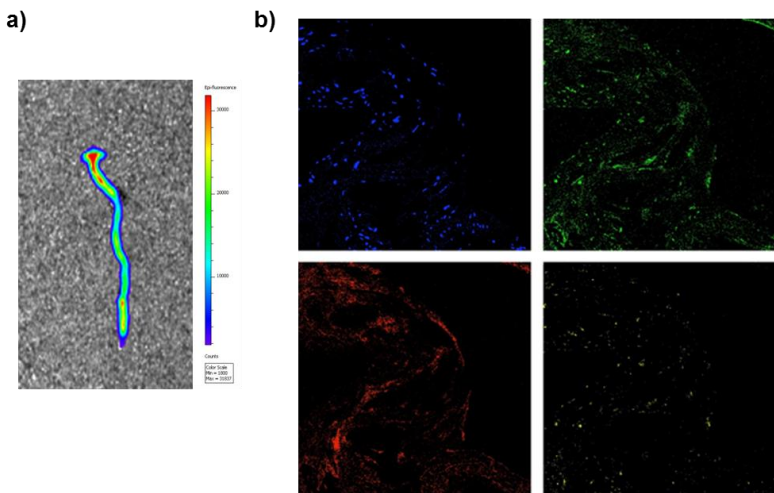

Figure 2.11. a) *Ex vivo* fluorescence of the aorta (IVIS, DsRed ex/em filter), b) Confocal images of atherosclerotic plaque where we can observed nucleous (DAPI 1:1000-blue), endogenous expression of the protein PL-C (PL-C antibody 1:30 - green), NPs accumulation into plaque (red) and macrophages (F480 antibody 1:20 - yellow).

105

3. Conclusions

Host macrophages in atherosclerosis plaques are currently the main biological target used for detection imaging with nanoparticulate contrast agents. Here, we proposed a contrast agent, designed specifically to accumulate passively in plaques. We show that PC IONP is rapidly degraded by PC-PLC, an enzyme upregulated in the vascular endothelial cells of the atherosclerotic lesions. The enzymatic reaction leads to aggregation of PC IONP because of the cleavage of the choline head, the moiety responsible of the aqueous stabilisation of the NPs coating. These aggregates have been observed to be resistant to the uptake by MΦ *in vitro* and so PC IONP is predetermined to remain in the inflamed plaque areas. This was confirmed by successful *in vivo* MR imaging of plaques in apoE-KO mice due to the accumulation of the contrast agent. Histology of these plaques confirms, by bright field microscopy and immunofluorescence, the endogenous degradation of the PC IONP by PC-PLC and the low phagocytosis of the probes by the macrophages. We believe that this new proposed method for contrast agent accumulation in atherosclerotic plaque opens promising bio-applications for improved its characterization. Enzyme modification pathway is a tool already applied with success for molecular imaging, and this new use with NP based probe can provides an early indicator of atherosclerotic plaque development. Finally, the *in vitro* cytotoxicity of the by-products of the enzymatic degradation

against macrophages could be a track for potential anti-inflammatory actions and theranostic applications, providing a new target in atherosclerotic plaque therapy.

4. Materials and Methods

Materials

All chemicals for the preparation of the BSA-NPs were purchased from Sigma-Aldrich Co. (St. Louis, USA) except. All reagents were of analytical grade except phosphatidylcholine (90%),oleic acid and oleylamine of technical grade. They were used without any further purification. Distilled water (milliQ) or phosphate buffered saline PBS were used throughout the experiments.

Synthesis

Oleic acid coated Fe3O4 magnetite nanoparticle

Protocol described in Chapter1.4

PC IONP micelles. (1.1)

Protocol described in Chapter1.4. The same protocol was used for the preparation of the Dil(18) labelled PC IONP except that 1mg of Dil(18) was added to the nanoemulsion formulation.

***In vitro* degradation of PC IONP by PC-PLC**

Evolution of the hydrodynamic size of PC IONP dispersion in presence of PC-PLC. We used a solution of PC IONP ([Fe]=0.035 mg.ml^{-1}) mixed with PC-PLC (0.2 U). The hydrodynamic size and polydispersity index were measured at different time points (from 5 to 380 min) at 25ºC by dynamic light spectroscopy with a Zetasizer Nano ZS90 (Malvern Instruments, UK) using folded capillary cells.

Evolution of the T2 relaxation time of PC IONP dispersion in presence of PC-PLC. Serial solutions (600 µl final volume) of PC IONP ([Fe]=0.035 mg.ml^{-1}) mixed with PC-PLC at different concentrations (0.1, 0.3 and 0.6 unit) were prepared. Reaction buffer used was a 50 mM TrisHCl (pH 7.5), 0.14 M NaCl, 2 mM CaCl2 solution. Thereafter

the addition of the enzyme, T2 relaxation times were measured at 37ºC in a Bruker Biospec spectrometer with a T2 Carr-Purcell-Meiboom-Gill sequence (Bruker Biospec 47/40, 1.5 T, Bruker Biospin, Germany) at echoes from 0 to 150 min.

In vitro macrophage uptake of PC IONP micelles

Cell culture and media. The murine macrophage cell line RAW 264.7 was grown in Dulbecco's Modified Eagle Medium (DMEM) supplemented with 10% heat-inactivated fetal bovine serum (FBS) and 1% penicillin-streptomycin. Cells were cultured at 37ºC in a humidified atmosphere with 5% CO_2. For each experiment, cells were plated at a concentration of 0.5 x10^6 cells/ml in 12-well plates in complete growing medium. Twenty-four hours later, cells were polarised to M1 (25 ng/ml interferon gamma and 25 ng/ml tumour necrosis factor alpha) or M2 (20 ng/ml interleukin-4) macrophages for additional 24 hours. Polarised macrophages were incubated with PC-IONP or DiI(18) labeled PC IONP (50 μg Fe/ml medium) in the absence or in the presence of phospholipase C (2 mU/ml) for 24 hours. Control cells were incubated without nanoparticles (vehicle, water).

Citotoxicity assays

Cell viability is determined by adding DNA binding dyes. DAPI was then added to a final concentration of 0.001% (w/v), and cells were analysed by flow-cytometry using the BD FACSCanto™ II system. All experiments were performed in triplicate.

Microscopy cell cultures stained by Prussian Blue. Cells were grown on glass coverslips in 12-well plates. Perls Prussian Blue staining was performed following standard immunocytochemical procedures. Briefly, Slides were stained with 1% aqueous potassium ferrocyanide in 2% solution of HCl for 15 min and counterstained with nuclear fast red. Labeled cells were visualised on Nikon ECLIPSE 90i- Upright bright field microscope (Acquisition Software: NIS-Elements 3.22.11) and then, slides were processed and digitalised.

Nanoparticle Uptake assays. After 24 hours of treatment with DiI(18) labelled PC IONP, cells were scrapped and washed thoroughly with phosphate buffered saline (PBS) and harvested in 1 ml PBS. Cell populations were centrifuged at 300 x *g* for 5 min RT, washed 3 times with PBS. To determine cell viability, the resulting pellets were resuspended in 200 μl PBS containing Annexin V and DAPI, at a final concentration of

0.001% (w/v). A total of 10.000 events were recorded for each sample using the FACSCanto™ II system(BD Biosciences). All experiments were performed in triplicate. Samples are analysed with BD FACSDivaTM Software and an average of the medians and standard deviations was calculated using FlowJo Software. Additionally, cell culture was stained with Perls' Staining to detect SPIO labeled cells.

In vitro inmunofluorescence assays. For immunofluorescence, cells seeded on coverslips were washed in PBS, fixed (4% formaldehyde) and permeabilised in PBS with 0.1% Triton X-100, before staining with primary antibodies and secondary Alexa Fluor antibodies (LifeTechnologies) in blocking solution (5% BSA). *Samples were incubated with* **primary antibodies** *rat anti-mouse F480 (1:50) and anti-mouse* PLC-gamma 1 Antibody (1:100; Novus Biologicals (2C11)) Optical sections were acquired using a Leica TCS SP5 confocal system. Colocalisation analyses were performed using LAS AF software (Leica Microsystems, Germany) and ImageJ (National Institutes of Health, USA).

Accumulation of PC IONP in atherosclerosis plaque for in vivo imaging

Animals. Mice were housed in specific facilities (pathogen-free for mice) at the Centro Nacional de Investigaciones Cardiovasculares. Experimental procedures were approved by the local Animal Care and Ethics Committee and regional authorities.

Magnetic resonance imaging. In vivo MRI in mice was performed with an Agilent/Varian scanner (Agilent, Santa Clara, USA) equipped with a DD2 console and an active-shielded 205/120 gradient insert coil with 130 mT/m maximum gradient strength and a combination of volume coil/two channel phased-array (Rapid Biomedical GmbH, Rimpar, Germany). Mice were anesthetised with 2% isoflurane (Abbott) and oxygen and positioned on a thermoregulated (38.7ºC) mouse bed and the respiratory cycle was monitored constantly. Ophthalmic gel was placed in their eyes to prevent retinal drying. Baseline images were acquired before i.v.a of PC IONP ([Fe]=1 mg.ml^{-1}, 100 µl). Images were acquired at basal, 1hour post-injection and 24 hours later. For each animal, consecutive axial 1 mm thick slices were acquired to image the aorta. Images were acquired in free-breathing animals, using a gradient echo sequence with 4 ms/40 ms echo/repetition times, BW of 100 kHz, FOV of 6 cm x 6 cm,

for a total acquisition time of about 80 seconds; the flip angle (FA) was fixed at 20 degrees.

Histolological confirmation. After 24 hours of i.v.a dosis of PC IONP, 2 mice were killed and aortas were fixed by pefusing the animal with a PBS followed by a formalin lavage and was incubated in 10% formalin for 24 hours. Tissue was dehydrated and embedded in molten paraffin and stored at RT until the sectioning. Consecutive sections of the aorta were taken off for immunohistochemistry. Respectively staining for Hematoloxilin/Eosin staining, Perl´s Prussian Blue(Iron), PC-PLC with Ab, F4/80 for Mφ, and Manson thrichrome staining for fibrosis. Tissues slides were visualised on Nikon ECLIPSE 90i- Upright bright field microscope (Acquisition Software: NIS-Elements 3.22.11) and then, slides were processed and digitalised.

Ex vivo fluorescence and microscopy fluorescence study

DiI(18) labelled PC IONP (100 µl, 0.5 mg.ml^{-1} [Fe]) were i.v. administrated in apoE mice (N=3) that were sacrificed after 24 h. After perfusion, the aortas were extracted and *ex vivo* fluorescence was performed with IVIS Imaging System 200 series (Xenogen®) (parameters of acquisition: DsRed ex/em filter, high level, BIN-HR, FOV 13.3, f2, 4s).

Immunofluorescence .Slides was deparafinised and rehydrated (xylene 5´, xylene 5', 100%EtOH 3', 100% EtOH 3', 95-90-80-70-50% EtOH 30", dH2O: 5').Heat induced epitope retrieval with citrate buffer (10 mM pH6 during 15 minutes). Slides were allowed to cool 20 minutes. Wash slides 5' PBS-T (x3) and permeabilised during 15' in PBS-T 0,5%. Wash slides 5' PBS-T (x3) and non-specific binding was blocked by a dilution of 1%BSA+PBS-T during 1 hour. Primary antibodies *rat anti-mouse F480 (1:20) and anti-mouse* PLC-gamma 1 Antibody (1:50; Novus Biologicals (2C11)) was added in blocking solution and incubated overnight at 4ºC. Sections was washed thrice with blocking solution during 5 minutes each and incubated with secondary antibody (Alexa Fluor antibodies,1:500) for 45 minutes. Slides were washed twice with PBS and dH20 and applied one drop of ProLong® Gold Antifade Reagent with DAPI. Confocal fluorescence microscopy images were obtained on a Leica SP5-Inverted Confocal, using the following objectives: HCX PL APO CS 40x 1,25 oil, HCX PL APO lambda blue 63x 1,40 oil. LAS-AF 2.6.0 Acquisition Software was used.

5. Bibliography

(1) Glass, C. K., and Witztum, J. L. (2001) Atherosclerosis. the road ahead. *Cell 104*, 503–516.
(2) Ross, R. (1999) Atherosclerosis--an inflammatory disease. *N. Engl. J. Med. 340*, 115–126.
(3) Lusis, A. J. (2000) Atherosclerosis. *Nature 407*, 233–241.
(4) Charo, I. F., and Taub, R. (2011) Anti-inflammatory therapeutics for the treatment of atherosclerosis. *Nat. Rev. Drug Discov. 10*, 365–376.
(5) Gershlick, A. H., de Belder, M., Chambers, J., Hackett, D., Keal, R., Kelion, A., Neubauer, S., Pennell, D. J., Rothman, M., Signy, M., and Wilde, P. (2007) Role of non-invasive imaging in the management of coronary artery disease: an assessment of likely change over the next 10 years. A report from the British Cardiovascular Society Working Group. *Heart 93*, 423–431.
(6) Sanz, J., and Fayad, Z. A. (2008) Imaging of atherosclerotic cardiovascular disease. *Nature 451*, 953–957.
(7) Choudhury, R. P., Fuster, V., and Fayad, Z. A. (2004) Molecular, cellular and functional imaging of atherothrombosis. *Nat. Rev. Drug Discov. 3*, 913–925.
(8) Wickline, S. A., Neubauer, A. M., Winter, P. M., Caruthers, S. D., and Lanza, G. M. (2007) Molecular imaging and therapy of atherosclerosis with targeted nanoparticles. *J. Magn. Reson. Imaging 25*, 667–680.
(9) Libby, P., DiCarli, M., and Weissleder, R. (2010) The Vascular Biology of Atherosclerosis and Imaging Targets. *J. Nucl. Med. 51*, 33S–37S.
(10) Libby, P. (2002) Inflammation and Atherosclerosis. *Circulation 105*, 1135–1143.
(11) Tang, T. Y., Muller, K. H., Graves, M. J., Li, Z. Y., Walsh, S. R., Young, V., Sadat, U., Howarth, S. P. S., and Gillard, J. H. (2009) Iron Oxide Particles for Atheroma Imaging. *Arterioscler. Thromb. Vasc. Biol. 29*, 1001–1008.
(12) Briley-Saebo, K. C., Mulder, W. J. M., Mani, V., Hyafil, F., Amirbekian, V., Aguinaldo, J. G. S., Fisher, E. A., and Fayad, Z. A. (2007) Magnetic resonance imaging of vulnerable atherosclerotic plaques: Current imaging strategies and molecular imaging probes. *J. Magn. Reson. Imaging 26*, 460–479.
(13) Choudhury, R. P., and Fisher, E. A. (2009) Molecular Imaging in Atherosclerosis, Thrombosis, and Vascular Inflammation. *Arterioscler. Thromb. Vasc. Biol. 29*, 983–991.
(14) Shah, F., Balan, P., Weinberg, M., Reddy, V., Neems, R., Feinstein, M., Dainauskas, J., Meyer, P., Goldin, M., and Feinstein, S. B. (2007) Contrast-enhanced ultrasound imaging of atherosclerotic carotid plaque neovascularization: a new surrogate marker of atherosclerosis? *Vasc. Med. 12*, 291–297.
(15) Flaumenhaft, R., Tanaka, E., Graham, G. J., De Grand, A. M., Laurence, R. G., Hoshino, K., Hajjar, R. J., and Frangioni, J. V. (2006) Localization and Quantification of Platelet-Rich Thrombi in Large Blood Vessels With Near-Infrared Fluorescence Imaging. *Circulation 115*, 84–93.
(16) Herranz, F., Salinas, B., Groult, H., Pellico, J., Lechuga-Vieco, A., Bhavesh, R., and Ruiz-Cabello, J. (2014) Superparamagnetic Nanoparticles for Atherosclerosis Imaging. *Nanomaterials 4*, 408–438.

(17) Mulder, W. J. M., Jaffer, F. A., Fayad, Z. A., and Nahrendorf, M. (2014) Imaging and Nanomedicine in Inflammatory Atherosclerosis. *Sci. Transl. Med. 6*, 239sr1–239sr1.

(18) Rudd, J. H. F., Myers, K. S., Bansilal, S., Machac, J., Rafique, A., Farkouh, M., Fuster, V., and Fayad, Z. A. (2007) 18Fluorodeoxyglucose Positron Emission Tomography Imaging of Atherosclerotic Plaque Inflammation Is Highly Reproducible. *J. Am. Coll. Cardiol. 50*, 892–896.

(19) Jaffer, F. A., Kim, D.-E., Quinti, L., Tung, C.-H., Aikawa, E., Pande, A. N., Kohler, R. H., Shi, G.-P., Libby, P., and Weissleder, R. (2007) Optical visualization of cathepsin K activity in atherosclerosis with a novel, protease-activatable fluorescence sensor. *Circulation 115*, 2292–2298.

(20) Rudd, J. H. F., Myers, K. S., Bansilal, S., Machac, J., Pinto, C. A., Tong, C., Rafique, A., Hargeaves, R., Farkouh, M., Fuster, V., and Fayad, Z. A. (2008) Atherosclerosis Inflammation Imaging with 18F-FDG PET: Carotid, Iliac, and Femoral Uptake Reproducibility, Quantification Methods, and Recommendations. *J. Nucl. Med. 49*, 871–878.

(21) Exton, J. H. (1994) Phosphatidylcholine breakdown and signal transduction. *Biochim. Biophys. Acta 1212*, 26–42.

(22) Spadaro, F., Ramoni, C., Mezzanzanica, D., Miotti, S., Alberti, P., Cecchetti, S., Iorio, E., Dolo, V., Canevari, S., and Podo, F. (2008) Phosphatidylcholine-Specific Phospholipase C Activation in Epithelial Ovarian Cancer Cells. *Cancer Res. 68*, 6541–6549.

(23) Zhang, L., Li, H. Y., Li, H., Zhao, J., Su, L., Zhang, Y., Zhang, S. L., and Miao, J. Y. (2011) Lipopolysaccharide activated phosphatidylcholine-specific phospholipase C and induced IL-8 and MCP-1 production in vascular endothelial cells. *J. Cell. Physiol. 226*, 1694–1701.

(24) Ramoni, C., Spadaro, F., Menegon, M., and Podo, F. (2001) Cellular Localization and Functional Role of Phosphatidylcholine-Specific Phospholipase C in NK Cells. *J. Immunol. 167*, 2642–2650.

(25) Ramoni, C., Spadaro, F., Barletta, B., Dupuis, M. L., and Podo, F. (2004) Phosphatidylcholine-specific phospholipase C in mitogen-stimulated fibroblasts. *Exp. Cell Res. 299*, 370–382.

(26) Li, H., Zhang, L., Yin, D., Zhang, Y., and Miao, J. (2010) Targeting Phosphatidylcholine-Specific Phospholipase C for Atherogenesis Therapy. *Trends Cardiovasc. Med. 20*, 172–176.

(27) Miao, J. Y., Kaji, K., Hayashi, H., and Araki, S. (1997) Suppression of apoptosis by inhibition of phosphatidylcholine-specific phospholipase C in vascular endothelial cells. *Endothel. J. Endothel. Cell Res. 5*, 231–239.

(28) Li, H., Huang, S., Wang, S., Zhao, J., Su, L., Zhao, B., Zhang, Y., Zhang, S., and Miao, J. (2013) Targeting annexin A7 by a small molecule suppressed the activity of phosphatidylcholine-specific phospholipase C in vascular endothelial cells and inhibited atherosclerosis in apolipoprotein E{/{mice. *Cell Death Dis. 4*.

(29) Lee, S., Birukov, K. G., Romanoski, C. E., Springstead, J. R., Lusis, A. J., and Berliner, J. A. (2012) Role of Phospholipid Oxidation Products in Atherosclerosis. *Circ. Res. 111*, 778–799.

(30) Zhang, L., Zhao, J., Su, L., Huang, B., Wang, L., Su, H., Zhang, Y., Zhang, S., and Miao, J. (2010) D609 Inhibits Progression of Preexisting Atheroma and Promotes

Lesion Stability in Apolipoprotein E-/- Mice: A Role of Phosphatidylcholine-Specific Phospholipase in Atherosclerosis. *Arterioscler. Thromb. Vasc. Biol. 30*, 411–418.

(31) Phosphatidylcholine-coated iron oxide nanomicelles for in vivo prolonged circulation time with an antibiofouling protein corona.

(32) Atanasijevic, T., Shusteff, M., Fam, P., and Jasanoff, A. Calcium-sensitive MRI contrast agents based on superparamagnetic iron oxide nanoparticles and calmodulin. *Proc. Natl. Acad. Sci. 103*, 14707–14712.

(33) Pellico, J., Lechuga-Vieco, A. V., Benito, M., García-Segura, J. M., Fuster, V., Ruiz-Cabello, J., and Herranz, F. (2015) Microwave-driven synthesis of bisphosphonate nanoparticles allows in vivo visualisation of atherosclerotic plaque. *RSC Adv. 5*, 1661–1665.

(34) Finn, A. V, Nakano, M., Polavarapu, R., Karmali, V., Saeed, O., Zhao, X., Yazdani, S., Otsuka, F., Davis, T., Habib, A., Narula, J., Kolodgie, F. D., and Virmani, R. (2012) Hemoglobin Directs Macrophage Differentiation and Prevents Foam Cell Formation in Human Atherosclerotic Plaques. *J. Am. Coll. Cardiol. 59*, 166–177.

(35) Roiter, Y., Ornatska, M., Rammohan, A. R., Balakrishnan, J., Heine, D. R., and Minko, S. (2008) Interaction of Nanoparticles with Lipid Membrane. *Nano Lett. 8*, 941–944.

(36) Fantuzzi, L., Spadaro, F., Purificato, C., Cecchetti, S., Podo, F., Belardelli, F., Gessani, S., and Ramoni, C. (2008) Phosphatidylcholine-specific phospholipase C activation is required for CCR5-dependent, NF-kB-driven CCL2 secretion elicited in response to HIV-1 gp120 in human primary macrophages. *Blood 111*, 3355–3363.

(37) Besterman, J. M., Duronio, V., and Cuatrecasas, P. (1986) Rapid formation of diacylglycerol from phosphatidylcholine: a pathway for generation of a second messenger. *Proc. Natl. Acad. Sci. U. S. A. 83*, 6785–6789.

Chapter 3

Parallel multifunctionalisation of

nanoparticles: A one-step modular

approach for *in vivo* imaging

Abstract

Multifunctional nanoparticles are usually produced by sequential synthesis, with long multi-step protocols. Our study reports a generic modular strategy for the parallel one-step multifunctionalisation of different hydrophobic nanoparticles. The method was designed and developed taking advantage of the natural non-covalent interactions between the fatty acid binding sites of the bovine serum albumin (BSA) and the aliphatic surfactants on different inorganic nanomaterials. As a general example of the approach, three different nanoparticles - iron oxide, upconverting nanophosphors and gold nanospheres- were nanomemulsioned in water with BSA. To support specific applications, multifunctional capability was incorporated with a variety of previously modified BSA modules. These modules include different conjugated groups, such as chelating agents for ^{68}Ga or ^{89}Zr and ligand molecules for enhanced *in vivo* targeting. A large library of thirteen multimodal contrast agents was developed with this convergent strategy. This platform allows a highly versatile and easy tailoring option for efficient incorporation of functional groups. Finally, as demonstration of this versatility, a bimodal (PET/MRI) probe including a maleimide-conjugated BSA was selectively sation with an RGD peptide for *in vivo* imaging detection of tumour angiogenesis

1. Introduction

Thermal decomposition is one of the most used synthetic methods rendering crystalline and highly monodispersed hydrophobic NP. These particles are stabilised with surfactants made of long aliphatic chain like oleic acid (OA) or oleylamine (OM), and are therefore dispersible only in different organic solvents.[1,2] Consequently, the multiple steps for the final multifunctionalisation start with the hydrophilic conversion of the NP to obtain a probe stable in physiological media, by ligand exchange[3], direct chemical modification of the surfactant[4,5] or stabilisation within a hydrophilic coating matrix.[6,7] The various hydrophilic coating matrix approaches proposed include inorganic or organic encapsulation, such as polymeric or protein based, and micellar or liposomal structures.[8–10] This hydrophilic coating provides an improved colloidal stability to the NP, protection from opsonisation and biocompatibility.[11] It is also of paramount importance that the coating allows stable drug entrapment or further functionalisation like attachment of targeting ligand and additional imaging probes.[10,14] Bovine serum albumin (BSA) fulfills all of these requirements, as several research groups have demonstrated.[15] Albumin is the most abundant protein in the blood and has crucial biological functions importantly, the transport of hydrophobic molecule to the tissues.[16] BSA as organic nanoparticle or coating for inorganic NP has also been reported to improve the *in vivo* properties of the probe.[15,17–19] Schäffler *et al.*[19] and others recently showed that albumin-NP conjugates not only have improved biocompatibility but also may be used as potential tool for organ targeting like brain or lungs.[20] Nonetheless, BSA (or Human serum albumin) conjugation on NP is always made on an existing hydrophilic coating, bringing into play covalent or ionic binding or just, simple adsorption.[22–24] As far as we know, no method that transfers directly hydrophobic OA/OM coated NP in aqueous phase with BSA has previously been described.

Multifunctionality is an unique characteristic of nanomaterials; the possibility of introducing several imaging agents, plus biological targeting moieties and drugs, is one of the most prominent features of this new type of chemistry. However, this multiplex incorporation presents some inherent problems, particularly the need for various complex sequential steps, in turn reducing the overall yield and lowering the reproducibility.[25–27] This is nowadays especially relevant for creating new PET/MRI and Fluorescence/MRI agents with the idea of combining sensitivity and improved spatial resolution.[23,25,28]

Following a modular approach, our proposal is different; by the hydrophobic interactions between fatty acid binding sites of albumin and the aliphatic chains on the coating of the NP we demonstrate how the parallel multifunctionalisation is achievable for a large variety of nanoparticles and coating possibilities. As for nanoparticles we apply our approach to IONP, UCNP and AuNP. Using each type of NP with different combination of natural BSA and fractions of pre-modified BSA with Alexa Fluor®647, DOTA (chelator for ^{68}Ga), DFO (chelator for ^{89}Zr) or maleimide reactive moiety; a large library of multifunctional contrast agents (BSA NP) was prepared. After a thorough characterisation of all the BSA NP the capacity of the platform for targeted bioimaging was finally assessed. For this, a bimodal contrast agent from the library was selected for RGD conjugation and its accumulation in a mouse model of cancer was studied by PET and MRI.

2. Results and discussion

2.1 Synthesis of OA IONP, OA UCNP and OM AuNP

Synthesis of OA IONP. Synthesis and characterisation of OA IONP was already described in Chapter 1, Section 2.3.

Synthesis of OA UCNP. As addressed in Introduction, Section 3; UCNP refers to a family of nanoparticles comprising a wide range of different types of inorganic core.[6,31] We have used a core composed of a $NaGdF_4$ host matrix with ytterbium (Yb) and thulium (Tm) lanthanide dopants embedded in a $NaGdF_4$ passive shell, abbreviated $NaGdF_4$:Yb,Tm@$NaGdF_4$ or in this study, OA UCNP. Oleic acid-OA coated UCNP were obtained by thermolysis method[27] described as the optimal to provide nanocrystals of the highest quality and well dispersed in organic solvent[28]. Small solid-state crystal nuclei were formed at room temperature by reaction between the lanthanide chloro-precursors and stoichiometric amounts of NH_4F fluoride reagent (Scheme 1) in an OA/OM mixture. Posterior thermic treatment allows further growth and ripening of the nuclei. With a similar method $NaGdF_4$:Yb,Tm were used as seed crystal to further epitaxial growth of a non-doped $NaGdF_4$ crystal shell layer on the surface[29] to obtain the core/shell structure OA coated $NaGdF_4$:Yb,Tm@ $NaGdF_4$ NP (OA UCNP). NP were uniform, with a polydispersity index (PDI) of 0.25, and had a hydrodynamic size of 29 nm measured in hexane (Table 3.1). TEM revealed the particles to be spherical, sometimes almost hexagonal and well dispersed. High Resolution TEM showed a high degree of crystallinity for the inorganic core of OA UCNP, with the possibility to observed different lattices of the crystal structure (Figure 3.1).
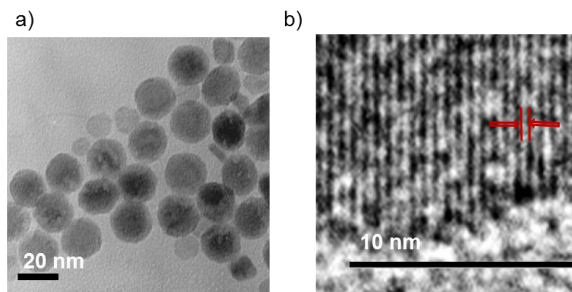
Figure 3.1. TEM pictures of OA UCNP at two different magnifications.

To confirm the composition and the crystallinity of the nanocrystals obtained, X-ray diffraction pattern of OA UCNP was achieved. We can see from Figure 3.2a that the diffraction peaks and intensities of the NP were in good accordance with the data of the β-hexagonal phase $NaGdF_4$ reference (Powder Diffraction File Card No. 27-0699). No peaks corresponding to the α-cubic phase or other impurity crystalline phase were found thus validating the high crystalline quality of the NP. It is of importance that the synthesis leads to the hexagonal crystal structure for the core as it ensured the up-conversion luminescence of highest intensity.[29] The energy-dispersive X-ray analysis pattern is presented in Figure 3.2b. It was checked that only the elements of the cores of OA UCNP were present. Not only the major components (Na, Gd, and F) were easily detected, but also the low content doping agents Yb were identified. Surfactant coating has been characterised by Fourier Transformed Infrared Spectroscopy shown in Figure 3.3. Spectrum displayed the characteristic vibration peaks of the OA. The ones of the aliphatic moieties were found at 2920 cm^{-1} (v_a C-H) and 2850 cm^{-1} (v_s C-H) while the ones of the carboxylic group appeared at 1625 cm^{-1} (v C-O) and 1530 cm^{-1} (v C-O). In comparison to the free carboxylic group, these last peaks were found at 1) a frequency lower than the C=O vibration band but 2) higher than the frequency of the C-O vibration band, also 3) the differences between the two bands were less than 110 cm^{-1}.
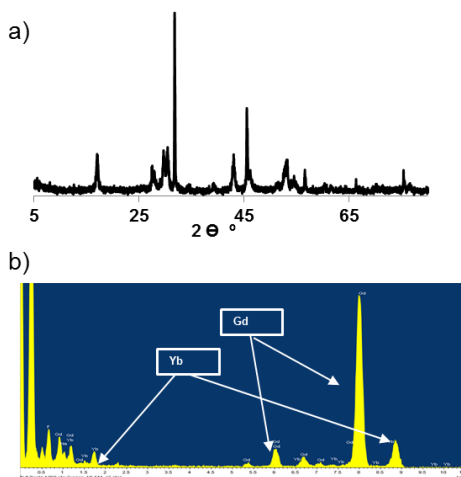
Figure 3.2. a) X-ray diffraction of OA UCNP powder b) Energy-dispersive X-ray analysis of OA UCNP.

All these information suggest that the carboxylic group of the oleic acid is coordinated to the gadoliniums atoms of the surface of the UCNP core through a bidentate complex with the oxygens. Indeed, as already mentioned, OA has a high affinity for the gadolinium ions. Finally the stretching band at 1461 cm^{-1} is characteristic of the Gd-O bound between the inorganic crystalline core structure and the carboxylic acid of OA.
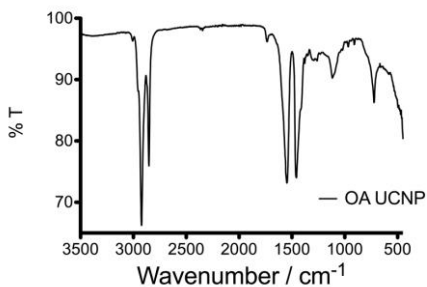

Figure 3.3. FTIR of OA UCNP.

Coating can be also characterised by mass spectroscopy. The mass spectrum of the OA UCNP was clearly representative of the OA adducts with peaks at m/z = 208 and 563 g.mol^{-1}, respectively the MW of OA subtracted of one proton and its double multiple. No peaks representative of OM, a side products used in the reaction and weak cheating ligand of UCNP core, was detected with MS highly sensitive technique. It confirmed the surfactant recovering the UCNP is made of only OA.

Finally TGA shows that the organic coating (corresponding to the removal of OA surfactant between 190ºC and 400ºC) represents 30 % of the total weight of OA UCNP (Figure 3.4). This is a value to put in perspective in front of presence of free OA in the sample. Similarly, it also indicates a high strength of union formed by the complex between carboxylic acid of OA and UCNP core, as no loss of surfactant is observed before 300ºC, the temperature used in the thermal synthesis. The first slight decrease of the weight between 0 and 190ºC is due to the combined evaporation of the remaining water and un-adsorbed OA.
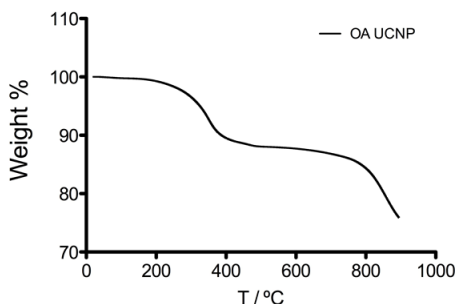

Figure 3.4. TGA of OA UCNP.

One of the most important properties of the UCNP further taken advantage of for bioapplications is their upconversion fluorescence (details in

Introduction, Section 3). The upconverting (UC) fluorescence of the OA UCNP, investigated under continuous wave CW excitation at 980 nm, are presented in Figure 3.5. It can be easily observed a strong upconversion with the main characteristic emission peaks at 360 nm, 451 nm, 476 nm and 800 nm corresponding to the 1D2->3H6, 1D2->3F4, 1G4-> 3H6 and 3H4->3H6 transitions in the system Yb,Tm [30] . As expected, UCL of the core/shell structure was significantly enhanced in the overall emission intensity. Indeed the inert shell made of the same non- doped material preserve the energy loss and transfer to the outer surface[31].
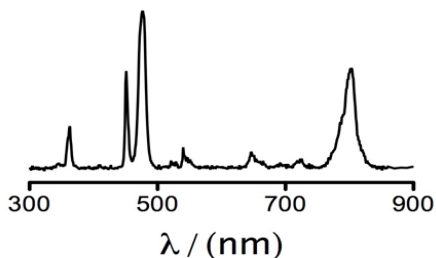

Figure 3.5. Fluorescence emission spectrum for *3.2* after excitation with C.W. laser at 980 nm. Normalised UCL intensity.

Synthesis of OM AuNP. For the synthesis of OM AuNP, we used the decomposition of chloroauric acid in a mixture of toluene and oleylamine following a well-known method describe in the Materials and Methods section of this chapter. NP were highly uniform with a pdi below 0.1 and had a hydrodynamic size of 14 ± 3 nm for a mean core diameter of 5 ± 2 nm (Figure 3.6a). Transmission electron microscopy (TEM) showed the particles to be spherical and well-dispersed (Figure 3.6b).
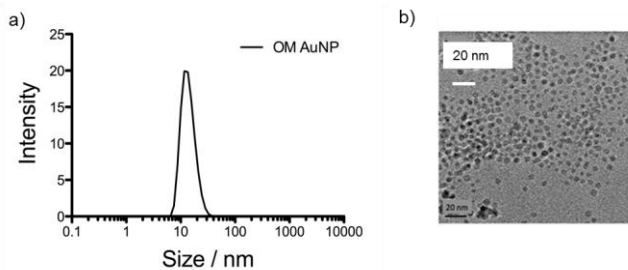
Figure 3.6. a) Hydrodynamic size and b) TEM of OM AuNP.

Surfactant coating has been characterised by FTIR shown in Figure 3.7. Spectrum displayed the characteristic vibration peaks of the OM. The ones of the aliphatic moieties were found at 2920 cm^{-1} (va C-H) and 2850 cm^{-1} (vs C-H) while the ones of the amine group appeared at 3290 cm^{-1}.
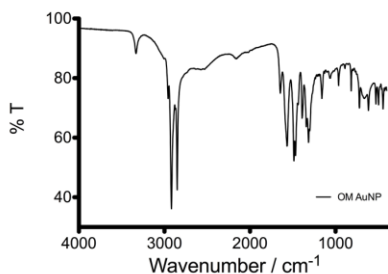

Figure 3.7. FTIR of OM AuNP.

One of the most prominent features of AuNP is their surface plasmon resonance due to the electromagnetic confinement, giving rise to their characteristic color variations with size. This has been extensively exploited in different applications (see Introduction, Section 4). The UV-VIS absorbance spectrum of the OM AuNP presented in Figure 3.X shows the typical broad absorbance band for AuNP of around 5nm core size.
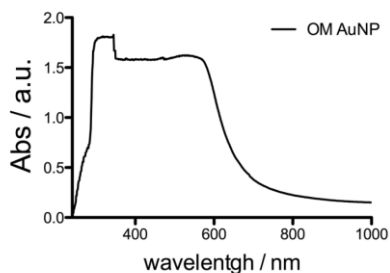
Figure 3.8. UV-VIS spectrum of OM AuNP.

A summary of the main characterisations and differences of the three hydrophobic NP prepared are presented below in Table 3.1.

Table 3.1. Basic physicochemical characterisations of the hydrophobic NP (IONP, UCNP, AuNP).

OA/OM NP	Core diameter	Hydrodynamic Size (nm)	pdi
OA IONP	7	10	0.24
OA UCNP	20	29	0.25
OM AuNP	5	14	0.07

2.2 Synthesis and physicochemical characterisation of BSA coated IONP, UCNP and AuNP

The first step was to demonstrate the feasibility of aqueous stabilisation through BSA binding to the aliphatic chains. This was achieved, as represented in Figure 3.9, by adapting a simple, fast and reproducible nanoemulsion method.[32] It is similar to the method described in chapter 1, section 2.2. It involved, mixing a small volume of NP dispersed in hexane with

126

an aqueous phase (phosphate buffer, pH 7.2), 1/10 in v/v, containing BSA protein. Upon homogenisation and stirring, an oil-in-water nanoemulsion is formed and gradual evaporation of the organic phase leads to a stable colloidal aqueous solution of BSA IONP (*3.1*), BSA UCNP (*3.2*) and BSA AuNP (*3.3*). Stabilisation was achieved by hydrophobic van der Waals interactions between the surfactant (OA or OM) of the hydrophobic NP and the fatty acid binding sites of the albumin. The BSA stabilised NP did not show re-dispersion, if mixed again with hexane phase (1/1 in volume). This method is more flexible, easier, and faster than the widely common adsorption, conjugation or desolvation routes used to coat NP with albumin.[20,23,24] To confirm that the stabilisation was achieved via hydrophobic interactions between OA and BSA fatty acid binding sites, several control reactions were performed. These consisted in repeating the nanoemulsion formulation with a pre-targeted BSA, in which, the fatty acid binding sites were previously saturated with free OA. As expected, the BSA was not able to bind to the surface, making the formation of a stable aqueous colloidal solution of nanoparticles *3.1*, *3.2* and *3.3*, impossible. This confirms that the binding origin is mainly through hydrophobic interactions and not simple adsorption on the surface of the NP. This straightforward use of the fatty acid binding sites of BSA simplifies the process against other synthetic strategies that use multiple steps and/or harsh reactive conditions.
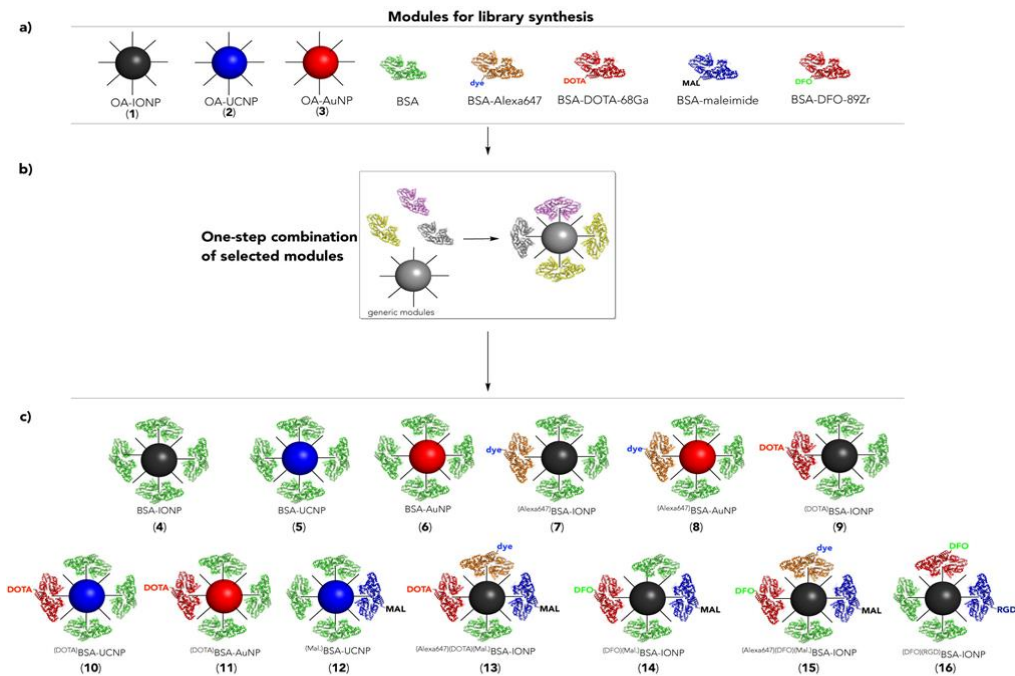
Figure 3.9. a) Modules for combination in the nanoemulsion process; b) Nanoemulsion step with selected modules (many other combinations are possible) and c) Library of multifunctional nanoparticles synthesised in this work.

Final hydrodynamic sizes of *3.1*, *3.2* and *3.3* were 97.2 nm, 94.3 nm and 102.5 nm with pdi below 0.25, showing that this approach leads to very homogeneous dispersions with high reproducibility (Section 2.3 of this chapter, Table 3.2). TEM images shown in Figure 3.10a, confirms that the sizes match with the formation of well-defined small clusters made up of few hydrophobic self-assembled NP and surrounded by the BSA. Colloidal stability was checked by measuring the zeta-potential (ζ) variation, as a function of the pH (Figure 3.10b). As expected, it followed the same evolution as the electric charge of the BSA protein, with no net superficial charge around the BSA isoelectric point (pH 4.7, 25ºC) and a negative potential at physiological pH, preventing aggregation by strong repulsive electrostatic interactions and steric effects. The presence of protein on the nanoparticle surface was further characterised by FTIR, (Figure 3.11a), TGA (Figure 3.11b) and MS (Figure 3.12). The three types of BSA-stabilised particles ((*3.1*), (*3.2*) and (*3.3*)), showed the characteristic absorption spectrum of the protein, with bands at 3284, 1642, 1530 and 1391 cm^{-1} together with signals of the NP hydrophobic surfactant: OA/OM aliphatic chain moiety at 2920 cm^{-1} (va C-H), 2850 cm^{-1} (vs C-H), 1641 cm^{-1} (vs C=O) 1576 cm^{-1}, 1436 cm^{-1} (v C-N) and 1534 cm^{-1} (v N-H) and inorganic core (for example Fe-O at 580 cm^{-1} for IONP).
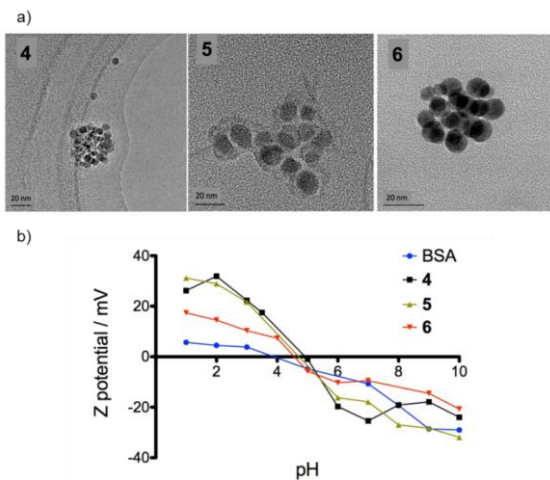
Figure 3.10. a) TEM images of BSA coated NP (*3.1*), (*3.2*), (*3.3*) b) Zeta potential of BSA coated NP (*3.1*), (*3.2*), (*3.3*) as a function of pH.

TGA shows that organic coating (corresponding to the removal of protein and surfactant between 300 ºC - 900ºC) represents approximately 43 % (*3.1*), 50% (*3.2*) and 27% (*3.3*) of the total weight of each NP. The smaller amount of organic phase for gold nanoparticles is most likely due to a lower amount of OM on the surface of *3.3* in comparison to the use of OA. MS data of the three kinds of NP (analysed in positive ionisation) were representative of the expected BSA adducts and was similar to the unbound BSA control spectrum.
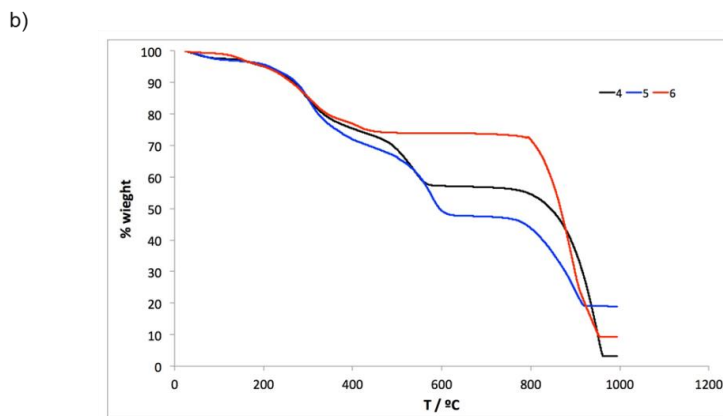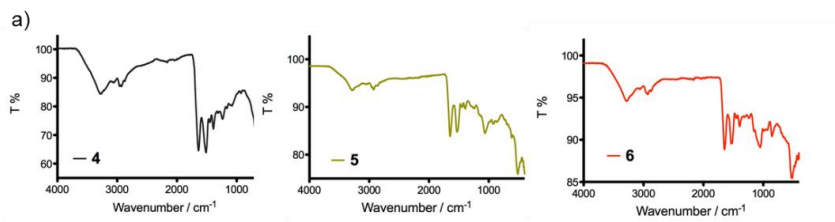
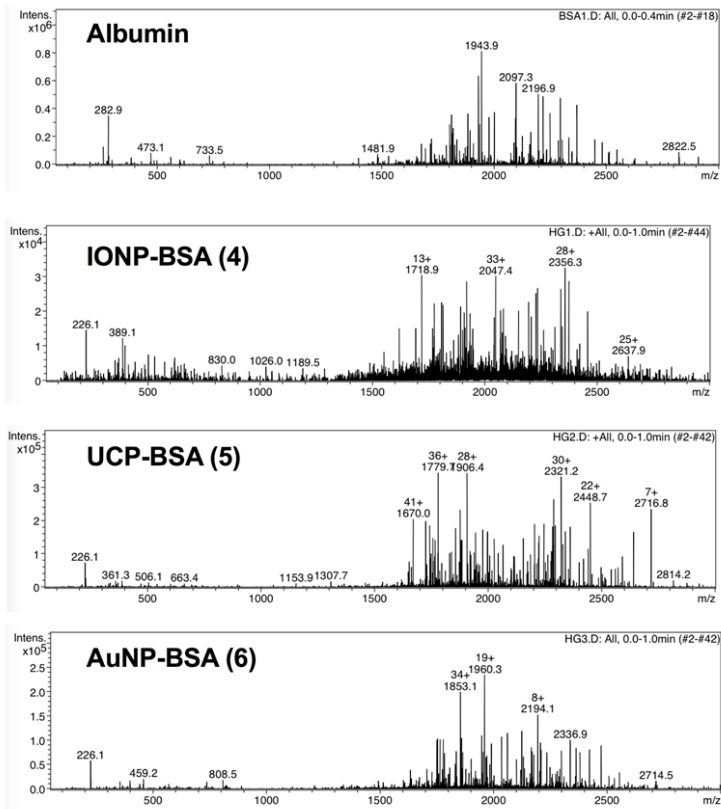**Figure 3.11**. a) FTIR spectra and b) Thermogravimetric curves of BSA coated NP (*3.1*), (*3.2*), (*3.3*).

Figure 3.12. Mass spectra for pure BSA and BSA NP *3.1*, *3.2* and *3.3.*

2.3 Library of multifunctional nanoparticles by modular integration of pre-labeled BSA

Through traditional bioconjugation (especially succinimide-activated carboxylic groups) it is possible to incorporate a covalent linkage of additional probes and adds new functionalities to the protein. One key aspect of our approach is the possibility of using the nanoemulsion method with small fractions of modified BSA in addition to the native BSA, a straightforward method of obtaining water stable and multimodal NP. In this flexible modular approach, we have used BSA modules conjugated with i) Alexa Fluor®647 fluorophore (optical modality); ii) DOTA chelating agent for short half-life isotope like ^{68}Ga (PET modality); iii) DFO as chelating agent for long half-life isotope like ^{89}Zr (PET modality) and iv) a maleimide moiety (functional group for easy attachment of a targeting peptide by click chemistry). Different combinations between hydrophobic NP and the modified BSA modules were performed so as to obtain a large molecular imaging portfolio of multifunctional contrast agents (thirteen different BSA NP, Figure 3.9).

Table 3.2 summarises the different composition, physicochemical properties and imaging possibilities of each contrast agent. Hydrodynamic sizes of the BSA NP ranged between 78.4 and 108.9 nm with a pdi for all of them below 0.25 and a negative zeta potential ζ at neutral pH. It demonstrates the versatility of this modular approach, in all cases, resulting in very homogeneous and particularly reproducible dispersions.

Table 3.2. Library of the BSA NP contrast agents. Main physicochemical properties and imaging modalities.

BSA NP	NP#	% BSA	Size (nm)	pdi	Zeta potential (mV)	Imaging properties
BSA IONP	3.1	n.a.	97.2	0.18	-19.7	T_2 MRI
BSA UCNP	3.2	n.a	94.3	0.19	-17.9	T_1 MRI / Fluorescence
BSA AuNP	3.3	n.a.	102.5	0.15	-9.5	UVvis/ fluorescence
(Alexa647)BSA IONP	3.4	3 % Alexa647	93.0	0.15	-13.5	T_2 MRI / Fluorescence
(Alexa647)BSA AuNP	3.5	3 % Alexa647	108.9	0.22	-11.1	UVvis / fluorescence/ FRET
(DOTA)BSA IONP	3.6	8 % DOTA	104.9	0.17	-10.8	T_2 MRI / PET
(DOTA)BSA UCNP	3.7	8 % DOTA	78.7	0.20	-25.7	T_1 MRI / Fluorescence / PET
(DOTA)BSA AuNP	3.8	8 % DOTA	87.5	0.13	-19.8	PET / UVvis
(Mal.)BSA UCNP	3.9	30 % Mal	100.9	0.15	-23.1	T_1 MRI / Fluorescence / targeting
(Alexa647)(DOTA)(Mal.)BSA IONP	3.10	6 % Alexa647 3 % DOTA 30 % Mal	90.2	0.19	-8.9	T_2 MRI / PET / Fluorescence / targeting
(DFO)(Mal.)BSA IONP	3.11	20 % DFO 20 % Mal	91.9	0.18	-13.9	T_2 MRI / PET / targeting

Table 3.2. (Cont.)

(Alexa647)(DFO)(Mal.)BSA IONP	3.12	6 % Alexa647 20 % DFO 15 % Mal	78.4	0.16	-12.0	T_2 MRI / PET / Fluorescence / targeting
(DFO)(RGD)BSA IONP	3.13	20 % DFO 20 % RGD	94.2	0.15	-14.5	T_2 MRI / PET / Angiogenesis

Imaging modalities provided by the inorganic core of the nanoparticles. Our modular approach is valid for different types of nanoparticles, independently on the nature and physicochemical properties of each IONP, UCNP and AuNP. The imaging functions of each preparation, depends on the core of the nanoparticles, and the modified BSA modules in the coating. Thus, we first evaluated the characteristics of the core of the nanoparticles *3.1*, *3.2* and *3.3* as contrast agents for different imaging techniques.

<u>Iron Oxide core.</u> Fe_3O_4 core confers superparamagnetic behaviour and normally high transversal relaxivity (r_2) for T_2-weighted MRI.[1] BSA IONP (*3.1*) shows a large saturation magnetisation value of 70 emu g^{-1} similar to the hydrophobic particles, measured in a Vibrating Sample Magnetometer, both displayed in Figure 3.13a. This large value explains the high transversal r_2 value of 203.4 $s^{-1}mM^{-1}$ (r_1 = 3.2 $s^{-1}mM^{-1}$), which confirms these particles as an excellent probe for T_2-weighted MRI (Figure 3.13b). This was finally evaluated by *in vitro* MRI with a series of dilutions in a T_2-weighted sequence (upper row of the Figure 3.13c).
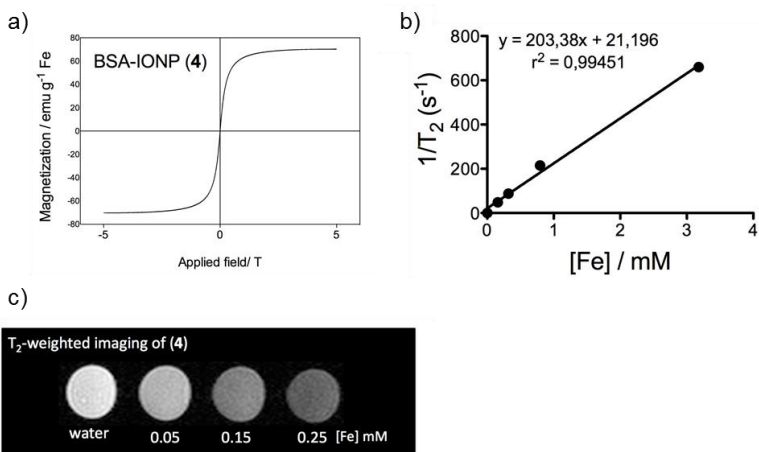
Figure 3.13. a) Magnetisation curves at 298 K for *3.1* b) Plot of the T_2 relaxation rate against iron concentration for BSA IONP (*3.1*); c) T_2-weighted MRI phantoms for BSA IONP *3.1.*

Upconverting NP core. Upconverting nanophosphor cores display upconversion fluorescence upon 980 nm c.w. laser excitation. In our case the NaGdF$_4$:Yb,Tm@NaGdF$_4$ allows a strong upconversion at three distinct and simultaneous sharp emissions in uv (360 nm), visible blue (451 and 476 nm) and NIR (800 nm) as shown in Figure 3.14a.
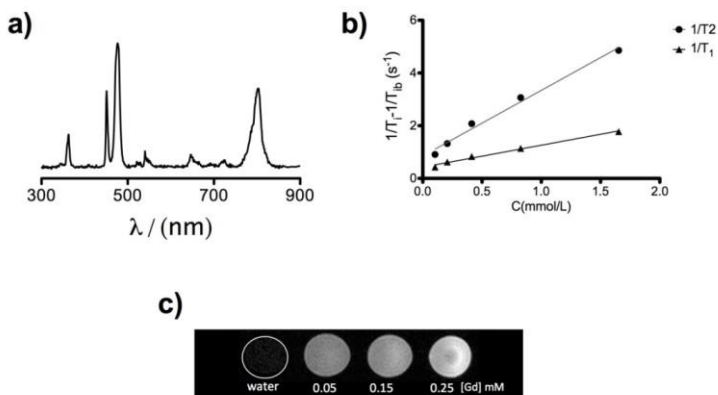
Figure 3.14. a) Fluorescence emission spectrum for **3.2** after excitation with C.W. laser at 980 nm. Normalised UCL intensity. b) Plot of the T_1 and T2 relaxation rate against Gd concentration for BSA UCNP (**3.2**); c) T_1-weighted MRI phantoms for BSA UCNP **3.2.**

As proof of concept of the cell labeling capabilities of the BSA UCNP, nanoparticles **3.2** were cultured for 24 h with HT1080 cells (expressing green fluorescent protein). Then the fluorescence of the internalised particles was studied using two-photon imaging (Figure 3.15). Images clearly show the signal from the nanoparticles, mainly surrounding their nucleus, when excited at 980 nm. Although the UCNP are mainly designed for optical imaging, here the presence of gadolinium in the core also confers paramagnetic properties and thus MRI contrast agent capability. The longitudinal (r_1) and transversal (r_2) relaxivity values of **3.2** were measured (r_1 = 0.8 s^{-1}mM^{-1} and r_2 = 2.5 s^{-1}mM^{-1}) in Figure 3.14b. The relaxometric properties are modest since a compromise must be reached between relaxometric and optical properties, the better the fluorescence the lower the r_1 value (due to size effects). These values show that UCNP based contrast agents can also be tuned for T_1-weighted MRI applications, as the results summarised in the bottom row of the

137

Figure 3.14c demonstrates. A positive contrast is observed upon increase in the nanoparticle concentration in comparison with water (encircled dark signal).
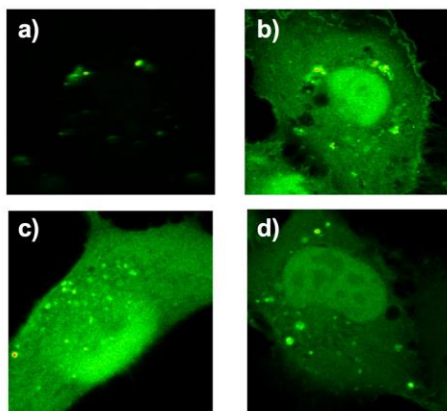

Figure 3.15. Two-photon images of HT1080 cells labeled with nanoparticle *3.2*. a) image corresponding to the signal only in the nanoparticles channel (BP460/60 nm filter); b) same cell with combined signal from the nanoparticle and cell autofluorescence (BP609/54 nm filter); c) and d) combined images (signal from nanoparticles + cell autofluorescence) for different cells.

Contrast agent AuNP-based. The most prominent feature of Gold nanoparticles is their surface plasmon resonance due to the electromagnetic confinement, giving rise to their characteristic color variations with size. This has been extensively exploited, particularly for *in vitro* applications.[29] The UV-VIS absorbance spectrum of the BSA AuNP (*3.3*) presented in Figure 3.16 confirms, as proof of concept of the suitability of the BSA AuNP series for these applications. The spectrum shows the typical broad absorbance band for albumin around 250 nm and the one typical of gold nanoparticles of this size at about 590 nm.[29]
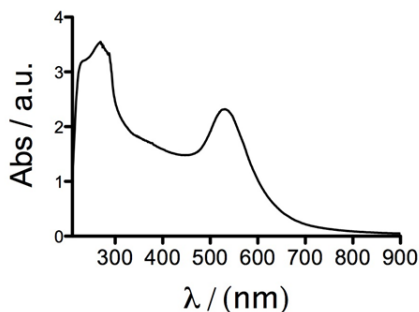
Figure 3.16. UV-VIS absorbance spectrum of BSA AuNP (*3.3*).

Characterisation of the functionalities provided by the BSA modules of the contrast agents. The fluorescence and PET imaging properties provided by the different modified BSA modules were characterised.

Alexa Fluor© 647 conjugated BSA(*3.4*, *3.5*, *3.10*, and *3.12*). The $^{(Alexa647)}$BSA module was added at maximum 6 % weight of the total BSA weight used. The presence of the dye, in nanoparticles *3.4* and *3.5*, was checked by aborbance spectra (Figure 3.17a) and by Fluorescence Molecular Tomography using several phantoms of varying concentration for nanoparticles (Figure 3.17b).

DOTA conjugated BSA (*3.6*, *3.7*, *3.8* and *3.10*) and DFO conjugated BSA (*3.11*, *3.12*, and *3.13*). To obtain nanoparticles ready for PET imaging, radiometals and chelators are commonly incorporated in the coating.[30] We have demonstrated the benefit of our proposal using a short half-life isotope obtained from a generator (^{68}Ga, $t_{1/2}$= 68 min) and a long half-life isotope delivered from a cyclotron (^{89}Zr, $t_{1/2}$= 78.4 hrs). In the case of ^{68}Ga, DOTA is the most often used chelator.[31] NHS-activated DOTA was covalently attached to BSA to obtain $^{(DOTA)}$BSA module, fractions of which, were added at different proportion into the nanoemulsion formulation for synthesis of *3.6*, *3.7* and *3.8* (Table 3.2). These particles were then labeled with ^{68}GaCl$_3$ eluted from a

In all the cases, radiolabeling yield was up to 20% (Figure 3.17c), calculated after subtraction of the nonspecific ^{68}Ga chelation by the native BSA coating.
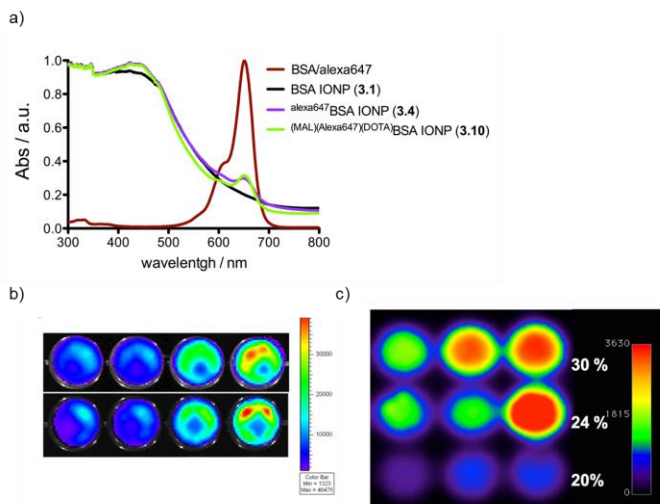

Figure 3.17. a) Absorbance spectra of $^{(Alexa647)}$BSA, BSA IONP (**3.1**), $^{(Alexa647)}$BSA IONP (**3.4**) and $^{(Mal)(Alexa647)(DOTA)}$BSA IONP (**3.10**) b) *In vitro* fluorescence imaging of nanoparticles $^{(Alexa647)}$BSA IONP (**3.4**) and $^{(Alexa647)}$BSA AuNP (**3.5**) c) *In vitro* PET imaging of nanoparticles $^{(DOTA)}$BSA UCNP (**3.7**, 0.5 mM, upper row), $^{(DOTA)}$BSA IONP (**3.6**, 0.5 mM, middle row) and $^{(DOTA)}$BSA AuNP (**3.8**, 0.25 mM, bottom row), percentages indicate radiolabeling efficiency.

     In vitro PET imaging of phantoms for nanoparticles **3.6**, **3.7** and **3.8** were carried out showing a strong signal over the range of concentrations (Figure 3.17c). The intensity for nanoparticles **3.8** is clearly lower due to two factors; a smaller amount of $^{(DOTA)}$BSA module on the surface and also a smaller AuNP concentration (0.25 mM of Au for **3.8** in comparison to 0.5 mM of Fe for **3.6** and Gd for **3.7**). In the case of ^{89}Zr, a common chelating agent is DFO.[32] A previously prepared module of BSA covalently attached to DFO

groups was incorporated in *3.11* and *3.12* coating and radiolabeling yield of the probe obtained was up to 14 %. All these radiolabeling yields are particularly high if we consider that the amount of ^(chelators)BSA is no higher than 8% in case of ^{68}Ga and 20 % for ^{89}Zr and that from that percentage, only a fraction of chelators would be available for coordination with the radioisotope.

Maleimide conjugated BSA and biofunctionalisation (*3.9*, *3.10*, *3.11* and *3.12*). Maleimide is often used to attach biomolecules in a specific manner, through click chemistry with thiol groups.[5,33] In the synthesis of *3.9*, *3.10*, *3.11* and *3.12* a fraction of commercial ^(maleimide)BSA module (10-20 maleimide per BSA) was incorporated. Presence of BSA bearing maleimide module in the coating of these NP was verified by FTIR with a characteristic band from the maleimide at 1130 cm^{-1}, the example for *3.9* is shown in Figure **3.18**. This module adds to the platform the possibility of an easy functionalisation with thiol bearing targeting molecule. This was further verified by the conjugation of a thiol derived cyclic RGD peptide on the coating of *3.11*.
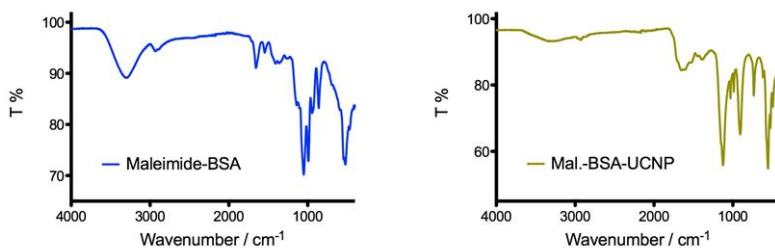

Figure 3.18. FTIR spectra for selected BSA module and BSA NP *3.9.*

Evaluation of cytotoxic effects and biodistribution. Cytotoxicity studies were carried out for each type of inorganic core with a full natural BSA coating (*3.1*, *3.2* and *3.3*). Cytotoxicity was evaluated after incubation of each agent at different doses with C57BL/6 mouse adult fibroblasts (MAFs) over 72 h. As

displayed in Figure 3.19, in the cell viability assay we did not observe any toxic effect for **3.1** and **3.3**, only for **3.2**, when a slightly more pronounced effect is observed at the higher dose.
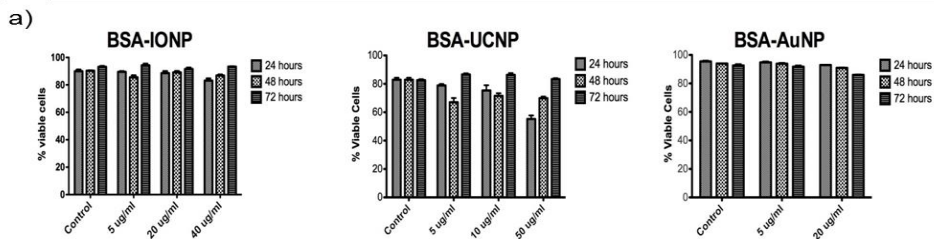
Figure 3.19. Cell viability study of MEFs incubated with nanoparticles **3.1**, **3.2** and **3.3** at different concentration (between 5 to 50 μg.ml^{-1} of Fe^{3+}, Gd^{3+} or Au^{3+}).

An additional experiment studied the internalisation of **3.4** in the MEFs at 40 μg$\cdot$mL^{-1} over 24 h by fluorescent cytometry analysis. The presence of AlexaFluor® 647 conjugated BSA fraction in the coating of **3.4**, enhanced the sensitivity for detection and thus the possibility of observing the cellular internalisation of the nanoparticle by flow cytometry (Figure 3.20a). Cell fluorescence and SSC (side-scattered light-related to cell internal complexity) increased in the cells treated and confirmed a high uptake of the NP (Figure 3.20b).[37] The strain caused on MAFs by such high internalisation can explain the small cytotoxic effect observed at the highest doses. Gold and gadolinium inorganic cores have been described as less biocompatible than iron oxide,[2,35] also explaining the higher apoptotic occurrence found for **3.2**. As expected, due to the presence of BSA in the coating, the BSA NP show a very low *in vitro* toxicity.
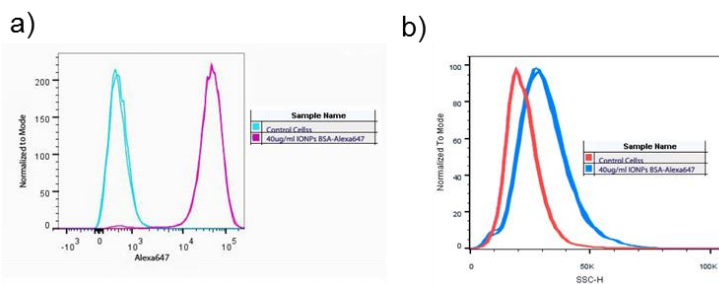
Figure 3.20. a) Cell labeling with nanoparticle *3.4* (24 h) confirmed by flow cytometry and c) side-scattered light (SSC-H) of control cells and cells labeled with *3.4* (24 h).

The biodistribution of BSA nanoparticles was studied by fluorescence, using also nanoparticle *3.4* in mice (N=3). After 24 h, mice were sacrificed and after saline perfusion, the main organs were extracted. *Ex vivo* fluorescence showed in Figure 3.21a, as expected, revealed a large proportion of *3.4* in the liver and in spleen.
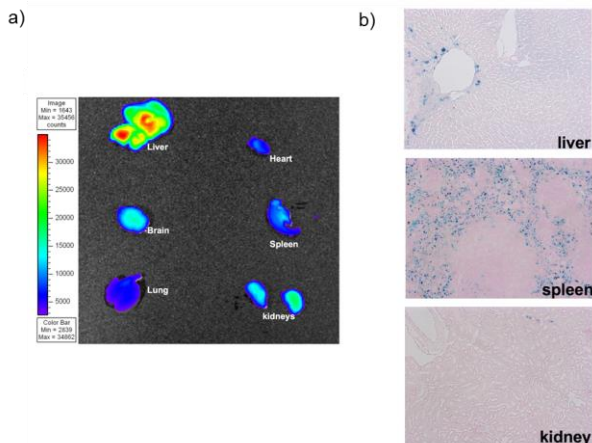
Figure 3.21. Biodistribution of nanoparticles *3.4* after 24h. a) *Ex vivo* fluorescence of different organs and b) histology of liver, spleen and kidneys (40x) with Prussian Blue staining.

Substantial accumulation of the probe was also observed in other organ of the RES system (kidney) and interestingly, a fraction also appears to target the brain. The results were confirmed by microscopy of histological organs sections stained with Prussian blue for iron detection (Figure 3.21b).

2.4 *In vivo* targeted multimodal imaging of tumour in mice with selected BSA NP contrast agent

Due to the excellent colloidal stability and *in vitro* MRI/PET/OI contrast properties, we finally examined the multimodal imaging performance of one of the probes from the library for *in vivo* biomedical application. One advantage of the modular approach is the ease of further tailoring for biofunctionalisation; for instance the addition of a targeting ligand. Arginine-glycine-aspartic acid peptide (RGD) binds to the $\alpha_v\beta_3$ and $\alpha_v\beta_5$ integrins that are overexpressed in nascent endothelial cells during angiogenesis in various tumours, and yet not in inactive endothelial cells.[40] This property has been many times used for successful tumour and angiogenesis detection, with a wide range of probes from small chelators, polymeric nanoparticles, iron oxide nanoparticles, or quantum dots.[41] Thus, taking advantage of the presence of maleimide-BSA module in the coating of *3.11*, RGD modified with a thiol functionality was covalently linked to the protein *via* a covalent thioether linkage with maleimide group.[38] **(DFO)(RGD)**BSA IONP (*3.13*) was labeled with ^{89}Zr and intravenously injected in tumour-bearing mice for PET/CT imaging and MRI. One hour after the injection high accumulation was found in the liver and spleen, as usual with imaging probes. It is also clear that a large fraction of the probe remained in systemic circulation. After 24 h, accumulation in tumour was observed with persistent and intense signal until 72 h, clearly delimiting the affected area (Figure 3.22a). For T_2-weighted MRI basal image and 24 h post injection are

shown (Figure 3.22b). A loss of MRI signal intensity is clearly seen, especially delimiting the tumour.
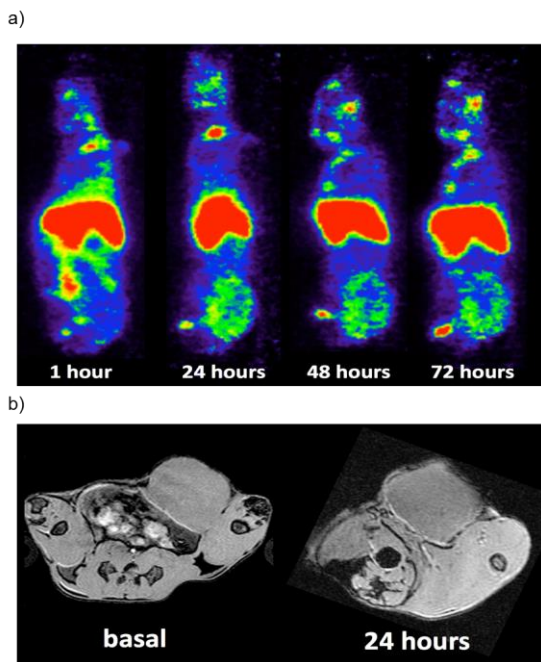
Figure 3.22. a) PET imaging of $^{(89Zr)(RGD)}$BSA IONP (*3.13*) at different time points postinjection in mouse bearing allograft tumour. b) Axial T_2 weighted MRI located at the tumour before and 24 h postinjection.

The quantification in both types of images (PET and MRI) provides similar results. The tumour to muscle relative signal intensity in MRI clearly decays 24 hours post-injection in a similar way in which the SUVmean (the decay corrected radioactive signal intensity from PET images) increases, in both cases as the $^{(89Zr)-(RGD)}$BSA IONP (*3.13*) accumulates in the tumour (Figure 3.23).
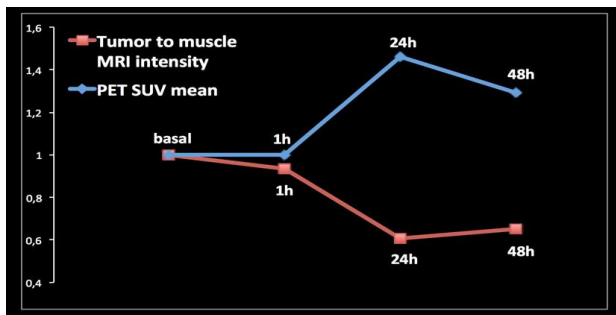
Figure 3.23. Standardised uptake value (SUV) of tumour (blue) and relative MRI mean intensities at different days post injection (to the intensity in a ROI located in the leg muscles, in red).

Ex vivo radioactive signal of main organs was measured; Figure 3.24a shows the % of injected dose as function of the tissue weight for different organs. High signal in liver and spleen is observed, like we saw in the images, as well as in the tumour. Finally, bright field microscopy of different sections of the tumour harvested 72 h after i.v. injection revealed numerous Prussian blue stained areas (Figure 3.24b). It allowed investigating the localisation of *3.13* in the tumour. Distribution was heterogeneous (as already suggested by the PET and MRI) with a high uptake in the periphery, in accordance with the ensured RGD peptide targeting directed to the nascent endothelial cells.

146
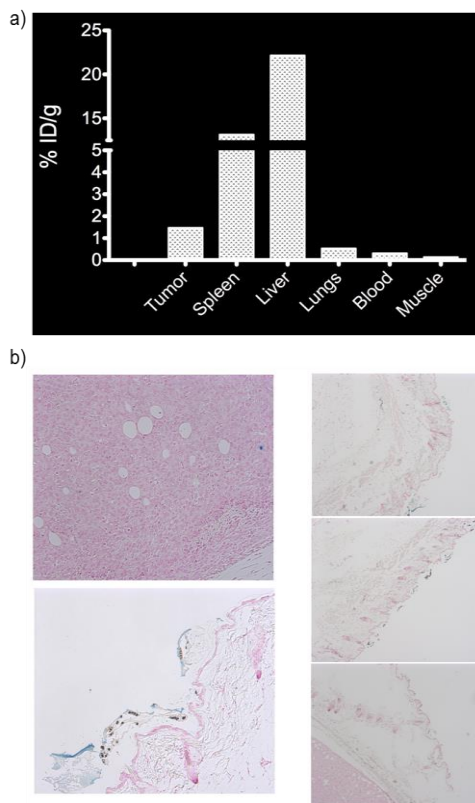
Figure 3.24. a) Activity measured in a gamma counter of specific organs (72 h postinjection). b) Tumour histology slides, stained with Prussian blue after 72 h, showing blue dots due to the accumulation of iron oxide nanoparticles.

3. Conclusions

Here we present a new approach for the modular multifunctionalisation of different hydrophobic nanoparticles. This takes advantage of the parallel synthesis concept, rather than the traditional sequential process used in nanoparticles chemistry. In a single and rapid step, NP are conjugated with native/modified BSA to prepare "ready to use" multifunctional nanoparticles.

Using this modular albumin based platform, we have developed a wide library of contrast agents for cell labeling, drug delivery and non-invasive imaging. Because of the ease and versatility of the route, a large range of BSA modules and ligands can be conjugated to the surface; therefore it could convert in a routine methodology for preparation of a library of new molecular imaging agents. As an example, one of these candidates was selected and used for targeted PET/MRI multimodal *in vivo* imaging in a murine tumour model. Moreover, as a translational improvement in the field, the method presents notable advantages such as high reproducibility, facile scaling up production and the use of biocompatible albumin coating. Finally, since albumin plays a role as a drug carrier in the clinical setting, our findings can be simply extended to incorporate new theranostic functions due to the versatility and high binding capacity of this protein. This modular proposal is very helpful, since it simplifies complex tailored functionalisation and circumvents typical cumbersome problems associated to the reactions on the surface of the nanoparticles.

4. Materials and Methods

Materials

All chemicals for the preparation of the BSA NP were purchased from Sigma-Aldrich Co. (St. Louis, USA) except Alexa Fluor® 647 conjugated BSA purchase with life technologies [TM]. All reagents were of analytical grade except oleic acid and oleylamine of technical grade. They were used without any further purification.

Animals and ethics

All animal experiments conducted in this work were approved by the ethics and animal welfare committee at CNIC and were developed according to the Spanish and UE legislation.

Synthesis

Synthesis of OA IONP, OA UCNP and OM AuNP

These protocols are described in the chapter "General Materials and Methods".

Synthesis of BSA NP. Bovine serum Albumin (BSA) and fraction of modified BSA (Alexa Fluor® 647 conjugated BSA, DOTA conjugated BSA, DFO conjugated BSA or Maleimide conjugated BSA) -total BSA weight 30 mg- were first dispersed in 10 mL of phosphate buffer (pH=7.2, 5 mM). Then 0.75 mL of hydrophobic NP (OA IONP, OA UCNP or OM AuNP) in n-hexane (5-10 mg·mL^{-1} of the metal core Fe, Gd or Au) was added to the solution and the resultant mixture was sonicated (Branson 250, 42 +/- 6 KHz) under robust stirring for 20 min at 37ºC. Oil in water (o/w) nanoemulsion was further kept under sonication for 30 min to evaporate all traces of n-hexane resulting in the formation of a homogenous BSA NP colloidal aqueous solution. Aggregates were removed by filtration (0.45 and 0.22 µm filter unit, Sterivex-GP) and excess of BSA discarded by ultrafiltration with Amicon®Ultra-15 mL 100K, Merck Millipore Ltd. (X5000g, 10 min, 2 cycles) to obtain the purified hydrophilic BSA NP.

Preparation of the modified BSA modules. For preparation of DOTA ^{68}Ga chelator conjugated BSA, 5 mg of BSA were dissolved in 2 mL HEPES Buffer (1mM, pH=7.7). Then, 1.5 mg of DOTA-NHS dissolved in 0.5 mL of same buffer was added and the reaction was kept under stirring at room temperature for 2 h. After this time, excess of DOTA-NHS was removed by gel filtration with a PD-10 column (GE Healthcare) and DOTA conjugated BSA dissolved in 3 mL of PBS 1X.

For preparation of DFO ^{89}Zr chelator conjugated BSA, 5 mg of BSA were dissolved in 1 mL of water and the pH adjusted to 8.9-9.1 with 0.1 M Na_2CO_3. To this solution, 22.5 µl of 10 mM SCN-Bz-Df in DMSO was added. Then, the mixture was incubated at 37ºC for 60 min in thermomixer. Finally, the mixture was purified by ultrafiltration with a 30 kDa cutoff (Amicon®Ultra, Merck Millipore Ltd.) and DFO conjugated BSA resuspended in 1 mL of water.

Imaging properties of the BSA NP

Imaging properties of the inorganic cores of the BSA NP contrast agents. Magnetic characterisation of OA IONP and BSA IONP (*3.1*) were carried out in a vibrating sample magnetometer using 100 μL of solution in a special sample holder. Magnetisation curves were recorded at room temperature by first saturating the sample in a field of 1 T. The magnetisation values were normalised to the amount of iron to yield the specific magnetisation (emu/g Fe). The initial susceptibility of the suspensions was measured in the field range ±100 Oe, and the saturation magnetisation values (Ms) were evaluated by extrapolating to infinite field the experimental results obtained in the high field range where the magnetisation linearly increases with 1/H. For determination of the NMR relaxometric values of based IONP and based UCNP BSA NP, the T_2 and T_1 relaxation times were measured at 37ºC in a Bruker MQ60 (Bruker Optics, Germany) with a T_2 Carr-Purcell-Meiboom-Gill spin echo sequence and with a standard inversion recovery pulse sequence for measuring T_1 . The relaxation rate Ri values ($1/Ti$, s^{-1},$i = 1, 2$), obtained from the measured relaxation times (Ti, s) were corrected by subtracting the water relaxation rate in the absence of the contrast agent. Linear fitting of the data gives straight lines whose slopes are the relaxivities (r_i, s^{-1} mM^{-1}) related to the iron concentration (mM): $Ri = r_{i0} + r_i [Fe]$.

The optical measurements of OA UCNP and BSA UCNP (*3.2*) solutions in standard cuvettes were performed using a JENOPTIK laser diode source at 980 nm with different excitation powers. The VIS/NIR luminescence was dispersed by using an ARC Spectrapro 500-I monochromator and then detected with a photomultiplier tube with a 1 nm resolution.

UV-Vis absorbance spectra of OM AuNP and BSA AuNP (*3.3*) were performed in standard cuvettes using a UV-Vis spectrophotometer DUº 730 Beckman Coulter with a 1 nm resolution from 190 to 1000 nm.

Imaging properties of the modified BSA modules of the BSA NP contrast agents. UV-Vis absorbance spectra of BSA NP with Alexa Fluor® 647 conjugated BSA in the coating were performed in standard cuvettes using a UV-Vis spectrophotometer DUº 730 Beckman Coulter with a 1 nm resolution from 190 to 1000 nm.

^{68}Ga ($t_{1/2}$= 68 min, β^+= 89% and EC = 11%) was available from a ^{68}Ge/^{68}Ga generator system (ITG Isotope Technologies Garching GmbH, Germany) in which ^{68}Ge ($T_{1/2}$= 270 d) was attached to a column based on organic matrix generator. The ^{68}Ga was eluted with 5 mL of 0.05 M hydrochloric acid. Then HEPES (0.048 g, 0.20 mmol) was dissolved with 1mL of the ^{68}Ga acidic eluate in a 2 mL Eppendorf. The pH was adjusted to 4.6-5 if necessary by minor addition of 2 M NaOH aqueous solution. Thereafter, 500 µl of an aqueous solution of a NP with DOTA conjugated BSA (*3.6*, *3.7, 3.8*) in the coating was added and the chelation was conducted at 37ºC during 30 min. For purification from the unlabeled ^{68}Ga, the reaction mixture was centrifuged using Amicon®Ultra-0.5 mL (Ultracel®-100K, Merck Millipore Ltd.). Total activity of the 0.5 mL BSA NP solution obtained was finally measured with ATOMLAB^{TM} 500 BIODEX activimeter.

200 µl of ^{89}Zr-oxalate (in 1 M oxalic) acid provided by Perkin Elmer was mixed with 90 µl of 2 M Na_2CO_3 in a 2 mL Eppendorf tube and the solution incubated for 3 minutes at room temperature. It was then introduced successively: 0.30 mL 0.5 M HEPES (pH = 7.2), 0.71 mL of DFO conjugated BSA IONP (*3.11*, **3.13**) and 0.70 mL 0.5 M HEPES (pH = 7.2) and the resultant mixture was incubated under gently shaking for 1 h at RT. Solution was purified by elution on a PD-10 column (GE Healthcare) with a 0.9% NaCl/gentisic acid 5 mg·mL^{-1} (pH = 4.9-5.3) buffer and unlabeled ^{89}Zr were finally discard using Amicon®Ultra-0.5 mL (Ultracel®-100K, Merck Millipore Ltd.) ultrafiltration to get the purified ^{89}Zr radiolabeled DFO conjugated BSA. Total activity of the 0.5 mL solution obtained of *3.11* and *3.13* were finally measured with ATOMLAB^{TM} 500 BIODEX activimeter.

Culture and Two-photon imaging of labeled HT1080 cells. HT1080 cells (CCL-121 from American Type Culture Collection number, ATCC, Rockville, MD) were cultured in Dulbecco's Modified Eagle's Medium (DMEM, Gibco Laboratories, Grand Island, NY, USA) supplemented with 10% FCS, 100 U/mL penicillin/streptomycin, and 2 mmol/L glutamine. These cells were transduced with a lentiviral vector expressing the JRed fluorescent protein (Evrogen Joint Stock Company, Moscow, Russia) at an MOI of 5 as previously described (Mol Ther. 2007 Aug;15(8):1487-94). After 7 days of transduction 6x10^5 HT1080–Red cells were plated in p35 glass plates (MatTek, Ashland, MA, USA).

The cells were incubated with 400ug/ml BSA UCNP diluted in culture medium during 24 hours. After incubation the cells were washed three times with PBS (Gibco) and fixed with PFA (paraformaldehyde) 4% during 30 minutes at room temperature; then washed again with PBS and maintained covered with PBA (PBS + 0.1% BSA + 0.02% NaN_3) at 4ºC until imaging was performed.

Fluorescence images were collected in raster scan mode using a 2-channels ALBA spectrophotometer (ISS iNC., Urbana-Champain, IL, USA) equipped with H7422 fast photomultipliers (Hamamatsu Photonics, K.K., Hamamatsi City, Japan). The ALBA module was coupled to an inverted Nikon Ti-E microscope (Nikon Corp., Tokyo, Japan), endowed with a Nikon, MRD07600, CFI 60x1.2 WI Plan Apochromatic objective, epifluorescence lamp, bright field and top stage incubator and heating chamber (Okolab, S.r.l., Napoli, Italy). Excitation at 980 nm was provided by a femtosecond-pulsed mode-locked tunable MaiTai DeepSee laser (Newport Corp., Irvine, CA, USA). After a blocking FF01-680/SP filter, emission was collected, using a blocking FF01-680/SP filter, in channel 1 after a BP460/60 filter and in channel 2 after a BP609/54 filter. Filters were from Semrock Inc., IDEX Corporation Lake Forest, IL, USA). The laser power at the objective was 10 mW. A series of 20-100 consecutive images of 256x256 pixels, collected at the rate of 64 us/pixels, were averaged.

Cytotoxicity effects of BSA coated IONP, UCNP, AuNP (*3.1*, *3.2* and *3.3*)

Cell lines and media. C57BL/6 mouse adult fibroblasts (MAFs) were grown in DMEM (Dulbecco's Modified Eagle Medium) supplemented with 1% penicillin-streptomycin and 1 mM sodium pyruvate in a humidified atmosphere of 5% CO_2 at 37ºC. Cytotoxicity and nanoparticle uptake were assessed in MAFs exposed at different concentrations (BSA IONP (*3.1*) 5, 20 and 40 µg·mL^{-1}; BSA UCNP (*3.2*) 5,10 and 50 µg·mL^{-1}; BSA AuNP (*3.3*) 5 and 20 µg·mL^{-1}) and times of incubation (24h, 48h and 72h). Control cells were treated with vehicle (water). After culturing for 24h, 48h and 72 h, the cells were trypsinised and cell proliferation was assessed using the Neubauer counting-chamber under optical microscope.

Cytotoxicity assays. In the presence of Ca^{2+}, Annexin V binds to phosphatidylserine residues exposed on the outer surface of the plasma membrane of apoptotic cells.

1x10^6 cells were collected in 500 µl PBS, washed before they were pelleted and resuspended in 195 µL binding buffer (10mM HEPES/NaOH, pH 7.4; 140 mM NaCl; 2.5 mM CaCl2). Then APC-Annexin V (BD PharmingenTM) was added (5 µl) and cells were incubated for 15 minutes at room temperature in the dark. Cell viability is determined using DNA binding dyes and DAPI was added until a final concentration of 0.001% (w/v). Cells were finally analysed by flow-cytometry using the BD FACSCanto™ II system. All experiments were performed in triplicate. As a result, viable cells are negative for both APC Annexin V and DAPI; early apoptotic cells are APC Annexin V positive and DAPI negative; and late apoptotic and dead cells are both APC Annexin V and DAPI positive. Cytotoxicity was estimated by comparison between the proportions of viable cells in populations exposed to the BSA NP with the ones in control cells.

Flow Cytometry Assay for determination of the BSA NP uptake by MAFs cells. Approximately 1x10^6 control and treated cells with ^{alexa647}BSA IONP, (**3.4**) (40 µg·mL^{-1}) were collected after 24 h of incubation. Cells were trypsinised and measured in PBS. Because of the fraction of Alexa Fluor® 647 conjugated BSA module in the **3.4** coating, APC channel was used for detection. A total of 10,000 events were recorded for each sample using the BD FACSCanto™ II system. Samples were analysed with the BD FACSDiva^{TM} Software and averages of the medians were determined. Histograms were realised using FlowJo Software. In addition to cell fluorescence, different cell populations in a flow cytometer can be distinguished by the forward-scattered light (FSC), side-scattered light (SCC) related respectively to cell size and cell internal complexity.

*Biodistribution in mice of $^{(alexa647)}$BSA IONP, (**3.4**)*

3.4 (100 µl, 0.5 mg·mL^{-1} [Fe]) were i.v. administrated in mice (N=2) that were sacrificed after 24 h. After perfusion, the main organs (brain, heart, lungs, liver, spleen, and kidney) were extracted and *ex vivo* fluorescence was performed with IVIS Imaging System 200 series (Xenogen®) (acquisition parameters: Cy5.5 ex/em filter, high level, BIN-HR, FOV 13.3, f2, 4s). Sections of tissues of the organs were then taken off and stained with Perls' Prussian blue to detect iron oxide cores. Briefly, slides were stained with 1% aqueous potassium ferrocyanide in 2% solution of HCl for 30 min and

counterstained with nuclear fast red. Microscopy was performed with a Nikon 90i for pictures in bright field with 10X and 40X objectives.

In vivo **targeted multimodal bioimaging of tumour in mice with the selected contrast agent (*3.13*)**

Procedure for RGD functionalisation was adapted from a previously described method[43]. The peptide cyclo [Arg-Gly-Asp-D-Phe-Lys(Ac-SCH2CO)], RGDpep was purchased from Peptide International. Basically, to a 1 mL solution of *3.11* ([Fe]= 1 mg·mL^{-1}) in PBS, 40µl of RGDpep (10 mg·mL^{-1} in an acetonitrile-water mixture 1:4) was added dropwise. After addition of 120 µl of a freshly prepared solution of 1 M hydroxylamine, the mixture was allowed to react 24h at room temperature. Remaining maleimide groups were quenched with cysteine (20 µl of a 5 mg·mL^{-1} solution) after which the mixture was reacted for an extra hour. Reaction mixture was first purified by steric exclusion chromatography on a PD-10 column (GE Healthcare) to discard the side products from the RGD activated BSA coated IONP (*3.13*). Remaining unreacted reagents were removed by ultrafiltration with Amicon®Ultra-0.5 mL (Ultracel®-100K, Merck Millipore Ltd.) and the probe finally redispersed in 0.5mL of PBS before *in vivo* experiments.

Tumour allografts. We have used a murine breast adenocarcinoma cell line (EO771) cultured in DMEM+ 10% Newborn calf serum (Gibco, Life Technologies).Female C57BL6 mice, 8 weeks old, were bred and housed under pathogen-free conditions in our animal facilities at CNIC. Prior to injection, tumour cells were trypsin detached, washed twice, and resuspended in PBS to a final concentration of 10^6 cells/13 µL. The cell suspension was then mixed with 5-µL growth factor–reduced Matrigel (BD Biocoat) and 2-µL trypan blue solution (Sigma Aldrich) and maintained on ice until injection. Mice were anesthetised with 5% Isofluorane (Abbott), laid on their backs, and injected with 20-µL cell suspension in Matrigel directly in the fourth mammary fad pad through the nipple with a Hamilton syringe. Tumour growth was monitored weekly using digital callipers, and tumour volume was calculated according to the formula: L × W2/2 = mm^3. Imaging studies were performed after 5 weeks after implant when tumours reached.

PET imaging. In vivo PET/CT Imaging in mice was performed with a nanoPET/CT small-animal imaging system (Mediso Medical Imaging Systems, Budapest, Hungary). List-mode PET data acquisition commenced 1 h, 24 h, 48 h and 72 h after bolus injection of 1 mCi of ^{89}Zr labeled **3.13** through the tail vein of CD45 8 weeks female mice and additional acquisitions were recorded each 24h for 3 days. Acquisition and reconstruction were performed with proprietary Nucline software (Mediso, Budapest, Hungary). At the end of PET, microCT was performed for attenuation correction and anatomic reference. The PET images in a 105x105 matrix (frame rates: 3 x 10 min, 1 x 30 min, 1 x 60 min) were reconstructed using a Tera-Tomo 3D iterative algorithm. Qualitative Image analysis in mice was performed using Osirix software (Pixmeo, Switzerland).

MRI acquisition. In vivo MRI in mice was performed with an Agilent/Varian scanner (Agilent, Santa Clara, USA) equipped with a DD2 console and an active-shielded 205/120 gradient insert coil with 130 mT/m maximum gradient strength and a combination of volume coil/two channel phased-array (Rapid Biomedical GmbH, Rimpar, Germany). CD45 eight weeks old female mice were anesthetised with 2% isoflurane (Abbott) and oxygen and positioned on a thermoregulated (38.7ºC) mouse bed and the respiratory cycle was monitored constantly. Ophthalmic gel was placed in their eyes to prevent retinal drying. Baseline images were acquired before i.v.a of **3.13** ([Fe]=1 mg per kg body weight). MR images of xenograft tumours were acquired at 24 h intervals from injection up to 3 days. For each animal, eight consecutive axial 1 mm thick slices were acquired to image the liver. Images were acquired in free-breathing animals, using a gradient echo sequence with 4 ms/40 ms echo/repetition times, BW of 100 kHz, FOV of 6 cm x 6 cm, for a total acquisition time of about 80 seconds; the flip angle (FA) was fixed at 20 degrees.

Histological analysis. After last images (72 hours post i.v.a), tumours were extracted and fixed in 4% paraformaldehyde before being embedded in paraffin blocks. Sections were deparaffinised and rehydrate before staining with Perls' Prussian blue to detect iron oxide cores.

5. Bibliography

(1) Laurent, S., Forge, D., Port, M., Roch, A., Robic, C., Vander Elst, L., and Muller, R. N. (2008) Magnetic Iron Oxide Nanoparticles: Synthesis, Stabilization, Vectorization, Physicochemical Characterizations, and Biological Applications. *Chem. Rev. 108*, 2064–2110.

(2) Ghosh Chaudhuri, R., and Paria, S. (2012) Core/Shell Nanoparticles: Classes, Properties, Synthesis Mechanisms, Characterization, and Applications. *Chem. Rev. 112*, 2373–2433.

(3) Erathodiyil, N., and Ying, J. Y. (2011) Functionalization of Inorganic Nanoparticles for Bioimaging Applications. *Acc. Chem. Res. 44*, 925–935.

(4) Chen, Z., Chen, H., Hu, H., Yu, M., Li, F., Zhang, Q., Zhou, Z., Yi, T., and Huang, C. (2008) Versatile Synthesis Strategy for Carboxylic Acid−functionalized Upconverting Nanophosphors as Biological Labels. *J. Am. Chem. Soc. 130*, 3023–3029.

(5) Herranz, F., Morales, M. P., Roca, A. G., Desco, M., and Ruiz-Cabello, J. (2008) A New Method for the Rapid Synthesis of Water Stable Superparamagnetic Nanoparticles. *Chem. - Eur. J. 14*, 9126–9130.

(6) Sperling, R. A., and Parak, W. J. (2010) Surface modification, functionalization and bioconjugation of colloidal inorganic nanoparticles. *Philos. Trans. R. Soc. Math. Phys. Eng. Sci. 368*, 1333–1383.

(7) Veiseh, O., Gunn, J. W., and Zhang, M. (2010) Design and fabrication of magnetic nanoparticles for targeted drug delivery and imaging. *Adv. Drug Deliv. Rev. 62*, 284–304.

(8) Liong, M., Lu, J., Kovochich, M., Xia, T., Ruehm, S. G., Nel, A. E., Tamanoi, F., and Zink, J. I. (2008) Multifunctional Inorganic Nanoparticles for Imaging, Targeting, and Drug Delivery. *ACS Nano 2*, 889–896.

(9) Niemeyer, C. M. (2001) Nanoparticles, Proteins, and Nucleic Acids: Biotechnology Meets Materials Science. *Angew. Chem. Int. Ed. 40*, 4128–4158.

(10) Groult, H., Ruiz-Cabello, J., Lechuga-Vieco, A. V., Mateo, J., Benito, M., Bilbao, I., Martínez-Alcázar, M. P., Lopez, J. A., Vázquez, J., and Herranz, F. F. (2014) Phosphatidylcholine-Coated Iron Oxide Nanomicelles for In Vivo Prolonged Circulation Time with an Antibiofouling Protein Corona. *Chem. Weinh. Bergstr. Ger. in press*.

(11) Longmire, M., Choyke, P. L., and Kobayashi, H. (2008) Clearance properties of nano-sized particles and molecules as imaging agents: considerations and caveats. *Nanomed. 3*, 703–717.

(12) Thanh, N. T. K., and Green, L. A. W. (2010) Functionalisation of nanoparticles for biomedical applications. *Nano Today 5*, 213–230.

(13) Kratz, F. (2008) Albumin as a drug carrier: Design of prodrugs, drug conjugates and nanoparticles. *J. Controlled Release 132*, 171–183.

(14) Peters, T. (1996) All about albumin: biochemistry, genetics, and medical applications. Academic Press, San Diego.

(15) Peng, Z. G., Hidajat, K., and Uddin, M. S. (2004) Adsorption of bovine serum albumin on nanosized magnetic particles. *J. Colloid Interface Sci. 271*, 277–283.

(16) Lynch, I., and Dawson, K. A. (2008) Protein-nanoparticle interactions. *Nano Today 3*, 40–47.

(17) Caravan, P., Cloutier, N. J., Greenfield, M. T., McDermid, S. A., Dunham, S. U., Bulte, J. W. M., Amedio, J. C., Looby, R. J., Supkowski, R. M., Horrocks, W. D., McMurry, T. J., and Lauffer, R. B. (2002) The interaction of MS-325 with human serum albumin and its effect on proton relaxation rates. *J. Am. Chem. Soc. 124*, 3152–3162.

(18) Schäffler, M., Sousa, F., Wenk, A., Sitia, L., Hirn, S., Schleh, C., Haberl, N., Violatto, M., Canovi, M., Andreozzi, P., Salmona, M., Bigini, P., Kreyling, W. G., and Krol, S. (2014) Blood protein coating of gold nanoparticles as potential tool for organ targeting. *Biomaterials 35*, 3455–3466.

(19) Gessner, A., Olbrich, C., Schröder, W., Kayser, O., and Müller, R. H. (2001) The role of plasma proteins in brain targeting: species dependent protein adsorption patterns on brain-specific lipid drug conjugate (LDC) nanoparticles. *Int. J. Pharm. 214*, 87–91.

(20) Mikhaylova, M., Kim, D. K., Berry, C. C., Zagorodni, A., Toprak, M., Curtis, A. S. G., and Muhammed, M. (2004) BSA Immobilization on Amine-Functionalized Superparamagnetic Iron Oxide Nanoparticles. *Chem. Mater. 16*, 2344–2354.

(21) Xie, J., Chen, K., Huang, J., Lee, S., Wang, J., Gao, J., Li, X., and Chen, X. (2010) PET/NIRF/MRI triple functional iron oxide nanoparticles. *Biomaterials 31*, 3016–3022.

(22) Wilhelm, C., Billotey, C., Roger, J., Pons, J. N., Bacri, J.-C., and Gazeau, F. (2003) Intracellular uptake of anionic superparamagnetic nanoparticles as a function of their surface coating. *Biomaterials 24*, 1001–1011.

(23) Sanvicens, N., and Marco, M. P. (2008) Multifunctional nanoparticles – properties and prospects for their use in human medicine. *Trends Biotechnol. 26*, 425–433.

(24) Cheng, Z., Al Zaki, A., Hui, J. Z., Muzykantov, V. R., and Tsourkas, A. (2012) Multifunctional Nanoparticles: Cost Versus Benefit of Adding Targeting and Imaging Capabilities. *Science 338*, 903–910.

(25) Hao, R., Xing, R., Xu, Z., Hou, Y., Gao, S., and Sun, S. (2010) Synthesis, Functionalization, and Biomedical Applications of Multifunctional Magnetic Nanoparticles. *Adv. Mater. 22*, 2729–2742.

(26) Choi, J., Park, J. C., Nah, H., Woo, S., Oh, J., Kim, K. M., Cheon, G. J., Chang, Y., Yoo, J., and Cheon, J. (2008) A Hybrid Nanoparticle Probe for Dual-Modality Positron Emission Tomography and Magnetic Resonance Imaging. *Angew. Chem. Int. Ed. 47*, 6259–6262.

(27) Ryu, J., Park, H.-Y., Kim, K., Kim, H., Yoo, J. H., Kang, M., Im, K., Grailhe, R., and Song, R. (2010) Facile Synthesis of Ultrasmall and Hexagonal NaGdF4: Yb3+, Er3+ Nanoparticles with Magnetic and Upconversion Imaging Properties. *J. Phys. Chem. C 114*, 21077–21082.

(28) Li, Z., and Zhang, Y. (2008) An efficient and user-friendly method for the synthesis of hexagonal-phase NaYF4:Yb, Er/Tm nanocrystals with controllable shape and upconversion fluorescence. *Nanotechnology 19*, 345606.

(29) Qian, H.-S., and Zhang, Y. (2008) Synthesis of Hexagonal-Phase Core−Shell NaYF4Nanocrystals with Tunable Upconversion Fluorescence. *Langmuir 24*, 12123–12125.

(30) Tian, Q., Liu, N., Qin, G., Zheng, K., Zhang, D., and Qin, W. (2011) Synthesis and Upconversion Luminescence of Uniform βNaYF4:Yb3+/Tm3+ Hexagonal Nanoplates. *J. Nanosci. Nanotechnol. 11*, 9576–9579.

(31) Wang, F., Wang, J., and Liu, X. (2010) Direct Evidence of a Surface Quenching Effect on Size-Dependent Luminescence of Upconversion Nanoparticles. *Angew. Chem. 122*, 7618–7622.

157

(32) Daniel, M.-C., and Astruc, D. (2004) Gold Nanoparticles: Assembly, Supramolecular Chemistry, Quantum-Size-Related Properties, and Applications toward Biology, Catalysis, and Nanotechnology. *Chem. Rev. 104*, 293–346.

(33) Liu, Y., and Welch, M. J. (2012) Nanoparticles Labeled with Positron Emitting Nuclides: Advantages, Methods, and Applications. *Bioconjug. Chem. 23*, 671–682.

(34) Breeman, W. A. P., de Blois, E., Sze Chan, H., Konijnenberg, M., Kwekkeboom, D. J., and Krenning, E. P. (2011) 68Ga-labeled DOTA-Peptides and 68Ga-labeled Radiopharmaceuticals for Positron Emission Tomography: Current Status of Research, Clinical Applications, and Future Perspectives. *Semin. Nucl. Med. 41*, 314–321.

(35) Zhang, Y., Hong, H., and Cai, W. (2011) PET tracers based on Zirconium-89. *Curr. Radiopharm. 4*, 131–139.

(36) Sapsford, K. E., Algar, W. R., Berti, L., Gemmill, K. B., Casey, B. J., Oh, E., Stewart, M. H., and Medintz, I. L. (2013) Functionalizing Nanoparticles with Biological Molecules: Developing Chemistries that Facilitate Nanotechnology. *Chem. Rev. 113*, 1904–2074.

(37) Zucker, R. M., Daniel, K. M., Massaro, E. J., Karafas, S. J., Degn, L. L., and Boyes, W. K. (2013) Detection of silver nanoparticles in cells by flow cytometry using light scatter and far-red fluorescence. *Cytom. Part J. Int. Soc. Anal. Cytol.*

(38) Fadeel, B., and Garcia-Bennett, A. E. (2010) Better safe than sorry: Understanding the toxicological properties of inorganic nanoparticles manufactured for biomedical applications. *Adv. Drug Deliv. Rev. 62*, 362–374.

(39) Cho, E. C., Glaus, C., Chen, J., Welch, M. J., and Xia, Y. (2010) Inorganic nanoparticle-based contrast agents for molecular imaging. *Trends Mol. Med. 16*, 561–573.

(40) Gaertner, F. C., Kessler, H., Wester, H.-J., Schwaiger, M., and Beer, A. J. (2012) Radiolabelled RGD peptides for imaging and therapy. *Eur. J. Nucl. Med. Mol. Imaging 39*, 126–138.

(41) Liu, Z., and Peng, R. (2010) Inorganic nanomaterials for tumor angiogenesis imaging. *Eur. J. Nucl. Med. Mol. Imaging 37 Suppl 1*, S147–63.

(42) Kok, R. J., Schraa, A. J., Bos, E. J., Moorlag, H. E., Ásgeirsdóttir, S. A., Everts, M., Meijer, D. K. F., and Molema, G. (2002) Preparation and Functional Evaluation of RGD-Modified Proteins as $\alpha_v \beta_3$ Integrin Directed Therapeutics. *Bioconjug. Chem. 13*, 128–135.

Chapter 4

Antitumoural glycosides-coated iron oxide micelles

European patent, application number E9544WW00

Abstract

Glycosides comprising hydrophilic sugar moiety conjugated to oleyl hydrophobic chains have promising antimitotic activity on cancer cell cultures but limited *in vivo* perspectives because of their low solubility in physiological media and rapid enzymatic degradation. Thermal degradation method yields high quality oleic acid coated iron oxide nanoparticles (OA IONP) with exceptional physicochemical properties of the core but dispersible only in organic solvents. We report here the synthesis of micelles formed by the OA IONP encapsulated within a hydrophilic layer of the amphiphilic glycosides. These nanomicelles were fully characterised especially their suitability as *in vivo* MRI contrast agents and for its *in vitro* antimitotic activity on cell cultures from rat glioma and from human lung carcinoma and compared with the activity of the corresponding free glycosides. The results show that the formulation of glycosides in the form of OA IONP encapsulated micelles have preserved antitumoural effects and in one case provides a significant therapeutic gain. Moreover, the micelles present excellent relaxometric properties for their use as contrast agent based T2 MRI. Ours findings suggest that synergetic bioactive hydrophilic nanostructures can be obtained to generate theranostic agents, from two entities previously not suitable for *in vivo* applications and strengthen the possibility to use biomolecules at the same time as coating for OA IONP micellar stabilisation and as drugs for therapy.

1. Introduction

The most important application of nanotechnology in biomedicine is mainly confined to the field of oncology.[1] Indeed, the singular structural properties of NP enable the design of easy tailoring drug delivery platform which answer the main challenges of chemotherapeutically-based cancer treatments, especially adding the specificity of a drug against tumour and not perturbing healthy cells and tissues.[2,3] Nanotechnology provides targeting possibilities either by passive accumulation of the NP inside tumours as a result of the enhanced permeability and retention effect (EPR) (Figure 4.1) or actively by ligand attachment to the NP.[4–6] This leads in many occasions to an improved pharmacokinetic, a local delivery in optimal dose ranges, the ability to overcome biological barriers as well as a reduced toxicity or minimum side effects by controlled release of the toxic drug.[7,8] In the large family of nanomaterials, drug delivery using superparamagnetic iron oxide nanoparticles (IONP) is particularly interesting for the opportunity to target drugs to the pathological area by the application of a magnetic field, which can be externally applied, internally implanted or even spatially directed.[9,10] Furthermore, IONP are at the same time very good contrast agents for MRI, giving theranostic capabilities to the agent.[11,12] Several studies of magnetic drug targeting in small animal models and clinical trials have already reported successful partial remission of the tumour.[13,14]
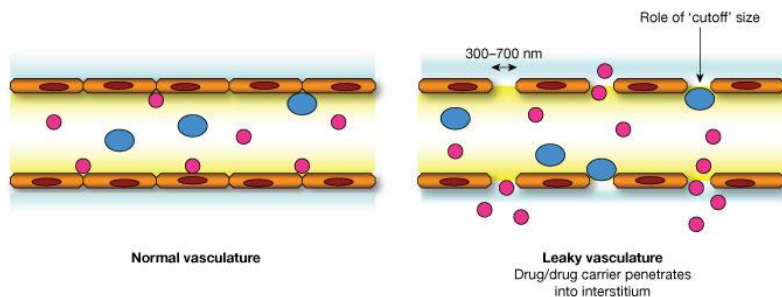
Figure 4.1. Scheme of the EPR effect.

A family of synthetic glycosides has been recently proposed as inhibitors of glioma and adenocarcinoma cell proliferation.[15] The molecules are derivatives of N-acyl-glucosamine and previous results indicate that the activity is increased if a long hydrocarbon chain is present at position C-1 of the glycoside scaffold. Other groups have shown that the conjugation of a sugar with an oleyl chain is beneficial for the antitumoural action.[16] The proposed mechanism of growth inhibition suggest an alteration in the lipid metabolism; important changes of levels of glycosphingolipid and ganglioside[17,18], two intermediates which have regulatory roles in tumour progression and are involved in pathways of cell death and proliferation.[19–21] However, *in vivo* preliminary experiments with the best candidates offered modest results.[22] Because of their long alkyl chain, the compounds show low or no solubility in aqueous physiological medium and were also subjected to enzymatic degradation with reduced biological stability.[23] Consequently, it was only possible to use intratumoural administration of drug dispersed in a DMSO/H_2O mixture with BSA as carrier and only a single enzymatic resistant

165

thioglycoside derivative led to significant tumour growth inhibition at high repetitive doses.[22,24] Regarding all these considerations, IONP based drug delivery system appears promising for stabilisation and targeting of the bioactive glycosides to the tumour site for improved activity or therapy. In this case the IONP, contrary to the other chapters, are used as a drug-delivery platform and the study of their imaging properties will be limited.

In the different approaches of IONP drug delivery system described before, the therapeutic agents were covalently attached or electrostatically adsorbed onto the IONP coating/surface, dispersed into a polymer matrix, or encapsulated in amphiphilic nanostructures.[5,25] All these approaches require a pre-existing hydrophilic coating with functional groups on the IONP platform. For this, the coprecipitation method which yields aqueous IONP is still preferred in the bibliography for its easiness and possibilities of further surface tailoring although the NP are of low quality (see the Introduction, Section 2.3). Moreover, additional steps are then required for the integration of the drugs.[26] Thermal degradation method is known to provide the best solution in terms of physicochemical properties (size, size dispersion, crystallinity, reproducibility) of the IONP but as we have already shown, thermal decomposition yields IONP only stable in organic solvent and thus requires an additional step for aqueous stabilisation of the NP before any integration of drugs.[27] A general solution along this thesis is the stabilisation within a micelle, formed with amphiphilic polymers or molecules and the hydrophobic surfactant of the NP.[28] In this chapter, we address the possibility of directly stabilising OA IONP prepared by thermal degradation through micellisation with the bioactive glycosides, similarly to what we have done previously with PC.[29] This unusual configuration where the therapeutic agent also acts as the micellar coating requires strong verification on the viability of the drug delivery system. First, one must test if the bioactive coatings satisfy the requirements of hydrophilic

166

matrix for *in vivo* use of the probes (improved colloidal stability to the NP, enhanced protection from opsonisation and biocompatibility, suitable relaxometric properties). Then it is crucial to check if the antitumoural activity is preserved in such micellar formulation of the therapeutic compounds.

2. Results

2.1 Synthesis of the glycoside IONP micelles

Oleic acid coated Fe_3O_4 nanoparticles (OA IONP) were prepared by thermal degradation of iron organic precursors at high temperature blended with the OA surfactant.
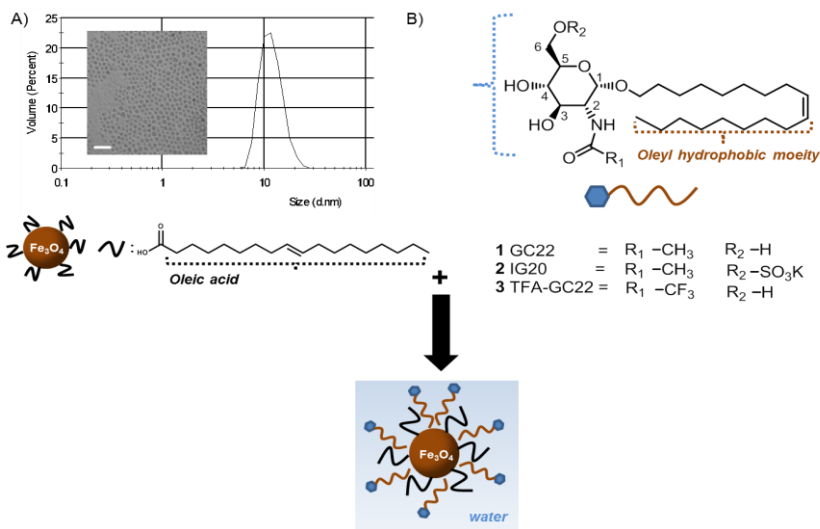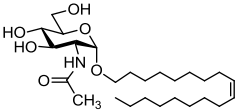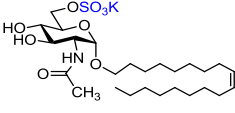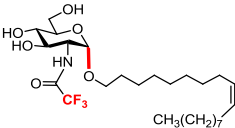

Figure 4.2. Scheme of the synthesis of the glycosides coated IONP micelles.

Characterisation and protocol are detailed respectively in Chapter 1, Section 2.1 and chapter General Materials and Methods. As we showed OA IONP colloidal solution was stable and monodispersed with a polydispersity index of 0.25 for a mean hydrodynamic size of 10 ± 3 nm in hexane. Iron oxide cores were spherical with a diameter of 7 ± 2 nm determined by TEM (Figure 4.2a).Fernández-Mayoralas et al. described a family of synthetic glycoside derivatives as inhibitors of glioma and adenocarcinoma growth, of which we selected three compounds for the preparation of OA IONP encapsulated antitumoural micelles (Figure 4.2b). Main characteristic of GC22 (*4.1*), IG20 (*4.2*), TFA-GC22 (*4.3*) and their antimitotic activities against C6 (glioma rats) and A549 (adenocarcinoma lung human) are described in Table 4.1.[15] The corresponding OA IONP encapsulated micelles are named (*4.4*), (*4.5*) and (*4.6*) for respectively GC22 coated IONP micelles, IG20 coated IONP micelles and TFA-GC22 coated IONP micelles. In all cases, the compounds *4.1, 4.2* and *4.3* have an oleyl chain moeity in α anomeric configuration at position C-1 of the glucosamine scaffold, described as optimal for improved antitumoural bioactivity (Figure 4.2b and Table 4.1).[22] GC22 *4.1* -taken as reference-*,* presented an ID 50 below the micromolar range for the two cell lines. Influence of a different amide group (R1) at position C-2 (trifluoroacetamide, *4.3*) and the change induced by attachment of a negative hydrophilic oxosulfonyl group at position C-6 (R2), *4.2* were studied. If trifluoroacetamide group did not seem to strongly affect the antimitotic activity, the presence of the oxosulfonyl has a deleterious effect on the bioactivity, ID 50 ten times higher, >100 μM.

Table 4.1. Main characteristic and antimitotic activities of the glycosides used for the preparation of the glycoside coated IONP micelles.

Name of the compound	Formula M.W. (g.mol^{-1})	Solubility	ID 50 (activity)	
			A549	C6
GC22, (**4.1**)	$C_{26}H_{49}NO_6$ 471.67	MeOH, EtOH, isopropanol, DMSO dioxane, H_2O mixture	10	15.5±0.3
IG-20, (**4.2**)	$C_{26}H_{48}KNO_9S$ 589.82	Low H_2O solubility	97	>100
TFA-GC22, (**4.3**)	$C_{26}H_{46}F_3NO_6$ 525.3	MeOH, EtOH, isopropanol, DMSO dioxane, H_2O mixture	8.6	14.2±0.3

Deeper information about the effects of the substituted groups on the glucosamine backbone on the inhibition of cancerous cell lines can be found in a previously published report.[15] Chemistry for the preparations of such derivatives is well-known in the field and synthetic procedures can be obtained in ours and others' publications.[15,30,31] In brief, **4.1** was obtained from a stereoselective glycosylation of oleyl alcohol on α-D-glucosaminyl chloride peracetate **4.7** using acid promotor $SnCl_4$ followed by a deacetylation step. From **4.1**, protection of C-3 and C-4 positions with butane-2,3-dione led to an acetal intermediate **4.8** which yielded **4.2** after sulfation and acid deprotection hydrolysis. For synthesis of **4.3**, the 2-amino-2-deoxy-D-glucose precursor **4.4** was used and subjected to *N*-(trifluoroacetyl)ation next oleyl glycosylation via H_2SO_4-silica catalysation (Figure 4.3).
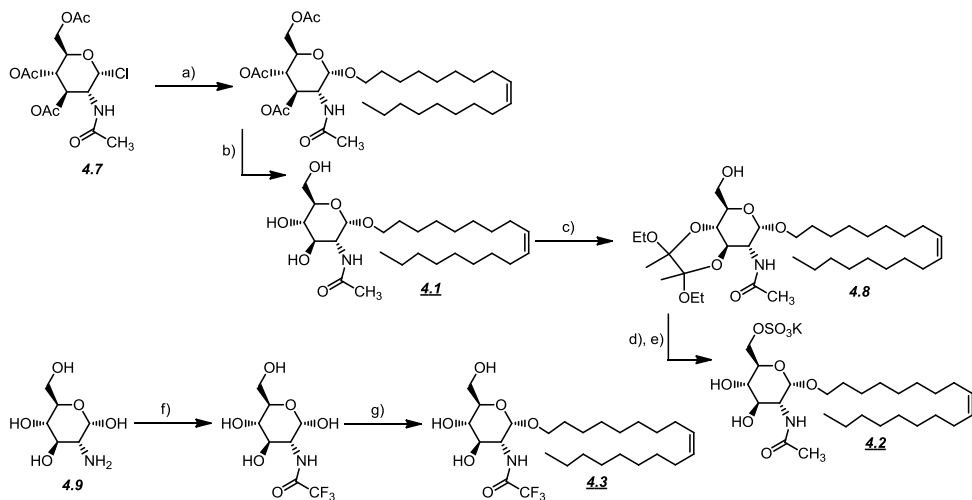
Figure 4.3. Synthesis of the glycosides GC22 (*4.1*), IG20 (*4.2*), TFA-GC22 (*4.3*).

The hydrophobic OA IONP were then encapsulated by means of a nanoemulsion method, similar to the one used for PC and BSA NP, within micelles made of the oleyl glycosides to get *4.4*, *4.5* and *4.6* micelles. Basically in the process the oleyl moeity of the glycoside intercalate with the OA aliphatic chain of the magnetite NP through hydrophobic van der Waals interactions while the hydrophilic sugar part lines up around the outer surface providing the water stability as shown in scheme of Figure 4.2.[29] The nanostructure was defined as codependent because just like the OA IONP, the glycosides -except *4.2*- are not soluble in water and only the pairing of both led to final hydrophilic micelles. In this sense OA IONP act in the same time as additional probe and as promoter of micelle formation since free glycosides did not form spontaneous micelles.

2.2 Physicochemical characterisation of the glycoside IONP micelles

Hydrodynamic sizes of the micelles were in the range of ~50 nm (Table 4.2) with pdi below 0.25, the standard to consider a mono-dispersed population. TEM pictures confirmed that the NP were well dispersed with no aggregation (Figure 4.4a). However micelles hydrodynamic size´s increase indicates probably the encapsulation of few OA IONP within a same micelle or a slight aggregation in solution of different micelles. Absolute values of zeta potential are in all cases upper than 25 mV at physiological pH (Table 4.2), a key indicator of the good stability of the micellar colloidal dispersions by electrostatic repulsion. Micelle **4.4** shows a ζ potential around -25mV attributable to the glucosamine layer. Thus, **4.5** had a higher negative ζ potential (- 50 mV) because of the additional presence of the negatively charged oxosulfonyl group on the glucosamine scaffold. Surprisingly **4.6** had a positive ζ which maybe explain by the de-acetylation and formation of a positive amine group at position C2. FTIR, and MS of **3.6** are presented in Figure 4.4b and 4.4c as additional data for the characterisation of the micelle coatings. FTIR of the micelles confirmed the presence of the sugar in the outer layer with characteristic vibrations of the oleyl glucosamide observed at 620 cm^{-1}, 2920 cm^{-1} and 1700 cm^{-1}, in addition to the peaks characteristic of OA IONP (detailed in Chapter 1, Section 2.1). Formation of the amine derivative of **4.3** in the coating of the **4.6** micelle was also confirmed. IR spectra showed a strong absorption band at 3400 cm^{-1} corresponding to primary amine vibration (v C-NH$_2$) and adduct in the MS spectra corresponding to the MW of the glucoasime de-acetylated.

171
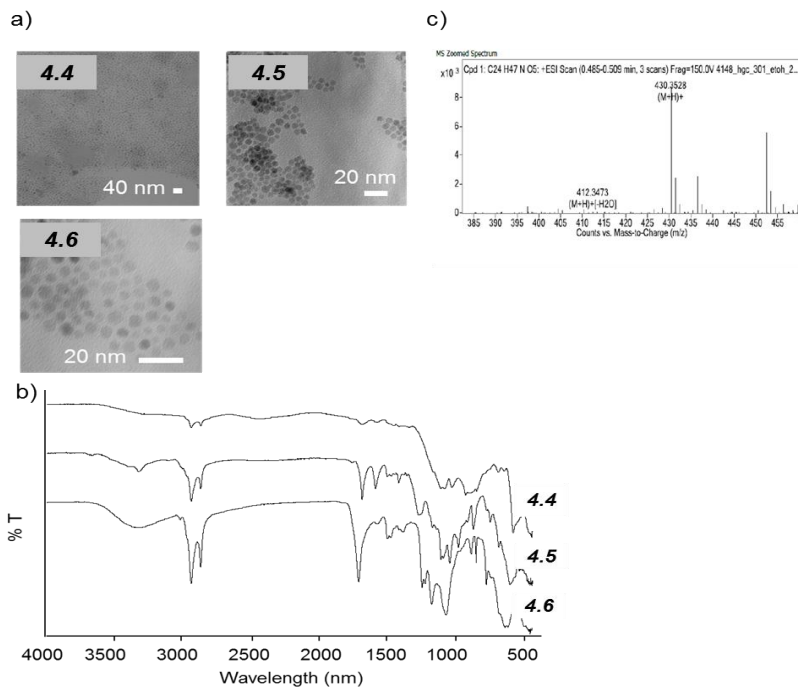
Figure 4.4. a) TEM pictures and b) FTIR of the glycosides coated IONP micelles c) MS of the *4.6* IONP micelle.

Magnetic properties of *4.4*, *4.5* and *4.6* IONP micelles are important features for their applications as magnetic drug targeting platforms and MRI contrast agents. NMR relaxometric properties were investigated and the longitudinal (r_1) and transverse (r_2) relaxivities were calculated in water suspensions. They were nearly similar for each micelle with high r_2 (from 180 to 220 $s^{-1}mM^{-1}$) and small r_1 (below 5 $s^{-1}mM^{-1}$); a ratio particularly appropriate for T_2-weighted MRI based contrast agent (Table 4.2).[32]

Table 4.2. Main characteristic of the glycoside coated IONP micelles.

Glycoside IONP micelles	Size (nm)	pdi	Zeta potential (mV)	[Fe] (mg/ml)	C^0 [glyco] (mg/ml)	Relaxometric values ($s^{-1}.mM^{-1}$)
4.4	40.5	0.24	-27	0.6	≈ 2.5	r_1 2.7/r_2 140
4.5	52.2	0.15	-42	1.1	3.1	r_1 4.4/r_2 195
4.6	49.1	0.17	+53	0.3	≈ 2.5	r_1 3.6/r_2 137

In vivo behaviour of the IONP micelles. When NP are used as drug delivery system, it is important to study its *in vivo* biological fate. Indeed the physicochemical properties of the NP (charge, curvature, composition, size) regulate their interactions with biological systems and determine their systemic circulation, clearance, interaction with cells, internalisation or subcellular localisation.[33] Especially in cancer therapy, long vascular circulation times favour passive tumour targeting of the probes *via* the EPR.[3] So we wanted to check if the glycosidic surface modification of the micelles promotes protection from opsonisation therefore increasing their vascular circulation times after *in vivo* injection. We measured the clearance rate of *4.4* in rat liver, from the loss of the MRI signal in this organ. The negative signal enhancement in the liver was measured at different times after i.v.a. by averaging signal intensities from a selected region of interest (ROI) and normalising to the basal image (Figure 4.5). We observed a signal decrease reaching a minimum 20 minutes after injection. This value is in the average range of the lifetimes reported in literature of similar size.[34] Indeed, coatings for NP made of glycoside or in general, sugars are described in literature as favourable for long circulation time in blood.[34–36]
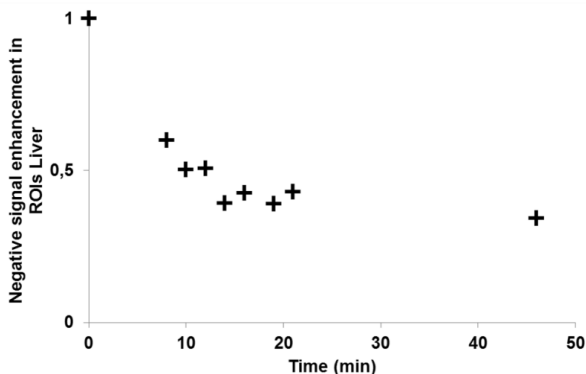
Figure 4.5. Negative signal enhancement for a set of ROI in rat liver after i.v.a. of **4.4** ([Fe]=1mg.ml^{-1}; 100 ul).

2.3 *In vitro* inhibition activities of the glycosides coated IONP micelles

We assessed if the glycosides under the IONP encapsulated micellar formulation have preserved their antimitotic activity in rat glioma (C6) and human lung carcinoma (A549 cell cultures). **4.4**, **4.5** and **4.6** were designed for a final amount of bioactive coating molecules from 2.5 to 5 mg.ml^{-1}. To know the exact concentration of the glycosides in the colloidal dispersion, micelles were lyophilised and partitioned in a water/ethanol mixture under sonication. After centrifugation, the supernatant containing the free glycoside was quantified by HPLC.

The cells were treated with dilutions of the micelle solution and cell growth was measured at 48 hours by MTT assays. Control NP were also used in the experiment. Inhibitory activities of the micelles on rat glioma and lung carcinoma cells with respect to the molar concentration of the glycosides are shown respectively in Figure 4.6 and 4.7. For lung carcinoma cells, biological

174

activity is also determined in the presence of a magnetic field in the bottom of each well of the plate. The results of the 50% inhibitory dose values (ID50) compared with the ID50 of the free glycosides are summarised in Table 4.3.
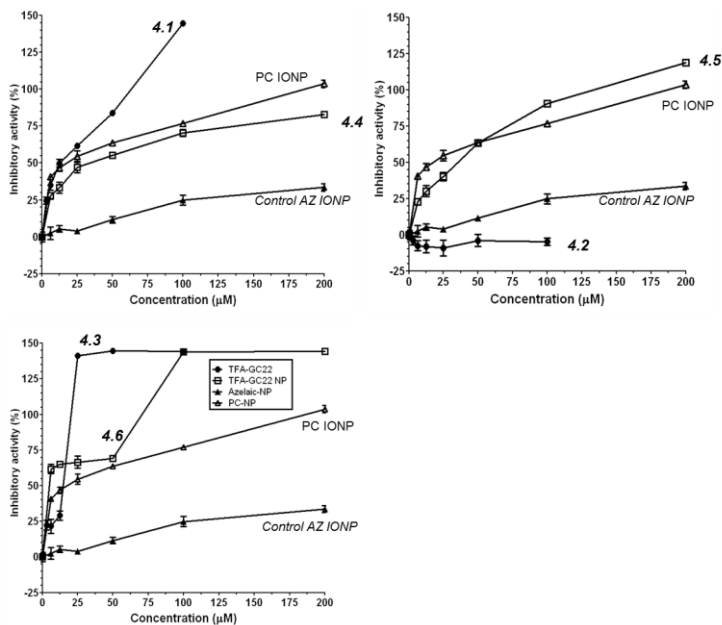
F

Figure 4.6. Inhibitory activities of the free glycosides (*4.1*, *4.2* and *4.3*) and the glycosides coated IONP micelles (*4.4*, *4.5* and *4.6*) with respect to their molar concentration against rat glioma cells (C6) after 48 hours incubation.

As it can be seen, all *4.4*, *4.5* and *4.6* inhibit proliferation of the both cancer cell lines with ID50 in the micromolar range. In general, the 50% inhibitory drug concentrations were in the same range but consistently lower in all micellar preparations that the correspondent free glycoside used in the formulation; with exception for *4.5*, which had higher inhibitory activity as free molecule. In all the cases, these antitumoural effects were higher for the C6

cell line than the lung carcinoma both for the micellar formulations and free glycosides.
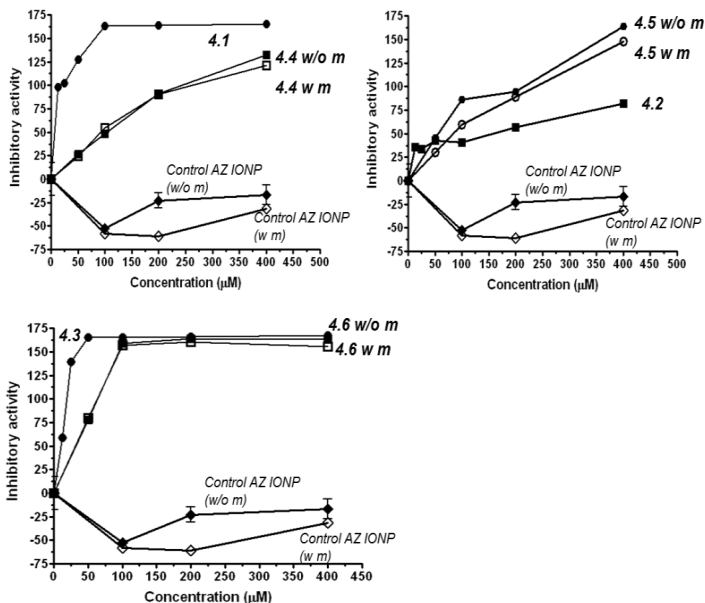
Figure 4.7. Inhibitory activities of the free glycosides (*4.1*, *4.2* and *4.3*) and the glycosides coated IONP micelles (*4.4*, *4.5* and *4.6*) with respect to their molar concentration against lung carcinoma cells (A549) after 48 hours incubation. w/o : without magnet ; w m: with magnet.

The greatest antimitotic activity was obtained for *4.6* on rat glioma cells. It can also be seen that when the biological activity against lung carcinoma cells (A549) is determined in the presence of magnetic field, the results are worse. This maybe because the magnet attracts straight away the NP in the centre of the plate thus they cannot disperse in all the plate where there is the cell culture.

Table 4.3. Comparison of the ID 50 of the free glycosides (*4.1*, *4.2* and *4.3*) and the glycosides coated IONP micelles (*4.4*, *4.5* and *4.6*). w/o : without magnet ; w m: with magnet.

Compound	ID_{50} (µM) C6	ID_{50} (µM) A549
4.1	15.5±0.3	10
4.2	>100	97
4.3	14.2±0.3	8.6
4.4	55 w/o m	100.5 w/o m
		95 w m
4.5	68.5 w/o m	64.4 w/o m
		91 w m
4.6	24.4 w/o m	40.3 w/o m
		42 w m

3. Discussion

We have synthesised a range of theranostic micelles formed of OA IONP stabilised in water by a coating made of different antitumoural oleyl glycosides. OA IONP were first prepared by thermal degradation of organic iron precursors at high temperature resulting in iron oxide cores of higher quality than the ones yielded by hydrolytic routes for optimum use as contrast agent and magnetically driven carrier as suggested by previous studies.[9,37] Three oleyl derivative glycosides previously reported as antitumoural were then used[15] to create amphiphilic structures where in all the cases the oleic acid surfactant of the NP and oleyl moiety of the sugars formed a van der walls hydrophobic interaction pair while the hydrophilic part of the glycoside stands around the outer layer for aqueous stabilisation. We get this micellar-like structure by spontaneous arrangement of the two entities under a nanoemulsion method.[29] This approach is now currently used for preparation

of other NP based amphiphilic assemblies as it simplified and accelerates the synthesis and provides reproducible and highly homogeneous dispersion especially if compared to the other prevalent reverse evaporation method known in the field.[28]

Our approach is different to normal controlled drug delivery system nanoparticle-based drug delivery system (e.g. liposomes/polymeric NP), in which the drug is usually incorporated by encapsulation (drug carrier vehicle) or by ionic/covalent conjugations onto a prior hydrophilic NP coating.[25] This enables diffusion and releasing of the drug by diffusion or enzymatic cleavage once the NP has reached to the site of therapeutic interest. Additional surface conjugations of peptides, proteins or antibodies lead to active targeting multifunctional carrier for an even more efficient delivery.[11] The originality of our probes lies in the fact that the stabilising biocompatible coating of the NP is by itself the active component of the drug and therefore should fulfil the requirements of the second role in the preparation whilst maintaining the therapeutic efficiency. For this reason, we first verified that the antitumoural activity was fully preserved upon the micelle formation. The presence of the oleyl conjugate on the glycosides was described as the main positive factor for cancerous cell growth inhibition but in the OA IONP encapsulated glycoside micelles; while the aliphatic chain is hindered inside the amphiphilic nanoassembly. Interestingly, although this should proceed against our purpose, bioactivity was maintained and in one case (*4.5*) was higher than the one of the free molecule coating component. We assume that under this micellar form, a better hydrophilicity is assured for the bioactive glycoside until cell uptake in a rich hydrophobic environment and a partial dissociation and oleyl-glycoside release of the assembly contents occurred. Besides, the free oleyl glycosides were previously used *in vivo* associated to the BSA protein, a

fatty acid transporter which plays a similar role than the micelle´s one described above.[22]

One of the main challenges of chemotherapy against cancer is that it usually affects both tumours and healthy tissues. New strategies of targeting comprised the drug delivery platforms (either biological such as targeting organic ligand or physical such as magnetic guided NP) begin to bring different alternative, although the optimal solution is still getting specific activity of the drugs only against cancerous cells looking after the small differences in the tumoural cell biological pathway.[38] Here, it will be a synthetic challenge to conjugate a targeting organic ligand on the micelle assemblies based drug delivery platform. However, in our case, oleyl glycoside acts on the activated lipid synthesis pathway of the tumoural cells, which need cell membrane materials to sustain the uncontrolled malign cell proliferation.[17] This first property combined to the ones of IONP based drug delivery platform like the possible EPR effect which enhances the accumulation of NP in tumours, or magnetic guided delivery, can be a strong point for an *in vivo* chemotherapy with high specificity to the cancerous cells. On this purpose, EPR effects shall be facilitated by the size of the micelles which range around 50 nm and are particularly adapted for an easy accumulation/diffusion through the leaky vessels[39] and also by the vascular circulation time after i.v.a determined in the same order or up to the reported standards for IONP of similar hydrodynamic size.[40] This contributes to increase the chance of higher accumulation and to get bioactive local dose at optimal dose range of the glycosides.

4. Conclusion

We have presented a theranostic micellar agent with anti-tumoural active glycosides acting as hydrophilic moiety to stabilize IONP at physiological conditions. We observed in all the cases that the use of this drug delivery formulation maintain or increase the therapeutic efficacy. Gathering all the information, glycosides coated IONP micelles has a slight adverse influence on the inhibitory activity but maintain antitumoural properties and get higher aqueous solubility and *in vivo* stability. These results are promising for future assessment *in vivo* of these theranostic micellar agents.

5. Materials and Methods

Materials and general synthetic methods

All chemicals were of reagent grade or higher and were purchased from commercial suppliers or purified by standard techniques. Thin-layer chromatography (TLC) was performed on aluminum sheets 60 F254 Merck silica gel, and compounds were visualised by irradiation with UV light and/or by treatment with a solution of Ce2MoO4 or 5% H2SO4 in EtOH, followed by heating. Flash column chromatography was performed using thickwalled columns, employing silica gel (Merck 60: 0.0400.063 mm). The eluent used is indicated, and solvent ratios refer to volume. Melting points are not corrected and were measured with a Reicher Jung Thermovar micromelting apparatus. Optical rotations were recorded on a Perkin-Elmer 241 Polarimeter (λ = 589 nm, 1 dm cell). ^{1}H NMR spectra were registered at 400 or 300 MHz, and 13C NMR spectra were obtained at 100 MHz on a Varian INOVA spectrometers, using $CDCl_3$, CD_3OD, or D_2O as the solvent at room temperature. Chemical shift values are reported in parts per million (δ). Coupling constant values (J) are reported in hertz (Hz), and spin multiplicities are indicated by the following symbols: s (singlet), d (doublet), t (triplet), q (quartet), and(multiplet). High-resolution mass spectra (HRMS) were recorded on an Agilent 6520 Accurate Mass Q-TOF spectrometer with an ESI source.

Synthesis

Synthesis of OA IONP

Protocol described in Chapter "General Materials and Methods"

*Synthesis of Oleyl 2-Acetamido-2-deoxy-β-D-glucopyraroside, GC-22 (**4.1**).*

A solution of **4.7** [41] (500 mg, 1.37 mmol) and oleic alcohol (85%) (1.53 mL, 4.11 mmol) in anhydrous CH3CN(55 mL) containing 4 Å molecular sieves was stirred at room temperature for 10 min. Then, SnCl4 (0.3 mL, 2.4 mmol) was added, and the reaction mixture was stirred at 55 ºC for 24 h. After this time, the mixture was heated at 80 ºC (under reflux) and stirred for 1 h. The reaction mixture was cooled at room temperature, treated with Et3N (0.4 mL), filtered under Celite, and concentrated in vacuo. The residue was purified by silica gel column chromatography (hexane-EtOAc, 1:1) to give the oleyl intermediate Oleyl 2-Acetamido-3,4,6-tri-O-acetyl-2-deoxy-β-D-glucopyranoside (396 mg, 48%). [α]$_D$ -9.6º (c 1.1, MeOH). ^{1}H NMR (400 MHz, CD$_3$OD): δ 5.5-5.3 (m, 2H), 5.22 (dd, 1H, J = 10.5, 9.3 Hz), 4.98 (dd, 1H, J = 10.1, 9.5 Hz), 4.63 (d, 1H, J = 8.5 Hz), 4.28 (dd, 1H, J = 12.4, 4.8 Hz), 4.11 (dd, 1H, J = 12.3, 2.4 Hz), 3.9-3.7 (m, 2H), 3.6-3.4 (m, 2H), 2.1-2.0 (m, 13H), 1.90 (s, 3-H), 1.6-1.5 (m, 2H), 1.4-1.2 (m, 22 H), 0.90 (t, 3H, J = 6.9 Hz) ppm. ^{13}C NMR (100 MHz, CD$_3$OD): δ 173.2, 172.3, 171.9, 171.3, 130.9, 130.8, 102.1, 74.2, 72.8, 70.9, 70.2, 63.3, 55.5, 33.6, 33.1, 30.9, 30.8, 30.8, 30.8, 30.7, 30.6, 30.5, 30.3, 30.2, 28.2, 28.1, 27.1, 23.7, 22.8, 20.7, 20.6, 20.6, 14.5 ppm. HRMS (ESI) m/z calcd for $C_{32}H_{55}NO_9$, 597.3897; found, 598.3970 (M + H)$^+$.

This intermediate was dissolved in MeOH (2 mL) and treated with a 0.1 M solution of NaOMe (10 mL). The reaction was stirred at room temperature for 2 h. After this time, the mixture was neutralised with Amberlite IR-120 (H$^+$ form), filtered off, and concentrated. The residue was purified by silica gel column chromatography (EtOAc-MeOH, 10:0 to 10:1) to give **4.1** (840 mg, quantitative) as a white solid; mp 155-160 ºC; [α]$_D$ -9.0º (c 0.5, MeOH). ^{1}H NMR (400 MHz, CD$_3$OD): δ 5.4-5.3 (m, 2H), 4.38 (d, 1H, J = 8.4 Hz), 3.9-3.8 (m, 2H), 3.69 (dd, 1H, J = 11.9, 5.5 Hz), 3.62 (dd, 1H, J = 10.3, 8.4), 3.5-3.4 (m, 1H), 3.34 (d, 1H, J = 9.6 Hz), 3.25 (ddd, 1H, J = 9.6, 5.5, 2.4 Hz), 2.1-1.9 (m, 7H), 1.5-1.4 (m, 2H), 1.3-1.2 (m, 26H), 0.88 (t, 3H, J = 7.0 Hz) ppm. ^{13}C NMR

(100 MHz, CD$_3$OD): δ 173.4, 130.6, 130.5, 102.3, 79.1, 78.8, 78.5, 77.4, 75.7, 71.8, 70.5, 62.5, 57.1, 33,4, 32.8, 30.6, 30.6, 30.5, 30.5, 30.4, 30.40, 30.3, 30.3, 30.2, 30.9, 30.1, 30.1, 29.9, 28.0, 26.9, 23.5, 23.0, 14.4 ppm. HRMS (ESI) m/z calcd for C$_{26}$H$_{49}$NO$_6$, 471.3570; found, 472.3643 (M +H)+, 494.3461 (M+ Na)+.

Synthesis of oleyl 2-acetamido-2-deoxy-6-O-(oxosulfonyl)- α -D-glucopyranoside potassium salt, IG-20 (**4.2**)

A solution of **4.1** (100 mg, 0.21 mmol) in ethanol (1.5 mL) was treated with butane-2,3-dione (41 ul, 0.47 mmol), camphorsulfonic acid (10 mg, 0.04 mmol), and triethylorthoformiate (0.23 mL, 1.4 mmol) under Ar. The mixture was stirred for 3.5 h at 60 °C. After cooling, the mixture was neutralised with triethylamine, concentrated, and purified by column chromatography (hexane-EtOAc, 1:1 to 0:1) to give a solid (98 mg), which was dissolved in anhydrous pyridine (5 mL) and then treated with SO3-pyridine complex (509 mg, 3.20 mmol), with stirring at room temperature under Ar for 1 h. After this time, the mixture was concentrated, and the residue was dissolved in methanol-water (2:1, 7 mL), neutralised with a 0.5M KOH solution, and concentrated. The residue was purified by column chromatography (CH$_2$Cl$_2$-methanol, 6:1) to give **4.8** (95 mg, 61%). ^{1}H NMR (200 MHz, CD$_3$OD): δ 5.4-5.3 (m, 2H), 4.83 (d, 1H) 3.4 Hz), 4.6-4.4 (m, 2H), 4.3-3.4 (m, 8H), 2.2-2.0 (m, 7H), 1.6-1.2 (m, 36H), 1.0-0.9 (m, 3H).

4.8 (79 mg, 0.11 mmol) was dissolved in a mixture of acetic acid-water (2:1, 10 mL) and stirred at 65 °C for 3 h. The mixture was concentrated and the residue was purified by column chromatography (CH$_2$Cl$_2$-methanol, 5:1 to 4:1) to give **4.2** (42 mg, 66%). [R]D: +69.0° (*c* 1.18, MeOH). ^{1}H NMR (300 MHz, CD$_3$OD): δ 5.4-5.3 (m, 2H), 4.76 (d, 1H, *J* = 3.4 Hz), 4.26 (dd,1H, *J* = 2.4 Hz, *J* = 11.0 Hz), 4.18 (dd, 1H, *J* = 5.6 Hz, *J* = 10.7 Hz), 3.89 (dd, 1H, *J* = 3.7 Hz, *J* = 10.7 Hz), 3.8-3.6 (m, 4H), 3.4-3.3 (m, 2H), 2.0-1.9 (m, 7H), 1.6-1.5 (m, 2H), 1.3-1.2 (m, 22H), 0.90 (t, 3H, *J* = 6.8 Hz). MS (ES) *m/z* (calcd 589.3): 590.3 (M + 1). Anal. (C$_{26}$H$_{48}$KNO$_9$S) C, H, N, S.

Synthesis of oleyl 2-deoxy-2-trifluoroacetamido- α -D-glucopyranoside, TFA-GC22 (**4.3**).

N-trifluoroacetyl-D-glucosamine (1.18 g, 4.29 mmol), prepared from **4.4**. as described in the literature [30], was dissolved in oleic alcohol (85%) (8 ml, 21.4 mmol)

and was treated with H_2SO_4-silica (35%) (236 mg). The reaction mixture was stirred under argon at 180 ºC for 20 min (TLC: EtOAc). After this time, the mixture was cooled at room temperature and purified by silica gel column chromatography (hexane-EtOAc, 2:1 to 0:1) to give *4.3* (604 mg, 29%) as a white solid. Mp: 118-123 ºC. [α]D: +86.0º (c 0.5, MeOH). ^{1}H NMR (400 MHz, CD$_3$OD): δ 5.4-5.3 (m, 2H), 4.86 (d, 1H, J=3.6 Hz), 3.90 (dd, 1H, J=10.8, 3.6 Hz), 3.9-3.8 (m, 1H), 3.80 (t, 1H, J=1.9 Hz), 3.8-3.7 (m, 2H), 3.60 (ddd, 1H, J=9.9, 5.5, 2.3 Hz), 3.5-3.3 (m, 2H), 2.1-1.9 (m, 4H), 1.8-1.5 (m, 2H), 1.5-1.1 (m, 22H), 0.90 (t, 3H, J=7.0 Hz). ^{13}C RMN (100 MHz, CD$_3$OD): δ 159.2, (q, J=37.5 Hz), 117.5 (q, J=287.6 Hz), 130.8, 130.8, 97.7, 73.8, 72.3, 71.9, 68.98, 62.6, 56.2, 33.1, 30.9, 30.9, 30.6, 30.6, 30.6, 30.5, 30.5, 30.4, 30.3, 28.1, 28.1, 27.3, 23.8, 14.5 ppm. HRMS (ESI+) m/z (calcd 525.3283): 526.3345 (M-H)+, 543.3621 (M-NH4)+. HRMS (ESI+) m/z (calcd 525.3283): 526.3345 (M-H)+, 543.3621 (M-NH4)+. For preparation of H2SO4-silica catalyst (35%), silica gel (200-325 mesh) (10 g) was resuspended in ethylic ether (50 mL) and concentrated H2SO4 (3 mL) was slowly added drop by drop with stirring. During the absorption process, 10 min, the suspension was gently stirred at room temperature. After this time, the solvent was removed by distillation and the silica was dried under reduced pressure (2-4 mbar) and heated at 60 ºC for 3 h.

*Synthesis of glycoside coated IONP micelles **4.4**, **4.5** and **4.6**.*

The glycosides *4.1*, *4.2* or *4.3* (10 to 20 mg) in ethanol (1 mL) was first dispersed in 15 mL of phosphate buffer (pH=7.2, 5 mM). 1 mL of the suspension comprising OA IONP in hexane (10 to 15 mg.mL^{-1} in iron concentration) was then added to the solution and the resultant mixture was sonicated (Branson 250, 42 +/- 6 KHz) under robust stirring for 20 min at 37 ºC. Oil in water (o/w) nanoemulsion was further kept under sonication for 1 hour to evaporate all traces of hexane and ethanol resulting in the formation of a homogenous micellar aqueous solution. Aggregates were removed after filtration (0.22 µm, PVDF membrane) and excess of free glycoside was removed by gel filtration in a PD-10 column (GE Healthcare).

Evaluation of 4.4 uptake in liver by MRI after i.v.a.

Rat (n = 2, Wistar, 350 g) was anesthetised with 2% isoflurane in a mixture of N2/O2 (80:20). Baseline images were acquired before the intravenous administration of 300 µl, [Fe]=1.5 mg.ml^{-1} of **4.4** micelle. Magnetic resonance images of the rat´s liver were acquired at different times, from 5 minutes up to 1 hour after the injection. Specific region of interests (ROI) were selected and the reduction of the signal measured. After normalisation to the baseline, curve representing the kinetic of elimination of the liver was represented.

MRI protocol. The images were acquired with a 7 T Biospec MRI spectrometer (Bruker, Ettlingen, Germany), using a transmitter/receiver quadrature coil of 25 mm inner diameter (Bruker, Ettlingen, Germany). Rat was kept anaesthetised with 2% isoflurane in a mixture of N2/O2 (80:20) via facial mask and placed prone in a custom-built plastic holder. The body temperature was kept constant using warm circulating water and the respiratory cycle was monitored constantly. 8 axial slices of 1 mm thickness were acquired to image the liver. The acquisition was performed in free-breathing animals, using a FLASH sequence.

In vitro activity of the micelles _4.4_, _4.5_ and _4.6_. Inhibition of A549 and C6 tumour cell proliferation

Human A549 cell line and C6 rat glioma cell line were maintained in Dulbecco's modified Eagle's medium (DMEM) complete medium (Sigma-Aldrich, St. Louis, MO), supplemented with fetal bovine serum (FBS, 10%; GLinus, Madrid, Spain), glutamine (2 mM), penicillin (50 IU/mL), and streptomycin (50 mg/mL), at 37 ºC in a 5% CO2 humidified atmosphere. Exponentially growing cells were seeded on 96-well plates (Beckton Dickinson, Le Pont de Claix, France), in DMEM complete medium, at a density of 1.5 x 10^4 cells/well for C6 cell and 5 x 10^3 cells/well for A549 cells respectively. The cells were allowed to attach with 5% of CO2 at 37ºC for overnight, and then, to serum starve the cells, the medium was replaced by 100 μL of fresh DMEM without FBS and maintained overnight. Stock solutions in EtOH of the free glycosides (**4.1**, **4.2** and **4.3**) derivatives of or stock solutions in PBS of the micelles

(*4.4*, *4.5* and *4.6*) were finally dissolved in DMEM complete medium for the treatments. The cells were treated with serial dilutions of glycoside derivatives or micelles for 48 h. For the experiments with micelles, some 96-well plates were placed over a MagnetoFACTOR-96 device (Chemicell) to produce a strong magnetic field to each well and increase the proximity of the nanoparticles to the cells. Also, IONP coated with azelaic acid and PC IONP (*1.1*) were tested (Azelaic-NP, obtained as described in previous work of us. [42]) Cell proliferation was evaluated with an MTT assay (Sigma-Aldrich), based on the conversion of the water-soluble MTT into an insoluble formazan. Briefly, after 48 h of compound treatment, the medium was replaced by 100 μL of fresh DMEM without phenol red containing MTT (5 mg/mL) solution, and cells were incubated for additional 3 h at 37 ºC with 5% CO2. After this time, the medium was removed, the precipitated formazan was dissolved in 100 μL of DMSO, and the solution optical density was measured at 595 nm in Spectramax Plus equipment (Molecular Devices Corporation). Absorption values were referred to positive proliferation controls (cells cultured in DMEM complete medium) and negative proliferation controls cells cultured in DMEM without FBS). Inhibition was expressed as an ID50 value, the compound concentration that reduced maximal proliferation by 50%.

6. Bibliography

(1) Ferrari, M. (2005) Cancer nanotechnology: opportunities and challenges. *Nat. Rev. Cancer 5*, 161–171.
(2) Gupta, A. K., and Gupta, M. (2005) Synthesis and surface engineering of iron oxide nanoparticles for biomedical applications. *Biomaterials 26*, 3995–4021.
(3) Cho, K., Wang, X., Nie, S., Chen, Z., and Shin, D. M. (2008) Therapeutic Nanoparticles for Drug Delivery in Cancer. *Clin. Cancer Res. 14*, 1310–1316.
(4) Mccarthy, J., and Weissleder, R. (2008) Multifunctional magnetic nanoparticles for targeted imaging and therapy☆. *Adv. Drug Deliv. Rev. 60*, 1241–1251.
(5) Veiseh, O., Gunn, J. W., and Zhang, M. (2010) Design and fabrication of magnetic nanoparticles for targeted drug delivery and imaging. *Adv. Drug Deliv. Rev. 62*, 284–304.
(6) Maeda, H., Wu, J., Sawa, T., Matsumura, Y., and Hori, K. (2000) Tumor vascular permeability and the EPR effect in macromolecular therapeutics: a review. *J. Control. Release Off. J. Control. Release Soc. 65*, 271–284.
(7) Alexis, F., Pridgen, E., Molnar, L. K., and Farokhzad, O. C. (2008) Factors Affecting the Clearance and Biodistribution of Polymeric Nanoparticles. *Mol. Pharm. 5*, 505–515.
(8) Emerich, D. F., and Thanos, C. G. (2006) The pinpoint promise of nanoparticle-based drug delivery and molecular diagnosis. *Biomol. Eng. 23*, 171–184.

(9) Arruebo, M., Fernández-Pacheco, R., Ibarra, M. R., and Santamaría, J. (2007) Magnetic nanoparticles for drug delivery. *Nano Today 2*, 22–32.

(10) Alexiou, C., Schmid, R. J., Jurgons, R., Kremer, M., Wanner, G., Bergemann, C., Huenges, E., Nawroth, T., Arnold, W., and Parak, F. G. (2006) Targeting cancer cells: magnetic nanoparticles as drug carriers. *Eur. Biophys. J. 35*, 446–450.

(11) Brigger, I., Dubernet, C., and Couvreur, P. (2002) Nanoparticles in cancer therapy and diagnosis. *Adv. Drug Deliv. Rev. 54*, 631–651.

(12) Janib, S. M., Moses, A. S., and MacKay, J. A. (2010) Imaging and drug delivery using theranostic nanoparticles. *Adv. Drug Deliv. Rev. 62*, 1052–1063.

(13) Lübbe, A. S., Bergemann, C., Huhnt, W., Fricke, T., Riess, H., Brock, J. W., and Huhn, D. (1996) Preclinical experiences with magnetic drug targeting: tolerance and efficacy. *Cancer Res. 56*, 4694–4701.

(14) Lübbe, A. S., Bergemann, C., Riess, H., Schriever, F., Reichardt, P., Possinger, K., Matthias, M., Dörken, B., Herrmann, F., Gürtler, R., Hohenberger, P., Haas, N., Sohr, R., Sander, B., Lemke, A. J., Ohlendorf, D., Huhnt, W., and Huhn, D. (1996) Clinical experiences with magnetic drug targeting: a phase I study with 4'-epidoxorubicin in 14 patients with advanced solid tumors. *Cancer Res. 56*, 4686–4693.

(15) García-Alvarez, I., Corrales, G., Doncel-Pérez, E., Muñoz, A., Nieto-Sampedro, M., and Fernández-Mayoralas, A. (2007) Design and synthesis of glycoside inhibitors of glioma and melanoma growth. *J. Med. Chem. 50*, 364–373.

(16) Fernández-Mayoralas, Alfonso, Nieto, Manuel, Casas, Josefina, García, Isabel, and Romero, Lorenzo. DERIVADOS DE N-TRIFLUOROACETILHEXOSAMINAS Y SU USO COMO INHIBIDORES DE LA DIVISION DE CELULAS TUMORALES.

(17) García-Alvarez, I., Garrido, L., Doncel-Pérez, E., Nieto-Sampedro, M., and Fernández-Mayoralas, A. (2009) Detection of metabolite changes in C6 glioma cells cultured with antimitotic oleyl glycoside by 1H MAS NMR. *J. Med. Chem. 52*, 1263–1267.

(18) García-Álvarez, I., Egido-Gabás, M., Romero-Ramírez, L., Doncel-Pérez, E., Nieto-Sampedro, M., Casas, J., and Fernández-Mayoralas, A. (2011) Lipid and ganglioside alterations in tumor cells treated with antimitotic oleyl glycoside. *Mol. Biosyst. 7*, 129–138.

(19) Birklé, S., Zeng, G., Gao, L., Yu, R. K., and Aubry, J. (2003) Role of tumor-associated gangliosides in cancer progression. *Biochimie 85*, 455–463.

(20) Lahiri, S., and Futerman, A. H. (2007) The metabolism and function of sphingolipids and glycosphingolipids. *Cell. Mol. life Sci. C. 64*, 2270–2284.

(21) Bektas, M., and Spiegel, S. (2004) Glycosphingolipids and cell death. *Glycoconj. J. 20*, 39–47.

(22) García-Álvarez, I., Groult, H., Casas, J., Barreda-Manso, M. A., Yanguas-Casás, N., Nieto-Sampedro, M., Romero-Ramírez, L., and Fernández-Mayoralas, A. (2011) Synthesis of Antimitotic Thioglycosides: In Vitro and in Vivo Evaluation of Their Anticancer Activity. *J. Med. Chem. 54*, 6949–6955.

(23) Chojnowska, S., Kępka, A., Szajda, S. D., Waszkiewicz, N., Bierć, M., and Zwierz, K. (2011) Exoglycosidase markers of diseases. *Biochem. Soc. Trans. 39*, 406–409.

(24) Driguez, H. (1997) Thiooligosaccharides in glycobiology, in *Glycoscience Synthesis of Substrate Analogs and Mimetics* (Driguez, H., and Thiem, J., Eds.), pp 85–116. Springer Berlin Heidelberg, Berlin, Heidelberg.

(25) Kingsley, J. D., Dou, H., Morehead, J., Rabinow, B., Gendelman, H. E., and Destache, C. J. (2006) Nanotechnology: a focus on nanoparticles as a drug delivery

system. *J. Neuroimmune Pharmacol. Off. J. Soc. NeuroImmune Pharmacol. 1*, 340–350.

(26) Hao, R., Xing, R., Xu, Z., Hou, Y., Gao, S., and Sun, S. (2010) Synthesis, Functionalization, and Biomedical Applications of Multifunctional Magnetic Nanoparticles. *Adv. Mater. 22*, 2729–2742.

(27) Laurent, S., Forge, D., Port, M., Roch, A., Robic, C., Vander Elst, L., and Muller, R. N. (2008) Magnetic Iron Oxide Nanoparticles: Synthesis, Stabilization, Vectorization, Physicochemical Characterizations, and Biological Applications. *Chem. Rev. 108*, 2064–2110.

(28) Nasongkla, N., Bey, E., Ren, J., Ai, H., Khemtong, C., Guthi, J. S., Chin, S.-F., Sherry, A. D., Boothman, D. A., and Gao, J. (2006) Multifunctional Polymeric Micelles as Cancer-Targeted, MRI-Ultrasensitive Drug Delivery Systems. *Nano Lett. 6*, 2427–2430.

(29) Phosphatidylcholine-coated iron oxide nanomicelles for in vivo prolonged circulation time with an antibiofouling protein corona.

(30) Wolfrom, M. L., and Conigliaro, P. J. (1969) Trifluoroacetyl as an N-protective group in the synthesis of purine nucleosides of 2-amino-2-deoxy saccharides. *Carbohydr. Res. 11*, 63–76.

(31) Fernández-Mayoralas, A., De La Figuera, N., Zurita, M., Vaquero, J., Abraham, G. A., San Román, J., and Nieto-Sampedro, M. (2003) Central neural tumor destruction by controlled release of a synthetic glycoside dispersed in a biodegradable polymeric matrix. *J. Med. Chem. 46*, 1286–1288.

(32) Na, H. Bin, Song, I. C., and Hyeon, T. (2009) Inorganic Nanoparticles for MRI Contrast Agents. *Adv. Mater. 21*, 2133–2148.

(33) Monopoli, M. P., Walczyk, D., Campbell, A., Elia, G., Lynch, I., Baldelli Bombelli, F., and Dawson, K. A. (2011) Physical−Chemical Aspects of Protein Corona: Relevance to *in Vitro* and *in Vivo* Biological Impacts of Nanoparticles. *J. Am. Chem. Soc. 133*, 2525–2534.

(34) Moghimi, S. M., Hunter, A. C., and Murray, J. C. (2001) Long-circulating and target-specific nanoparticles: theory to practice. *Pharmacol. Rev. 53*, 283–318.

(35) García, I., Marradi, M., and Penadés, S. (2010) Glyconanoparticles: multifunctional nanomaterials for biomedical applications. *Nanomedicine 5*, 777–792.

(36) Lartigue, L., Innocenti, C., Kalaivani, T., Awwad, A., Sanchez Duque, M. del M., Guari, Y., Larionova, J., Guérin, C., Montero, J. G., Barragan-Montero, V., Arosio, P., Lascialfari, A., Gatteschi, D., and Sangregorio, C. (2011) Water-dispersible sugar-coated iron oxide nanoparticles. An evaluation of their relaxometric and magnetic hyperthermia properties. *J. Am. Chem. Soc. 133*, 10459–72.

(37) Mejías, R., Pérez-yagüe, S., Gutiérrez, L., Cabrera, L. I., Spada, R., Acedo, P., Serna, C. J., Lázaro, F. J., Villanueva, Á., Morales, P., and Barber, D. F. (2011) Biomaterials Dimercaptosuccinic acid-coated magnetite nanoparticles for magnetically guided in vivo delivery of interferon gamma for cancer immunotherapy. *Biomaterials 32*, 2938–2952.

(38) Liu, Y., Miyoshi, H., and Nakamura, M. (2007) Nanomedicine for drug delivery and imaging: A promising avenue for cancer therapy and diagnosis using targeted functional nanoparticles. *Int. J. Cancer 120*, 2527–2537.

(39) Jang, S. H., Wientjes, M. G., Lu, D., and Au, J. L. S. (2003) Drug delivery and transport to solid tumors. *Pharm. Res. 20*, 1337–1350.

(40) Antonelli, A., Sfara, C., Battistelli, S., Canonico, B., Arcangeletti, M., Manuali, E., Salamida, S., Papa, S., and Magnani, M. (2013) New Strategies to Prolong the In Vivo Life Span of Iron-Based Contrast Agents for MRI. *PLoS One* (Louie, A., Ed.) *8*.
(41) Whistler, R. L., Wolfrom, M. L., and BeMiller, J. N. (1962) Methods in carbohydrate chemistry. Academic Press, New York.
(42) Herranz, F., Morales, M. P., Roca, A. G., Desco, M., and Ruiz-Cabello, J. (2008) A New Method for the Rapid Synthesis of Water Stable Superparamagnetic Nanoparticles. *Chem. - A Eur. J. 14*, 9126–9130.

Conclusions

1- We have synthesised and fully characterised a new probe made of OA IONP encapsulated in a Phosphatydilcholine (PC) based micelle. These NP are valuable T_2 MRI contrast agent with a significantly extended vascular lifetime above 10 hours.

2- The protein corona adsorbed on PC IONP was fully elucidated at 3 different times and compared with those from standard IONP blood pool agent coated with PEG. Results allow correlating the antibiofouling character of the corona of PC IONP with its prolonged systemic circulation.

3- We have demonstrated that PC IONP can be degraded by the enzyme PC-PLC leading to the formation of aggregates and showing that this enzymatic reaction has effect on uptake and cytotoxicity of *in vit*ro cell cultures of macrophage type I and II.

4- We have employed this selective enzymatic property to use PC IONP for the specific detection of the atherosclerosis plaque. After i.v.a of the probe in a mice model of atherosclerosis, we were able to detect the accumulation of the nanoparticles in the plaque of the aorta by T_2 MRI. Histology confirmed an entrapment of the probe inside the plaque elicited by the PC-PLC enzyme activity, and a slower uptake of PC IONP by the host macrophages.

5- We have presented a new approach for the parallel multifunctionalisation of hydrophobic NP in a single step. The method is generic for different types of NP coated with aliphatic surfactants and uses the interactions with BSA pre-functionalised modules. It can be a standard and simple methodology for the versatile preparation of NP incorporating functionalisation on demand of multimodal nanoparticles.

6- We have used this methodology for the preparation of a library of 13 different multimodal agents based on IONP, UCNP and AuNP and with BSA modules for PET imaging, fluorescence imaging and targeting of tumours. All the probes show excellent colloidal properties, low toxicity and good bioacceptability.

7- As proof of concept of the flexibility and suitability for different *in vivo* applications of the probes prepared by this modular approach, we prepared one IONP based candidate for targeted (RGD) PET/MRI multimodal *in vivo* imaging in a murine tumour model.

8- We have designed innovative theranostic NP agents for cancer therapy. They are constructed by stabilizing OA IONP inside a micelle assembly made of antimitotic oleyl glycosides. We have illustrated the possibility to obtain hydrophilic nanostructures with higher aqueous solubility and *in vivo* stability from two entities previously not suitable for *in vivo* applications.

9- We have demonstrated that these glycoside-coated IONP micelles have maintained or, in some cases, increased the antimitotic activity against two cancerous cell lines *in vitro* in comparison to the original free glycosides. These glycosidic biomolecules confer at the same time stabilisation as coating for OA IONP micellar and antitumoural chemotherapeutic properties.

Summary in English

Nanotechnology studies materials and systems whose structures and components exhibit novel or significantly improved physical, chemical and biological properties, phenomena and processes due to their nanoscale size. When nanotechnology is used specifically for medical applications, we refer then to "Nanomedicine". It is nowadays mostly related to the application of nanostructures for treatment, diagnosis, monitoring and control of biological systems. The term Nanoparticle (NP) is used in medicine in a generic way including a wide range of distinct nanostructures some of them hybrid or combination of different ones. In this work we have focused in metallic nanoparticles since they show very interesting properties for imaging. NP have special structures which places them at the cross of many different disciplines. They are basically composed of a metallic core surrounded by an organic coating bound to the surface. The metallic core provides the size-dependent properties for which the material is most well-known. The surface of the NP is of paramount importance, it determines the targeting capabilities, colloidal stability and much of the *in vivo* fate of the NP. Most recent advances deal with the term functionalisation; the attachment of molecules on the surface of the particles to provide colloidal stability and/or biological targeting. Surface coating is responsible for a range of specific requirements for the in vivo biological use of the NP, which concern multidisciplinary fields such as biochemistry, molecular and cell biology, pharmacokinetics or toxicity. In this work, we proposed different functionalisations of various coatings of three kind of metallic NP (Iron oxide NP, UpConverting NP and Gold NP). These coatings tailoring aimed at applications in medical imaging and therapy in oncology and cardiovascular diseases.

In the Chapter 1, we report the synthesis of micellar Phosphatidylcholine-coated Superparamagnetic Iron Oxide Nanoparticles as a new long circulation contrast agents for magnetic resonance imaging. Oleic acid-coated Fe_3O_4 nanoparticles were first prepared via thermal degradation and then encapsulated into small clusters with a Phosphatidylcholine coating to obtain hydrophilic nanomicelles. A thoroughly characterisation confirmed the chemical nature of the coating and the excellent colloidal stability of these nanomicelles in aqueous media. Magnetisation and relaxivity properties proved their suitability as MRI contrast agent and *in vitro* cell viability data showed low toxicity. Vascular lifetime and elimination kinetics in liver were assessed by blood relaxometry and *in vivo* MRI in rats and compared with "control" particles prepared with a polyethylene glycol derivative. These micellar particles had a lifetime in blood of more than 10 hours, much longer than the control nanoparticles (~ 2 hours) really remarkable considering that the coating molecule is a small biocompatible zwitterionic phospholipid. The protein corona was characterised after incubation with rat serum at different times by high-throughput proteomics, showing a higher proportion of bound apolipoproteins and other dysopsonins for the Phosphatidylcholine particles. The antibiofouling properties of this corona and its resistance to the adsorption of proteins corroborate the observed enhanced stability and prolonged systemic circulation.

In the Chapter 2, we propose iron oxide coated phosphatidylcholine micelles (PC IONP) as an imaging probe for the molecular characterisation of atherosclerotic plaque formation. Phosphatidylcholine-specific phospholipase C (PC-PLC) is involved in atherosclerosis as a regulator of apoptosis and autophagy in vascular endothelial cells (VECs). Because PC-PLC can specifically degrade the polar moiety of phosphatidylcholine, we examined if this enzymatic regulation could trigger the accumulation of PC IONP by

changing their colloidal stability. We first considered the *in vitro* interaction between PC-PLC and the iron oxide micelles in order to demonstrate the effectiveness of enzymatic cleavage of PC coating leading to the formation of hydrophobic aggregates. We then showed the consequences of this enzymatic degradation in the uptake of PC IONP and associated cytotoxicity effects in cellular cultures of macrophages. Finally, we studied the intravenous injection of PC IONP in ApoE-KO mice for multimodal *in vivo* visualisation and imaging characterisation of atherosclerotic plaques, underlining the importance of the interaction of the probe with the PC-PLC enzyme and the uptake by macrophages. The proposed probe represents a new platform for targeting of atherosclerosis thanks to an original enzymatically driven entrapment route, which opens promising bioapplications not only for specific diagnosis (quantification of plaque burden) but also to predict clinical relevant events for potential anti-inflammatory therapies in the context of atherosclerosis. Our approach allows studying the regulation of this pro-atherogenic enzyme in the plaque progression and thus contributing with new molecular imaging solutions to understand different biochemical processes in the context of atheriosclerosis.

In the Chapter 3,. we reports a generic modular strategy for the parallel one-step multifunctionalisation of different hydrophobic nanoparticles. The method was designed and developed taking advantage of the natural non-covalent interactions between the fatty acid binding sites of the bovine serum albumin (BSA) and the aliphatic surfactants on different inorganic nanomaterials. As a general example of the approach, three different nanoparticles - iron oxide, upconverting nanophosphors and gold nanospheres- were nanomemulsioned in water with BSA. To support specific applications, multifunctional capability was incorporated with a variety of previously modified BSA modules. These modules include different conjugated groups, such as chelating agents for

^{68}Ga or ^{89}Zr and ligand molecules for enhanced *in vivo* targeting. A large library of thirteen multimodal contrast agents was developed with this convergent strategy. This platform allows a highly versatile and easy tailoring option for efficient incorporation of functional groups. Finally, as demonstration of this versatility, a bimodal (PET/MRI) probe including a maleimide-conjugated BSA was selectively sation with an RGD peptide for *in vivo* imaging detection of tumour angiogenesis

In the Chapter 4, we used glycosides comprising hydrophilic sugar moiety conjugated to oleyl hydrophobic chains that have promising antimitotic activity on cancer cell cultures but limited *in vivo* perspectives because of their low solubility in physiological media and rapid enzymatic degradation. We report here the synthesis of micelles formed by the OA IONP encapsulated within a hydrophilic layer of the amphiphilic glycosides. These nanomicelles were fully characterised especially their suitability as *in vivo* MRI contrast agents and for its *in vitro* antimitotic activity on cell cultures from rat glioma and from human lung carcinoma and compared with the activity of the corresponding free glycosides. The results show that the formulation of glycosides in the form of OA IONP encapsulated micelles have preserved antitumoural effects and in one case provides a significant therapeutic gain. Moreover, the micelles present excellent relaxometric properties for their use as contrast agent based T2 MRI. Ours findings suggest that synergetic bioactive hydrophilic nanostructures can be obtained to generate theranostic agents, from two entities previously not suitable for *in vivo* applications and strengthen the possibility to use biomolecules at the same time as coating for OA IONP micellar stabilisation and as drugs for therapy.

Summary in Spanish

1. Introducción

La Nanotecnología es la ciencia que trata el diseño, la síntesis, la caracterización y la aplicación de materiales con al menos una dimensión menor de 100 nm. Además, debido a este tamaño, aparecen propiedades fisicoquímica nuevas o mejoradas respecto al material macroscópico. El tremendo desarrollo de la nanotecnología en los últimos años ha llevado a su aplicación en el campo de la medicina, dando lugar a la Nanomedicina, en la cual se engloba el presente trabajo.

En la aplicación de la nanotecnología a la medicina es fundamental el uso de nanopartículas (NP). La variedad de dichos compuestos es inmensa, debido fundamentalmente al número de variables que se pueden modificar; tamaño del núcleo, tamaño hidrodinámico, composición del núcleo, composición del surfactante, carga superficial, etc. La estructura básica de una nanopartícula incluye un núcleo, que suele ser metálico o de óxidos metálicos, y una superficie que suele ser orgánica. Tradicionalmente el desarrollo de NP para imagen o terapia se ha centrado en la optimización del núcleo de la nanopartícula, dejando como secundario la superficie orgánica. En este trabajo sin embargo nos centraremos más en dicha superficie, en el desarrollo de nuevos métodos para su estabilización en medios acuosos, la funcionalización para una determinada actividad biológica y en el estudio de las interacciones in vivo de la superficie de las partículas con las proteínas presentes en el torrente circulatorio, lo que conoce como la "protein corona". Una parte fundamental de esta aproximación es el concepto de "multifuncional", entendiendo como tal una nanopartícula que puede integrar en su estructura sondas para varias técnicas de imagen más una molécula que permita la acumulación selectiva en el área de la patología o que por ejemplo incorpore un fármaco, permitiendo desarrollar el concepto de

"theranostics", la combinación de terapia y diagnóstico en una sola sonda (Figura 5.1). La representación de la Figura 5.1 deja claro la importancia de la superficie de las NP en esta aproximación.
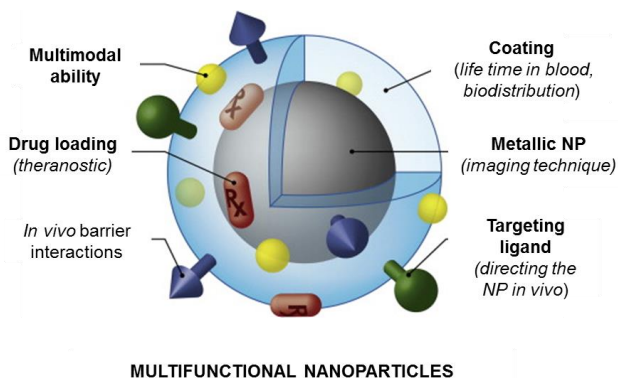

Figura 5.1. Representación esquemática de una nanopartícula metálica multifuncional.

La aplicación de NP en biomedicina tiene dos grandes campos de actuación; la imagen médica y el transporte de fármacos. En la presente tesis veremos ejemplos de las dos aplicaciones, desde el diseño de partículas para imagen dual PET/MRI hasta el desarrollo de nuevos antitumorales nanoparticulados. Las NP que emplearemos para dicha aproximación son de tres tipos; Óxido de hierro, Up-converting nanophosphors y partículas de Oro.

Nanopartículas de Óxido de hierro (IONP). La importancia de estas partículas en aplicaciones biomédicas es de sobra conocida y cubren desde la imagen por resonancia magnética, el transporte de fármacos y la terapia por hipertermia, por citar las más destacadas. Estas NP pueden obtenerse con tamaños de núcleo de 2 a 50 nm y presentan una composición de Magnetita (Fe_3O_4), Maghemita (Fe_2O_3) o una mezcla de ambos óxidos. La

principal propiedad de estas NP, razón de su amplia rango de aplicaciones y consecuencia de su tamaño es el superparamagnetismo. De forma muy simple dicha propiedad se traduce en una respuesta magnética muy intensa por parte del material cuando se aplica un campo magnético externo y la pérdida de todo magnetismo cuando dicho campo es eliminado. En términos de imagen en MRI esta propiedad hace que, incluso a muy bajas concentraciones, la señal sea muy intensa en comparación con las sondas paramagnéticas. Como es sabido el fenómeno de la relajación en Resonancia Magnética Nuclear está principalmente gobernado por dos magnitudes, el tiempo de relajación longitudinal o T_1 y el tiempo de relajación transversal o T_2. Los agentes de contraste para MRI reducen ambos tiempos de relajación haciendo que la muestra vuelva antes a la situación de equilibrio térmico. Sin embargo, según las propiedades fisicoquímicas del agente el efecto será mayor sobre T_1 o sobre T_2. Las nanopartículas de óxido de hierro que presentan carácter superparamagnético y normalmente un momento magnético muy grande son ejemplo característico de agente T_2. Dichas sondas, con las secuencias de pulso más habituales en imagen, proporcionan lo que se conoce como contraste negativo, es decir una área hipointensa en aquellas zonas donde las partículas se han acumulado. Dicho contraste para tejidos ricos en agua, por tanto con una señal "brillante", son ideales y fáciles de identificar. Para otras aplicaciones son preferibles el uso de sondas T_1, esto ha hecho que la investigación de métodos para desarrollar sondas de óxido de hierro para contraste T_1 haya avanzado mucho en los últimos años.

Up-converting nanophosphors. Recientemente se ha empezado a aplicar un nuevo tipo de nanomaterial, las que podríamos traducir como nanopartículas fluorescentes de conversión ascendente (UCNP, acrónimo derivado del inglés). Dichas partículas están compuestas por una matriz cuya composición puede ser muy variada y dopadas con diferentes metales. Una

de las combinaciones de matriz-dopantes más empleadas es aquella que usa $NaYF_4$ como matriz y Yb^{3+}, Er^{3+} o Tm^{3+} como dopantes. La principal característica de estas partículas es que, contrariamente a los fluoróforos tradicionales, la fluorescencia se produce de menor a mayor energía mediante la absorción de 2 o 3 fotones de forma secuencial. Esto hace posible por ejemplo excitar a longitudes onda tan grandes como 980 nm, en el infrarrojo cercano, y obtener emisión de fluorescencia a 800 nm, consiguiendo mayor penetración en el tejido y pudiendo realizar imagen de un ratón completo sin los problemas habituales en la imagen óptica con las sondas más habituales.
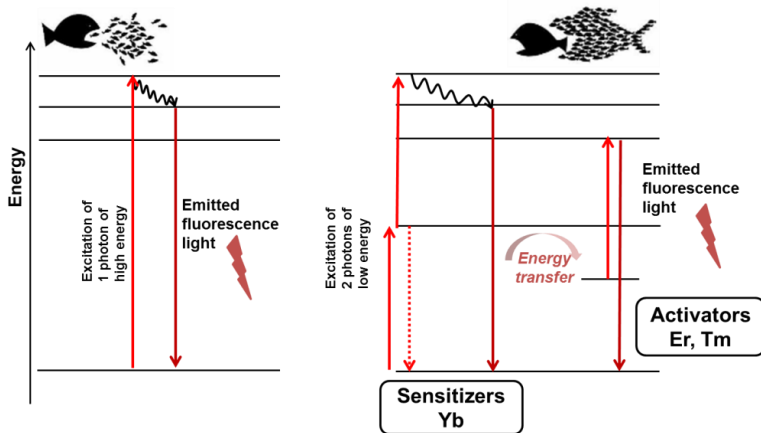

Figura 5.2. Comparativa de los principios básicos de la fluorescencia tradicional y la fluorescencia por conversión ascendente.

De las distintas matrices que como decíamos se pueden emplear en este trabajo nos hemos centrado en β-NaGdF$_4$:Yb,Tm@β-NaGdF$_4$. Dichas partículas consisten en una matriz de NaGdF$_4$ la cual además de ser una buena matriz para el fenómeno de la conversión ascendente permite realizar imagen T_1 en MRI gracias a la presencia del Gd en la estructura. Dicha matriz

está dopada con Yb^{3+} como activador y Tm^{3+} como dador del fenómeno de conversión ascendente, además se añade una "concha" (shell) del mismo material, NaGdF4, sin dopar lo cual aumenta la eficacia de la fluorescencia al aislar el material del disolvente.

Nanopartículas de oro. El último nanomaterial con el que se trabaja en esta tesis son las nanopartículas de oro. La importancia de este material en las aplicaciones biomédicas de la nanotecnología es bien conocida. Ello se debe a varias de sus propiedades, especialmente a la resonancia del plasmón de superficie que hace que estas partículas presenten propiedades ópticas muy interesantes en función del tamaño de partícula. Dicha propiedad es utilizada ampliamente para una gran variedad de aplicaciones como sensores y transporte de fármacos. Además y dado el elevado peso atómico del Au las nanopartículas de este material también se emplean como agentes de contraste en CT, aunque esta última propiedad no será desarrollada en este trabajo.

Síntesis y funcionalización. Por lo que se refiere a la síntesis de estos tres nanomateriales hay una gran variedad de métodos. De las distintas opciones es ampliamente reconocido que la síntesis mediante descomposición térmica de precursores orgánicos es la que proporciona nanopartículas con las mejores características, especialmente en el caso de las IONP y UCNP. La síntesis de esta forma genera nanopartículas hidrófobas con lo que para su empleo en condiciones fisiológicas deben ser transformadas en hidrófilas. Este hecho solía citarse como desventaja de este método, sin embargo, este trabajo es una buena muestra de que más que una desventaja es una oportunidad para, en un solo paso, conseguir la estabilidad en agua y la biofuncionalización en lugar de largas y complejas modificaciones que

resultan en un menor rendimiento y un empeoramiento de las propiedades coloidales de las partículas.

2. Nanomicelas de óxido de hierro recubiertas con fosfatidilcolina: largos tiempos de circulación en sangre y estudio de la corona proteica.

En este apartado se describe la síntesis de nanopartículas superparamagnéticas de óxido de hierro recubiertas con fosfatidilcolina (PC) como nuevos agente de contraste para T_2 en MRI. Las IONPs recubiertas de ácido oleico fueron sintetizadas mediante la descomposición de Fe(acac)$_3$ a elevada temperatura. Como se aprecia en la figura 5.3 se obtienen partículas de unos 10 ± 3 nm de tamaño hidrodinámico, monodispersas, y un tamaño de núcleo, medido por TEM de 7 ± 2 nm, valores típicos para la síntesis mediante este proceso. Tanto la estructura cristalina como la composición del surfactante fueron caracterizados, por rayos-X, espectrometría de masas e Infrarrojo, dando los resultados esperados.
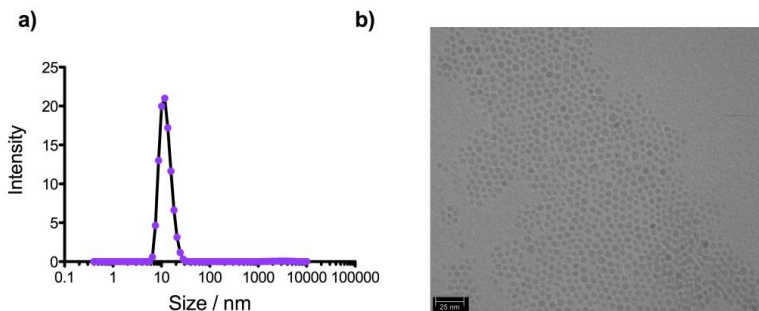

Figura 5.3. a) tamaño hidrodinámico de las IONPs recubiertas de ácido oleico

Finalmente el carácter superparamagnético de la muestra fue confirmado mediante medidas del momento magnético en un campo externo, dando la curva típica sin histéresis ni coercitividad y un valor de magnetización de saturación de 70 emu.g^{-1} Fe.

A continuación dichas partículas fueron funcionalizadas con PC mediante un método de nanoemulsión, generando micelas en las que se encuentran agrupadas varias IONP y con el grupo polar de la PC hacia el exterior de la micela. El método de la nanoemulsión consiste en mezclar un volumen pequeño de IONPs hidrófobas en hexano con un volumen mucho mayor de la PC disuelta en tampón fosfato. Esto conlleva la formación de una monocapa de PC, la cual ocurre de forma espontanea al 1% de concentración. A continuación y mediante sonicación se induce la evaporación del hexano y la formación de las micelas como situación energéticamente más favorable (Figura 5.4).
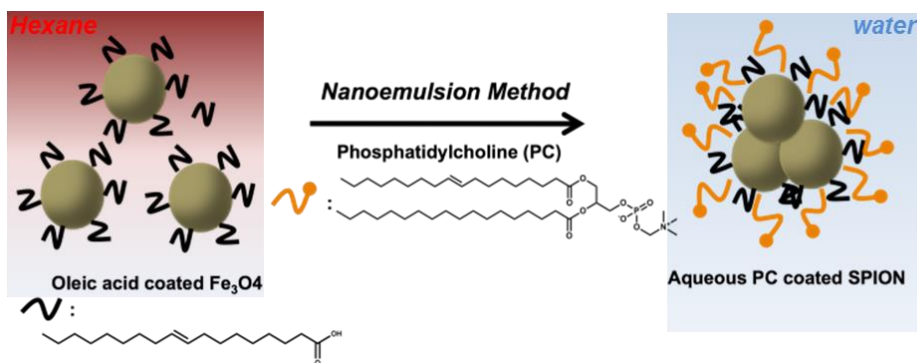

Figura 5.4. Nanoemulsión para la síntesis de IONP recubiertas con fosfatidilcolina.

De esta forma se obtuvieron micelas estables en agua de 74.9 nm de radio hidrodinámico con un PDI muy bajo de 0.14. El aumento de tamaño respecto a las partículas hidrófobas se debe en este caso a que cada micela engloba varias partículas de oleico originales. Para evaluar la estabilidad de las

micelas se midió el potencial Z a distintos valores de pH así como el cambio en el tamaño hidrodinámico en distintos tampones de fuerza iónica elevada (Figura 5.5). La figura 5b muestra cómo, a pesar de un valor de potencial Z bajo a pH 7 (-11.5 mV, Figura 5.5.a), las partículas muestran una gran estabilidad incluso en PBS 10x.
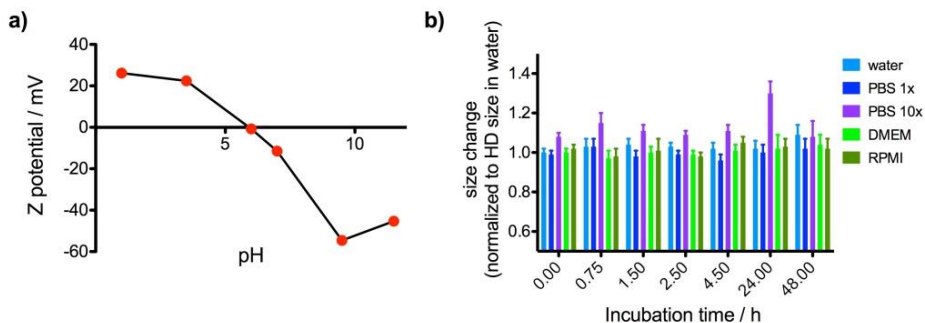

Figura 5.5. a) Potencial Z de las nanomicelas de PC en función del pH. b) Cambio en el tamaño hidrodinámico en función del tampón y del tiempo.

La composición superficial de las micelas fue estudiada de nuevo empleando FTIR y espectrometría de masas, así como mediante termogravimetría. Los resultados en los tres casos fueron los esperados, confirmando la presencia de la molécula en la superficie de la micela. Las propiedades magnéticas fueron estudiadas obteniendo un valor similar al de las IONP hidrófobas, 60 emu.g^{-1} Fe. En cuanto a la relaxometría, para determinar cómo de adecuadas para MRI son estas micelas, se obtuvieron unos valores de 1.3 s^{-1}mM^{-1} y 147.4 s^{-1}mM^{-1} para r_1 y r_2 respectivamente, confirmando la utilidad de estas partículas como agentes T$_2$ para MRI.

Después de comprobar la falta de toxicidad de las partículas en fibroblastos, se estudió el tiempo de circulación en sangre. El conseguir que las nanopartículas circulen por el torrente sanguíneo después de una inyección intravenosa es un requisito indispensable tanto para imagen como

para el transporte de fármacos. Para conseguir esto las partículas deben ser "invisibles" para el sistema inmune ya que de otra forma son rápidamente (4-5 minutos) transportadas al hígado y bazo. A efectos comparativos se sinterizaron micelas, mediante el mismo proceso, pero empleando un polímero anfifílico derivado de polietilenglicol al ser este el estándar más empleado para la síntesis de nanopartículas hidrófilas.

Tabla 5.1. Principales características fisicoquímica de PC IONP y P80 IONP.

	PC IONP	P80 IONP
Tamaño hidrodinámico (nm)	74.9	25
PDI	0.14	0.19
Potencial zeta (pH=7.1) (mV)	-11.5	-4
Magnetizacion de saturación	70	65
Relaxividad (s^{-1}.mM^{-1})	r_1 : 1.3	r_1 : 2.3
	r_2 : 147.4	r_2 : 127.2
Tiempo de circulación en sangre (relaxometría)	10 h	2h

Como puede apreciarse en la tabla 5.1 las nanopartículas de referencia, P80 IONP, presentan un tiempo de circulación en sangre muy elevado de 2 horas, medido por relaxometría y por MRI. Sin embargo, en el caso de las nanomicelas de PC el tiempo de circulación es extraordinariamente largo, 10 horas. Este hecho nos llevó a interesarnos por la composición de la corona proteica. Dicha corona consiste en la formación de una capa de proteínas que rodean a cualquier nanopartícula tan pronto entra en el torrente sanguíneo. La composición de dicha corona es dinámica y está determinada por la composición y tamaño de la nanopartícula. Aunque hasta hace relativamente poco este hecho era totalmente ignorado en la actualidad está claro que la composición de dicha corona determina en gran medida el destino de las partículas. Por ejemplo en nuestro caso estudiamos la composición de la corona de las PC IONP y P80 IONP para comprobar si la razón del diferente tiempo de circulación residía ahí. Para ello las dos

partículas se incubaron con suero a distintos tiempos (15, 90 y 180 minutos), se aislaron los complejos NP-proteínas y su composición se analizó mediante high-throughput LC-MS. La sensibilidad de la técnica nos permitió identificar más de 300 proteínas. En resumen, el análisis semicuantitativo de la corona proteíca permitió identificar una mayor proporción de disopsoninas en todos los puntos para las PC IONP lo que justifica su mucho mayor tiempo de circulación en sangre.
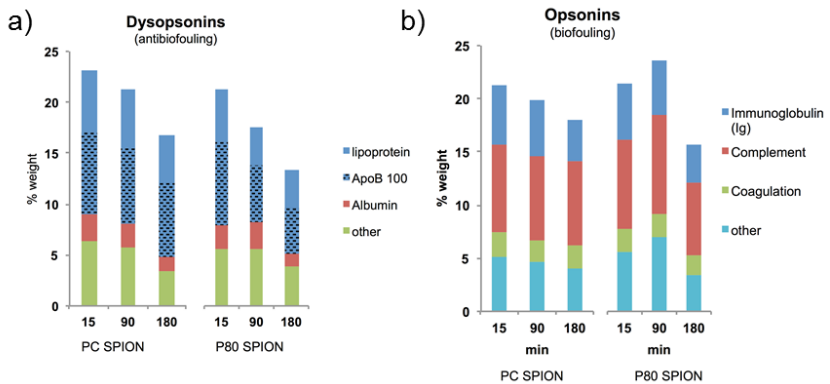

Figura 5.6. Porcentaje relativo en peso de proteínas a) disopsoninas y b) opsoninas, clasificadas por su función biológica, en las coronas de PC IONP y P80 IONP a distintos tiempos.

3. Caracterización de la placa de aterosclerosis mediante "trampa enzimática" de nanopartículas recubiertas de fosfatidilcolina.

En este apartado nos propusimos estudiar el empleo de las PC IONP anteriormente descritas como sondas para la detección de la placa de aterosclerosis. La hipótesis para este estudio se basa en la abundante presencia de la enzima Fosfolipasa-C en la placa. Dicha enzima está

216

implicada en la regulación de fenómenos de apoptosis y autofagia de las células del endotelio vascular. Además, su actividad catalítica se basa en la degradación específica de la cabeza polar en la molécula de fosfatidilcolina. Por lo tanto nuestra hipótesis consistió en que, si las PC IONP se acumulan en la placa, debido a su composición podrían quedar "atrapadas" en la zona de la lesión por la acción de la fosfolipasa-C. Dicha enzima degradaría las cabezas polares que dan estabilidad coloidal a las partículas, de esta forma perderían dicha estabilidad y se acumularían de forma selectiva allá donde la enzima es activa. El efecto final sería similar al que se consigue con la ^{18}F-fluorodeoxiglucosa en PET, la acumulación metabólica de la sonda. En primer lugar se probó esta aproximación *in vitro* con la enzima activa y se monitorizó la evolución del tamaño y de los valores de relaxividad en función del tiempo y de la concentración de enzima (figura 5.7). Como se observa en la Figura 5.7 el efecto es el esperado al eliminar la cabeza polar que estabiliza la micela y volver a tener nanopartículas con carácter hidrófobo. El mismo efecto se observa al medir la relaxividad, un aumento del T_2 al agregarse las nanopartículas. El mismo comportamiento se observó al analizar la captación por parte de los macrófagos de las PC IONP. Los macrófagos M1, proinflamatorios, presentan una expresión mucho mayor de la enzima que los M2, antiinflamatorios. Esta diferencia se comprobó que se correlaciona perfectamente con una mayor captación de las PC IONP por parte de los M1. Debido a la sobreexpresión de la enzima en estos la cantidad de nanopartículas atrapadas es también mucho mayor.
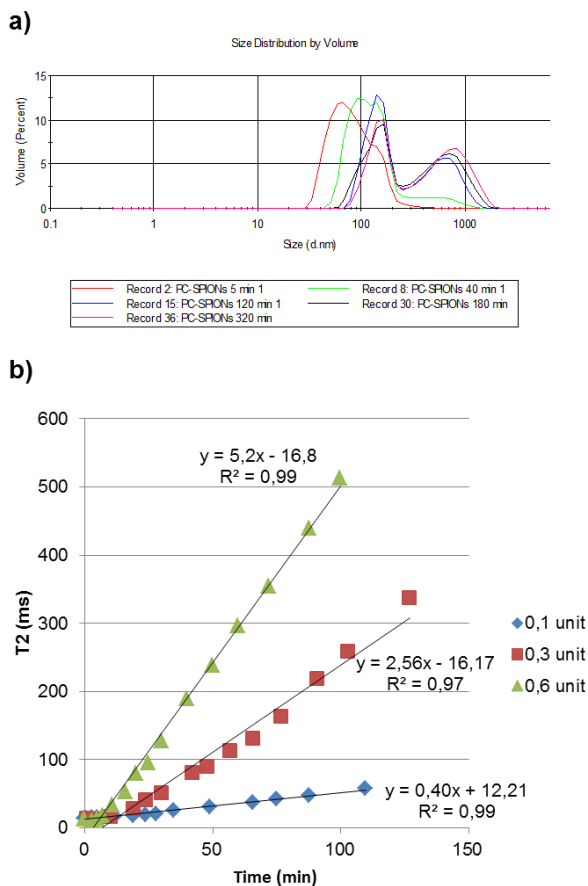
a)

Size Distribution by Volume

Record 2: PC-SPIONs 5 min 1 — Record 8: PC-SPIONs 40 min 1
Record 15: PC-SPIONs 120 min 1 — Record 30: PC-SPIONs 180 min
Record 36: PC-SPIONs 320 min

b)

Figura 5.7. a) evolución del tamaño hidrodinámico de las PC IONP (0.035 mg Fe ml^{-1}), desde 5 minutos a 180 minutos, al incubar las partículas a 37ºC con fosfolipasa-C (0.6 U). b) Relaxividad T_2 de las PC IONP (0.035 mg Fe .ml^{-1}) al incubarlas con distintas concentraciones de enzima (0.1 U, 0.3 U and 0.6 U).

Con estos resultados decidimos probar nuestra hipótesis *in vivo*. Para ello se emplearon ratones ApoE-KO de 48 semanas, 18 semanas en dieta hipercolesterolémica. La imagen se realizó en un equipo de MRI de 7 T, basal y 24 horas después de la inyección de las partículas. Como se aprecia en las

imágenes seleccionadas en la figura 5.8 la acumulación es claramente visible en la zona de la lesión con la típica señal hipointensa, así como con la cuantificación que demuestra la reducción en la intensidad de la señal en comparación con la imagen basal y referenciándolo al músculo del animal.
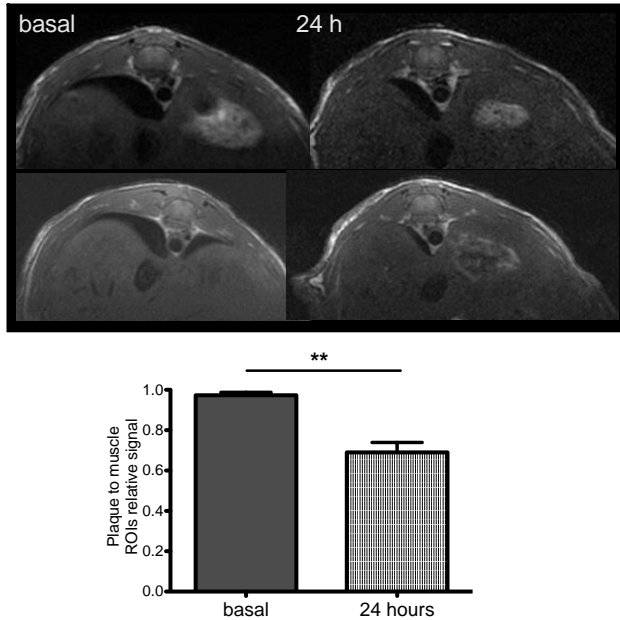

Figure 5.8. a) Imágenes en T_2 de ratones apoE-KO antes de la inyección y 24 horas después b) Cuantificación de la señal relativa placa-músculo basal y a 24 horas.

En resumen creemos que en este apartado demostramos la acumulación selectiva de las PC IONP en la placa de aterosclerosis debido a tres factores; 1) El largo tiempo de circulación de las nanopartículas, visto en el apartado anterior, 2) la acumulación de apolipoproteínas en la corona proteica, también visto en el primer partado y 3) la degradación enzimática por parte de la fosfolipasa-C. Estos tres factores puestos en conjunto explican la

acumulación pasiva de las partículas en la zona de la lesión y su posterior retención por la actividad de la enzima.

4. Multifuncionalización paralela de nanopartículas: Síntesis modular en un solo paso para imagen molecular *in vivo*.

La capacidad de sintetizar sondas multifuncionales es una de las principales ventajas del uso de nanopartículas. Sin embargo hasta la fecha dicha multifuncionalización suele llevarse a cabo mediante largos y tediosos procesos sintéticos que, entre otras cosas, tienen efectos perjudiciales para la estabilidad coloidal de las nanopartículas. Con esta idea nos planteamos desarrollar un método que permitiera, en solo paso, la obtención de nanopartículas estables en agua y con propiedades multifuncionales. Para ello el primer paso fue la síntesis de partículas hidrófobas recubiertas de ácido oleico. El propósito de esta aproximación era obtener un método sencillo, convergente, que se pudiera aplicar a una gama variada de nanopartículas, por esta razón se sintetizaron IONP, UCNP y AuNP recubiertas de oleico por el mismo método descrito en anteriores capítulos. Nuestra aproximación en paralelo se basa en el empleo de la Albúmina (BSA) como agente que proporcione estabilidad en agua y que pueda ser prefuncionalizado. De esta forma el primer paso era comprobar si se podía emplear la BSA para la estabilización directa de las NP hidrófobas. Para ello se aplicó el proceso de la nanoemulsión previamente descrito pero usando la BSA en lugar de la PC. La interacción, en este caso, se produce entre las cadenas hidrófobas de ácido oleico y los centros receptores de sustancias hidrófobas que están presentes en la BSA. Dicha emulsión produjo NP estables en agua, BSA IONP, BSA UCNP y BSA AuNP de unos 100 nm de tamaño. Las partículas fueron caracterizadas y la presencia de BSA en la superficie confirmada por entre otras técnicas, espectrometría de masas.

Además, se llevaron acabo reacciones control para descartar que la BSA estuviera simplemente adsorbida sobre la superficie hidrófoba de las partículas. Para ello, previo a la nanoemulsión, la BSA se incubó con una concentración elevada de ácido oleico libre de forma que nos aseguramos que los centros receptores están saturados. Estas OA-BSA fueron utilizadas entonces en el proceso de nanoemulsión, sin embargo esta vez fue imposible obtener partículas estables en agua, recuperándose las partículas hidrófobas originales en los tres casos.

Una vez que el método demostró ser capaz de generar partículas estables en agua lo aplicamos a la síntesis de sondas multifuncionales. Para ello se llevó a cabo la prefuncionalización de los diferentes módulos de BSA; con un fluoróforo (Alexa647), otro con DOTA, un agente quelante para ^{68}Ga, otro con DFO, un agente quelante para [89]Zr y por último con maleimida para la unión de biomoléculas a través de grupos tioles libre.
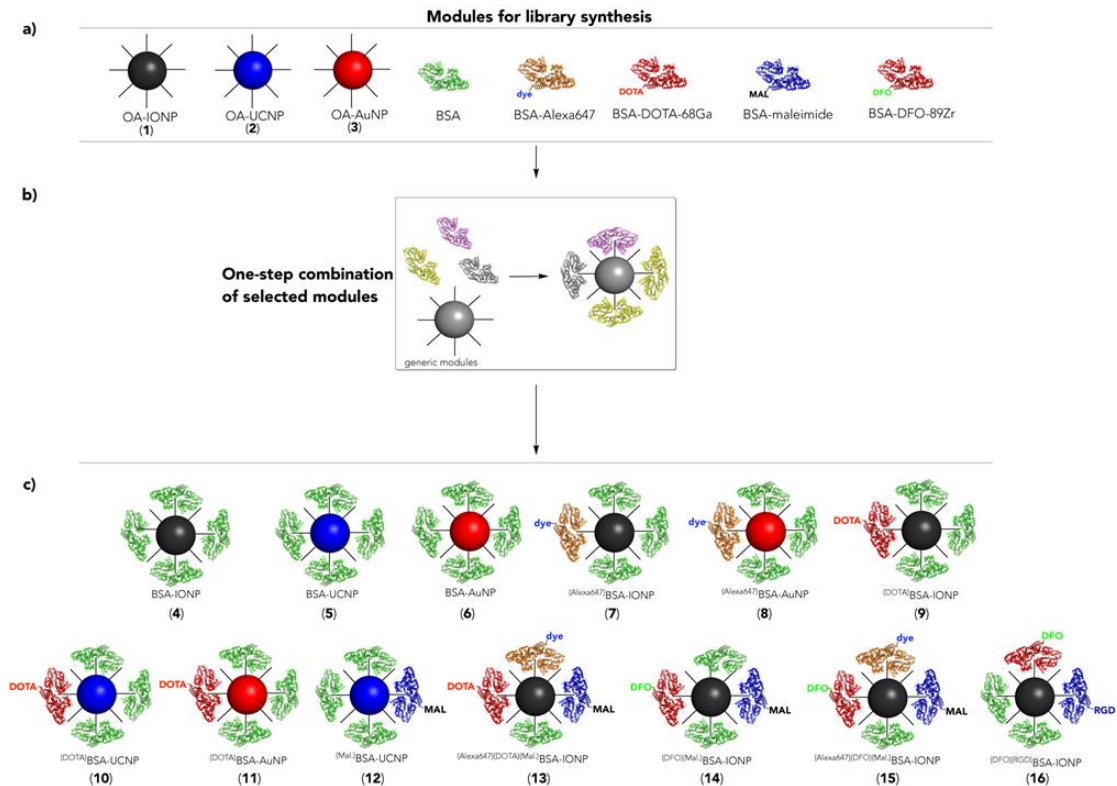
Figura 5.9. a) módulos prefuncionalizados para la síntesis, b) proceso de nanoemulsión y c) librería de nanopartículas multifuncionalizadas por combinación de los distintos módulos.

Con esta aproximación se preparó una librería de 13 nanopartículas diferentes (Figura 5.9), desde partículas para fluorescencia y MRI, para PET y MRI a partículas para, al menos dos técnicas de imagen, y la posibilidad de unir alguna biomolécula vía el grupo maleimida. Las principales características fisicoquímicas de la librería de nanopartículas fueron estudiadas; tamaño hidrodinámico, composición superficial, valores relaxométricos, propiedades ópticas y magnéticas, algunas de dichas propiedades se recogen en la tabla 5.1.

Tabla 5.1. Librería de nanopartículas preparada, principales propiedades fisicoquímicas y modalidades de imagen en las que pueden ser empleadas.

BSA NP	% modified BSA	Size (nm)	pdi	Zeta potential (mV)	Imaging properties
BSA IONP	n.a.	97.2	0.18	-19.7	T_2 MRI
BSA UCNP	n.a	94.3	0.19	-17.9	T_1 MRI/ Fluorescence
BSA AuNP	n.a.	102.5	0.15	-9.5	UVvis/ fluorescence
(Alexa647)BSA IONP	3% Alexa647	93.0	0.15	-13.5	T_2 MRI / Fluorescence
(Alexa647)BSA AuNP	3% Alexa647	108.9	0.22	-11.1	UVvis / fluorescence/ FRET
(DOTA)BSA IONP	8 % DOTA	104.9	0.17	-10.8	T_2 MRI / PET
(DOTA)BSA UCNP	8 % DOTA	78.7	0.20	-25.7	T_1 MRI / Fluorescence / PET
(DOTA)BSA AuNP	8 % DOTA	87.5	0.13	-19.8	PET / UVvis

Tabla 5.1. (Cont.)

(Mal.)BSA UCNP	30 % Mal	100.9	0.15	-23.1	T_1 MRI / Fluorescence / targeting
(Alexa647)(DOTA)(Mal.)BSA IONP	6% Alexa647 3 % DOTA 30 % Mal	90.2	0.19	-8.9	T_2 MRI / PET / Fluorescence / targeting
(DFO)(Mal.)BSA IONP	20 % DFO 20 % Mal	91.9	0.18	-13.9	T_2 MRI / PET / targeting
(Alexa647)(DFO)(Mal.)BSA IONP	6% Alexa647 20 % DFO 15 % Mal	78.4	0.16	-12.0	T_2 MRI / PET / Fluorescence / targeting
(DFO)(RGD)BSA IONP	20 % DFO 20 % RGD	94.2	0.15	-14.5	T_2 MRI / PET / Angiogenesis

Finalmente, como demostración de la utilidad de esta aproximación se desarrolló una sonda triple la cual contenía óxido de hierro en el núcleo, el agente quelante DFO en la superficie para el marcaje con ^{89}Zr y el péptido RGD para la detección de zonas de angiogénesis.
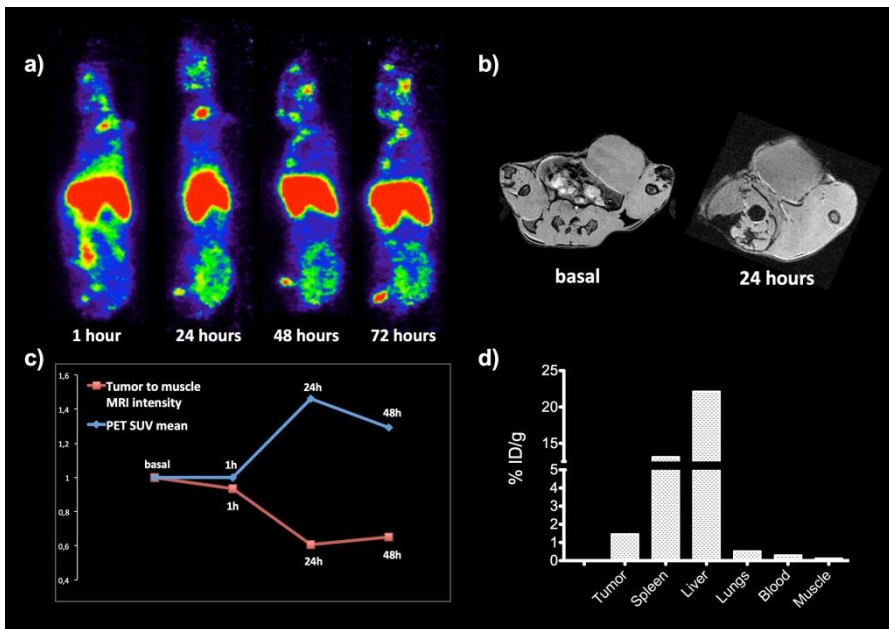
Figura 5.10. a) Imagen PET de $(^{89Zr})(^{RGD})$BSA IONP a diferentes tiempos post-inyección en modelo murino alograft de tumores; b) imagen T_2-MRI del mismo ratón previo a la inyección de la sonda y 24 horas post-inyección; c) Intensidad de la señal en la zona tumoral por PET (azul) y MRI (rojo) a diferentes tiempos y d) actividad medida en contador gamma de distintos órganos (72 h post-inyección).

Los resultados obtenidos al inyectar dicha sonda en modelos tumorales en ratones se recoge en la figura 5.10. En dicha figura puede apreciarse claramente la acumulación en la zona tumoral por PET (Figura 5.10 a) y por T_2-MRI (Figura 5.10 b). Como puede apreciarse la cuantificación de la señal en la zona del tumor claramente coincide con los resultados de la imagen. Asimismo la biodistribución muestra una gran acumulación de actividad en la zona del tumor, además de la típica en hígado y bazo. Finalmente, la histología del tumor confirmó la presencia de óxido de hierro mediante el uso de azul de Prusia como tinción.

225

4. Micelas de óxido de hierro recubiertas con glicósidos con propiedades antitumorales.E

El uso de conjugados entre glicósidos y cadenas alifáticas derivadas del ácido oleico han demostrado poseer propiedades prometedoras dada su capacidad antimitótica en cultivos de células cancerosas pero limitadas posibilidades de actuación *in vivo* debido a su baja solubilidad en medio fisiológico y rápida degradación enzimática. Dada la estructura de estos glicósidos (Figura 5.11 b) nuestra hipótesis se basó en que el empleo de dichos compuestos podría llevar a la obtención de estructuras tipo liposomas en las que la doble capa lipídica estuviera formada entre las cadenas alifáticas del ácido oleico de las nanopartículas de óxido de hierro y las cadenas hidrófobas de los glicósidos. De esta forma la estructura glicosídica, polar, quedaría hacia el exterior dando estabilidad en agua a las nanopartículas y, en un solo paso, se habría conseguido la estabilización en agua y la introducción de funcionalidad biológica a las nanopartículas.
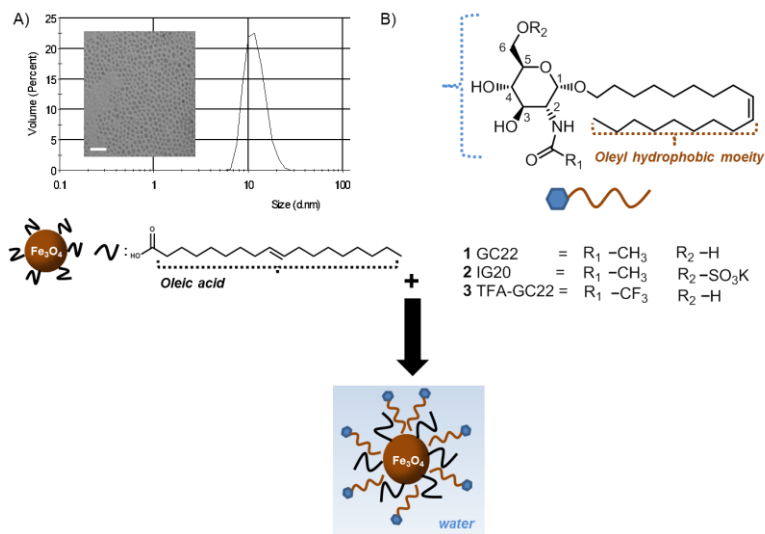

Figura 5.11. Esquema general de la síntesis de micelas de óxido de hierro recubiertas de glicósidos.

Las tres micelas así sintetizadas fueron caracterizadas y sus principales propiedades se recogen en la tabla 5.2.

Tabla 5.2. Caracterización de las micellas.

Glicósido IONP micela	Tamaño (nm)	pdi	potential Z (mV)	[Fe] (mg/ml)	[glicósido] (mg/ml)	Relaxometría ($s^{-1}.mM^{-1}$)
IV.IV	40.5	0.24	-27	0.6	≈ 2.5	r_1 2.7/r_2 140
IV.V	52.2	0.15	-42	1.1	3.1	r_1 4.4/r_2 195
IV.VI	49.1	0.17	+53	0.3	≈ 2.5	r_1 3.6/r_2 137

El tiempo de circulación en sangre de las nanopartículas, valor clave para su utilización *in vivo* especialmente en aplicaciones de transporte de fármacos, fue de unos 20 minutos para las tres micelas. Este valor además de ser similar al de partículas sintetizadas mediante rutas mucho más complejas, es más que suficiente para su utilización. A continuación se estudió la capacidad antitumoral de las micelas sintetizadas en cultivos celulares con células de glioma de rata (Figura 5.12) y humanas de tumor pulmonar (Figura 5.13) y se comparó con el resultados de los glicósidos libres.
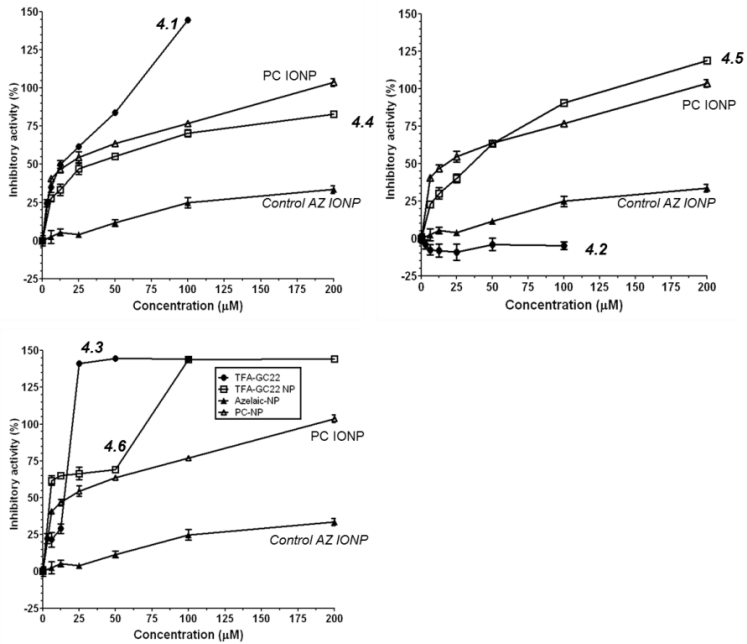
Figura 5.12. Actividades inhibitorias de los glicósidos libres (4.1, 4.2 y 4.3) y de las micelas glicosido-IONP (4.4, 4.5 y 4.6) con respecto a su concentración molar en células de glioma de rata (C6) después de 48 h de incubación.
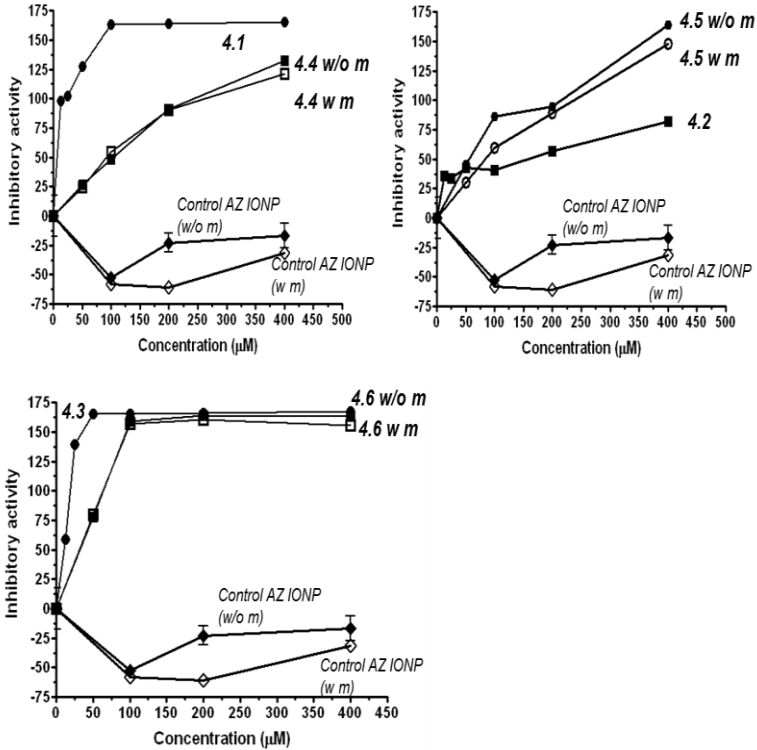
Figura 5.13. Actividades inhibitorias de los glicósidos libres (4.1, 4.2 y 4.3) y de las micelas glicosido-IONP (4.4, 4.5 y 4.6), con y sin imán en la placa de cultivo, con respecto a su concentración molar en células humanas de tumor pulmonar (A549) después de 48 h de incubación.

De estos resultados lo más interesante es el caso de la micela 4.5 ya que consigue unas muy buenas actividades inhibitorias en ambas líneas celulares con un glicósido que no muestra actividad, en glioma, o la que presenta es muy baja, en tumor pulmonar. El siguiente paso en este proyecto será el estudio de estas micelas *in vivo* en modelos tumorales para comprobar si se produce el mismo efecto inhibitorio.

General Materials and Methods

Synthesis of OA IONP, OA UCNP and OM AuNP

The OA IONP were synthesised using iron acetylacetonate as precursor and phenyl ether as solvent based on a method we published before.[7] A mixture of Fe(acac)3 (0.71 g, 2 mmol), 1,2-hexadecanediol (2.38 g, 10 mmol), oleic acid (1.69 g, 6 mmol), oleylamine (1.60 g, 6 mmol) and phenyl ether (20 mL) was added to a three-neck flask. The reaction mixture was heated under mechanical stirring and a flow of nitrogen gas up to a temperature of 200 ºC. This temperature was maintained for 120 min and the solution was then heated under reflux at 254 ºC for 30 min with a nitrogen balloon on the top of the condenser. Subsequently, the solution was cooled to room temperature. To remove side products, ethanol was added to the reaction mixture and the resulting solution was centrifuged at 8500 rpm for 10 min. The supernatant was decanted, n-hexane (20 mL) and oleic acid (0.05 mL) were added to the NP, and the suspension was centrifuged at 8500 rpm to remove aggregates and obtain a stable suspension.

The OA UCNP in this case refers to the OA coated $NaGd_{74.5\%}F_4:Yb_{25\%}$, $Tm_{0.5\%}$ @$NaGdF_4$ nanoparticles. In a typical procedure[44], lanthanide precursors $GdCl_3.6H_2O$ (2.235 mmol; 830.7 mg) $Yb.6H_2O$ (0.75 mmol; 290.6 mg) $TmCl_3.6H2O$ (0.015 mmol; 5.73 mg) were mixed in a three neck round bottom flask with a mixture of 30 mL oleic acid and 45 mL 1-octadecene. The mixture was heated to 130ºC during 30 min to obtain a homogeneous and optically clear lightly brownish solution. Reaction mixture was then cooled to room temperature before the dropwise addition of a 30 mL methanolic solution containing NaOH (0.3 g) and NH_4F (0.446 g). The solution was kept stirring for 30 min and then temperature was raised until 110ºC with moderate vacuum in order to completely evaporate the methanol. Then a thermic treatment under nitrogen atmosphere was applied by increasing the temperature rapidly at 300ºC and maintaining it for 90 min. Finally the solution was cooled down to room temperature and the nanoparticles were next precipitated by addition of ethanol (30 mL) and methanol (20 mL). After centrifugation at 5000 rpm for 20 min, the supernatant was decanted and nanoparticles collected for other two washes with ethanol. Finally the OA coated $NaGd_{74.5\%}F_4:Yb_{25\%}$, $Tm_{0.5\%}$ were dried before being dispersed and stabilised in n-hexane (30 mL). The procedure for the core addition synthesis was very

analogous. $GdCl_3 \cdot 6H_2O$ (2 mmol; 0.7434 g) was added to a three neck round bottom flask with a mixture of 20 mL oleic acid and 30 mL of 1-octadecene and was heated at 130ºC during 30 min to obtain a homogeneous solution. Temperature was cooled down to 25ºC for the addition of 20 mL of n-hexane solution of the $NaGd_{74.5\%}F_4$:$Yb_{25\%}$, $Tm_{0.5\%}$ previously prepared (2 mmol). After evaporation of the n-hexane at 100ºC, solution was brought back again to room temperature before the dropwise addition of a 20 mL methanolic solution containing NaOH (0.2 g) and NH_4F (0.2964 g). A thermic treatment under nitrogen atmosphere was then applied by increasing the temperature rapidly at 300ºC for 90 minutes. Finally the solution was cooled down and the core/shell nanoparticles were next precipitated by addition of ethanol (30 mL). The nanoparticles were washed with ethanol thrice by centrifugation cycles (5000 rpm, 20 min). The obtained OA coated $NaGd_{74.5\%}F_4$:$Yb_{25\%}$, $Tm_{0.5\%}$ @$NaGdF_4$, abbreviated OA UCNP were finally dispersed in n-hexane.

The OM AuNP were synthesised through the thermal decomposition route.[45] Briefly, 100 mg of $HAuCl_4 \cdot xH_2O$ was added in a 1:1 mixture of toluene and oleylamine (20 mL net volume). Following a brief sonication, so as to homogenize the solution, the mixture was transferred to reflux system, with continuous stirring at 80ºC and under inert atmosphere, for 3 h. The sample thereafter was cooled down to room temperature, and an equal amount of n-hexane added to it. After this, ethanol purification was done in order to remove the excess of oleylamine. This involved addition of ethanol to the above solution and centrifugation at 12000 rpm at 15ºC for 30 minutes. After 3 consecutive washings, the precipitate was finally re-dispersed in 10 mL of n-hexane.

Physicochemical characterisation of the NPs

The hydrodynamic size, polydispersity index and zeta potential of the nanomicelles were measured with a Zetasizer Nano ZS90 (Malvern Instruments, UK) using folded capillary cells. Morphology and core size were determined using a 200-keV JEOL-2000 FXII transmission microscope (Jeol Ltd. Japan) at the National Center of Electron Microscopy of the University Complutense of Madrid. For the preparation of the sample, a drop of a dilute magnetic nanoparticle suspension was placed on a carbon-coated copper grid and the solvent allowed to evaporate at room temperature (RT) for

24h. Fourier transform infrared spectroscopy (FT-IR) spectra were obtained on a Perkin Elmer Spectrum 400 Series spectrometer (Perkin Elmer, USA); each spectrum was obtained by averaging 32 interferograms with a resolution of 1 cm^{-1}. Thermogravimetric analysis (TGA) spectra were obtained with a Seiko TG/ATD 320 U, SSC 5200 (Seiko Instruments, Japan) at the Institute of Materials Science of the University Autónoma of Madrid. The dried PC NPs were heated from 20ºC to 1000ºC at 10ºC/min under an air flow of 100 ml.min-1. Mass spectrometry was performed with in a Bruker Esquire 3000 apparatus (Bruker Daltonik, Germany) equipped with an ESI source and an ion trap analyzer, coupled to an Agilent 1100 capillary LC system (Agilent Technologies, USA). The sample was diluted 1/10 in water/methanol (1:1) before the LC/MS analysis. The analysis were carried out by FIA (flow injection analysis), working in both polarities, using a 0.1% formic acid/methanol (50/50) mix as the mobile phase to promote ionisation, at 0.1 mL/min.

Magnetic characterisation. Magnetic characterisation of the samples was carried out in a vibrating sample magnetometer using 100 µL of solution in a special sample holder. Magnetisation curves were recorded at room temperature by first saturating the sample in a field of 1 T. The magnetisation values were normalised to the amount of iron to yield the specific magnetisation (emu/g Fe). The initial susceptibility of the suspensions was measured in the field range ±100 Oe, and the saturation magnetisation values (Ms) were evaluated by extrapolating to infinite field the experimental results obtained in the high field range where the magnetisation linearly increases with 1/H. For determination of the NMR relaxometric values, the T_2 and T_1 relaxation times were measured in a Bruker MQ60 (Bruker Biospin, Germany) with a T_2 cp and T_1 ir mb sequences. The relaxation rate Ri values ($1/T_i$, s-1,i = 1, 2), obtained from the measured relaxation times (T_i, s) were corrected by subtracting the water relaxation rate in the absence of the contrast agent. Linear fitting of the data gives straight lines whose slopes are the relaxivities (r_i, s^{-1} mM^{-1}) related to the iron concentration (mM): $R_i = R_{bi} + r_i$ [Fe].